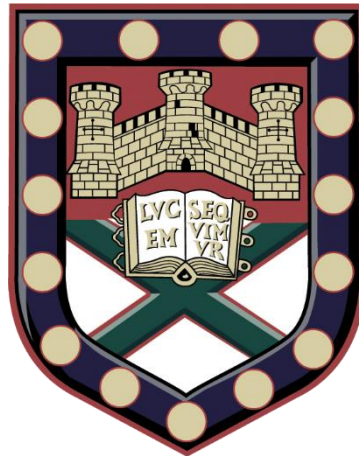# The Multiscale Biomechanics and Mechanochemistry of the Extracellular Matrix Protein Fibres: Collagen & Elastin

Submitted by

RYAN STUART EDGINTON
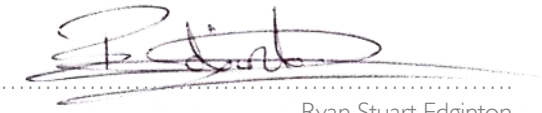
to the University of Exeter as a thesis for the degree of

DOCTOR OF PHILOSOPHY IN PHYSICS

June 2018

....
Ryan Stuart Edginton

Thesis Supervisors:

Dr. Francesca Palombo | Prof. C. Peter Winlove | Prof. Nick Stone

Abstract

Collagen is the most abundant protein in the animal kingdom and, together with elastin, forms extensive fibrous networks that constitute the primary structure of the mammalian extracellular matrix, respectively endowing it with the tensile and elastic properties that fulfil its principal role as the passive framework of the body. The fibrous proteins are distinctly hierarchically organised from the molecular scale upwards; for example, the nanoscale tropocollagen monomer assembles in arrays that form the micrometer scale microfibrils and fibrils, and thence into collections of millimetre scale collagen fibres, that in-turn, constitute functional tissues such as skin, tendon and bone. Much is known about the structure at each of these individual scales – collagen being the most extensively researched – and the macromechanics of the fibres are well established. However, far less is known about the micromechanics of these proteins, in particular how the monomers influence the functional mechanics of the macroscopic fibres. In this thesis, I explore the multiscale mechanics of collagen and elastin fibres over a range of hydrations – with fibres in direct contact with aqueous solution, and progressively dehydrated in humidity-controlled environments. I use quasi-static tensile testing to probe the macroscopic mechanical response (Young's modulus and stress relaxation) of the fibres, and employ Brillouin and Raman microscopy to assess the longitudinal modulus in the GHz range and corresponding molecular properties of the proteins. Brillouin microscopy is an emerging technique in the biomedical field. It enables the all-optical, contact-free and non-

destructive testing of tissue micromechanics through detection of frequency shifted light scattered off thermally excited acoustic waves or "phonons" in the GHz range. As one of the first studies of Brillouin light scattering in these fibres, it sets the basis for further investigation of tissue biomechanics. In particular, I provide the full description of the protein fibre micromechanics by performing angular measurements using a so-called platelet-like configuration with sample mounted onto a reflective substrate at 45° angle to the excitation beam. I derive the high-frequency longitudinal modulus, and discuss the results in comparison to the Young's modulus, in terms of the different frequency and spatial scale of the measurements. I obtained a full description of elasticity using Brillouin spectroscopy applied to dried fibres; however, obtaining the same description in hydrated fibres is a challenge, as the Brillouin spectrum is dominated by water. An assessment of the mechanical differences between type-I and type-II collagens is also given here.

Water is known to be a primary determinant of tissue biomechanics, and I identified for the first time, the critical hydration ranges between 100 and 85% relative humidity (RH) for collagen, and around 85% RH for elastin, at which point each macroscopic fibre switched from viscoelastic to plastic-like behaviour. Dehydration below these critical points was shown to severely diminish collagen fibrillar sliding, and completely rob elastin of its ability to reversibly deform under strain. The Young's modulus increased markedly below these hydrations, and I observed a parallel increase in the longitudinal modulus at high frequencies in each protein, indicating a concomitant increase in stiffness at the two scales. The major difference observed between the two fibrous proteins is that, in the case of elastin, I observe a two-fold increase in the longitudinal modulus as the hydration is decreased from 100 to 21% RH, whilst the Young's modulus increases by two *orders* of magnitude. This discrepancy was not observed in collagen, which confirmed that the protein maintained its long-range order in the form of the triple helix at all hydrations employed in this work, whilst the elastin ultrastructure experiences a liquid-to-solid state change at a critical hydration.

I demonstrate through the analysis of the low-wavenumber region (<500 cm^{-1}) of the Raman spectrum, that the increase in molecular stiffness of both proteins, is reflected in an increase in torsional rigidity of the peptide backbone upon dehydration. Moreover in collagen, I observe a reduction in the number of inter-protein water bridges, which I propose causes a collapse of the lateral spacing between monomers and an increase in direct backbone-backbone hydrogen bonding, that further stiffens the fibre. Small strain induced reorientations of the amide III and C–C stretching modes in dehydrated collagen fibres suggest that macroscopic

stresses may be transferred to the triple helix, otherwise left unperturbed in the hydrated state. I postulate that this is a result of the degraded intra- and interfibrillar sliding mechanism below the critical hydration. Hence in its dehydrated state, the collagen whole-fibre mechanics are similar to those at the molecular scale. The role of proteoglycans and glycosaminoglycans and their potential connection to hydration, is also discussed.

In agreement with previous work, I found no Raman spectral changes as a result of stretching hydrated elastin fibres, indicating that even large strains e.g. 80%, have no significant effect on the structural scale probed by Raman microscopy, nor in the air-dried state where the brittle fibres break at low strains. I suggest this may imply a limited sensitivity of Raman bands to these changes, possibly an indication of elastin's dynamic ultrastructure, or that stress is dissipated at a higher level of the fibre structure. On the macroscopic scale, it is the poroelastic nature of elastin which controls the stress relaxation under strain, and the elastic recovery is mediated by an interplay of hydrophobic interactions and hydration forces.

Acknowledgements

Who would have thought that a Feltham Community College boy crossing the airpark from Oriel, would write a doctoral thesis on biomedical physics!? Certainly not me! But here it is.

Many people think science and physics in particular, a lonely venture, but nothing could be further from the truth. It is a massive social endeavour and I owe so many thanks to all my friends, family, supervisors and colleagues for pulling me through these last four years, and giving me a vibrant new perspective on the world.

Firstly, to Francesca, my long-suffering supervisor who never stopped believing in what I was capable of, even when I refused to believe in it myself. I still have so much to learn and do in this regard, but thank you for your endless patience, for taking a chance on me that afternoon in July 2013 and for supporting me along the path ever since. You have been the most brilliant supervisor and mentor. Your passion and constant energy continue to amaze me every day, and it has been my greatest pleasure to have been your first doctoral student.

Second to Peter, the professor who I blame for getting me into this mess in the first place, and who's not been able to get rid of me since he first interviewed me for my undergraduate place

at Exeter back in 2008. Thank you for introducing me to the world of biophysics and for putting me forwards to Nick and Francesca as a half-decent bloke to consider for a PhD, after putting up with me in your own lab for two years. But thank you most for instilling in me a wider view of the research community, with a healthy disregard of the accepted rules, and for being the one academic who taught us that the occasional (or frequent!) failure was okay. I only wish that I'd come up to you more often for chats over a properly boiled cuppa and the occasional biscuit extravagance.

Thank you also to Nick, who's door has always been open with a beaming smile on the other side, even when he was desperate to hide from the constant barrage of PhD, post-doc and staff hands knocking to take him away from work, or give him even more to do. I will forever be in awe of your ability to manage a million different thoughts and problems at once, and still find the time to stop, laugh, and help us with each of our own struggles.

And to Ellen, thank you so much for your all your support and guidance in the lab over these last six years.

I have been lucky enough to have worked in THE most talented, fun and diverse research group at Exeter. You guys have made every day an absolute treat and I cannot thank you ALL enough for all the care you've shown me, and all the fun times that we've shared together (after I'd eventually rocked up, anyway! #WhereTheFuckIsRyan #EdgintonTime #ThatImpyOvation). The BioPhys list is long, but this is MY thesis and this is the only bit anyone ever reads, so I'm going to write as much as I bloody well like! Alex, my brilliant, sneaky lab partner-in-crime who probably bears equal responsibility with Peter for getting me stuck in the world of biophysics – thanks for the continued belief and encouragement mate, the #Team will live forever on (and maybe one day we'll write that RBC paper together!). Kelly, for always being behind me whenever I turned around and for being my criminal, chief chatting buddy – thanks for always listening and letting me listen to you. . . oh and for bringing all the doggy friends for me to make a fuss of too! Sahand (who Theresa still hasn't managed to deport – and a good job too, because life wouldn't be the same without you nearby mate) and Krups, who've been my main Known Associates in politically incorrect fun these last few years! The founding members of H.I.T.L.E.R, who trampled the countryside of the South West under the mighty heel of their jackwalkingboots, and originated several of what some would describe as the "Top Ten: Least Worst Days in the UK": Lou (my work wife who I

could not have done without); Mr Claudio (of Endorsement fame); Jen (for turning up on time and generally being bloody grand!); Sarah (who continues to put up with my English merde); Dave 'Not the Hubspace we deserve but the constant Heart of Biophysics that we need' Colridge; and Toby (my preferred choice of street wedding priest). Thanks also to Ben, my fellow Rebel Scum; Leanne, for some great times on the road; Lauren for being a great desk buddy even though I delayed her submission with the constant distractions; Natalie, Inge, Carl, Adrian and more recently to Rikke, Fay, Rich, Nick, King Bob! Seb, Noemi, Michelle, Michael (& Uli), Pascaline, Anna, CHRISTMAS!-Beth, and by no means least Skye, who has and have each brought an immense new life to the end of my time here in Exeter.

I was also so fortunate to be part of the supervisory group of the Exeter iGEM team, and I am indebted to Paul, Chloe, John, Tom, Christine and Jamie, for giving me the opportunity to help shape and support our fantastic gold medal winning undergraduate teams, who delivered some truly inspiring SynBio projects. Every year it was without fail, the most entertaining escape from the day-to-day PhD struggle, I learnt so much, and the trips to Boston weren't a bad perk of the job either! After all, where would I be without a visit to James Hook & Co!?

Grazie mille alla mia famiglia di ricercatori a Perugia, a Daniele, Silvia, Paola, Marco e soprattutto a Sara, Maria e Beatrice per avermi accolto nel gruppo e avermi fatto conoscere la brillantezza della spettroscopia Brillouin e la bellezza dell'Italia. . . (E su Google Translate perché sto ancora lavorando al mio Duolingo!)

The final office thanks goes to Alice Mills, for introducing me to the fantastical world of science outreach and for generally being the most lovely, nuts human being.

. . . Oh! And of course, Her Majesty the Queen, for beaming constant good vibes from the picture frame on my desk. Thanks Ma'am!

To my housemates: Tim, for the regular late-night sit downs and the nightly Mash Reports that made the first three years more manageable (MOVE!!!); Lucy for absorbing all my Franco abuse; Jess, for being the most unassuming inspiration – we shall watch your career with great interest; Sam, now SEVENTEEN months on from those original two months that I was gonna stay, I cannot tell you how grateful I am to you for giving me a home and never asking for anything in return – you will forever be welcome under any roof that I call my own; Martha, who wasn't physically in the house but whom I wouldn't have had the home without – thank

you for being the little bundle bursting with all the Hellenic passion and energy that you are, for being my desk buddy and my friend. And of course, to Chris, the repeat offender, who knows that the journey doesn't end here. There are white shores ahead mellonamin, and beyond, a far green country under a swift sunrise.

And finally, to the old guard who've been there through it all. To Gaz and Stace, who come every year to remind me of home. To my Mum and Dad who've given me the world and the freedom to explore it, and who are always there for me when it all gets a bit too much. To my uncle Graham, who's always been cheering for me. And to my grandparents: Grandad Bernard, Grandad John and Nan Moyra, who are with me every day, but who I wish could still occasionally rock up in that old blue Transit, set for the latest shenanigans, or be just round the corner for a cuppa and a chat about everything that's happened over the last week; and of course to Nan Doreen who's still causing trouble at the other end of the phone, and to whom I will always be eternally grateful to, along with uncle Billy, for opening up so many possibilities for the new adventures to come.

Ryan Edginton   *The Window, Queen's Crescent Garden*

April 2018

Updated September 2018

Oh look! Something that wasn't there. Fantastic!

- Jim Carrey | Comedians in Cars Getting Coffee (2015)

List of Publications

Research Articles

- Rayko I. Stantchev, Jessica C. Mansfield, **Ryan S. Edginton**, Peter Hobson, Francesca Palombo and Euan Hendry, *Subwavelength hyperspectral THz studies of articular cartilage*, Scientific Reports, 8: 6924 (2018)

- **Ryan S. Edginton**, Ellen M. Green, C. Peter Winlove, Daniele Fioretto and Francesca Palombo, *Dual scale biomechanics of extracellular matrix proteins probed by Brillouin scattering and quasistatic tensile testing*, Proc. SPIE 10504, Biophysics, Biology and Biophotonics III: The Crossroads, 105040J (2018)

- **Ryan S. Edginton**, Sara Mattana, Silvia Caponi, Daniele Fioretto, Ellen Green, C. Peter Winlove and Francesca Palombo, *Preparation of Extracellular Matrix Protein Fibres for Brillouin Spectroscopy,* J. Vis. Exp. (115) e54648 (2016)

- Francesca Palombo, C. Peter Winlove, **Ryan S. Edginton**, Ellen Green, Nick Stone, Silvia Caponi, Marco Madami and Daniele Fioretto, *Biomechanics of fibrous proteins of the extracellular matrix studied by Brillouin scattering*, J. R. Soc. Interface 11: 20140739 (2014)

Manuscripts in Preparation

- **Ryan S. Edginton**, Ellen M. Green, C. Peter Winlove and Francesca Palombo, *The influence of water on the ultrastructure of collagen and elastin: a polarisation resolved Raman study*

- Jessica Hopson, Lucy Hawkett, **Ryan S. Edginton**, Jane Hancock, Kyle Wedgewood, Francesco Tamagnini and Francesca Palombo, *Label-free chemical imaging applied to a model of progressive tauopathy*

Conference Presentations

- **Poster:** The Hierarchical Water-Mediated Mechanics of the Extracellular Matrix: A Multimodal Approach - *1st BioBrillouin Meeting* (Vienna - 2017)
- **Oral & Poster:** A multiscale analysis of the mechanical properties of the fibrous proteins of the extracellular matrix using Brillouin light scattering spectroscopy - *SciX2016* (Minneapolis - 2016)
- **Public Talk:** More than just a laser pointer: Light Scattering and the Physics of Biology - *Pint of Science* (Exeter - 2016)
- **Poster:** Brillouin Light Scattering Spectroscopy: Sensing the Elasticity of Connective Tissue – *SET for Britain* (Houses of Parliament, Westminster - 2016)
- **Oral:** Brillouin Light Scattering Spectroscopy and Elasticity in Hydrated Connective Tissue - *13th Martin & Willis Student Meeting - Infrared & Raman Discussion Group* (Exeter - 2015)
- **Oral:** The Effect of Hydration on the Macroscopic Elastic Modulus of Type I Collagen and Elastin Fibres - *21st Congress of the European Society of Biomechanics* (Prague - 2015)
- **Invited Talk:** The Biophysics of the Extracellular Matrix - *University of Perugia Department of Physics* (Perugia - 2015)

Research Awards

AUG 2016	**IPEM Student and Trainee Travel Grant**	£300 supporting conference attendance
JUL 2016	**C R Barber Trust Fund**	£175 supporting conference attendance
JUL 2016	**IOP Student Conference Fund**	£300 supporting conference attendance
JUL 2016	**Exe-BioCon Poster Prize**	£50 for best final year poster
JAN 2015	**Santander Postgraduate Research Award**	£1000 for residential and facilities usage at the Department of Physics, University of Perugia, Italy

Contents

I

Introduction

1.1.   The Extracellular Matrix

The mammalian extracellular matrix (ECM) is the dynamic network that forms the main structural scaffold of many tissues. Generated and maintained by the cells that it houses and protects, it acts as a mediator for the exchange of cellular signals and nutrients, and transfers the forces and electrical signals through which we interact with the world around us. The ECM is composed mainly of water, fibrous proteins and polysaccharide rich glycosaminoglycans (GAGs) and proteoglycans (PGs). However, tissues vary widely in their structure and in their topology; a comparatively rigid calcified bone for instance, responsible for supporting the weight of the body, is noticeably a very different material to the elastic lungs undergoing repeated deformation with each breath. Indeed, each tissue, whether connective, muscle, nervous or epithelial, plays a distinctly different role in our body appropriate to its location, highlighting the importance of composition, the balance of the base materials, and their interactions, to the highly adapted function of that particular ECM. Composition therefore plays a crucial role in the maintenance of homeostasis and in the pathology of a given tissue; but these are complex, composite materials of which many physical and chemical features of the constitutive parts are still not completely understood. It is sensible therefore, to separate the major components of the matrix and consider their contribution to the structure and function of the ECM on an individual basis. Fibrous collagen and elastin are the primary structural

proteins that constitute the mammalian ECM, endowing it with the tensile and elastic properties that fulfil its principal role as the passive framework of the body. There is an extensive literature on changes in the biochemistry of each of these polymers, and changes in their organization in the tissue with age and disease. However, it is at present impossible to determine how these changes are related to the functional biomechanics of the tissues. This lack of knowledge in turn limits understanding of the process of ageing and the development of disease, and further impedes efforts to target therapeutic measures and diagnostic techniques. A fundamental problem is our lack of understanding of tissue mechanics at the microscopic and molecular level, and this is the subject of the research described in this thesis.

1.2.   The Mechanics of Collagen and Elastin

1.2.1.   Fibre Structure and Assembly

1.2.1.1.   Collagen

Collagen comprises the largest proportion of protein in the human body (30%) and is the predominant component of the ECM. The collagens are a large family of proteins, with some twenty-eight types currently known in vertebrates. All of them are defined by a common repeating amino acid triplet, Gly-X-Y, which forms the ubiquitous triple-helix. Here every third amino acid is occupied by a glycine (Gly) residue and the X and Y positions are frequently occupied by proline (Pro) and hydroxyproline (Hyp) residues. Variations in the wider amino acid sequence lead to the unique properties that separate the different types and tertiary structures, though seven of these (I, II, III, V, XI, XXIV and XXVII) take a fibrous form. 80-90% of the collagen in the human body consists of types I-III [6], of which type-I collagen is the best-characterized and most ubiquitous. Collagen fibres are extremely stable structures with turnover times of tens of years [7, 8]. In consequence, damage or changes in their physical properties through slow chemical reactions such as glycation, can be particularly serious.

Collagen begins its synthesis in the endoplasmic reticulum (ER) of fibroblasts, where single helical chains termed procollagen are formed. These polypeptide α-chains contain the central Gly-X-Y amino acid repeating region of approximately 1000 residues, terminating at either end, in non-helical sequences known respectively as the C- and N-terminal propeptides. Self-recognition sequences contained in the C-terminal promote the alignment of three individual

α-chains, and cystine (Cys) residues similarly located, facilitate the initial inter-chain disulphide bonding at the terminus, which promotes a zipper like assembly running up to the N-terminal. Strong inter-chain hydrogen bonds form sequentially between the hydrogen atom of the Gly amide bond (N-H), and the carbonyl oxygen atom (C=O) of the residue at the X-position in the adjacent strand [3]. The nucleation process completes with the cleaving of the propeptides by N- and C-proteinases, resulting in a 300 nm long, <2 nm diameter triple-helix flanked by terminal non-helical telopeptide regions [9]. This tropocollagen monomer is the base unit of the collagen superfamily, from which mutations in amino acid sequences form specific α-chains, and varying trimeric combinations of these form specific tropocollagens appropriate to their purpose. For example, type-I collagen is formed of two $\alpha_1(I)$ chains and one $\alpha_2(I)$ chain (termed a heterotrimer – different chain combinations), whilst type-II collagen found in cartilage, consists of three identical $\alpha_1(II)$ chains (a homotrimer) [10].

Fibrillogenesis occurs spontaneously *in vitro* after the molecules have been excreted from the cell, but is mediated by the glycoprotein fibronectin *in vivo*, which is believed to aggregate collagen monomers for location-specific fibril assembly [11]. In either case, tropocollagens associate through an entropy-driven process [12] into thin microfibrils, packed in a quasi-hexagonal lattice [13] to form composite fibrils of between 10~300 nm in diameter, aligned in parallel arrays, C-terminal to N-terminal, with a characteristic D-period of 67 nm. This reflects the overlap and consequent gap regions which are instrumental to the flexibility of the fibrils. The lysine (Lys) and hydroxylysine side-chains in telopeptides also form cross-links between adjacent microfibrils in this region, imparting mechanical strength and stability to the mature fibrillar structure. Parallel arrays of fibrils can further associate into collagen fibres with diameters tailored (between 1-500 μm) to the ensemble physiology of the macroscopic tissue that they form.

1.2.1.2.   Elastin

Elastin constitutes the core component of all elastic tissues in the human body. Primarily found in tissue such as lungs and vasculature it shows impressive mechanical performance. In the aorta, for example, it experiences 42 million pressure pulses annually, and it plays a vital role in matching the mechanics of the vessel to the pulsatile ejection of the heart which is essential for the hydrodynamic efficiency of the circulation [14]. It forms primarily within the early-stages of development (late fetal and early neonatal periods) and exhibits a rapid slowdown in

synthesis with age. With an average half-life of around 70 years, it is the longest lasting protein in the human body and we live most of our lives with the same elastin that we are born with. Without appreciable repair, it must endure billions of stretch-relaxation cycles without damage or permanent deformation. In fact, the functional lifetime of elastin has been posited as one of the major physiological determinants of the human lifespan [15]; so in prolonging this limit, furthering our understanding of elastin structure and function may be key.

Elastin fibres form around the common base unit known as tropoelastin. However, unlike tropocollagen, the secondary structure of the elastin monomer is highly disordered and consequently not as well defined, although x-ray scattering measurements of the protein have at least proposed a shape for the monomer [16] and attempts to attribute functional roles to its various regions are underway. Tropoelastin is formed in the ER of smooth muscle and endothelial cells, as well as in chondrocytes and fibroblasts, and it consists of alternating hydrophobic and cross-linking domains. The former contains predominantly glycine (Gly - G), valine (Val - V), proline (Pro - P), leucine (Leu - L) and alanine (Ala - A) residues, which are believed to organise in the $(VPGVG)_n$ repeating sequence, and the cross-linking domains contain two or three Lys residues separated by several Ala, Pro or Gly residues. Whilst the tropoelastin structure is highly disordered, there is growing evidence to suggest that it is not completely random [17, 18]. The extensible hydrophobic domains adopt local β-turns and polyproline-II helices, whilst the cross-linking domains take on an α-helical conformation, conferring strength and stability to the molecule. This is still very much an active area of research, and a review by Muiznieks and Keeley [19] discusses the current reductionist approach to structure determination, with a focus on the resulting mechanical properties.

In tissues, the process of elastic fibre formation begins with the deposition of an array of microfibrils separately to the production of tropoelastin [20]. The elastin monomers are then secreted into the extracellular space, where they spontaneously coalesce into globules through an entropy driven process (which can be replicated in vitro in an inverse temperature-solubility phenomenon known as coacervation). This is the first stage in the alignment of tropoelastin, in which the hydrophobic residues of adjacent monomers self-associate under optimal conditions of temperature, pH and salt content [21]. Subsequently, cells appear to coordinate a parallel deposition of the coacervate onto the fibrillin-rich microfibrils, which act as a scaffold for the further alignment and growth of the elastic fibre. The architecture, namely the length and thickness of the elastic fibres laid down during this stage, is highly tissue specific [22] and there is still debate over the exact role of the transporting cells, and in the mechanisms of

binding [11, 23]. Finally, the Lys-rich domains are cross-linked through the action of the copper dependent enzyme lysyl oxidase, introducing strength and stability to the now insoluble, mature fibre.

This thesis will concentrate on the mechanical properties of purified elastin. It is still not clear, in general, whether the microfibrils make an important contribution to the mechanics of elastic fibres in tissues or whether their role is solely to provide templates for formation

1.2.2.   Hierarchical Fibre Mechanics

The best studied of the collagen and elastin mechanics is at the macroscale of the tissues, where large-scale, single-mode testing devices can be employed to simulate physiological movements and loads of functional components of the body. However, increasingly, to understand the true function of a tissue – particularly in the fields of prosthesis development, tissue reconstruction and replacement – there is a requirement to understand the underlying structure and operation of its constituent parts, and how each of these combine to achieve the well-studied macroscopic behaviour. In this respect, there is a considerable body of literature that studies each of the individual scales of structure and mechanics in isolation [14, 24-38]; however, the study of hierarchical mechanics is more challenging, particularly when considering the micro- and nanoscale, where multimodal techniques must be employed to probe deformation mechanisms *in situ* at a specific length scale. Such experimental setups generally involve a purpose built macroscopic compressive or tensile testing stage coupled either to a microscope, or incorporated into some spectroscopic apparatus, allowing for the impact of functional, macroscopically applied forces to be measured closer to the fundamental scale of the structure.

The following outlines the structural changes known to occur in collagen and elastin fibres at each hierarchical level, with reference to the techniques currently employed in linking the mechanics between different length scales.

1.2.2.1.   Collagen

One of the most ubiquitous structural features of collagen, visible even by eye, is the sinusoidal arrangement of collagen fibrils that constitute the larger fibres. There is an active debate in the literature over the 2D-planar or 3D-helical arrangement of the fibrils that constitute the crimp

structure in tendon, which varies widely throughout the body. Recent work has posited a dependence on the physiological role of the tissue in question; with a helical arrangement associated with energy storing tissues such as the Achilles tendon, and the planar-type linked to positional tendons such as those in rat tail [39], the most commonly researched source of collagen.

The crimp is easily resolved by light [40] or polarised light microscopy [41], and with periods of around 100 µm, is the first major structural feature to respond to the application of macroscopic strain. The period of the sinusoid increases until around 4% strain where the fibrils become aligned completely parallel to the axis of the fibre. This corresponds to the toe region of the collagen fibre stress-strain response and is widely thought to function as a shock absorbing mechanism, designed to prevent damage to the ultrastructure of the fibrils during rapid applications of force. In fact, the crimp is recoverable at strains of up to 4%, the collagen fibres behaving in a spring-like fashion up until this strain in physiological conditions.

The distinctive J-shape of native collagen fibre's macroscopic stress-strain curves allude to the hierarchical nature of the protein fibre's mechanics. Fratzl and co-workers divided the curve into three distinct sections [42], beginning with the so-called 'toe' region (mentioned above) at low-strain, where the initial fibre extension is used to open the microscopic crimp structure, and there is very little force uptake within the fibre. The following 'heel' region sees a gradual increase in stress uptake and marks the first stage of strain transfer to the fibrillar structure, where Misof et al determined an increase in the equatorial x-ray scattering intensity, interpreted as an increase in order of the molecules within the gap region of the fibrils [43]. This showed that with the crimp removed, the liquid-like telopeptide regions are the next structural feature to straighten – the first ultrastructural component to experience the effects of macroscopic strain. Once these are extended, the third section of the macroscopic stress-strain curve, the 'linear' region, begins; however, work from a range of techniques has shown that strain at the fibrillar level of tendon is lower than that applied to the whole fibre [44, 45]. More recent investigations of collagen fibrils isolated from sea cucumber and mammalian tendon and studied using microelectromechanical systems (MEMS) tests – essentially a microscale stress-strain testing apparatus – showed the fibrils to be twice as strong as the wider collagen fibre, indicating that the non-collagenous matrix of the interfibrillar space contributes to reducing the stiffness at higher structural scales [46-48]. This has also been observed in bone, which primarily consists of calcified type I collagen. Here fibrillar strains were observed to be on average half the value of the tissue strain [49]. Indeed, multiscale observations of

bovine femur using wide-angle x-ray diffraction (WAXD) and small-angle x-ray scattering (SAXS) in situ tensile tests, found that the strain ratio decreased at each level down the structural hierarchy, between the macroscopic tissue strain to the fibrils (12:5), and the fibrils to the mineral (5:2) [50]. The conclusion being that the relatively stiff nanoscale elements, were protected from damage by successive levels of stiff elements being connected to the next hierarchical scale by a softer matrix, resulting in composites that sustain large deformations despite relatively un-deformable nanoscale structures. Similar strain dissipating mechanisms incorporating a lamellar arrangement of the fibres, have been observed in other collagen-rich tissues, such as the intervertebral disc [51] and the cornea [52], a common connection between otherwise distinctly different tissue types.

Although there is some debate over the length of collagen fibrils within a fibre [53], mechanical data indicates that they are discontinuous entities that slide with respect to one another, and that interfibrillar shear stress provides the loading mechanism within the collagen fibre [54, 55]. Work by Screen and co-workers incorporating a mix of fluorescence microscopy and SAXS experiments, has demonstrated that sliding at various scales of the structural hierarchy (interfibre, interfibril and intra-fibrillar) is instrumental in providing the extensibility of tendinous tissues [56-59], and that the non-collagenous matrix bridging each successive layer of the hierarchy, facilitates and modulates relaxation mechanisms under strain. Pulling tests using atomic force microscopy (AFM) confirm this viscoelastic behaviour in the single fibril [60-62], and even at the scale of the type I tropocollagen monomer, Sasaki and Odajima found that macroscopic strain activated a combined stretching of the stiff nanoscale triple helix, together with a simultaneous sliding of adjacent monomers and a small increase in the size of the intrafibrillar gap regions [63, 64]. The role of GAGs, PGs and water in mediating these hierarchical fibre mechanics and controlling viscoelastic behaviour, is a current area of interest [65-67]. In this thesis I will discuss the relation between the components of the ground substance and explore the multiscale mechanics over a range of hydrations, not just at the fully hydrated and dehydrated extremes as is generally the case in most literature.

Polarisation resolved Raman spectroscopy has been used to map the orientation of fibrils during opening of the microscopic crimp of rat tail tendon, and then to assess the response of the triple helix to macroscopic strain within the linear region of the stress-strain curve. The authors found that the molecular scale structure was unperturbed throughout the stretching of the hydrated fibre [68], suggesting that the strain was probably redistributed at higher levels of the structural hierarchy, likely through the various sliding mechanisms discussed above. The

same authors later studied the fibres under conditions of changing hydration [69], exploring the effects of passively straining the fibres by dehydration in a humidity controlled environment between 100 and 5% relative humidity (RH). They used a combination of Raman spectroscopy to assess chemical changes in the structure due to the gradual loss of water, and SAXS measurements using synchrotron radiation to assess changes in the length and distribution of the triple helix. They found that when free to change dimensions, the fibre, the fibril and the monomer all contracted axially with dehydration, each at increasingly smaller percentages down the structural hierarchy – dehydration through partial mineralisation of tendon is thought to drive an active contraction mechanism, placing stresses on the mineral content, generating the pre-strain required in tissues subject to compressive loads [70]. Interestingly when held at a fixed length, contraction was only observed at the macroscopic scale of the fibre, indicating again that some level of strain dissipation was happening at higher structural scales. However, this contraction resulted in incredible, passively induced stresses on the order of 100 MPa, which they compared to the forces generated in contractile muscle (only 0.3 MPa). They also noted marked changes in the Raman spectra that indicated conformational changes within the collagen backbone, although the extent to which these changes were associated with the reduction in water content or the change in strain, or simultaneous contributions from both, was not immediately clear. This question will be addressed in this thesis whilst tackling the active stretching of fibres rather than passive straining through dehydration. In both the zero-stress and iso-strain cases, all hierarchical structural elements shrank radially by approximately equal amounts relative to their size, showing that water affects the packing density and fibrillar spacing of the collagen fibre. This is in agreement with AFM work on mouse tail tendon [71] and a recent x-ray scattering study which analysed the shrinkage in intra- and interfibrillar spacing during dehydration of a collagen composite [72]. Here the authors speculated that drying disrupts the hydrogen bonding network in the space between collagen monomers, causing the increased stiffness in the fibres and reducing sliding capability at multiple hierarchical levels; in keeping with molecular models which propose water acts as a lubrication medium [73, 74]. The restructuring of the water network around dehydrating collagen has previously been observed using Raman spectroscopy [75], although no experimental work has assessed how the network of hydrogen bonding water relates to the protein structure under a macroscopic strain; something which I will consider in this present work.

Brillouin light scattering (BLS) is an inelastic scattering process in which thermally excited acoustic phonons are detected in the scattering medium [76]. The velocity of propagation of these high-frequency waves provides a measure of the elastic properties of the medium. The applicability of BLS to the study the mechanics of ECM proteins was demonstrated almost 40 years ago, but appears never to have been pursued. The first study on biopolymers by Harley et al [77] measured a microscopic elastic modulus in both type I collagen fibres and in muscle proteins, which they related to the forces of hydrogen bonding along the protein backbone. Later studies by Randall and Vaughan reported the acoustic wave velocity and acoustic attenuation of rat tail collagen [78] and the elastic moduli of refractive tissues of the eye [79]. Cusack & Miller [80] determined the angle dependence of both lateral and transverse modes in wet and dry collagen fibres to achieve a complete mechanical description of the protein. As in the previous study, these values were much higher than those determined by mechanical testing of macroscopic specimens. The authors speculated that this was possibly a viscoelastic effect attributable to the different timescales of the two measurement techniques. I aim to develop this discussion further by extending the measurements to elastin and cartilage tissue in this thesis, where I will use BLS spectroscopy as the probe of the molecular scale mechanics of the fibres under different conditions of hydration.

1.2.2.2.   Elastin

Elastic tissue is a major component of all mammalian tissues whose physiological role requires long-range elasticity. As noted above, elastic tissue is composed largely of elastin assembled on a skeleton of microfibrillar glycoproteins. Whether the microfibrils serve only to direct the assembly of the elastin structure or contribute to the mechanical properties of the elastic tissue is still not completely clear [81]. At the level of low magnification light microscopy, elastin appears to take a number of different structures. In large arteries, for example, it is described as "lamellar" [82, 83], whilst in the alveolar sac it forms a delicate meshwork [84, 85]. In cartilage [86-89] and intervertebral disc [90-93], where its presence has until recently been largely overlooked, it forms branching networks of single fibres approximately a micron in diameter. However, higher resolution imaging, reveals a fibrillary structure that is apparently common to ligaments and arteries with fibre diameters of around 100 nm, comparable to the type II collagen fibrils in cartilage [94, 95]. It is tempting to suggest therefore that this represents a basic unit of elastin structure. These are certainly the smallest componets that can be isolated from tissues by purely mechanical means.

In alkali-purified elastin these fibrils have a well-defined structure of hydrated pores accesible only to solutes with a molecular weight of less than 1 kD. Again this structure seems common to ligament and aorta derived elastin [96-98]. However, it is unclear whether these pore spaces exist in the tissue matrix. A question for this thesis, is whether water flow in this structure might contribute to the visoelastic proerties of elastin in the manner that has been suggested from measurements of the effects of solvent viscosity on the dynamics of whole tissue matrices [99-101].

A major question is how the tropoelastin molecules are assembeld into this structure. Early work demonstrating the entropy elasticity of elastin led to suggestions that this behaviour required a random molecular organisation, as in natural rubber. This argument is now recognised to be unduly simplistic [102]. The formation of tetravalent cross links during fibre formation has long been recognised [21], as has the imprtance of hydophobic inbteractions in determining molecular organisation [103]. Whatever the mechanism, it results in some level of ordering as evidenced from x-ray scattering experiments on single fibres [16, 104]. A SAXS experiment has demonstrated that this struture changes as mechanical loads are applied to the fibres [105], and a polarised Raman study found small changes in the bond angles within the protein backbone when exposed to macroscopic strain [106]. This thesis will expand on these microstructural measurements through experiments under controlled hydration conditions, to clarify how water might affect the composition of the ultrastructure under macroscopic strain.

1.3.   Thesis Outline

The main aim of this thesis is to investigate the relationship between the molecular scale mechanochemistry and the functional scale macromechanics of collagen and elastin fibres, through analysis of their hierarchical structural behaviour under different hydration conditions.

Chapter 2 contains the materials, methods and theory, where the isolation and/or purification of type-I collagen from rat tail tendon, type-II collagen from articular cartilage (equine metacarpophalangeal joint) and elastin from bovine nuchal ligament, is described. The experimental apparatus and protocols used for both macro and microscopic tensile testing in a controlled hydration environment, are outlined here. The reader is introduced to the theory of inelastic light scattering, with an outline of both polarisation resolved Raman and Brillouin

light scattering spectroscopies – the tools used to determine molecular scale structure and mechanics – together with their respective instrumentations and the techniques used for data analysis.

The macroscale mechanics of both protein fibres are well established; however, hydration studies are usually confined to the extremes of water content, and intermediate hydrations have rarely been studied. I begin with an analysis of the protein fibres at the macroscopic scale of the whole fibre in **chapter 3**. Here the results of quasi-static stress-strain and stress relaxation tests are presented, with an analysis of the Young's and relaxation moduli and the relaxation times of type-I collagen and bovine nuchal elastin fibres, each as a function of hydration, between 100 and 21% relative humidity. The viscoelastic nature of the fibres, poroelasticity and the role of the ground substance are all discussed. In **chapter 4**, I move several levels down the structural hierarchy to probe viscoelasticity at the molecular scale of the fibrous proteins, using Brillouin light scattering spectroscopy to achieve a mechanical characterisation of fully hydrated and air-dried fibres. As this is one of the first applications of this technique to study these fibres, I discuss some of the fundamentals of the Brillouin spectrum – the frequency shift and band shape – and how they change in the presence of water. I focus primarily on developing a physical explanation for the orders of magnitude difference between the elastic moduli obtained using the microscopic BLS approach, and those measured by stress-strain testing in the preceding chapter. A microfocussed approach is employed to determine the specific contribution of the intra- and extrafibrillar spaces, and I discuss the mechanical role of the non-collagenous matrix by comparing native and purified collagen fibres. I also address a longstanding debate over the mechanical differences between the different types of collagen, exploring the micromechanics of two fibrous-types: type-I and type-II.

In **chapter 5** I analyse the molecular scale structure of the fibres undergoing application of macroscopic strain in different hydration conditions. Polarisation resolved Raman spectra are presented assessing collagen fibres in two distinct locations within the crimp during the straightening of the collagen fibrils, and comparing spectra between individual elastin fibres. I identify strain dependent spectral features from the entire spectral range 135 to 3800 cm^{-1} and isolate hydration dependent bands.

Suggestions for extensions to my experimental approaches and potential future works are made throughout the discussions within each chapter. However, key highlights of these are presented alongside the concluding remarks in **chapter 6**, where the hydration dependent

mechanical properties observed at the whole-fibre scale, are connected to the lower level structure and mechanics of the proteins.

2

Materials, Methods & Theory

2.1.   Protein Fibre Preparation

2.1.1.   Collagen

2.1.1.1.   Type I

Rat tail tendons (RTT) consist of almost pure type I collagen, with only ~15% of other matrix material present therein [107, 108]. Unless otherwise stated, RTT collagen was measured in its native form with no further purification.

Tails were obtained from 7-8 week old Wistar rats euthanised by intra-peritoneal injection of 100 mg/kg of body weight sodium pentobarbitone, for purposes other than these experiments (in accordance with EU regulation 1099/2009 and the Welfare of Animals (slaughter or killing) Regulations 1995), severed directly at the point of contact with the body, and stored frozen at -20°C until required. Whilst still frozen, 20 mm long segments were cut from the proximal end of the tail and left to thaw in a Petri dish filled with phosphate buffered saline (PBS) at room temperature. The skin was then gently peeled back, after making an incision along the length of the segment to reveal four sheathed tendon bundles about the tail vertebra. Being careful not to apply any pre-strain, fine forceps were used to gently draw each fibre out of the sheath, and then the fibres were transferred to a vial containing PBS with 0.01% sodium azide (NaN_3), for storage at 2°C until required for measurement.

2.1.1.2.   Type II

Type II collagen fibres are too small (approx. 100 nm in diameter) to be gently extracted from their surrounding proteoglycan gel, so were studied set within their native hyaline cartilage. Square plates of intact articular cartilage were taken from the equine metacarpophalangeal joint (EMJ), cut using a scalpel parallel to the articular surface to encompass a cross-section from the superficial to the deep zone (approximately 0.5 mm thick). The excised tissue was divided into thin cuboids ~5x1 mm, washed in PBS and then transferred to a vial containing PBS with 0.01% NaN_3, for storage at 2°C until required for measurement. Some tissue was cryosectioned, after being soaked overnight in 2M sucrose solution to prevent ice crystal formation. Tissue plates were mounted in Bright Cryo-M-Bed medium (Bright Instruments, Huntingdon, UK), cooled down at -50°C, then placed in dry ice for around 20 minutes to ensure a secure adhesion prior to cryosectioning. 20 µm sections were cut using a cryomicrotome (Cryostat 7500, Bright Instruments), both parallel to the articular surface and orthogonal to it, from the superficial to the deep zone. Sections were re-floated in PBS with 0.01% NaN_3 overnight to wash away the sucrose, prior to transferring to distilled water for a further wash and finally dried onto a glass slide for storage at 2°C. Sections were subsequently re-floated using pure water prior to measurement.

2.1.1.3.   Purification of Type I & II Collagen

Pure collagens were obtained using a three-part enzymatic digestion process that removes around 97% of glycosaminoglycans and other non-collagenous material from the excised RTT fibres and cartilage blocks [109]. Tissues were immersed in the following solutions in a shaking incubator at 200 rpm set at 37°C: Firstly 1) 0.125 U/ml chondroitinase ABC in 0.05M Tris buffer and 0.06M sodium acetate (CH_3COONa), at pH 8.0 for 24 hrs. Transferred to 2) 1 U/ml streptomyces hyaluronidase in 0.05M Tris buffer and 0.15M sodium chloride (NaCl), at pH 6.0 for 24 hrs. Finally, 3) 1 mg/ml trypsin in 0.05M sodium phosphate (NaHPO4) and 0.15M NaCl at pH 7.2 for 16 hrs. Purified fibres were then stored in a vial containing PBS with 0.01% NaN_3 at 2°C until needed for measurement.

2.1.2.   Elastin

The nuchal ligament of large mammals contains the largest percentage of elastin of any tissue [110] and is generally found best developed in cattle [111], where the funiculus, the largest

part of the ligament, anatomically extends from the external occipital protuberance at the base of the skull, to the first of the thoracic vertebrae. Bovine nuchal ligaments were sourced from a local abattoir and stored frozen at -20°C until required. Ligaments were thawed and defatted, then digested in 0.1M sodium hydroxide (NaOH) solution at 95°C for 45 minutes following the Lansing procedure [112], to remove all other matrix components whilst maintaining the mechanical response of the tissue [113]. The remaining insoluble tissue was washed repeatedly in a bath of distilled water until a pH of 7.0 (monitored using a pH meter) was achieved. The purified elastin block was submerged in distilled water mixed with 0.01% NaN_3 to prevent bacterial growth, and stored at 2°C until needed. Being careful not to apply too much pre-strain, tweezers were used to gently pull smaller elastin segments from the larger block; these were then transferred to a Petri dish filled with PBS. Small fibre bundles around 1 mm thick were gently teased from the excised tissue and cut to lengths of a few mm using a scalpel. These fibres were stored refrigerated in a vial containing PBS (pH 7.4) with 0.01% NaN_3 until required for measurement.

2.2. Quasi-Static Mechanical Testing

2.2.1. Uniaxial Tensile Testing Stage

Quasi-static uniaxial stress-strain measurements of type-I collagen and elastin fibres were performed using a lab-built tensile testing device (fig. 2.1 – apparatus designed by Dr Ellen Green) consisting of a controlled humidity chamber with a Peltier heater set at 30°C and monitored using a submerged thermocouple (RS Temperature/Voltage Converter – Type K). To ensure a humidity controlled environment, the solution bath was sealed by a removable lid,
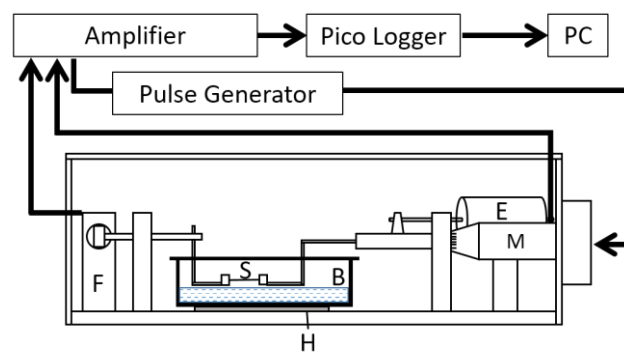
Figure 2.1: Schematic of the uniaxial tensile testing apparatus. (M): automated micrometer driven by a pulse generator and stepper motor; (E and F): extension and force transducers connected to a PC via a Pico logger (Pico Technology ADC-200) and a signal amplifier; (S): sample; (B): humidity chamber Perspex solution bath; H: Peltier heating stage.

featuring thin tracks allowing for the movement of the sample anchors under changing strain, whilst the whole stage was further enclosed in Perspex casing.

2.2.2. Controlling Fibre Hydration

All mechanical measurements were conducted under controlled humidity (relative humidity, RH), using saturated salt solutions in distilled water at 30°C: sodium chloride (NaCl), sodium bromide (NaBr) and sodium iodide (NaI) – all Sigma-Aldrich products – giving rise to 85%, 66% and 46% RH, respectively. Distilled water (100% RH) and paraffin oil (Fluka; 21% RH) were also employed. RH and air temperature were measured using a PCMini52 digital RH/temperature probe (Mitchell Instruments PCMINI52+4+XX+H+X+CB+F46), the RH single point calibrated to 49.4% RH with a precision of $\pm$ 5% RH and the temperature calibrated to a standard curve in the range 20-90°C, with an accuracy of $\pm$ 0.2°C. RH and air temperature were measured simultaneously, immediately before and after mechanical testing, to ensure the environment was maintained at the required conditions.

2.2.3. Experimental Protocol

For each measurement, a fibre sample was placed un-anchored inside the humidity chamber and allowed to air-dry for up to 30 minutes. During this time, the length of the suspended fibre was adjusted using the micrometer to ensure the uniaxial force acting on the fibre remained nominally at zero, whilst the fibre contracted during dehydration. Collagen fibres were then anchored to rubber-surfaced clamps to minimise slippage of the sample, whilst elastin fibres were fixed using super glue (Vibra-Tite). The solution bath was then filled with the desired humidity solution up to a level of approximately 5 mm below the sample, and the fibre allowed to equilibrate to the humidity in the chamber for up to 2 hours. During this time, the anchor separation was gradually increased to remove fibre slack whilst maintaining a nominal stress ($\sim$ 0.2 mN) as registered by the voltage response of the force transducer. Equilibration was assumed upon reaching a steady anchor separation, and this was used as the sample rest length prior to measurement. Each fibre bundle had a length between supports of approximately 10 mm at zero-stress.

Identical straining conditions were required for a comparison of the two proteins' mechanical responses with increasing dehydration. The breaking strain of 21% RH elastin provided the

upper limit for this range. Fibres were prepared in the humidity chamber as above and then extended at 0.25 mm/min, until they broke with an average breaking strain of 12 (± 2)% (n=10). To assess the effect of hydration on the mechanics of the fibres at different elongation, the fibres were measured both at low-strain (5%) and high-strain (10%; just below the breaking strain limit) in the experiment outlined below. This is determined to be within the linear response region of the stress-strain curves of type-I collagen, where the crimp has been removed (typically <4% strain [40]) and a measurement of the Young's modulus is possible.

Stress relaxation measurements were performed by recording the force response at constant strain following preconditioning with an instantaneous extension of the sample to 5% strain at 20 mm/min, holding for 600s, then returning to 0% strain at 0.25 mm/min (see note below). This was followed by three consecutive stress-strain extension/relaxation cycles to 5% strain at 0.25 mm/min. Two stress relaxation curves were then recorded using the same protocol as the pre-conditioning cycle. The second and third cycles of both measurements were generally indistinguishable and the third one was used for analysis (see appendix figures A 14-A 16). Measurements were finally repeated at 10% strain. Between successive extensions, the sample was held at 0% strain until no change in the force output was observed. Note that the dehydrated fibres exhibited a permanent elongation during the first extension cycle, so an initial stress-relaxation measurement (prior to the traditional slow-rate preconditioning), was performed to assess the relaxation behaviour occurring exclusively during this deformation process.

2.2.4.   Macromechanical Data Analysis

Voltage outputs for the force F and extension ΔL were converted to into values for stress $\sigma = F/A$ and strain $\varepsilon = \Delta L/L_0$ using a custom MATLAB (MathWorks Inc.) script. Here, A is the fibre cross-sectional area (see below), and L_0 is the anchor edge-to-anchor edge length of the suspended fibre measured at 0% strain prior to the first extension.

The dehydrated fibres exhibited a permanent elongation during preconditioning, resulting in macroscopic bending due to compression upon returning to 0% strain. The stress-strain plots manifest this unbending as a curvature, prior to the normal uptake of stress in the latter part of the curve. For this reason, the latter linear portion (assessed by eye with the aid of a ruler on the screen) was thought to best approximate the modulus of the unbent, fully extended fibre. The Young's modulus, $E_Y = \sigma/\varepsilon$, was calculated from linear fit analysis of this region of the
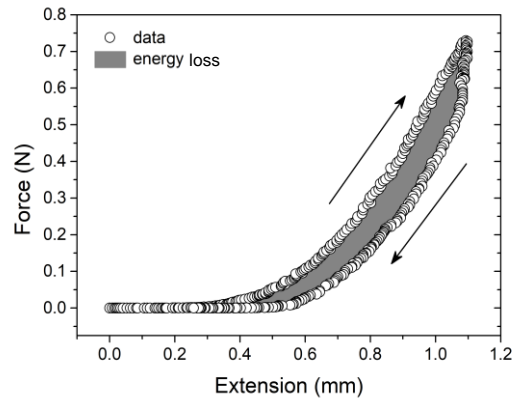
stress-strain curve (fig. 2.2), using Origin 9.0 (OriginLab Corp.) software. The cross-sectional area of the specimen was calculated as $A = m/\rho L_0$, with m the mass of the fibre measured after air-drying in an incubator at 37°C for 24 hrs, and ρ the density of the dry fibre – being 1350 kg m^{-3} and 1230 kg m^{-3} for collagen and elastin, respectively [80, 114].
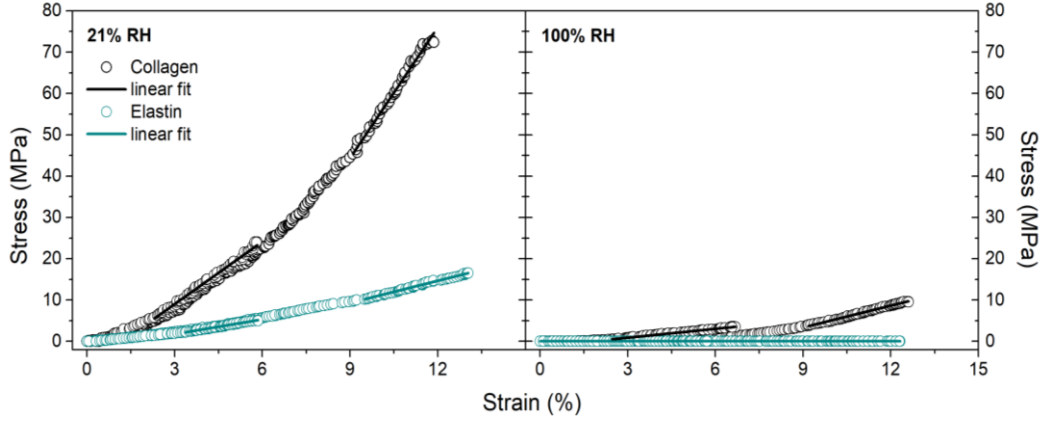
Figure 2.2: Stress-strain plots at the hydration extremes, 21% RH (left) and 100% RH (right), showing the least squares fit applied to the linear region of the curve for collagen and elastin fibres extended to 5 and 10% strain.

Mechanical lag in the extension transducer at the point of unloading introduced a systematic error to the hysteresis loops (note the force reduces at the beginning of the unloading cycle in figure 2.3, but the extension does not change), hence analysis of the energy dissipated by internal friction and heat transfer [115, 116] was not possible.

Figure 2.3: Hysteresis curve showing the extension and relaxation cycles (denoted by the arrows) of a collagen fibre at 100% RH. Shaded area corresponds to the energy loss.

The stress relaxation data were analysed by fitting to the Maxwell-Weichert model of relaxation [5]:

$$E_{relax}(t) = E_0 + \sum_n E_n \exp\left(-t/\tau_n\right) \qquad (1)$$

where E_0 is the time-independent elastic modulus and E_n, τ_n, are the characteristic modulus and relaxation time of the nth exponential component over time t. Figure 2.4a shows the model schematically, where n numbers of Maxwell elements (a spring in series with a dashpot) are connected in parallel with an additional spring. The relaxation time is a function of the viscosity of the dashpot η_n and the modulus E_n of the spring component, $\tau_n = \eta_n/E_n$, and each element represents a contribution to the stress relaxation owing to the sample structure. Stress data were converted into a relaxation modulus – dividing the stress as a function of time by the strain at which the fibres were held - and then plotted as a function of time. Using Origin 9.0 (OriginLab Corp.) software, up to three exponential decays were then fitted to the data to describe the relaxation process of each fibre across the hydration range (fig. 2.4b & c). This was achieved by setting the y-axis to a logarithmic scale and judging – by eye (with the aid of
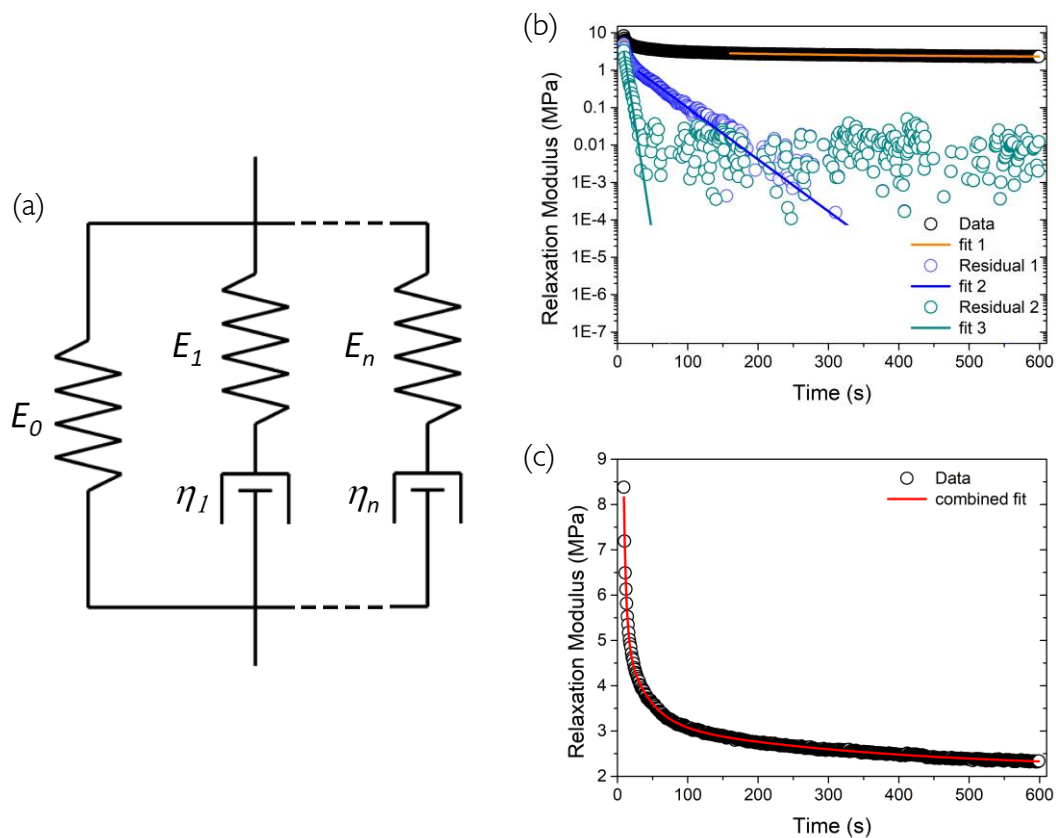
Figure 2.4: (a) Schematic representation of the Maxwell-Weichert model used to interpret the viscoelastic response of collagen and elastin fibres under different hydration conditions. n number of Maxwell elements with moduli E_n and viscosities η_n provide a model with relaxation times τ_n, which is used to fit the experimental data. Adapted from: [5]. (b) Plot showing the iterative fitting of single-exponentials to the relaxation curve and corresponding residuals. In this case a triple-exponential decay curve provides the best fit. Representative data from elastin at 85% RH. (c) Plot showing the result of the iterative fit, combining all three single-exponential components.

a ruler on the screen) – the first approximately linear region below 600 seconds. This was done to all data sets for all hydrations, and a common time range for the linear region was established. A single exponential was then fitted to the data within the limits of this time range for each set, and then subtracted from the raw data. The resulting residual decay was plotted as a function of time, and the procedure repeated for up to three exponential decays, fixing the E_0 parameter at the value established in the first fit. This method was considered to be more reliable than fitting a two or three-component exponential directly to the raw data due to co-dependency of some fitting components. Setting fixed time ranges for each exponential fit resolved this issue.

For each sample at each RH, stress-strain and stress relaxation data were collected at least in triplicate.

2.3.   Light Scattering Spectroscopy

The theory of light scattering was developed in the latter decades of the 19th century, and refined with the advent of quantum mechanics in the early decades of the 20th. The great names of Rayleigh, Stokes, Mie, Einstein, Brillouin, Raman and Debye are all associated with its development. Electromagnetic radiation impinging on an object is scattered off in all directions and, depending on whether the energy of the scattered photon is the same as the energy of the incident photon or different, it is defined as elastic or inelastic scattering. In the inelastic case, energy exchange occurs between the incident photons and the molecules of a system, leading to very small but detectable changes in the frequency of the scattered light, from which information about the sample can be extracted. The inelastic light scattering event is very inefficient – only around one in every billion photons are scattered in this way – and early implementations of these analytical techniques, were limited largely to pure liquids and crystal structures, due to the inherently low scattering intensities and consequently long acquisition times required. This changed with the introduction of the first lasers in the 1960s, and with continued development in automated spectrometers and digital photon counting detector designs, the spectral acquisition times have decreased making the analysis of biomedical samples possible. The work conducted in this thesis involves the inelastic light

scattering techniques of (vibrational) Raman and Brillouin spectroscopy, which are described below.

2.3.1. Raman Spectroscopy

This thesis is concerned with condensed phase matter, whereby molecules translate, rotate and vibrate, and by interaction with incoming photons, give rise to transitions between quantised energy states. Vibrational spectroscopy techniques such as Raman spectroscopy detect transitions between vibrational energy levels of molecules. Their characteristic frequency ranges enable chemical analysis to be made in a specific, label-free manner, based on vibrational normal modes of the molecule.

The Raman effect was first reported by Sir C. V. Raman in 1928 and earned him the 1930 Nobel Prize in Physics. It is described as the effect by which an incident monochromatic
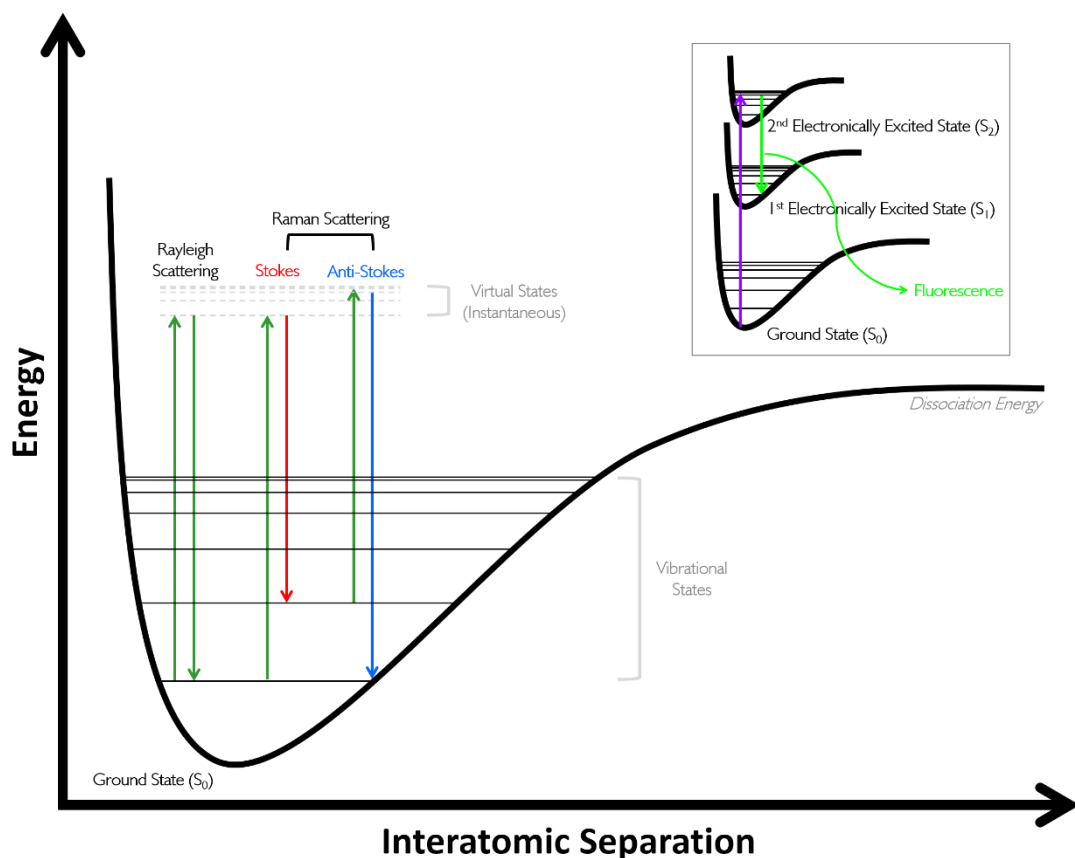
Figure 2.5: Diagram showing the vibrational energy level transitions that define Rayleigh scattering, and Stokes and anti-Stokes Raman scattering during interaction of a molecule with a *non-resonant photon*. (Inset): a *resonant photon* is absorbed by a molecule promoting the molecule into an electronically excited state, producing fluorescence upon decay.

(visible) light either gains or loses energy to the vibrations of molecules in a medium, leading to a measurable shift in frequency of the scattered light relative to the incident light (Raman shift, in units of cm^{-1}). Spontaneous Raman scattering is a two-photon event shown graphically in figure 2.5, where an incident photon with energy larger than that required for a vibrational transition (but smaller than that required for an electronic transition), promotes the molecule to a *virtual* state, from which the molecule returns either to the original state, emitting a photon with the same frequency as the incident photon (elastic or Rayleigh scattering), or to a higher or lower vibrational state, emitting a photon with lower (Stokes scattering) or higher frequency (anti-Stokes scattering) than the incident photon.

The Raman effect is mediated by the process of molecular polarisation, whereby an incident photon outside of the resonance condition induces a dipole moment by setting in motion the oscillation of the electron cloud in the molecule [117, 118]. The induced dipole moment μ_{ind} is proportional to the polarisability, α, a molecular property that measures how easily the electron cloud can be distorted by an external electric field, and the strength of the electric field E_{inc}

$$\mu_{ind} = \alpha E_{inc} \tag{2}$$

The incident electric field is expressed classically as:

$$E_{inc} = E_0 \sin(2\pi v_{inc} t) \tag{3}$$

where E_0 is the amplitude and v_{inc} the frequency of oscillation of the incident electric field at a time t. The oscillating electric field of the radiation induces a fluctuating dipole, with displacement Q from the equilibrium position, which scatters radiation at a frequency v_{vib}

$$Q = Q_0 \sin(2\pi v_{vib} t) \tag{4}$$

The polarisability of a molecule is not constant, and the vibrational motion can cause α to vary by small amounts, which can be expressed by a Taylor series with first-order approximation

$$\alpha = \alpha_0 + \frac{\partial \alpha}{\partial Q} Q \tag{5}$$

where α_0 is the static polarisability and $\partial \alpha / \partial Q$ the fluctuating polarisability with respect to the displacement from equilibrium. Combining equations (3-5) into (2) and rearranging using the identity $\sin A \; \sin B = 1/2 \left[\cos(A - B) - \cos(A + B)\right]$, the induced dipole moment can be rewritten as:

$$\mu_{ind} = \alpha_0 E_0 \sin(2\pi \nu_{inc} t) +$$
$$+ \left(\frac{\partial \alpha}{\partial Q}\right) \frac{Q_0 E_0}{2} \left[\cos 2\pi(\nu_{inc} - \nu_{vib})t - \cos 2\pi(\nu_{inc} + \nu_{vib})t\right] \tag{6}$$

The first term here represents the Rayleigh scattering contribution, whereby the induced dipole scatters light at the same frequency as that of the incident radiation. The second term describes the Raman scattering in both Stokes $(\nu_{inc} - \nu_{vib})$ and anti-Stokes $(\nu_{inc} + \nu_{vib})$ parts. Note that for Raman scattering to be observed, the condition $\frac{\partial \alpha}{\partial Q} \neq 0$ must be satisfied, i.e. a change in polarisability, or polarisability *anisotropy*, during the vibrational mode must occur. This is the gross selection rule for vibrational Raman spectroscopy, whilst the specific selection rule establishes transitions between adjacent vibrational levels ($\Delta v = \pm 1$, where v is the vibrational quantum number).

The polarisability introduced in equation (2) is a tensor, such that the induced dipole moment can better be described by

$$\boldsymbol{\mu}_{ind} = \underline{\alpha} \cdot \boldsymbol{E}_{inc}$$
$$\begin{pmatrix} \mu_x \\ \mu_y \\ \mu_z \end{pmatrix} = \begin{bmatrix} \alpha_{xx} \alpha_{xy} \alpha_{xz} \\ \alpha_{yx} \alpha_{yy} \alpha_{yz} \\ \alpha_{zx} \alpha_{zy} \alpha_{zz} \end{bmatrix} \begin{pmatrix} E_x \\ E_y \\ E_z \end{pmatrix} \tag{7}$$

where the terms α_{ij} represent the Cartesian direction component of the induced dipole i, and the electric field j. It can be seen that the orientation of the incident electric field, e.g. of a plane polarised radiation (laser), will dictate the magnitude of the induced dipole in an anisotropic molecule, depending on how it aligns with the electronic cloud. The intensity of Raman scattered photons is thus polarisation dependent, and contains information about the orientation of molecular bonds.

The total scattering cross-section per molecule (units: m^2 molecule^{-1}) is defined by

$$\sigma = \int_0^{4\pi} \sigma' d\Omega \tag{8}$$

where $d\Omega$ is an element of solid angle (unit: steradian) and σ' is the first differential scattering cross-section per molecule (units: m^2 sr^{-1} molecule^{-1}). Thus, when a beam with irradiance $\mathfrak{I}$ is incident on a system of N molecules, the intensity I of the scattered light is given by the general relation

$$I = N\sigma'\mathfrak{I} \tag{9}$$

Irradiance is the amount of radiation energy which passes through a unit area perpendicular to the direction of propagation of the incident light; thus, the scattering cross-section measures the rate at which energy is removed from the incident beam by scattering over 4π steradians.

Figure 2.6 shows the illumination-observation geometry of a typical back- or forward-scattering Raman experiment. The scattering molecule is at the origin of a Cartesian system with an incident beam travelling parallel to the z-axis, and polarised along the x-axis ($E_x\left(\parallel^i\right)$). In this configuration, the scattered radiation emitted by the oscillating induced molecular dipole is also detected along the z-axis (-ve $\boldsymbol{e}_z$ direction for backscattering; +ve $\boldsymbol{e}_z$ for forward scattering) such that the polarisation of the scattered beam is parallel to that of the incident beam, polarised along the x-axis ($\mu_x\left(\parallel^s\right)$) and depolarised along the y-axis ($\mu_y\left(\perp^s\right)$). It follows that only two polarisation resolved measurements of the scattered radiation are

Figure 2.6: Diagram of the illumination-observation geometry in the forward scattering configuration ($n_0^i = n_0^s = e_z$ – equivalent to backscatter $n_0^i = n_0^s = -e_z$). The unit vectors n_0^i and n_0^s define the direction of propagation of the incident and scattered light, respectively to and from the scattering molecule at the origin O of the cartesian axis (x, y and z). The unit vectors e_x, e_y and e_z are directly associated with these axes and define relative positions with respect to the molecule. The component of the incident electric field E_{inc}, plane polarised in the direction of the x-axis is represented by E_x ($\parallel^i$), whilst those of the scattered light μ_{ind} are given by μ_x ($\parallel^s$) and μ_y ($\perp^s$). Polarisation of the incident beam is selected by the orientation of the polariser, and the component of the scattered light that reaches the detector is set by rotating the analyser.

required to characterise the polarisability tensor: the μ_x and μ_y components of the induced electric dipole moment μ_{ind} which in this case are given by:

$$\mu_x = (\alpha_{xx})E_x \qquad \text{and} \qquad \mu_y = (\alpha_{yx})E_x \qquad (10a, b)$$

Thus the polarised $I_{\parallel}$ and depolarised $I_{\perp}$ intensities radiated by the oscillating electric dipole induced by an incident electric field polarised relative to the x-axis in this configuration are given by [119]:

$$I_{\parallel} = \kappa'(\nu_{inc} \pm \nu_{vib})^4 \mu_x^2 \tag{11}$$

$$I_{\perp} = \kappa'(\nu_{inc} \pm \nu_{vib})^4 \mu_y^2 \tag{12}$$

where $\kappa' = \pi^2/2\varepsilon_0 c_0^3$ is a constant containing the permittivity of free space (ε_0) and the speed of light in vacuum (c_0).

In practice, there are N randomly oriented molecules within the scattering volume, so scattering intensities are expressed using the isotropic averages $\langle(\alpha_{xx})\rangle$ and $\langle(\alpha_{yx})\rangle$, respectively, containing only the invariant (constant regardless of the orientation of the molecule) parts of the individual molecular polarisability tensors – α, the mean polarisability also called the isotropic component and β, the anisotropic component. The incident electric field may be defined in terms of the irradiance using the expression $\mathfrak{I} = \frac{1}{2}c_0\varepsilon_0 E_x^2$. Substituting this into equations (11) and (12) and expressing the isotropic averages in terms of the invariants of the polarisability tensor, expressions for the polarised $I_{\parallel}$ and depolarised $I_{\perp}$ scattering intensities are obtained:

$$I_{\parallel} = \kappa N(\nu_0 \pm \nu)^4 \left\{\frac{45\alpha^2 + 4\beta^2}{45}\right\} \mathfrak{I} \tag{13}$$

$$I_{\perp} = \kappa N(\nu_0 \pm \nu)^4 \left\{\frac{\beta^2}{15}\right\} \mathfrak{I} \tag{14}$$

where $\kappa = \pi^2/\varepsilon_0^2 c_0^4$. In the case where no analyser is used in the scattered light path, the total scattering intensity $I = I_{\parallel} + I_{\perp}$ is measured

$$I = \kappa N(\nu_0 \pm \nu)^4 \left\{\frac{45\alpha^2 + 7\beta^2}{45}\right\} \mathfrak{I} \tag{15}$$

Polarization-resolved experiments enable to selectively excite molecular vibrations along different bonds. This is achieved by selecting the polarization of the incident light and that of

the scattered light to be parallel or perpendicular to one another, hence producing the polarised $I_\parallel$ or depolarised spectrum $I_\perp$. The ratio between depolarised and polarised intensity of a vibrational band, the depolarisation ratio, contains information on the symmetry and orientation of a particular bond [120]. Molecules are classified into point groups based on their symmetry; normal modes of molecules are also classified depending on their symmetry, and their Raman activity depends on that [121]. In backscattering configuration, the depolarisation ratio ρ is given by the relation

$$\rho = \frac{I_\perp}{I_\parallel} = \frac{3\beta^2}{45\alpha^2 + 4\beta^2} \tag{16}$$

This equation can be reduced to a range of values that describe the extent to which a vibrational band of a molecule is polarised. For totally symmetric vibrations, the Raman spectral intensity is entirely given by the isotropic component (as $\beta = 0$), leading to a depolarisation ratio equal to zero, i.e. the vibration is in the same plane as the incident electric field. Conversely, non-symmetric vibrations can have the isotropic component equal to zero ($\alpha = 0$) and so the scattering intensity depends solely on the anisotropic part, such that $\rho = 3 / 4$. For all other vibrations, the depolarisation ratio is in the range $0 \leq \rho \leq 3 / 4$.

Comparing equations (13-15) with equation (9) it is clear to see that the scattering cross-section is intrinsically related to the polarisability (defined by the function in the braces) and the frequency of the scattered light such that $\sigma' = \kappa(\nu_0 \pm \nu)^4\{...\}$. This means that the scattering process is more efficient at lower wavelengths as the scattering intensity is inversely proportional to the fourth power of the wavelength of the incident photon, $I \propto \lambda_{inc}^{-4}$. Indeed, Raman scattering is most efficient at low wavelengths.

Raman scattering is a very weak process, orders of magnitude weaker than the Rayleigh scattering with an occurrence of around $1:10^{10}$ photon incidences [122]. Owing to the Boltzmann distribution, the anti-Stokes part of the Raman spectrum is far less intense than the Stokes part, which is conventionally measured in experiment. A Raman spectrum is a plot of the scattered intensity vs. frequency shift from the incident wavelength (in units of wavenumbers, cm^{-1}). The Raman spectra of six abundant biomolecules are displayed in figure
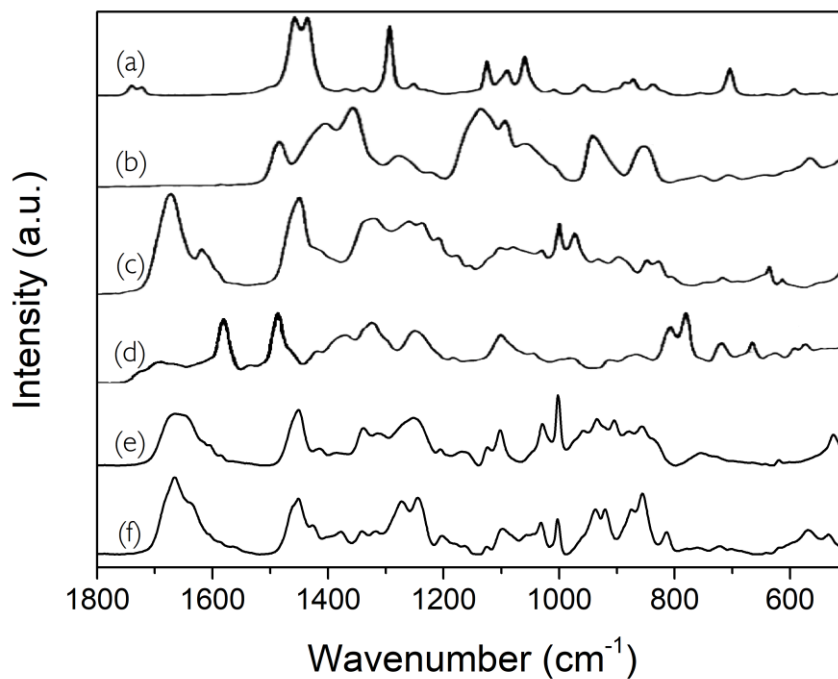
Figure 2.7: Raman spectra of six abundant biomolecules: (a) phospholipids, (b) glycogen, (c) ribonuclease A, (d) RNA, (e) elastin and (f) collagen. The range of unique peak patterns provide a fingerprint that identifies the specific material. Adapted from: [4]

2.7. Each band represents a vibrational mode of a functional group in the molecule, such that collectively these describe the unique signature of a given material providing chemical and structural information in a label-free manner. The key peaks/bands of interest to this thesis and their associated bond vibration(s) are shown in figure 2.8 for hydrated type-I collagen from RTT.

In this thesis, the main measurable is the peak or band area change. Increases or decreases in this correspond to the number of any given vibrational bond within a system (N in equations 13-15), that aligns with the polarisation of the incident radiation and is promoted into the excited vibrational state. However, it should be noted that without a specific knowledge of the density of a sample within a given scattering volume, it is difficult to separate the area increases and decreases as due to the change in angular distribution of the bond, and/or simply their number within the volume.
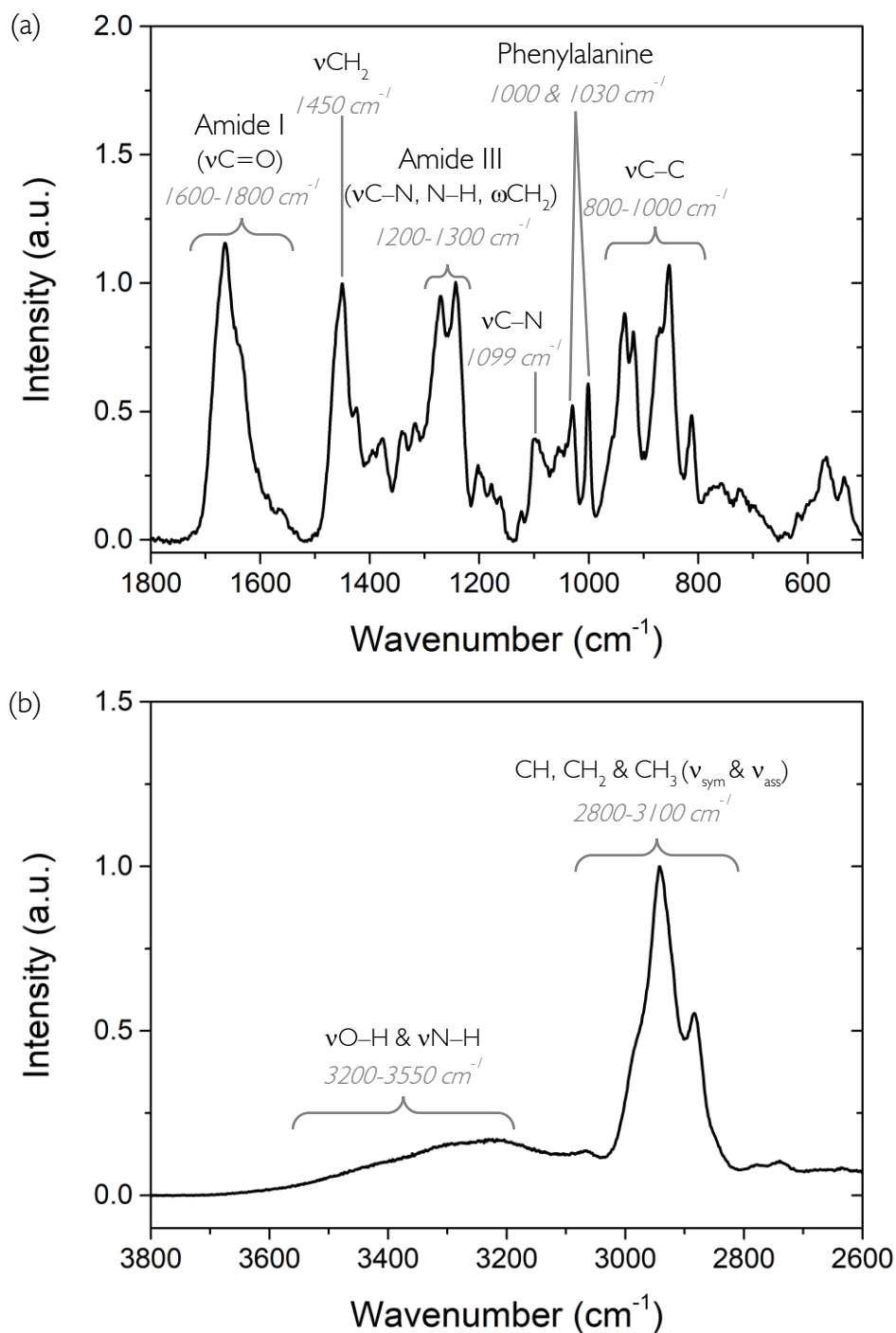
Figure 2.8: Raman spectra of a hydrated type-I collagen fibre from rat tail tendon with all peaks and bands of interest for this thesis labelled with their respective bond vibration(s). (a) Fingerprint region 500-1800 cm^{-1} normalised to the CH$_2$ peak at 1450 cm^{-1}. (b) High-wavenumber region normalised to the CH$_2$ peak at 2942 cm^{-1} (ν_{sym} – symmetric stretching vibration; ν_{ass} – asymmetric stretching vibration; ω – wagging deformation).

2.3.2. Raman Microscope

All micro-Raman scattering measurements were performed using a commercially available Raman microscope (InVia, Renishaw, UK) with polarisation resolution capability. The system has a degree of flexibility in that three diffraction gratings (300, 600 and 1200 lines/mm), two near-infrared diode lasers (at 785nm and 830nm) and three air objectives are available (5X, 20X and long-working distance 50X). Figure 2.9 shows the laser beam path and back-scattered light from the sample, and highlights the various important optical components of the system. The laser beam enters the microscope and is sent through a high numerical aperture (NA) objective (L50X) that is used both for focusing the laser light onto a sample and for collecting the backscattered light (180° scattering geometry), which then passes through a holographic notch filter (to reject the intense Rayleigh component) and thence onto the diffraction grating which disperses the different wavelengths of the scattered light and directs them towards the CCD camera for detection. Polarized spectra are acquired by introducing a half-wave plate into the laser beam path before the sample and an analyser (polariser plus half-wave plate) after the sample (see §2.3.2.4 below). The instrument is controlled through Wire 4.0 software (Renishaw, UK), which is also used for data handling and manipulation. Sample positioning is achieved through a motorised xyz stage with precision of 100 nm. The spectrometer is calibrated to the 520 cm^{-1} peak of silicon prior to each series of measurements.

Figure 2.9: Renishaw InVia Raman microscope. The insert shows the beam paths of the 785 nm laser (red line) to the sample in the enclosed microscope, and of the scattered light (yellow line) through the optical components of the spectrometer to the CCD [HWP: half-wave plate; NF: notch filter; P: analyser (half-wave plate and polariser); DG: diffraction grating]. Adapted from: [1]

2.3.2.1.   Excitation Source Selection

The choice of laser excitation wavelength and power is key to a Raman experiment. C.V. Raman's original experiments made use of finely focussed, filtered sunlight to observe the weak scattering signal of several liquids and gases [123]. Nowadays lasers in the visible to near-infrared (NIR) range are used, with wavelengths from 475 to 900 nm. Raman studies of biological materials generally require long excitation wavelengths, which reduce the achievable spatial resolution but have the double advantage of lowering the probability of fluorescence, largely absent above 600 nm [124] (specifically 280-350 nm for collagen and 300-370 nm for elastin [125]), and increasing the depth of penetration into the sample [126]. In these measurements, the 785 nm wavelength was selected, as it gives a scattering efficiency approximately 1.25 times greater than the 830 nm wavelength and provides Raman scattered photons with sufficient energy to be detected by the CCD in the high-wavenumber region (HWN – 2500 to 3800 cm^{-1}). Laser power at the sample (L50X objective) was 48 mW.

2.3.2.2.   Diffraction Grating Choice and Detector

The diffraction grating is a reflective plate bearing a holographically generated series of stepped or grooved mirror elements at set separations and depths, such that light reflected from the surface is dispersed through a range of wavelength-dependent angles [127]. Spatially localised light passing through a slit, is collimated and focussed onto the grating, where it is dispersed at different angles, to be recollimated and focussed into the detector, a Peltier-cooled deep-depletion charged coupled device (CCD). In effect, this images the slit at each dispersed wavelength of the scattered light, onto the 1040 x 256 array of doped silicon wafers, the 26 μm^2 *pixels* arranged in rows and columns. Charge is produced by the photoelectric effect when a photon impinges on any pixel. This is stored in sequential capacitors at the end of each column (the spectral dispersion, or wavelength axis), such that at the end of an acquisition, the total charge is summed across the rows, amplified into a final voltage and digitised to be transferred to a computer as photon count at each wavelength, i.e. the spectrum; a process often termed the photoelectron 'bucket brigade'. The CCD enables simultaneous photon counting of a large portion of the spectral range without scanning the spectrum by rotation of the diffraction grating, a distinct advantage in detection time, efficiency and reliability over the photomultiplier tube. This deep-depleted silicon arrangement is known to have a high quantum efficiency for photons in the NIR range.

There are three gratings available in the system: 300, 600 and 1200 l/mm. Choice is a trade-off between the spectral resolution and the spectral range achievable, which respectively increase and decrease by a factor of two when the number of lines per millimetre (l/mm) is doubled. Consideration should also be given to the acquisition time, which increases with increasing the spectral resolution. The 600 l/mm grating was chosen for all Raman measurements, giving a spectral range of approximately 2000 cm^{-1} and a spectral resolution of around $\sim$6 cm^{-1}. Measurements were conducted over the fingerprint region (135 to 2390 cm^{-1}) and the high-wavenumber (HWN) region (2400 to 3960 cm^{-1}).

2.3.2.3. Objective Lens

Two objectives were used in the micro-Raman experiments; a 50X, 0.5 NA long working distance lens (Leica, N-Plan) and a 60X, 1.0 NA water-dipping lens (Olympus, LUMPLFLN 60XW). A 5X 0.12 NA and 20X 0.4 NA objectives (Leica N-Plan) were also used for large field of view white light imaging. The laser spot size conferred by both high NA objectives is approximately 20 μm long and 3 μm

Figure 2.10: 785 nm laser line on a reflective silicon surface.

wide (fig. 2.10). The streamline mode was advantageous as spatially averaged spectra were desired (enhancing the acquisition speed in 1D or 2D mapping).
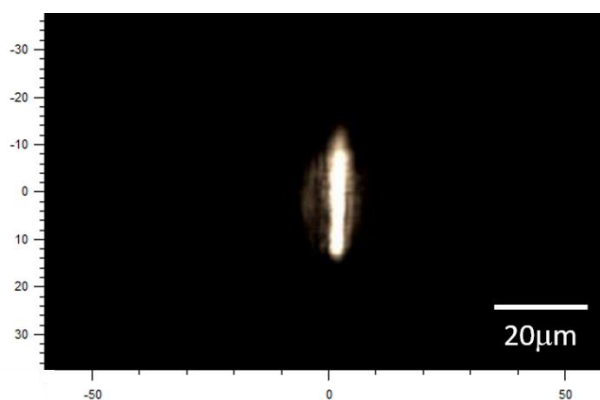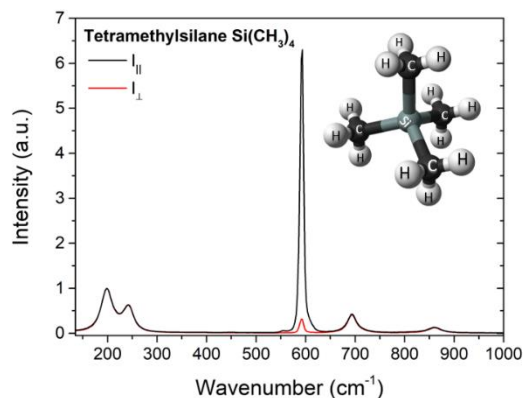
2.3.2.4. Polarisation Resolution

The system is equipped with a half-wave plate fixed in the incident laser beam path to rotate the polarisation plane of the laser (this was approximately radially aligned to the collagen and elastin fibre axes), and an analyser in the scattered beam path to alternatively measure a polarised $I_{\parallel}$ or depolarised spectrum $I_{\perp}$; the latter achieved inserting a further half-wave plate ahead of the analyser (see fig. 2.9). Prior to the experiment, a calibration of the polarisation was performed using tetramethylsilane (TMS; Si(CH$_3$)$_4$ – Sigma-Aldrich, $\geq$99.5% pure). For this highly symmetric molecule, the Si–C symmetric stretching mode is a totally symmetric

mode and hence gives rise to a strong peak (593 cm^{-1}) in the polarised Raman spectrum (fig. 2.11) [128-130]. The depolarisation ratio for this band was measured as $\rho = 0.035$, whilst for the depolarised bands $\rho = 0.70$.
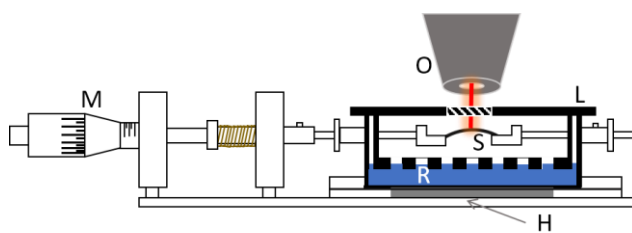

Figure 2.11: Polarisation-resolved micro-Raman spectra of TMS. Depolarisation ratio was calculated from the height of the peak at 593 cm^{-1} (ν_{sym} Si-C) in the depolarised (I$_\perp$) and polarised spectra (I$_{||}$). Spectra were normalised to the peak at 198 cm^{-1}.

2.3.2.5.   Mechanical Testing Stage

Figure 2.12 shows the custom-built uniaxial tensile testing device used in the micro-Raman measurements. It essentially consists of a controlled humidity chamber with separate reservoir and vapour compartments, clamped to a Peltier heater. To ensure a closed environment, the chamber is sealed by a removable lid, with only a tiny aperture for the laser beam to reach the sample. I designed the humidity chamber and modified the stage (originally designed by Dr Ellen Green) to include the mount for the chamber and Peltier heater.

For the Raman measurements, the chamber temperature was set at 30°C and three RHs were generated; 42% (paraffin oil), 82% (NaCl saturated distilled water) and 100% (distilled water). Additionally, samples were measured submerged in distilled water. RH and air temperature were measured using the same PCMini52 digital RH/temperature probe described in §2.2.2, and reservoir temperature was monitored using a submerged thermocouple (RS Temperature/Voltage Converter –


Figure 2.12: Schematic diagram of the uniaxial tensile testing apparatus used in the micro-Raman measurements. (M): manual micrometer; (O): L50X microscope objective; (L): removable lid of humidity chamber with small central aperture; (S): sample suspended between anchor points in the vapour chamber; (R): permeable reservoir containing the humidity generating solution; H: Peltier heating stage. The left anchor attached to the micrometer is free to move uniaxially, whilst the right remains fixed. The Perspex humidity chamber remains fixed, clamped in direct contact with the Peltier heater.

Type K). RHs and temperatures were measured immediately before and after any mechanical testing to ensure controlled experimental conditions.

2.3.3. Spectral Acquisition

Samples were removed from the buffer and washed in PBS (pH 7.4) then air-dried for up to 30 minutes suspended inside the humidity chamber; additional slack avoided application of strain due to contraction upon drying. Fibres were then fixed to anchors using Araldite 2012 (Huntsman) and allowed to cure for 1.5 hours to ensure a strong adhesion. Following this, the chamber humidity was set by inserting the required solution into the reservoir, and the fibre allowed to equilibrate to the local humidity for 2 hours. The rest length was set such that there was no visible slack left in the fibre, resulting in an approximate unstrained length of 6 mm for all samples. Prior to each measurement, a white light image of the fibres was acquired to select a region of interest (ROI) for spectral acquisition. Single-point spectra were collected as shown in figure 2.13 towards the centre of the suspended fibres: collagen – acquired from the centre of the 'apex' and 'diagonal' regions of at least two adjacent crimps per strain; elastin – at least three points were acquired radially across four fibres, and axially along a single fibre at each strain, to achieve a complete description of the fibres' structure during stress-strain testing. Polarised and depolarised spectra were collected in succession, each being an average of 3 accumulations at 2s acquisition time; this gave a good signal-to-noise ratio whist minimising thermal effects of the laser illumination on the sample. Spectra were acquired from a fixed location at each strain, only with minor adjustments of the focus. For collagen fibres,
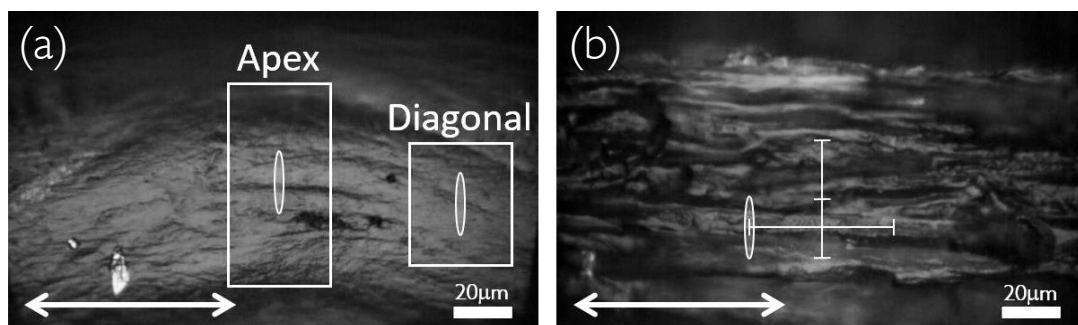
Figure 2.13: white-light images showing the regions where Raman spectra were collected. (a) *Collagen* fibre, where Raman spectra were acquired from a single spot at the centre of the 'apex' and 'diagonal' regions of the microscopic crimp structure. (b) *Elastin* fibre, where Raman spectra were acquired over multiple spots (shown by the white crosshair) in two lines: *vertically* – scanning over approximately four individual elastin fibres (each ~5 μm diameter) and *horizontally* – acquiring spectra from a single fibre. In both fibres, the ROI lies along the central axis at the middle of the suspended length. The macroscopic fibre axis is denoted by the arrow, and the oval represents the size of the laser line.

measurements were made from 0% strain in 5% increments until the sinusoidal crimp pattern was removed, whilst for elastin 10% increments were used, up to a maximum of 80% or until the fibre broke. A short relaxation period, judged by observing movement of the fibres in the white light image, was required after each ramp in strain prior to spectral acquisition.

2.3.4.   Spectral Analysis

2.3.4.1.   Data Pre-processing

After cosmic ray removal (using the nearest neighbours routing in Wire 4.0 software), micro-Raman spectra were transferred to a custom MATLAB (MathWorks) script where the x-axis (wavenumber) of each spectrum was converted into integer values using a piecewise cubic spline interpolation and cut to the desired wavenumber range (fingerprint: 135-1800 cm^{-1}; HWN region: 2600-3800 cm^{-1}). Depolarised spectral intensities ($I_\perp$) in the low-wavenumber region were reported as susceptibility spectra using the relation $\chi''(\tilde{v}) = I_\perp (n(\tilde{v}) + 1)^{-1}$, where $n(\tilde{v}) = [exp(hc\tilde{v})/kT]^{-1}$ is the Bose-Einstein occupation factor [131]. This enables reduction of the spectral intensity, removing the intense tail of the Rayleigh peak at lower wavenumbers. A baseline offset was applied at 1800 cm^{-1} and 3800 cm^{-1}, then each spectrum was normalised to the intensity (height) of the CH_2 peak (1450 cm^{-1}) and the CH stretching band (2935 cm^{-1}) in the fingerprint and HWN region, respectively.

2.3.4.2.   Peak Area Analysis

Peak areas were obtained using the integration tool in OPUS 5.5 (Bruker OpticGmbH). Table 2.1 lists the integration limits and linear baselines (see below) applied to the peaks of interest. This is shown in figure 2.14. It is usual to apply a baseline subtraction to Raman spectra to remove the background, which can be a result of sample autofluorescence, photoluminescence and stray light from scattering effects entering the spectrometer. Peaks of interest in the ranges 650-1800 cm^{-1} and 2600-3800 cm^{-1} were linearly baselined over limited ranges during peak area analysis (see table 2.1 and fig. 2.14).

To analyse the low-wavenumber region (LWN – 135-650 cm^{-1}), where a rising background makes a linear subtraction impossible, the inbuilt baseline subtraction tool in Wire 4.0 was used to fit and subtract a polynomial function to the wider spectra (135-1800cm^{-1}). In 'Intelligent fitting' mode, two parameters were set: the polynomial order and the noise

tolerance, respectively 12 and 1.9 for elastin and 11 and 1.5 for collagen. Each spectrum was visually inspected during this process and these values were selected as they successfully baselined all spectra with common zero points (collagen: 135, 363, 480, 655, 988, 1140, 1515 and 1800 cm^{-1}; elastin: 135, 353, 458 632, 798, 1138, 1515 and 1800 cm^{-1}), without introducing any negative intensity values outside of the noise. Collagen and elastin have different parameter values due to the intrinsic differences in their respective protein spectra.

Table 2.1: Peaks of interest and integration limits used to determine peak areas.

Peak/Band Centre (cm^{-1})	Integration Limits (cm^{-1})	Baseline Range[a] (cm^{-1})
O-H	3140-3700	3800 (H)
2970	2960-3030	3030 (H)
Amide I	1530-1740	1525-1752 (D)
1450	1430-1510	1140-1510 (D)
1243	1216-1257	
1099	1070-1117	988-1140 (D)
1030	1016-1036	
935	926-956	655-988 (D)
920	902-926	
875	868-902	
813	798-828	
570	550-585	135-1800 (P)
260	184-280	
170	135-190	

[a] Baseline is applied in three forms: a horizontal (H) baseline parallel to the wavenumber axis at the stipulated data point; a diagonal (D) baseline running through the two stipulated data points; and a polynomial (P) fit over the stipulated range.
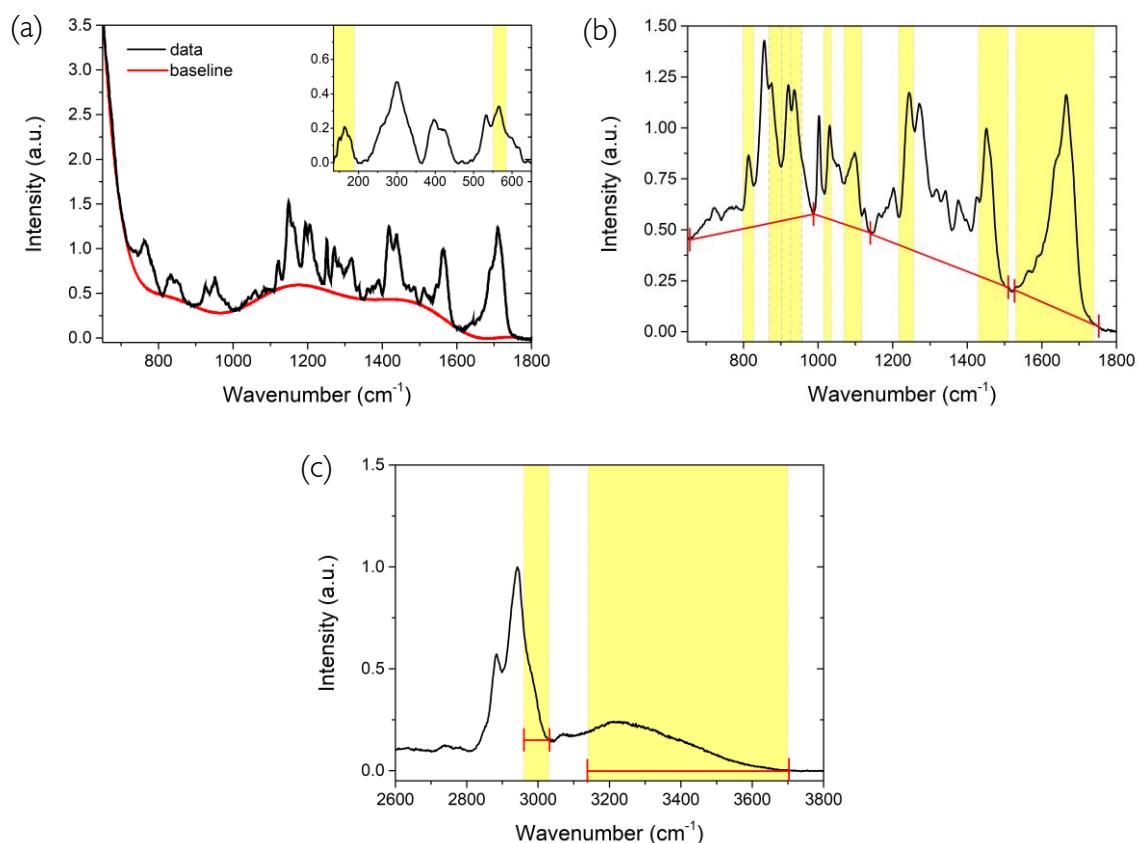
Figure 2.14: Raman spectra showing the peaks of interest and the baselining method used during analysis. (a) polynomial baseline applied to the 135-1800 cm^{-1} spectra to enable the analysis of the LWN region; inset shows the resulting subtraction over the range 135-650 cm^{-1} (b) four linear baselines applied to peaks in the fingerprint

2.3.4.3.   Statistical Analysis

Where peak areas were observed to increase or decrease as a function of strain, the differences were assessed with one-way analysis of variance (ANOVA) tests in MATLAB; with statistical significance set at 0.05. A multiple comparison test was subsequently carried out to assess which strains were significantly different to the zero-strain peak area. It was necessary to apply this only to collagen. In the water submerged fibre, peak areas from at least three point-spectra in a single crimp were grouped at each strain increment; for all other hydrations, peak areas from a single point-spectra in two successive crimps were grouped at each strain increment. Strain dependent peak area differences in the apex and diagonal regions were assessed independently. p-values are presented for peak area changes that were significantly different to the zero-strain peak area.

A similar approach was applied where peak areas were observed to change as a function of hydration. For collagen, peak areas were taken from single point-spectra in two successive

crimps *at maximum strain* and grouped at each hydration (at least three points from a *single* crimp at maximum strain for the water submerged fibre). For strain independent elastin, peak areas across all strains were grouped for a given hydration and passed into the one-way ANOVA (p<0.05). A multiple comparison test was subsequently carried out to assess which hydrations were significantly different to the water submerged peak area, and p-values are presented for the hydrations which met this criterion.

2.4.   Brillouin Spectroscopy

Brillouin light scattering (BLS) is a phenomenon arising from the interaction of incident photons with thermally excited acoustic waves or 'phonons' in a medium. First proposed by Leon Brillouin in 1922 [76] and observed experimentally for the first time in 1930 by Gross [132], it differs from Raman scattering as it probes the long range, in-phase density fluctuations of a system, rather than the local out-of-phase bond vibrations (optical phonons) that are detected in Raman spectroscopy (fig. 2.15). Brillouin frequency shifts are much smaller than Raman shifts – generally 5-20 GHz in biological materials as opposed to 10-120 THz. A typical Brillouin
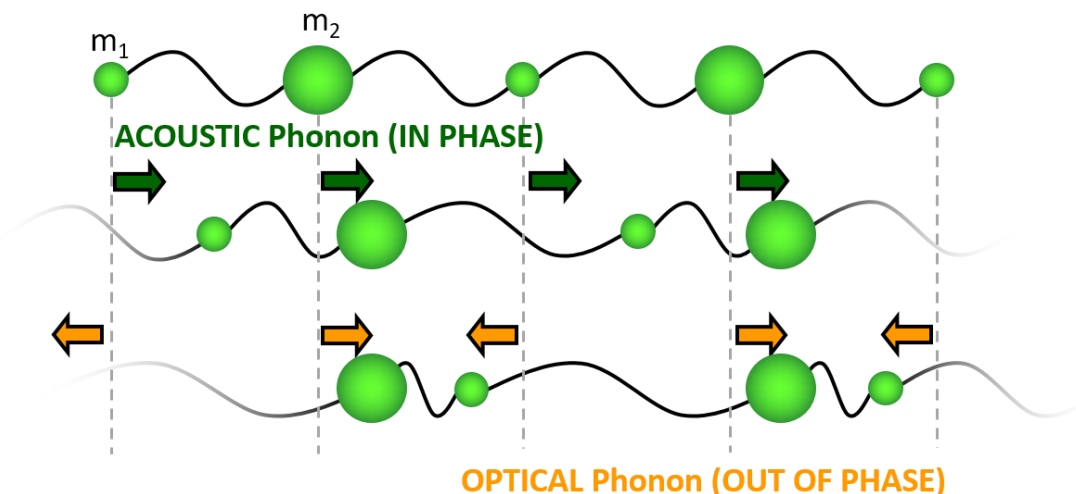
Figure 2.15: Schematic diagram showing a simple model of acoustic and optical vibrations in a one-dimensional diatomic chain. Atoms have mass m_1 and m_2 and are alternated. Arrows indicate the displacements of the atoms from their equilibrium positions (dotted lines). Acoustic phonons revealed by BLS, are in-phase movements of atoms in the chain with a displacement along the direction of propagation (longitudinal acoustic phonons) or perpendicular to the propagation direction (transverse acoustic phonons). Optical phonons probed by IR absorption and Raman scattering, are out-of-phase movements of the atoms producing an oscillating electrical dipole moment (longitudinal or transverse modes).
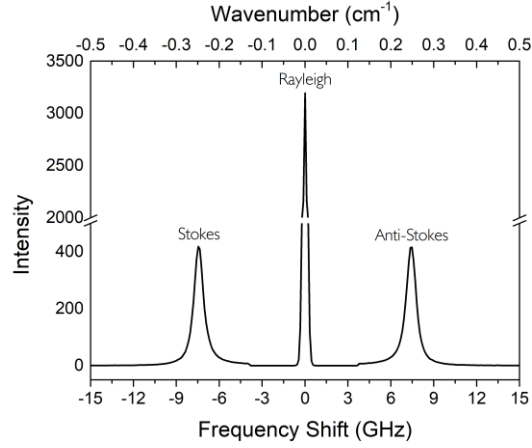
spectrum as shown in figure 2.16, is characterised by a doublet, centred around the Rayleigh peak, with the Stokes and anti-Stokes Brillouin peaks equally spaced and symmetric either side.

The origin of this spectrum is generally based on the hydrodynamic theory, reported by Berne & Pecora [2]. Here, the relevant equations that describe the mechanism of the scattering process by acoustic phonons and the origin of the Brillouin doublet are presented.

Figure 2.16: typical BLS spectrum featuring the Stokes and anti-Stokes Brillouin peaks symmetric about the intense central Rayleigh scattered line. A Brillouin spectrum is a plot of the scattering intensity as a function of the frequency shift from the incident wavelength. The top x-axis shows the spectral region in units of wavenumber (cm^{-1}).

The intensity of the scattered light incident on the detector is expressed by:

$$I_{if}(\boldsymbol{q}, \omega_f, R) = \left[\frac{|E_i|^2 \pi^2 n^4}{R^2 \lambda_i^4 \varepsilon_0^2} \right] \frac{1}{2\pi} \int_{-\infty}^{+\infty} \langle \delta\varepsilon_{if}(\boldsymbol{q}, 0)\delta\varepsilon_{if}(\boldsymbol{q}, t) \rangle \, e^{i(\omega_f - \omega_i)t} dt \quad (17)$$

where E_i is the amplitude of the incident electric field, $\boldsymbol{q}$ is the scattering wavevector (see equation 20), n is the refractive index of the scattering medium, R is the distance between the detector and the scatterer, λ_i is the wavelength of the incident radiation, and ε_0 is the dielectric constant of the scattering medium. This shows that the scattering intensity is inversely proportional to the fourth power of the incident radiation wavelength, and to the square of the distance that the scattered light travels before detection. The integral denotes the contribution to the scattering intensity due to the time autocorrelation function of the dielectric constant fluctuations, expressed by $\delta\varepsilon(\boldsymbol{r}, t) = \left(\frac{\partial\varepsilon}{\partial\rho}\right)_{T_0} \delta\rho(\boldsymbol{r}, t)$, where ρ is the local density and T_0 denotes the average temperature of the system. Taking the result of the integral, it can be shown that the scattering intensity due solely to the dielectric fluctuation, is described in terms of the dot product of the unit vectors of the incident ($\boldsymbol{n_i}$) and scattered light ($\boldsymbol{n_f}$)

$$I_{if}(\boldsymbol{q}, v) = \left(\boldsymbol{n_i} \cdot \boldsymbol{n_f}\right)^2 \left(\frac{\partial \varepsilon}{\partial \rho}\right)^2_{T_0} S_{\rho\rho}(\boldsymbol{q}, v) \tag{18}$$

where $S_{\rho\rho}(\boldsymbol{q}, v)$ is the intensity of the density correlation function which Einstein showed to be equal to $V\rho^2 k_B T \chi_T$. Here V is the scattering volume, ρ the mean number density, k_B the Boltzmann constant, T the temperature of the system, and χ_T the isothermal compressibility. There are a few points to note here, 1) there must be a change in dielectric constant due to a propagating density fluctuation (phonon) for BLS to occur, 2) the medium must have some compressible component for phonons to propagate; and 3) the scattering intensity is directly proportional to the scattering volume, the density of scatterers therein and the temperature of the medium.

Further development of equation (18) gives a correction term to Einstein's solution, such that the spectral density is defined as:

$$S_{\rho\rho}(\boldsymbol{q}, \omega) = \frac{1}{\pi} V\rho^2 k_b T \chi_T \left\{ \left(1 - \frac{1}{\gamma}\right) \left[\frac{D_T q^2}{\omega^2 + [D_T q^2]^2}\right] \right.$$
$$\left. + \frac{1}{\gamma} \left(\frac{\Gamma q^2}{[\omega - \omega(q)]^2 + [\Gamma q^2]^2} + \frac{\Gamma q^2}{[\omega + \omega(q)]^2 + [\Gamma q^2]^2}\right) \right\} \tag{19}$$

where $\Gamma \equiv \frac{1}{2}[(\gamma - 1)]D_T + D_V$ is the attenuation coefficient and γ the specific heat ratio. This equation explicitly describes the change in frequency when an incident photon of frequency ω interacts with a phonon of frequency $\pm\omega(q)$, travelling at a speed c_s in a medium, such that energy is gained or lost by the diffusion of momentum and heat; represented here by the longitudinal kinematic viscosity D_V and the thermal diffusivity D_T, respectively. The symbol q denotes the magnitude of the scattered wavevector, which is described below. Thus the triplet of the BLS spectra is given here in the two parts of equation (19) with the first part 1) describing the dominant Rayleigh scattered light corresponding to the central peak in figure 2.16; and the second 2) the 'Stokes' $(\omega - \omega(q))$ and 'anti-Stokes' $(\omega + \omega(q))$ parts of the Brillouin doublet, corresponding to the red or blue Doppler shift in frequency of the scattered light. The full solution to equation (19) includes a third part which

shifts the Brillouin peaks towards the Rayleigh line and renders their intensities slightly asymmetric (Mountain contribution), but this is a very small correction, thus equation (19) provides a good physical approximation. The symmetry of the 'Stokes' and 'anti-Stokes' parts of the BLS spectrum are consistent with the assumption of classically driven conservation of momentum.

Brillouin spectroscopy thus provides information on thermal properties of matter, which are represented in equation (19). Important for the work of this thesis are the acoustic attenuation and the adiabatic sound velocity. This last property gives access to several aspects of a material's viscoelastic properties; namely the elastic modulus, shear and bulk moduli and the Poisson's ratios in the GHz region (hypersounds), giving insight into the micro-scale mechanics of the sample medium. It suits the purpose of this thesis, having outlined the origins of the Brillouin frequency shift, to begin discussing the scattering geometry, before introducing how the speed of sound is extracted from the Brillouin spectra.

A generic scattering geometry is depicted in figure 2.17 for which the scattering wavevector is given as:
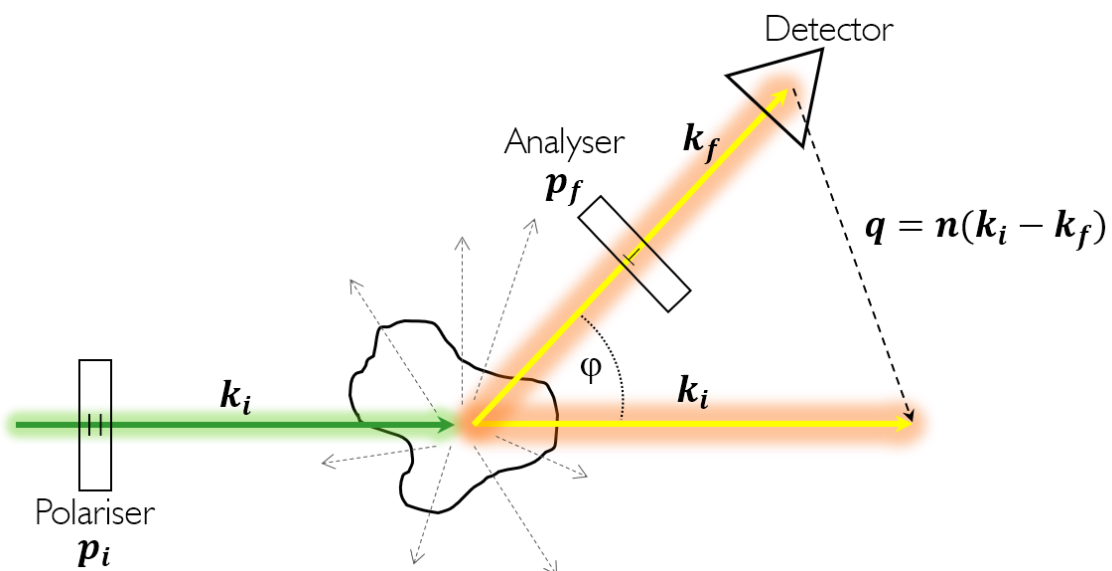
Figure 2.17: Diagram of a generic scattering geometry showing the origin of the scattering wavevector. Light of polarisation p_i and wavevector k_i is scattered in all directions. Only scattered light of wavevector k_f and polarisation p_f arrives at the detector. The scattering vector $q = n(k_i - k_f)$ is defined by the geometry and the refractive index n of the scattering medium. Adapted from: [2]

$$q = n(k_i - k_f) \tag{20}$$

where $k_i = 2\pi/\lambda_i$ and $k_f = 2\pi/\lambda_f$ are the wave vectors of the incident and scattered light, respectively. This is an expression of the principle of conservation of momentum. In these acoustic scattering processes, the wavelength changes very little, so the approximation that is made is that:

$$|k_i| \cong |k_f| \tag{21}$$

The vector triangle that represents the scattering process (fig. 2.17) is an isosceles triangle, such that the magnitude of q may be found using the law of cosines

$$q^2 = n^2 |k_i - k_f|^2 = n^2[2k_i^2 - 2(k_i \cdot k_i)] = 2n^2 k_i^2 (1 - cos\varphi)$$
$$= 4n^2 k_i^2 sin^2 \left(\frac{\varphi}{2}\right) \tag{22}$$

giving:

$$q = 2nk_i sin \left(\frac{\varphi}{2}\right) \tag{23}$$

There are two preferred scattering geometries employed in a BLS experiment: the one with scattering angle φ equal to 180°, the backscattering configuration that is typical of a microscopic approach; and 90°, where illumination and collection paths are orthogonal to one another. For the measurements of anisotropic materials such as the protein fibres, a preferred geometry involves 180° scattering geometry but with sample mounted on a reflective substrate at 45° to the incoming beam (a *platelet-like* configuration). This configuration (fig. 2.18a) enables two

'channels' to be detected, two phonon modes with wavevectors $q = q_b = 2nk_i$ and $q = q_s = 2k_i \sin\varphi = \sqrt{2}k_i$ respectively, the latter due to a scattering process with an exchanged wavevector [133, 134]. These are the bulk mode (q_b) which travels along the same direction as the incident beam and is the only mode probed in backscattering with beam orthogonal to the sample; and the parallel-to-surface mode (q_s) which allows for a directional analysis of the speed of sound by rotation of the sample in-plane (z-axis – see fig. 2.18b). These longitudinal modes are observed at distinct frequencies in the Brillouin spectra (fig. 2.19), according to the velocities [135, 136]:

$$V_L \approx \pm \frac{\omega_b}{q_b} \approx \pm \frac{\nu_b \lambda_i}{2n} \qquad \text{and} \qquad V_L \approx \pm \frac{\omega_s}{q_s} \approx \pm \frac{\nu_s \lambda_i}{\sqrt{2}} \qquad \text{(24a, b)}$$

where ν_b and ν_s are the frequency shifts of the longitudinal bulk and parallel-to-surface phonons, respectively, and are determined by curve fitting of the BLS spectra (see §2.4.3 below). It is worth highlighting that use of the platelet-like configuration enables – through the
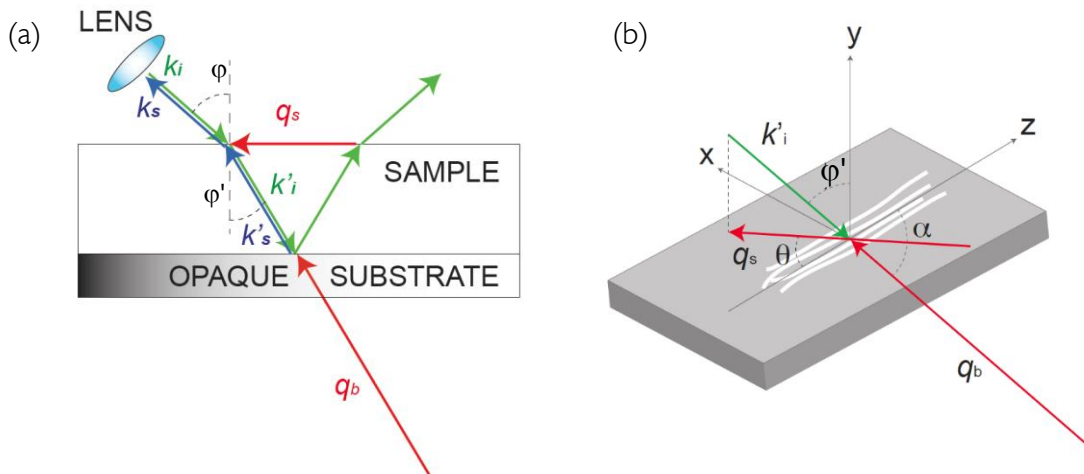
Figure 2.18: (a) Schematic diagram of the BLS scattering geometry using a specimen in contact with the surface of a reflective silicon substrate, the platelet-like configuration. The incident light (k_i) passes through the lens, is refracted at the air-sample interface (k'_i) and focused at the sample-substrate interface. The scattered light collected by the same lens (k'_s) results from interaction with both bulk phonons (q_b) and those travelling PS of the sample (q_s). Angles between the directions of light and the normal to the surface (determined by the scattering angle) are indicated as φ and φ'. (b) Schematic diagram of the sample and of the adopted coordinate system: z defines the extraordinary axis parallel to the direction of the fibres. Angles θ and α are those between the direction of phonons q_s and q_b to the z-axis, respectively. k_i, k'_i, k_s, k'_s: wavenumbers of the incident and scattered light; q_b, q_s, wavevectors of the bulk and PS modes, respectively.

parallel-to-surface (PS) mode – measurement of the speed of sound without prior knowledge of the refractive index of the sample, as the wavevector q_s does not depend on n (equation 24b). On the other hand, in this particular geometry, the BLS technique provides a measure of the refractive index from the ratio of the frequency shift of the phonon peaks, v_b and v_s:

$$n = \frac{v_b}{v_s}\sin(\varphi) \tag{25}$$
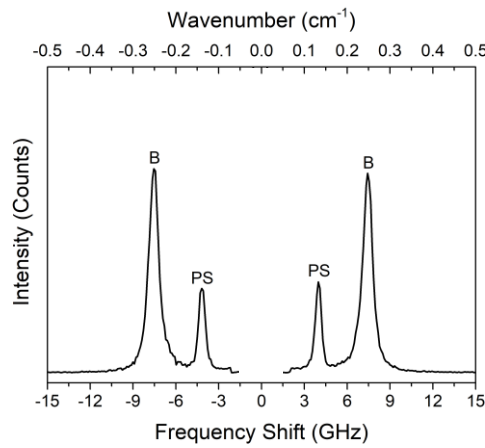
Figure 2.19: typical BLS spectrum using the platelet-like configuration to activate the parallel-to-surface (PS) phonon modes. These peaks manifest at a lower frequency than those representing the bulk phonon modes (B) of the traditional Brillouin doublet, but are equally symmetric about the central Rayleigh scattered line (R).

Collagen and elastin fibres are assumed to be as transversely isotropic materials with a hexagonal symmetry, such that the propagation of an elastic wave through the fibre is governed by a symmetric stiffness tensor with five independent elastic constants, c_{11}, c_{12}, c_{13}, c_{33} and c_{44}, which describe the proportionality of stress to strain in a defined direction [80]:

$$c_{ij} = \begin{bmatrix} c_{11} & c_{12} & c_{13} & 0 & 0 & 0 \\ & c_{11} & c_{13} & 0 & 0 & 0 \\ & & c_{33} & 0 & 0 & 0 \\ & SYM & & c_{44} & 0 & 0 \\ & & & & c_{44} & 0 \\ & & & & & \dfrac{c_{11} - c_{12}}{2} \end{bmatrix}$$

through the generalised tensor form of Hooke's law

$$\boldsymbol{\sigma_i} = c_{ij}\boldsymbol{\varepsilon_j} \tag{26}$$

These elastic constants are associated with the longitudinal phonon propagation speed with respect to the angle-to-fibre axis θ, through the expression:

$$
\begin{aligned}
V_L^2(\theta) = \frac{1}{2\rho}\Big\{ & c_{11}sin^2\theta + c_{33}cos^2\theta + c_{44} \\
& + \big\{[(c_{11} - c_{44})sin^2\theta + (c_{44} - c_{33})cos^2\theta]^2 \\
& + 4\big((c_{13} + c_{44})sin^2\theta cos^2\theta\big)\big\}^{1/2}\Big\}
\end{aligned} \tag{27}
$$

where, ρ is the density of the fibres. In addition to this longitudinal mode, there is also a transverse component to the acoustic wave, with a velocity given as:

$$V_T^2(\theta) = \frac{1}{\rho}\left(\frac{(c_{11} - c_{12})}{2}sin^2\theta + c_{44}cos^2\theta\right) \tag{28}$$

and accessed by the depolarised spectrum, VH (see §2.4.1 below). These expressions are further simplified by setting the angle-to-fibre axis such that V_L is equal to $\sqrt{c_{11}/\rho}$ ($\theta = 90°$) and $\sqrt{c_{33}/\rho}$ ($\theta = 0°$). The approximation [80] $c_{12} \sim c_{11} - 2c_{44}$ allows V_T to equate to $\sqrt{c_{44}/\rho}$ ($\theta = 0°$), leaving only c_{13} to be determined by fitting (see §2.4.3 below). Thus, having determined all the elastic constants from the Brillouin spectrum, the elastic properties of the fibres are defined as follows:

$$E_{\parallel} = c_{33} - \frac{2c_{13}^2}{c_{11} + c_{12}} \tag{29}$$

$$E_\perp = \frac{(c_{11} - c_{12})[c_{33}(c_{11} + c_{12}) - 2c_{13}^2]}{c_{11}c_{33} - c_{13}^2} \tag{30}$$

$$G = c_{44} \qquad\qquad K = \frac{-2c_{13}^2 + (c_{11} + c_{12})c_{33}}{c_{11} + c_{12} - 4c_{13} + 2c_{33}} \tag{31}$$

$$\nu_{13} = \frac{c_{13}}{c_{11} + c_{12}} \qquad\qquad \nu_{12} = \frac{c_{33}c_{12} - c_{13}^2}{c_{33}c_{11} - c_{13}^2} \tag{32}$$

with $E_\parallel$ and $E_\perp$ the axial and radial elastic modulus, G and K the shear and bulk moduli, and ν_{13} and ν_{12} the major and second Poisson's ratios.

2.4.1. Brillouin Instrumentation

The proximity to the intense Rayleigh line makes resolving the weak Brillouin peaks a challenge. Fabry-Perot interferometers (FPI) were introduced as early as the 1930s [132], but it was not until the development of the tandem multipass Fabry-Perot (TMFP) by John Sandercock in the 1970s and 80s [137, 138], that measurements with high contrast and large free spectral range (FSR) became possible. The interferometer used in this thesis is based on this design, and is based on filtering the scattered light by passing it thrice sequentially through two etalons scanning in tandem. The (3+3) multipass enhances the contrast above 10^{12} or 120 dB against the elastic background, whilst the double etalon supresses neighbouring interference orders, the so-called *ghosts*, making interpretation of the spectra over a wide frequency range clearer.

All BLS measurements were performed using a custom built apparatus with a Sandercock-type tandem multipass (3+3) Fabry-Perot interferometer, having high contrast and spectral resolution [139]. Figure 2.20 shows a schematic of the BLS system. A single-mode 532 nm solid state laser (Spectra Physics Excelsior) operated at 76 mW output power at the sample,

is split into a reference beam to the spectrometer and an incident beam which is focused onto the sample by a low-NA objective. A polariser selects a vertical polarisation (V) for the incident light just prior to a 20 cm achromatic lens (spot size of 30-40 μm) which focusses and collects light from the sample in backscattering. The sample is mounted vertically on a goniometer, fixed at a 45° angle to the incident beam, to enable in-plane rotation of the sample whilst maintaining a constant scattering angle ($2\varphi = 90°$; see figure 2.18 above) and scattering volume. Scattered light is collected by the same objective used for focusing, passed back through an analyser either in (vertical-horizontal – VH) or out (vertical-unpolarised – VU) of the beam path, and thus through a pinhole into the spectrometer and then a single-photon photomultiplier detector (JRS Scientific Instruments TFP-1). The interferometer is operated through a control unit and by the computer software (GHOST 6) for data handling and manipulation [140].

Polarisation-resolved Brillouin measurements determine which acoustic modes are detected. The polarised arrangement (VU – incident and scattered light both vertically polarised) detects only the longitudinal acoustic modes, whilst the depolarised arrangement (VH – scattered light horizontally polarised), detects the transverse modes.
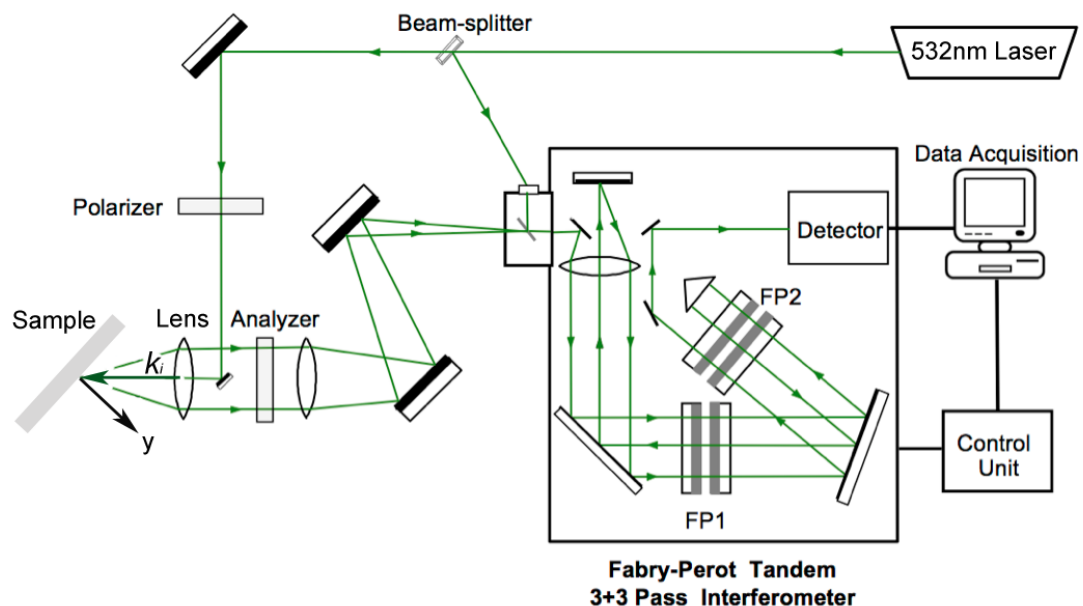
Figure 2.20: Schematic of the BLS apparatus with backscattering geometry used in the measurements; the incident light emitted by a solid-state laser is sent to the sample through an achromatic lens. The light scattered by bulk acoustic phonons and by those resulting from reflection of light at the substrate surface, which is in contact with the sample, is collected by the same lens, filtered by a tandem-multipass Fabry–Perot interferometer and detected by a photomultiplier. FP1 and FP2 indicate the two interferometers constituting the tandem scanning set-up. A polarizer selects the polarization of incident light, and an analyser is used to select the polarization of scattered light.

2.4.2. Spectral Acquisition

Fibres and tissue sections were removed from the buffer, washed in pure water and placed directly (fibres were aligned linearly) onto reflective silicon slides for BLS measurement. A glass cover-slip was placed on top of the sample, and sealed in place by a parafilm gasket sealed by a heated soldering iron passed gently over the glass surface. Once sealed, the excess water immediately surrounding the sample was maintained for several days. Water evaporation was enabled for dehydration kinetic measurements by leaving one side of the hydration compartment unsealed. Care was taken to avoid stretching or reorienting the samples throughout preparation.

2.4.2.1. Angle-Resolved Experiments

The sample hydration chamber was mounted on the goniometer and focussed as described above to activate the two phonon channels q_s and q_b. The desired polarisation was selected (VU or VH) and BLS spectra were acquired rotating the sample between acquisitions to adjust the angular propagation direction of q_s with respect to the fibre axis (generally $-15° > \theta > 120°$; see figure 2.18 above). Measurements were made over the frequency range –27 to 27 GHz at 0.2 GHz resolution, with a free spectral range of 30 GHz. Acquisition times varied due to differences in sample scattering cross-section, concentration and thickness, however, a good signal-to-noise ratio was generally achieved using a 10 minute acquisition time. Spectra were acquired in the VU polarisation at $\theta = 0°$ every 10 minutes for 12 hours. All experiments were conducted at least in duplicate.

2.4.2.2. Microfocussed Experiments

To determine the specific contribution of the intra- and extrafibrillar spaces to the micromechanics of the fibres, micro-BLS spectra were collected with a scanning BLS microscope. The system is similar to the macro-BLS system described above (see [141, 142] for full details), but operates at 5 mW, with a long working distance (4.7mm) Zeiss dark-field objective (NA 0.75) in backscattering geometry ($\varphi = 0°$; bulk phonon modes only – see figure 2.18 above). The lateral resolution of the set-up is approximately 250 nm [142] and the spectral resolution is 0.1 GHz. The sample chamber was mounted horizontally and positioned using a manually operated piezoelectric XYZ translation stage (PI 611-3S Nanocube with PI E-664 controller). Geometry of the fibres and sections was recorded in (455 nm) LED light

microscope images, obtained using the same Zeiss dark-field objective and a CCD camera. Regions of interest were located and single point spectra acquired using GHOST software as above.

2.4.3.   Spectral Analysis

If only a narrow frequency region around the Brillouin peaks is analysed, the spectrum of scattered light from viscoelastic media is most closely approximated by a damped harmonic oscillator (DHO) [139, 140, 143]
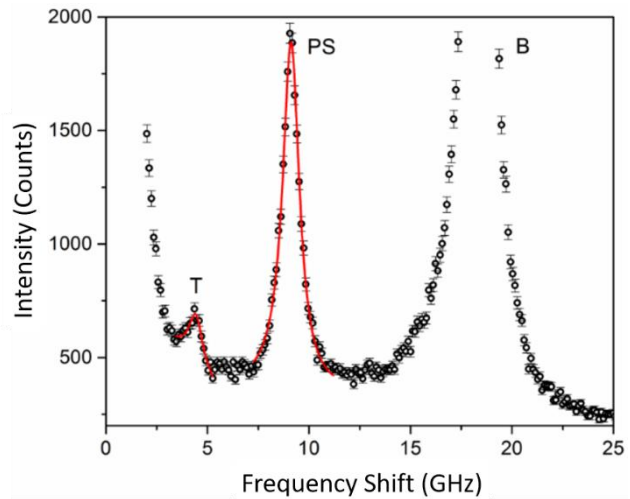
$$I(\omega) = \frac{I_0}{\pi} \frac{\omega_b^2 \Gamma_b}{(\omega^2 - \omega_b^2)^2 + \omega^2 \Gamma_b^2} \tag{33}$$

where ω_b and Γ_b correspond to the frequency position and linewidth of the Brillouin peaks.

Data analysis was performed using the GHOST software, where the intensity profile of each Brillouin band was fitted to the DHO function using a least-squares fitting function based on the Levenberg-Marquardt algorithm, and a convolution of the instrumental function was applied to correct for the finite linewidth of the laser spectrum [140]. Baselines were applied in a systematic, reproducible manner. Figure 2.21 shows the results of a DHO fit applied to both the PS and transverse peaks of a representative Brillouin spectrum. Results from the fit of each respective peak (including the fitting error calculated by the software) were averaged between the Stokes and anti-Stokes bands and the acoustic wave velocity was calculated, substituting the mean frequency position into equations (24a) for the bulk and (24b) for the PS and transverse peaks, respectively. Angle-resolved velocities from the PS and transverse modes were plotted as a function of the angle-to-fibre axis, θ (in radians) and equation (27) was subsequently fitted to the data with c_{11}, c_{33} and c_{44} fixed at the values obtained using the reduced formula described above and the remaining elastic constant, c_{13}, left freely varying. In the case of elastin, for which the transverse mode was not detected, c_{44} could not be derived by independent measurement. Thus, in the fit to equation (27), constraints to ensure positive sound velocities in all directions were [144]: $c_{11} > |c_{12}|$ and $c_{44} > 0$, and the remaining

constants were determined [136, 145]. Substitution of the elastic constants into equations (29-32) yielded the elastic moduli and Poisson's ratios as defined above.

Figure 2.21: Anti-Stokes BLS spectrum of dry trypsin-digested collagen fibre measured at $\theta = 30°$ with VH polarisation. Labels T, PS and B denote peaks related to transverse, parallel-to-surface and bulk modes, respectively. A leakage of the VV polarisation enables the PS and bulk peaks to still be observed. Results of fit analysis (red lines) using a damped harmonic oscillator (DHO) model for both T and PS modes are also shown. Error bars indicate the standard error (square root of number of counts).

The attenuation of the acoustic wave is a measure of viscoelastic damping and was calculated as the linewidth-to-frequency ratio of the bulk peak $tan(\delta) = \Gamma_b/\omega_b$ over all angles to the fibre axis, θ. This is a measure of the damping of the acoustic wave and relates to the viscosity of the medium.

2.4.4. Sample Morphology

After the Brillouin measurements, samples were air-dried and metallised by sputter coating the surface with a 1.5 nm layer of chromium prior to scanning electron microscopy (SEM-FEGLEO1525, Inlens detector), operating at an acceleration voltage of 5.0 kV.

The scanning electron micrographs in figure 2.22 show that (a) elastin specimens from bovine nuchal ligaments are composed of a roughly parallel array of fibres approximately 4-5 μm in diameter; (b) the bovine nuchal ligament is made of a roughly aligned assembly of the elastin fibres; (c) the high degree of alignment in the fibrillar (type-I collagen) substructure of an RTT fibre, with orientation predominantly along the diagonal from the upper left to the lower right corner of the image pane – fibril diameters are in the range of 100-300 nm; (d) a section of cartilage cut parallel to the articular surface from the deep zone, shows fibres of (type-II) collagen running perpendicular to the section plane.
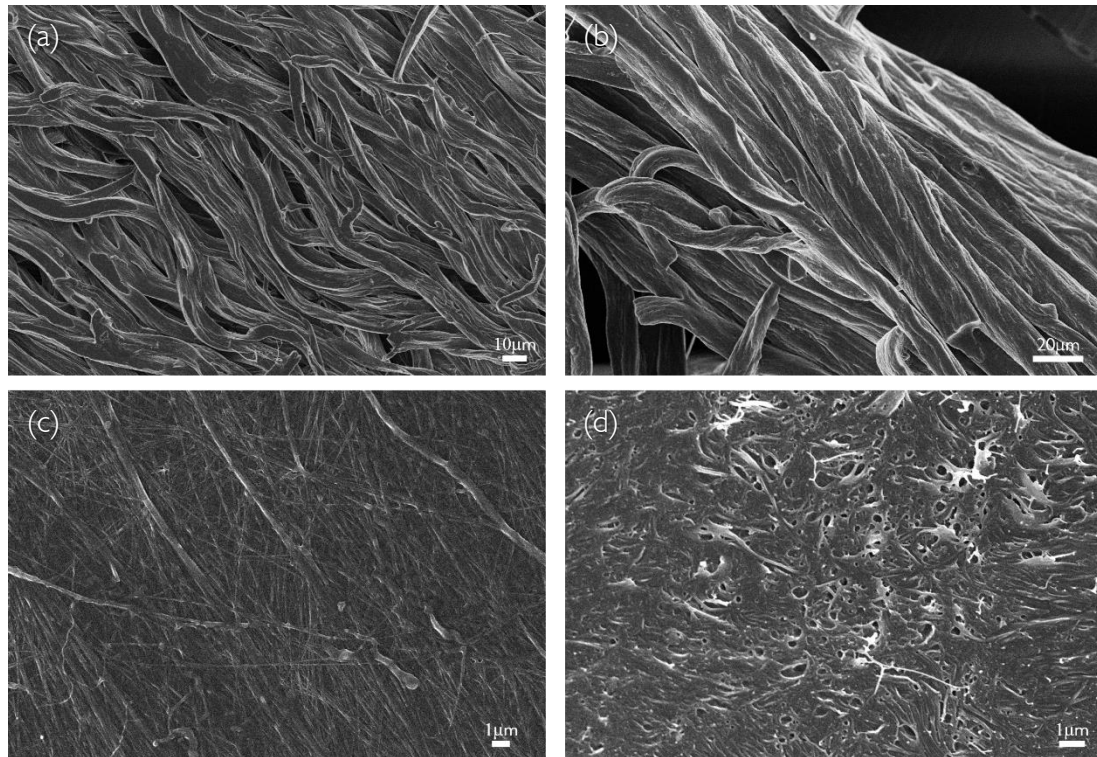
Figure 2.22: Scanning electron micrographs showing (a) individual elastin fibres within the bovine nuchal ligament; (b) wider view of the bovine nuchal ligament; (c) type-I collagen fibrils from RTT; and (d) type-II collagen fibrils in EMJ cartilage. All samples are from the same animals used in the BLS experiments.

2.4.5.   Estimating Wet Fibre Density

Using a macroscopic approach, aliquots of saturated sucrose solution were added cyclically to a bath of distilled water at room temperature, suspending a PBS soaked fibre of the same dimension as those used in experiment (excess PBS removed by gently dabbing with blue roll), after each addition of the solution. The fibre was considered buoyant upon reaching a solution density where it did not sink or float within 10 seconds of submersion in the bath (this short time ensured that bulk water in the fibre was not replaced by the sugar solution). The resulting suspension was then weighed in a glass pycnometer to determine the density of the fully hydrated fibres. To estimate the uncertainty, this process was repeated a second time with new fibre samples and fresh saturated sucrose solutions.

3

Protein Fibre Macromechanics

3.1.   Introduction

This chapter focusses on the macroscopic mechanical properties of the protein fibres and their relationship with hydration. It is well known that the removal of water from collagen and elastin produces stiffer, more brittle fibres [146, 147], however intermediate hydration states have rarely been studied and work is usually confined to the hydration extremes. Results presented here include the stress-strain and stress relaxation response of both protein fibres within a range of hydrations, 100 to 21% relative humidity (RH); accompanied by analysis of the Young's modulus, which will later be compared with the longitudinal modulus from Brillouin light scattering in chapter 4. Stress relaxation data are presented, to study the effects of water on the fibres' viscoelastic properties, namely the ability to stretch and reconfigure. The stress-strain and stress relaxation responses of each fibre were measured first to 5% tensile strain and then to 10%, a low- and a high-strain regime to assess to what extent water mediated the elongation of the fibres. Results from the two strain regimes are presented adjacently for evaluation and comparisons are drawn between the two protein fibres.

3.2.   Macroscopic Mechanical Properties

3.2.1.   Stress-Strain Plots

3.2.1.1.   Type-I Collagen Fibres

Figure 3.1 shows the effect of dehydration on the stress-strain response of preconditioned type-I collagen fibres in the low (5%) and high (10%) tensile strain regimes. The fully hydrated fibres, at 100% RH, displayed the typical J-shaped response of collagen, with clearly defined linear, heel and toe regions. A progressive decrease was observed in the length of the toe region at each dehydration with a gradual increase in the rate of initial stress uptake, becoming immediate upon application of strain at 21% RH. This resulted in an extension of the heel region of the dehydrated fibres. Figure 3.3 shows the change in strain that was required to achieve a stress equivalent to that measured at 5% in the low-strain regime, after preconditioning of the same fibre to twice its initial extension (high-strain regime). Fully hydrated fibres required an additional 2% strain, but dehydration gradually reduced this difference such that below 85%RH the stress-strain response was essentially the same within the error in both strain regimes.
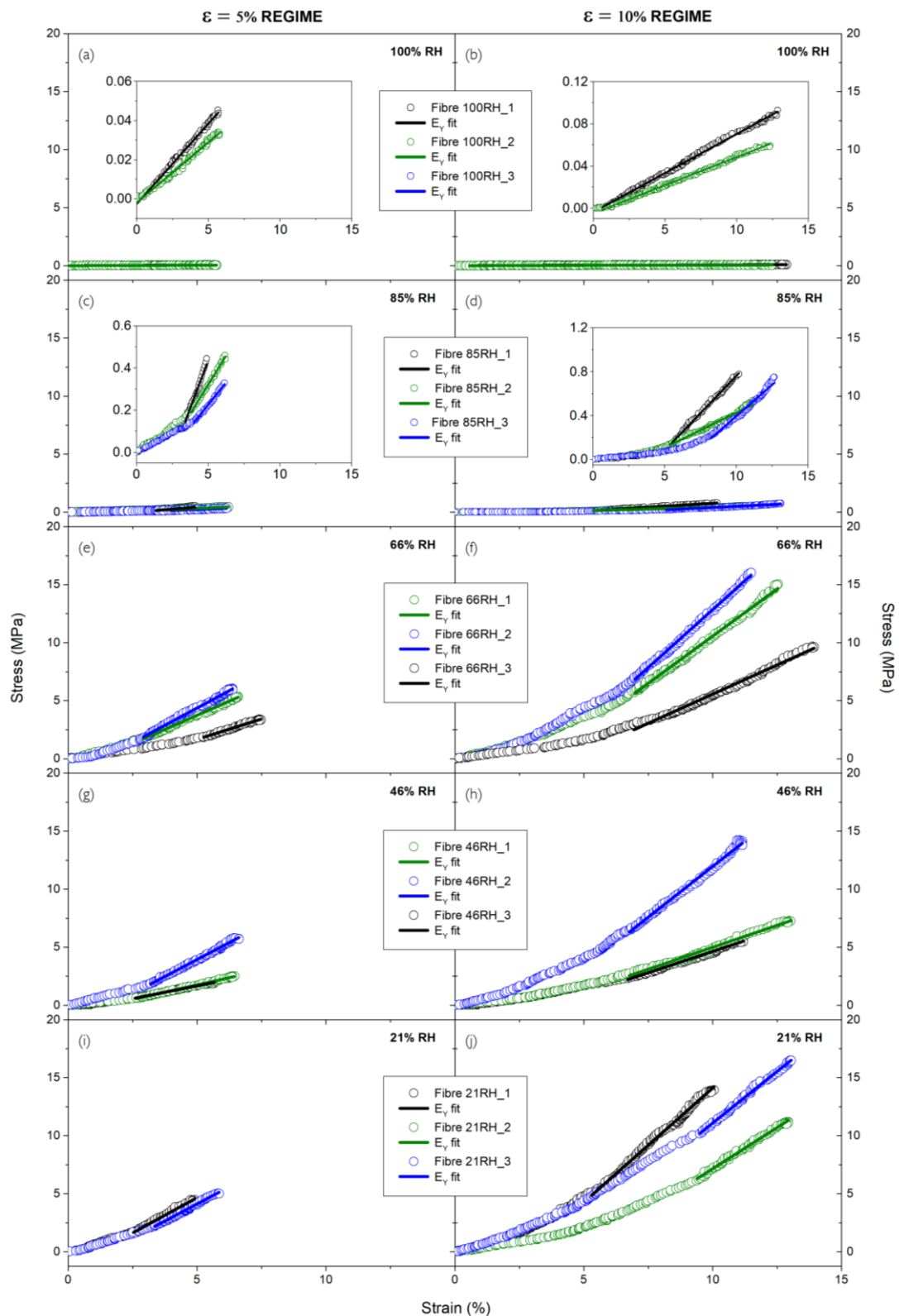
3.2.1.2.   Elastin Fibres

Figure 3.2 shows the effect of dehydration on the stress-strain response of preconditioned bovine nuchal elastin in the low (5%) and high (10%) tensile strain regimes. The fully hydrated fibres, at 100% RH, responded linearly to increasing strain whilst, at lower hydrations, a more gradual uptake of stress was observed through a curved stress-strain profile. Similar to collagen above, figure 3.3 shows that at high hydration, doubling the initial preconditioned extension of the elastin fibres increased the strain required to achieve a stress equivalent to that measured at 5% in the low-strain regime, by approximately 1 and 3% in the 100 and 85% RH states, respectively. Further dehydration lead to the stress-strain response being the same in both high- and low-strain regimes.
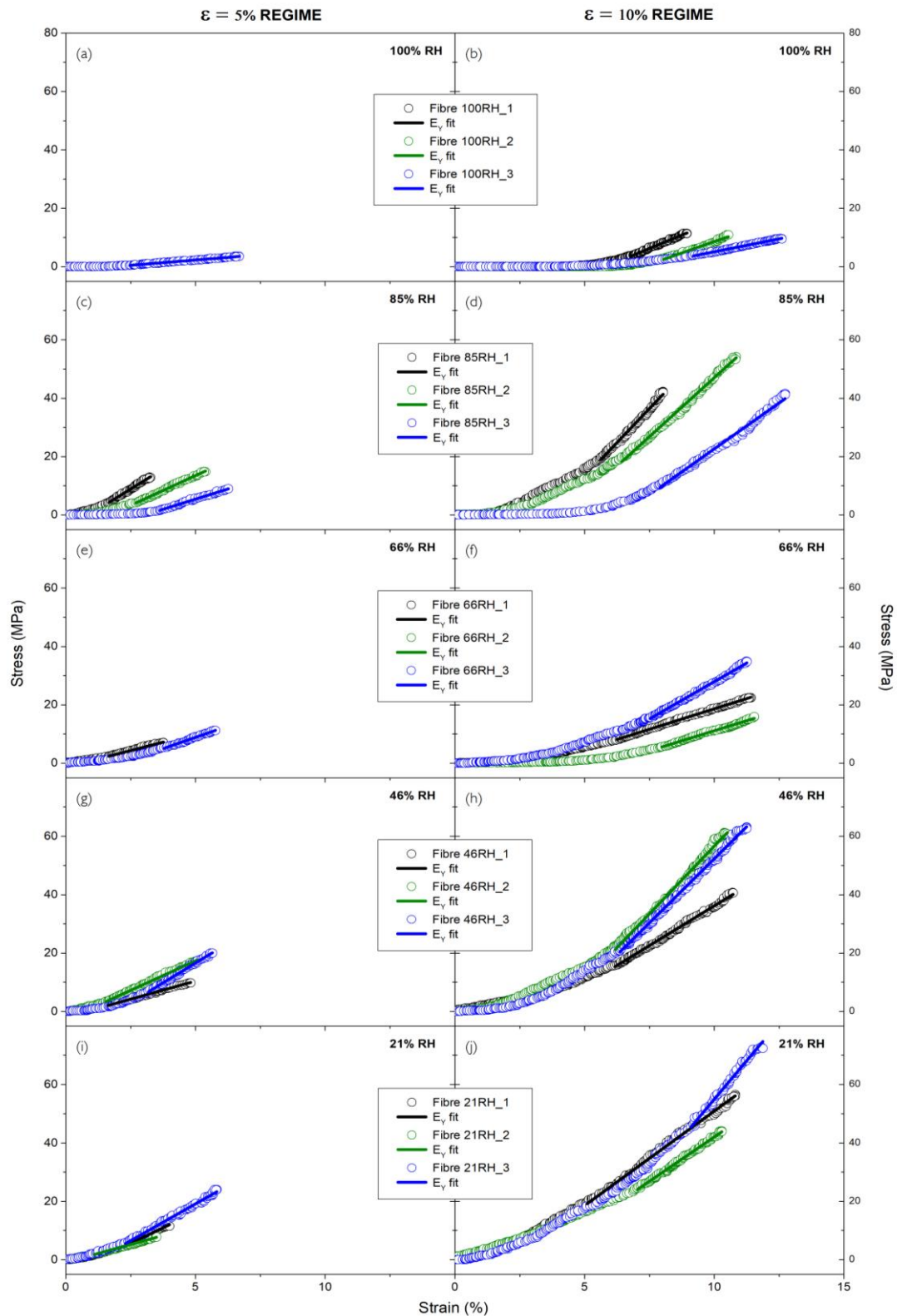
Figure 3.1: stress-strain plots of preconditioned type-I collagen fibres from rat tail tendon as a function of hydration: (a-b) 100% RH; (c-d) 85% RH; (e-f) 66% RH; (g-h) 46% RH; and (i-j) 21% RH. Responses are recorded in the 5% (left) and 10% (right) tensile strain regimes. Lines show fits of Young's modulus (E_Y). Mean R^2 = 0.997. Three different fibres were tested at each hydration (unique labels and colours identify the same respective fibre in all figures).

Figure 3.2: stress-strain plots of preconditioned elastin fibres from bovine nuchal ligament as a function of hydration: (a-b) 100% RH; (c-d) 85% RH; (e-f) 66% RH; (g-h) 46% RH; and (i-j) 21% RH. Responses are recorded in the 5% (left) and 10% (right) tensile strain regimes. Lines show fits of Young's modulus (E_Y). Mean $R^2 = 0.995$. The insets show a magnification of the 85 and 100% RH data. Three different fibres were tested at each hydration (unique labels and colours identify the same respective fibre in all figures).
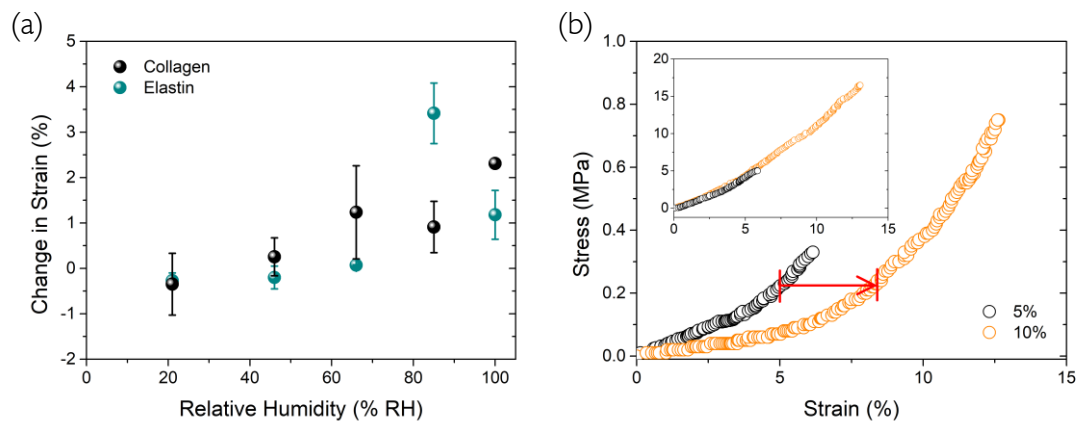
Figure 3.3: (a) plot as a function of hydration (100 to 21% RH) of the change in strain that was required to achieve a stress equivalent to that measured at 5% in the low-strain regime, after secondary preconditioning of the same fibre to twice its low-strain extension. Error bars are ± 1 stdev (n=3). (b) stress-strain plot of 85% RH elastin, showing an example of how doubling the preconditioning strain of a fibre to 10%, increases the strain required to achieve a stress equivalent to that measured at 5% in its initial low-strain preconditioning state. The inset shows the case for 21% RH elastin where the stress-strain response is essentially identical in both high- and low-strain regimes.

3.2.1.3.   Young's Modulus for Collagen and Elastin

The Young's modulus was calculated from linear fit analysis of the stress-strain curve (lines in figures 3.1 and 3.2). This best represented the actual modulus of the fibres, which below 100% RH (collagen) and 85% RH (elastin) exhibited a permanent deformation where the fibres would become elongated beyond their initial resting length under the applied stress, resulting in bending due to compression upon returning to 0% strain. Unbending manifested in the curvature of the stress-strain plots (figs. 3.1 and 3.2), prior to the linear uptake of stress in the latter part of each curve. Figure 3.4a shows the Young's modulus of type-I collagen fibres as a function of hydration. An initial increase in modulus (6-fold to 412 ± 136 MPa in the low strain regime and 3-fold to 790 ± 152 MPa in the high) was observed between the fully hydrated state at 100% RH and the first dehydration at 85% RH, after which the modulus remained unchanged within the error. This pattern was consistent in both the high- and the low-strain regimes, although the magnitudes of the former were larger, in keeping with the steeper stress-strain response at the higher strain.

Figure 3.4b shows the Young's modulus of elastin, which responded slightly differently to dehydration with a gradual increase in modulus. Initially this was by an order of magnitude between 100 and 85% RH, and then by a further order of magnitude between 85% RH and the subsequent dehydrations. Unlike in collagen, doubling the fibre extension in the high-strain

regime had no effect on the modulus, suggesting that the linear region of the stress-strain response is conserved at higher strain.

Generally, elastin had a lower Young's modulus than collagen, but the difference between the two decreased markedly with dehydration of the tissue, where elastin was approximately three orders of magnitude softer than collagen in the fully hydrated state, but only five times less stiff in the 'dry' state at 21% RH.
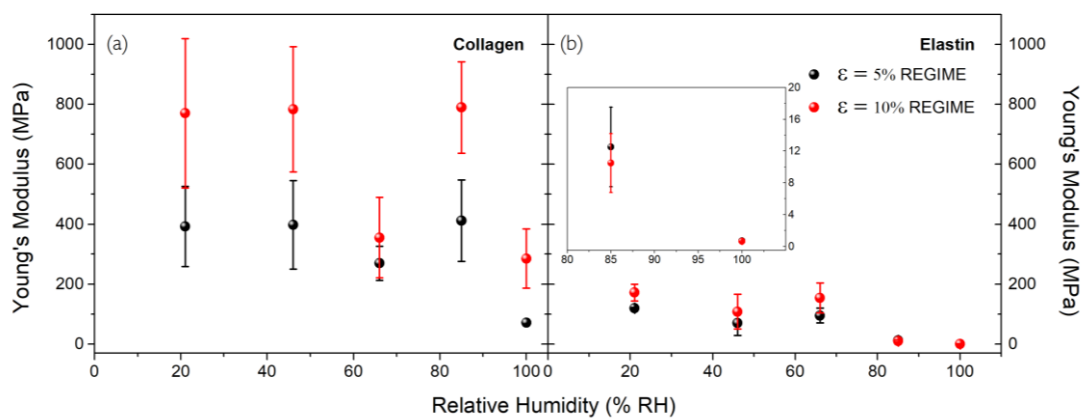

Figure 3.4: plots showing Young's moduli as a function of hydration in the range 100 to 21% RH for (a) type-I collagen from rat tail tendon and (b) elastin from bovine nuchal ligament in the 5 and 10% tensile strain regimes. The inset shows a magnification of the 80-100% RH section of the elastin data. Error bars are ± 1 stdev (n=3).

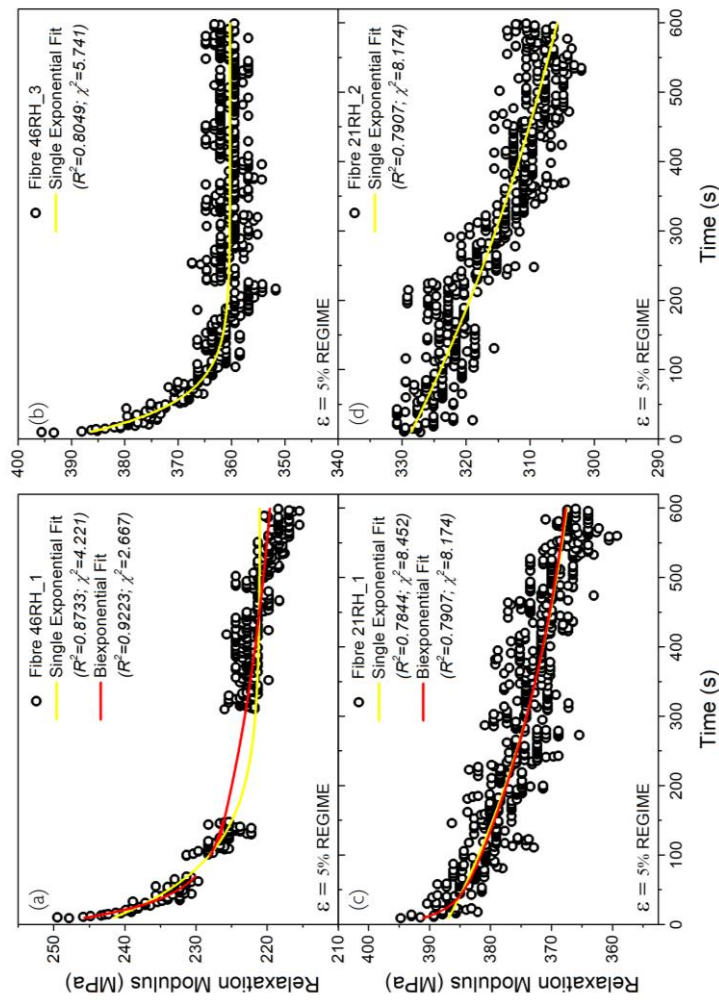## 3.2.2.   Stress Relaxation

3.2.2.1.   Type-I Collagen
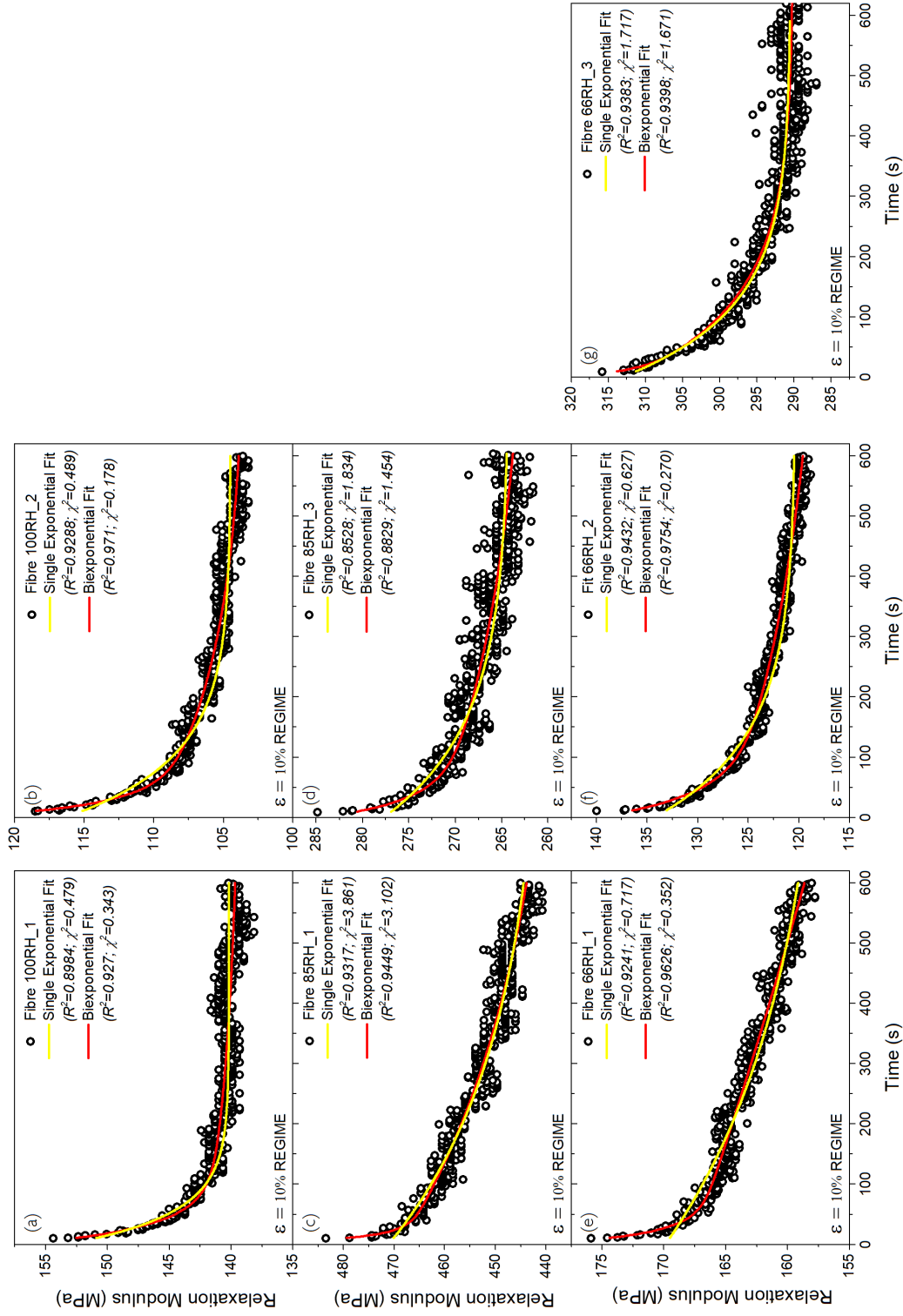
Figure 3.5-3.6 and 3.7-3.8 present the stress relaxation profiles of preconditioned type-I collagen fibres ramped to 5 and 10% strain, respectively, at 20 mm/min and held for 600s. Plots are given as the relaxation modulus as a function of time and display the fitting results of single- and double-exponential components of the Maxwell-Weichert model for each fibre at a respective hydration. Fitting statistics (R^2 and χ^2) are displayed. Corresponding results of the exponential fitting (average values) are presented in tables 3.1 and 3.2 for the low- and high-strain regimes, respectively. In all cases, except for 46 and 21% RH in the low-strain regime, a biexponential provided the best fit to the decays of the relaxation modulus. This well described the fast relaxation component (τ_1) at the beginning of each decay, which showed little variation with hydration, and had an average of 15 ± 8 seconds in the low-strain regime and 21 ± 9 seconds in the high. The corresponding modulus (E_1) of this first Maxwell
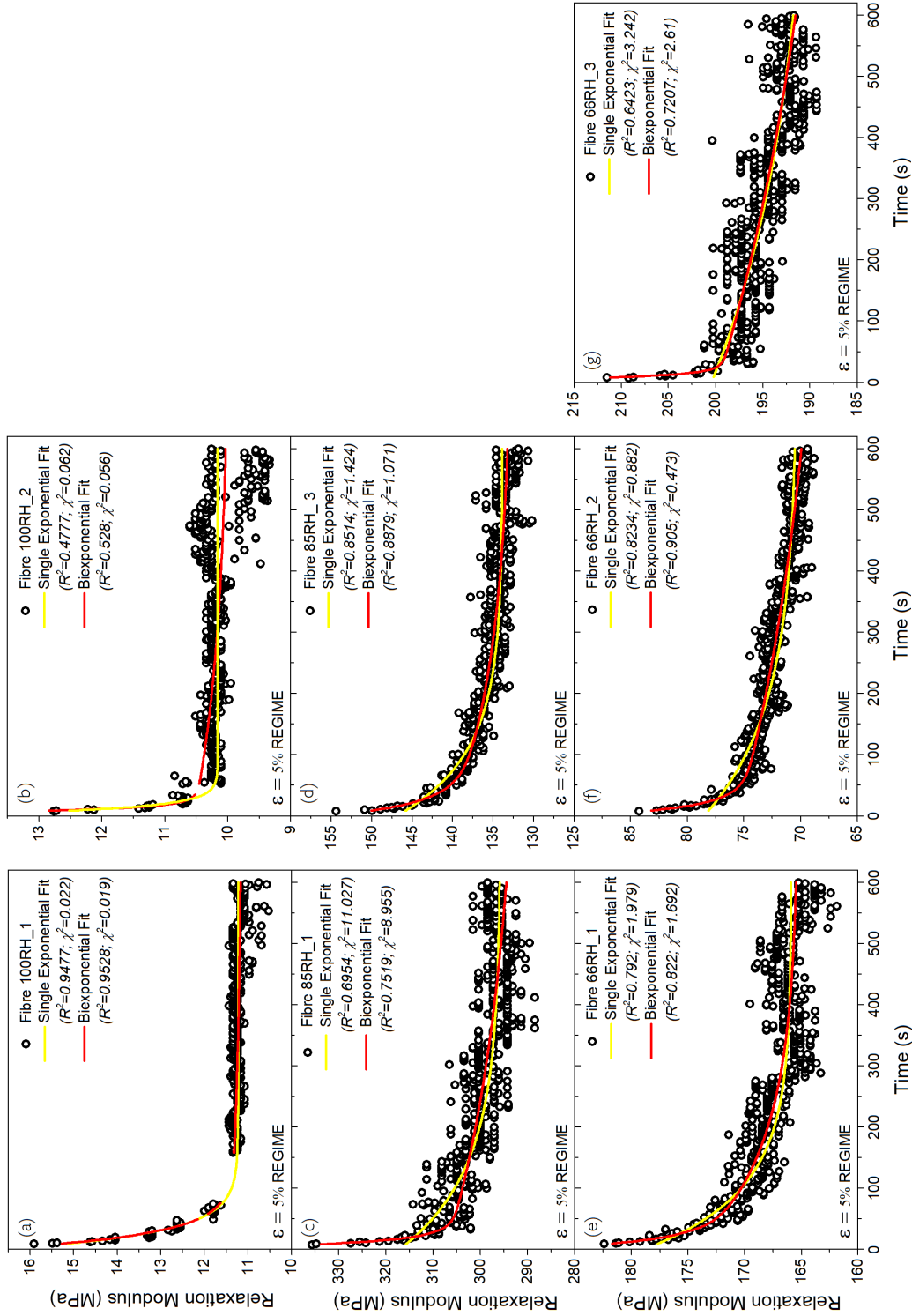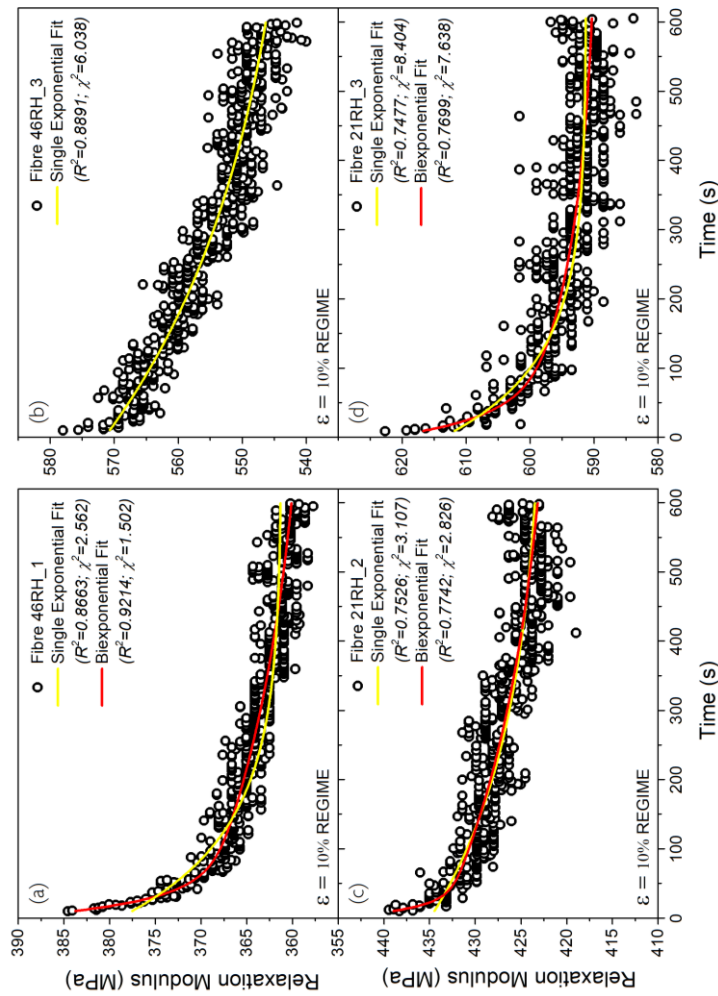
Figure 3.5: plots displaying the resultant fit of single (yellow; ave. $R^2=0.7471 \pm 0.2$) and double exponentials (red; ave. $R^2 = 0.7955 \pm 0.1$) to the stress-relaxation profiles of preconditioned type-I collagen fibres from rat tail tendon, ramped to 5% strain at 20 mm/min and held for 600s. Stress decays at three hydrations are displayed: (a-b) 100% RH, (c-d) 85% RH and (e-g) 66% RH (unique labels identify the same respective fibre in all figures).

Figure 3.6: plots displaying the resultant fit of single (yellow; ave. $R^2=0.8222 \pm 0.04$) and double exponentials (red; ave. $R^2=0.8565 \pm 0.1$) to the stress-relaxation profiles of preconditioned type-I collagen fibres from rat tail tendon, ramped to 5% strain at 20 mm/min and held for 600s. Stress decays from fibres at two hydrations are displayed: (a-b) 48% RH and (c-d) 21% RH (unique labels identify the same respective fibre in all figures).

Figure 3.7: plots displaying the resultant fit of single (yellow; ave. R^2=0.9168 ± 0.03) and double exponentials (red; ave. R^2=0.9434 ± 0.03) to the stress-relaxation profiles of preconditioned type-I collagen fibres from rat tail tendon, ramped to 10% strain at 20 mm/min and held for 600s. Stress decays from fibres at three hydrations are displayed: (a-b) 100% RH, (c-d) 85% RH and (e-g) 66% RH (unique labels identify the same respective fibre in all figures).

Figure 3.8: plots displaying the resultant fit of single (yellow; ave. R²=0.8139 ± 0.1) and double exponentials (red; ave. R²=0.8218 ± 0.1) to the stress-relaxation profiles of preconditioned type-I collagen fibres from rat tail tendon, ramped to 10% strain at 20 mm/min and held for 600s. Stress decays from fibres at two hydrations are displayed: (a-b) 46% RH and (c-d) 21% RH (unique labels identify the same respective fibre in all figures).

component similarly showed no discernible relation with the hydration, giving overall averages of 20 ± 17 MPa and 17 ± 9 MPa in the low- and high-strain regimes, respectively. The slow relaxation time component (τ_2) was longer than 600 seconds, though both this and the characteristic modulus of the second Maxwell element (E_2) were difficult to determine, as with the exception of the 100% RH fibres, none reached full relaxation equilibration within the 600s holding time. The time-independent modulus (E_0) displayed a dependence on the level of hydration, with a marked increase between 100 and 85% RH and subsequent maintenance of these values upon further dehydration, similar to the Young's modulus of the same fibres.

Figure 3.9 shows the collagen stress-relaxation profiles at each hydration as a percentage of peak stress (i.e. the stress at the beginning of the relaxation). The average percentage relaxation of the fibres in the low- and high-strain regimes is given as a function of hydration (100 to 21% RH) in figure 3.10. The fibres relaxed slightly more in the low-strain regime than in the high, but in both cases, the amount of relaxation decreased with dehydration.

Table 3.1: Results[a] of single [square brackets] and double exponential fits of the Maxwell-Weichert model, applied to stress-relaxation plots of type-I collagen fibres from rat tail tendon in the hydration range 21-100% RH, ramped to 5% tensile strain at 20 mm/min and held for 600s.

Relative Humidity (% RH)	E_0 (MPa)	E_1 (MPa)	E_2 (MPa)	τ_1 (s)	τ_2 (s)
100 (N=2)	11 (±1) [11 (±1)]	7 (±2) [5 (±0.4)]	0.5 (±0.2)	15 (±13) [19 (±12)]	290 (±0)
85 (N=2)	211 (±111) [215 (±115)]	38 (±33) [17 (±6)]	13 (±7)	15 (±8) [113 (±20)]	348 (±138)
66 (N=3)	139 (±63) [142 (±63)]	21 (±13) [11 (±2)]	11 (±3)	12 (±5) [232 (±180)]	520 (±318)
46 (N=2)	[291 (±98)]	[28 (±7)]		[66 (±27)]	
21 (N=2)	[322 (±55)]	[36 (±13)]		[635 (±287)]	

[a] Values are given as a mean of at least two repeats (± 1 stdev.). E_0 is the time-independent elastic modulus; E_1, τ_1, and E_2, τ_2, are the characteristic moduli and relaxation time of the fast and slow response, respectively.

Table 3.2: Results[a] of single [square brackets] and double exponential fits of the Maxwell-Weichert model, applied to stress-relaxation plots of type-I collagen fibres from rat tail tendon in the hydration range 21-100% RH, ramped to 10% tensile strain at 20 mm/min and held for 600s.

Relative Humidity (% RH)	E_0 (MPa)	E_1 (MPa)	E_2 (MPa)	τ_1 (s)	τ_2 (s)
100 (N=2)	121 (±25) [122 (±25)]	14 (±1) [12 (±1)]	5 (±3)	26 (±5) [74 (±32)]	291 (±59)
85 (N=2)	348 (±122) [352 (±124)]	21 (±14) [23 (±13)]	23 (±16)	20 (±13) [239 (±120)]	446 (±25)
66 (N=3)	173 (±102) [189 (±90)]	11 (±2) [17 (±5)]	30 (±23)	21 (±14) [218 (±168)]	1342 (±1788)
46 (N=2)	357 [450 (±126)]	21 [25 (±11)]	14	23 [265 (±203)]	407
21 (N=2)	505 (±119) [507 (±120)]	16 (±5) [18 (±7)]	14 (±0.3)	20 (±12) [186 (±112)]	317 (±103)

[a] Values are given as a mean of at least two repeats (± 1 stdev.). E_0 is the time-independent elastic modulus; E_1, τ_1, and E_2, τ_2, are the characteristic moduli and relaxation time of the fast and slow response, respectively.
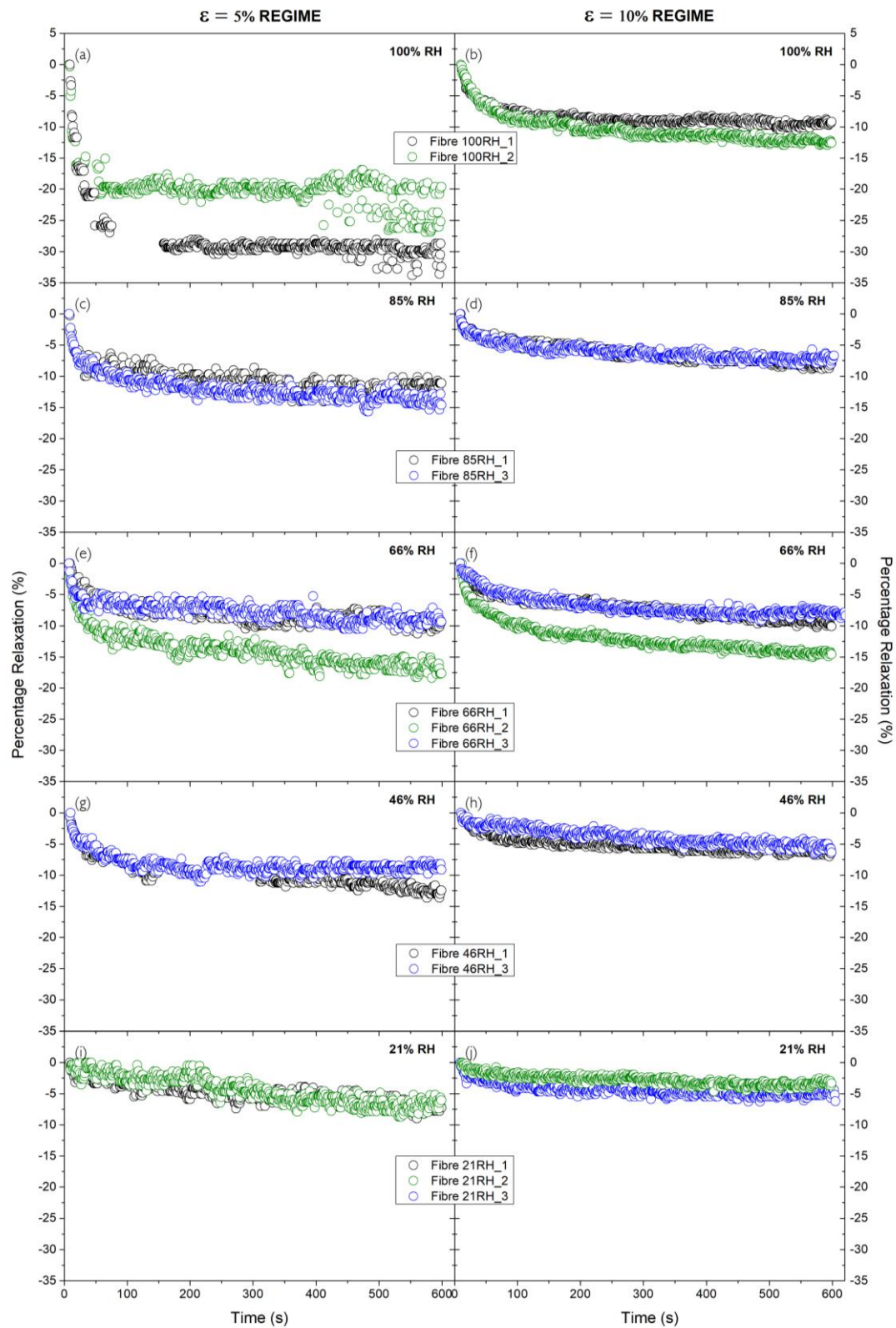
Figure 3.9: plots showing the percentage relaxation at different hydrations of preconditioned type-I collagen fibres from rat tail tendon, ramped to 5% (left) and 10% (right) tensile strain at 20 mm/min and held for 600s: (a-b) 100% RH; (c-d) 85% RH; (e-f) 66% RH; (g-h) 46% RH; and (i-j) 21% RH. Each decay is normalised to the peak stress and zeroed at this point. Three different fibres were tested at each hydration (unique labels and colours identify the same respective fibre in all figures).
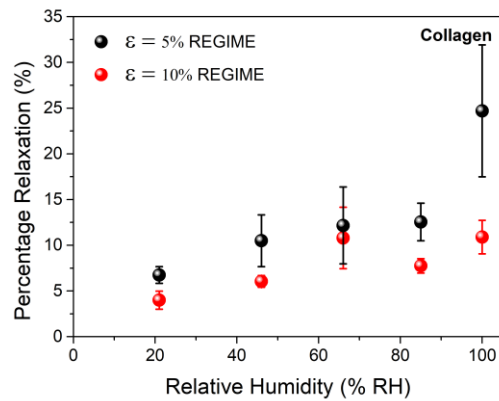
Figure 3.10: plot showing the percentage relaxation of type-I collagen fibres from rat tail tendon as a function of hydration in the range 100 to 21% RH, for the 5 and 10% tensile strain regimes. Error bars are ± 1 stdev (n=3).

3.2.2.2.   Elastin

Figure 3.11-3.12 present the stress relaxation profiles of preconditioned elastin fibres at 100, 85 and 66% RH, ramped to 5 and 10% strain, respectively, at 20 mm/min and held for 600s. Plots are given as the relaxation modulus as a function of time and display the fitting results of single-, double- and in the case of the 85% RH fibres, triple-exponential components of the Maxwell-Weichert model for each fibre at a respective hydration. Fitting statistics (R^2 and χ^2) are displayed. Corresponding results of the exponential fitting (average values) are presented in table 3.3. Elastin fibres below 85% RH in the low-strain regime, and 66% RH in the high, displayed no relaxation and maintained a constant stress for the full 600 second hold. For the decays at 100 and 66% RH a single-exponential was sufficient to fit the data (biexponential fits were essentially equivalent). The percentage relaxation in figure 3.13 shows that in the high-strain regime, these fibres behaved very similarly, with small relaxations of between 5 and 10%, and decay times with an overall average of 211 ± 80 seconds. The relaxation profiles of the 85% RH fibres were best fitted by a triple-exponential, that well described the large and rapid drop in stress at the beginning of the decay. These fibres had a percentage relaxation of around 80%, over half of which occurred in the first 14 seconds. The first and second Maxwell elements characterised this fast response of the fibre, with mean relaxation times of around 4 and 30 seconds, respectively. As with collagen above, the hydration dependence of the time-independent modulus was similar to that obtained for the Young's modulus of the same elastin fibres, with an increase of one order of magnitude between the 100 and 85% RH states, and a two order of magnitude increase between 85 and 66% RH (compared to only one in the case of the Young's).
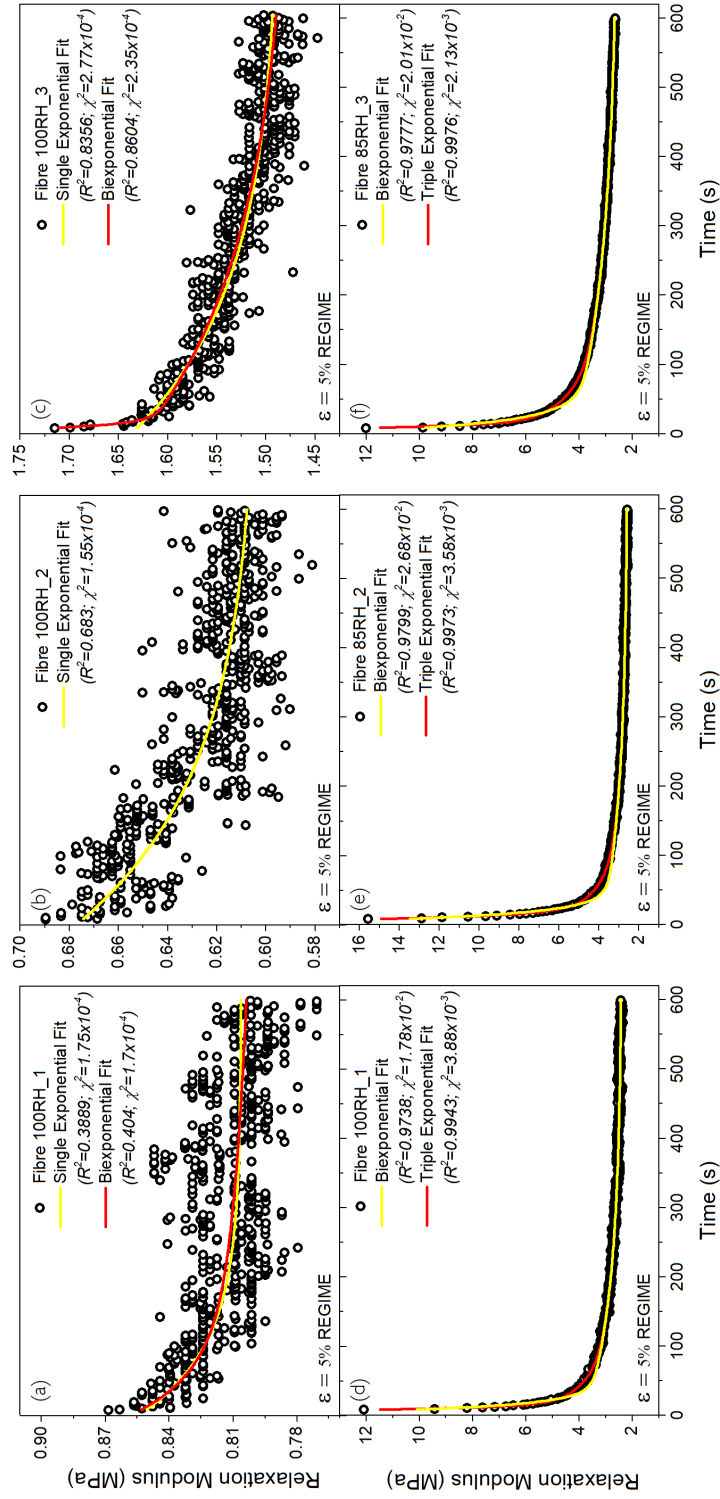
Figure 3.11: plots displaying the stress-relaxation profiles of preconditioned elastin fibres from bovine nuchal ligament ramped to 5% strain at 20 mm/min and held for 600s. Stress decays from fibres at 100% RH (a-c) show the results of single (yellow; ave. R^2=0.6358 ± 0.2) and double (red; ave. R^2=0.6322 ± 0.3) exponential fits, whilst the 85% RH fibres (d-f) are fitted by double (yellow; ave. R^2=0.9771 ± 0.003) and triple (red; ave. R^2=0.9964 ± 0.002) exponentials (unique labels identify the same respective fibre in all figures).
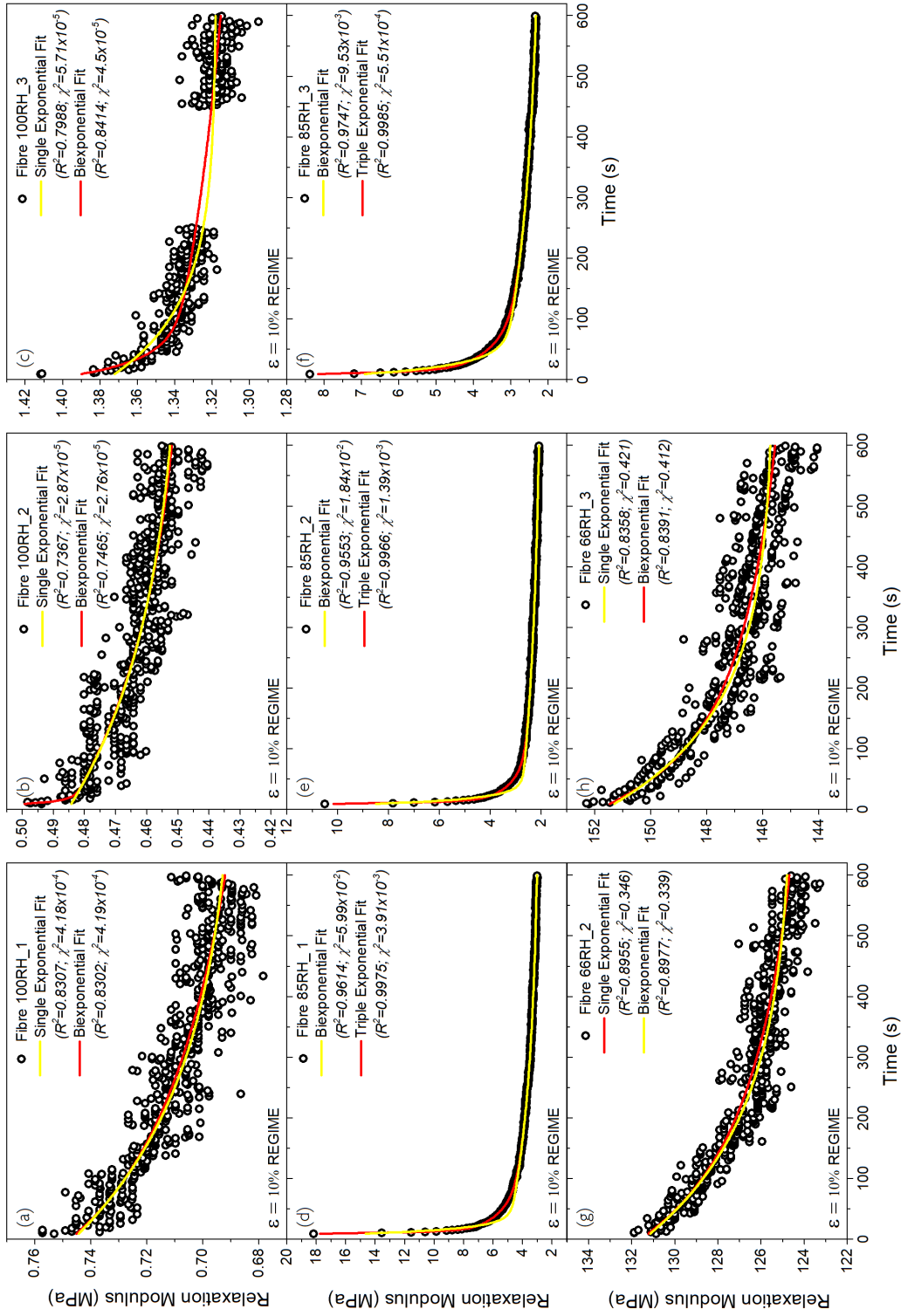
Figure 3.12: plots displaying the stress-relaxation profiles of preconditioned elastin fibres from bovine nuchal ligament ramped to 10% strain at 20 mm/min and held for 600s. Stress decays from fibres at 100% RH (a-c) and 66% RH (g-h) show the results of single (yellow; ave. R^2=0.8195 ± 0.1) and double (red; ave. R^2=0.8310 ± 0.1) exponential fits, whilst the 85% RH fibres (d-f) are fitted by double (yellow; ave. R^2=0.9638 ± 0.01) and triple (red; ave. R^2=0.9975 ± 0.001) exponentials (unique labels identify the same respective fibre in all figures).

Table 3.3: Results[a] of single [square brackets] and double exponential fits of the Maxwell-Weichert model, applied to stress-relaxation plots of 66 and 100% RH elastin fibres from bovine nuchal ligament, and of double [square brackets] and triple exponential fits applied to plots of the 85% RH elastin fibres, ramped to 5 and 10% tensile strain at 20 mm/min and held for 600s.

Relative Humidity (% RH)	E_0 (MPa)	E_1 (MPa)	E_2 (MPa)	E_3 (MPa)	τ_1 (s)	τ_2 (s)	τ_3 (s)
100 (ε = 5%) (N=3)	1.14 (±0.48) [0.96 (±0.46)]	0.19 (±0.22) [0.09 (±0.05)]	0.09 (±0.09)		31 (±36) [175 (±67)]	341 (±83)	
100 (ε = 10%) (N=3)	0.81 (±0.44) [0.82 (±0.45)]	0.06 (±0.04) [0.05 (±0.01)]	0.05 (±0.01)		44 (±50) [232 (±102)]	489 (±162)	
85 (ε = 5%) (N=3)	2.5 (±0.1) [2.5 (±0.1)]	46 (±13) [15 (±6)]	3.3 (±0.4) [1.5 (±0.2)]	1.5 (±0.2)	4 (±1) [11 (±3)]	28 (±4) [197 (±45)]	197 (±45)
85 (ε = 10%) (N=3)	2.3 (±0.5) [2.3 (±0.5)]	228 (±221) [17 (±11)]	3.4 (±1.4) [1.4 (±0.7)]	1.4 (±0.7)	2.8 (±0.7) [11 (±4)]	27 (±4) [304 (±50)]	304 (±50)
66 (ε = 10%) (N=2)	134 (±15) [135 (±15)]	2.83 (±0.33) [7 (±1)]	4.86 (±0.96)		92 (±15) [178 (±29)]	400 (±0)	

[a] Values are given as a mean of at least three repeats (± 1 stdev.). E_0 is the time-independent elastic modulus; E_1, τ_1, E_2, τ_2 and E_3, τ_3 are the characteristic moduli and relaxation times of the fast and two slower responses, respectively.

Interestingly, the modulus of the first Maxwell element of the 85% RH fibres is significantly larger than the corresponding time-independent modulus. In all cases, the relaxation of the elastin fibres was independent of the extension, with similar results for the fitting parameters and percentage relaxations obtained in both the high- and low-strain regimes. As in the case of collagen above, none of the fibres reached full relaxation equilibration within the 600 second holding time, so the actual relaxation times of the long components are likely in excess of this.
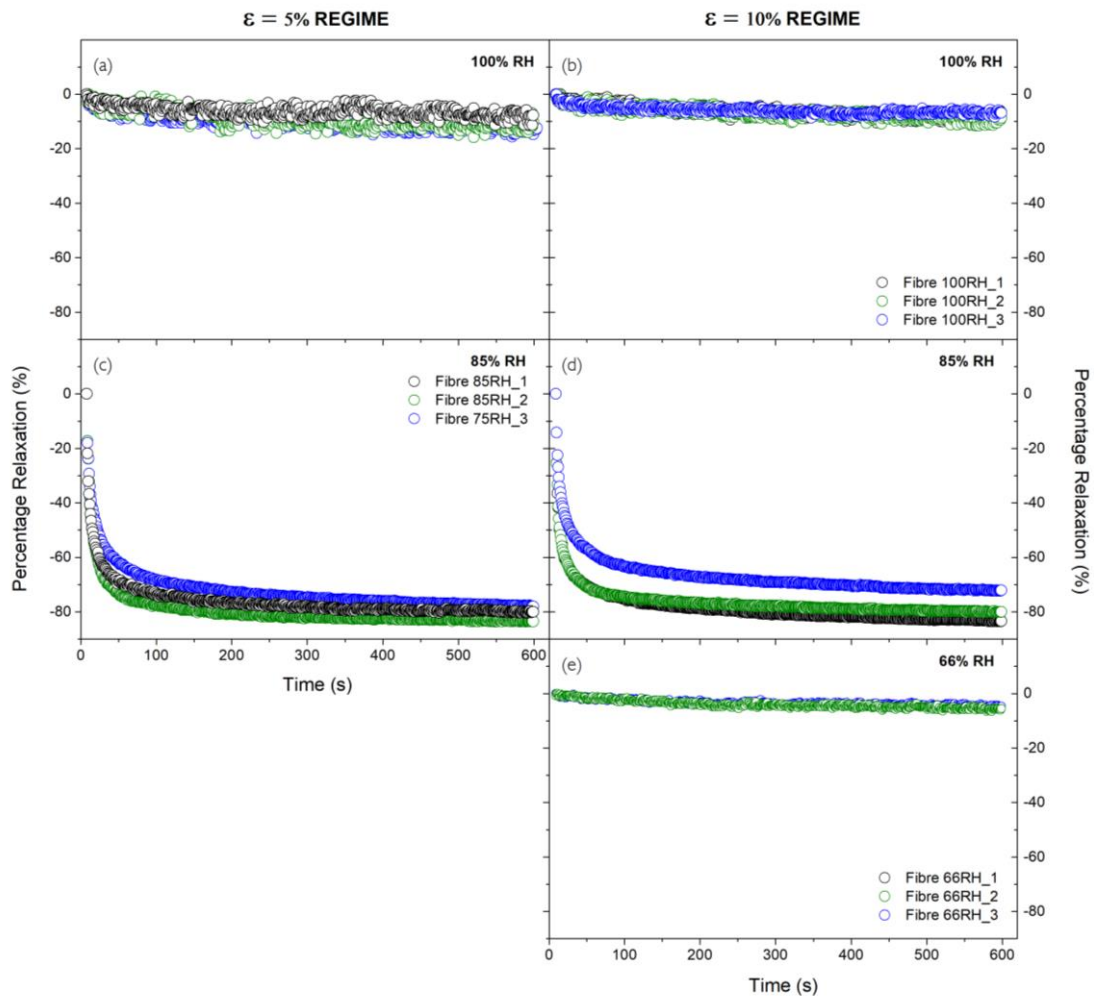
Figure 3.13: plots showing the percentage relaxation at different hydrations of preconditioned elastin fibres from bovine nuchal ligament, ramped to 5% (left) and 10% (right) tensile strain at 20 mm/min and held for 600s: (a-b) 100% RH; (c-d) 85% RH and (e) 66% RH (no relaxation was observed for these fibres in the 5% strain regime). Each decay is normalised to the peak stress and zeroed at this point. Three different fibres were tested at each hydration (unique labels and colours identify the same respective fibre in all figures).

3.3.   Discussion

Fully hydrated fibres reproduce behaviour described in the literature, with collagen showing a J-shaped stress-strain response [42] and a Young's modulus in the linear region of the curve at 286 ($\pm$ 99) MPa, towards the lower end of the literature range [40, 41, 63, 68, 148-150]. This variation can be attributed to the length of the sample, which is known to have a direct correlation with the elastic modulus [151], but is also plausibly attributed to the calculation of the cross-sectional area, which in this case is expressed in terms of the dry mass of each fibre. Other measures are used in some papers, but I feel this choice best reflects the intrinsic properties of the material. A more accurate approach would involve the use of a camera to

record the precise dimensions of the fibre between the anchors as strain is applied, or indeed a microscopic multiphoton approach, allowing for the visual isolation and tracking of smaller-scale fibre components. This would also enable in-situ observation of the change in cross-sectional area which is likely to decrease as the fibres stretch leading to a larger stress and a higher estimate for the Young's modulus. Elastin performs, as expected, as an almost pure elastomer with a completely linear response to applied strain, yielding a modulus in the mid-range of the literature [147, 152, 153] at 0.64 ($\pm$ 0.2) MPa. Young's moduli change differently with dehydration in the two protein fibres, with a gradual increase by up to two orders of magnitude to 172 ($\pm$ 28) MPa in elastin, as opposed to collagen which shows a sharp increase at the first stage of dehydration (85% RH) to 790 ($\pm$ 152) MPa, but displays no significant change beyond this. Similarly to the fully hydrated case, this value is low compared to available literature values [154, 155]. As expected, elastin has a consistently lower Young's modulus than collagen, but the difference is greatest between the fully hydrated fibres, where elastin is approximately three orders of magnitude softer than collagen. This decreases markedly with dehydration until elastin is only five times less stiff than collagen in the 'dry' state at 21% RH. This emphasises the major part played by water in imparting the remarkable elastic properties to elastin and further, demonstrates some critical level – to my knowledge, the first time this has been identified – at which these properties begin to change, between 100 and 85% RH in collagen and below 85% RH in elastin.

When doubling the preconditioned extension of the elastin fibres at 100 and 85% RH, a higher strain was required to achieve the stress originally recorded at 5% strain in the initial preconditioned state. At lower hydrations, no such change was observed, and the stress-strain profiles of either extension regime were essentially identical. This demonstrated the ability of the fibres to elongate and reconfigure under strain in the presence of a critical amount of water and was particularly marked in the case of elastin at 85% RH, which required more additional strain than the 100% RH incidence. A similar outcome was observed for collagen, although here the additional strain decreased at 85% RH. A permanent extension was conferred on the collagen fibres below 100% RH and elastin below 85% RH during preconditioning, and subsequent return to the original zero-strain position imposed a compressive force on the extended tissue, promoting the development of a macroscopic bend in the fibre. The curve of the stress-strain plots evidence the opening of this bend as the fibre gradually straightens on application of strain. Hence elastin suffered an apparent loss of linearity in its stress-strain response and the toe region of the collagen fibre disappeared. In this latter case, it may be that

the microscopic crimp was irreversibly straightened – and the addition of a microscope mounted camera to the experimental apparatus, would allow this to be unequivocally determined. In summary, dehydration simultaneously increases the stiffness of both fibres and destroys their ability to recover fully from applied strain, changing their physical nature from viscoelastic to plastic materials.

This is seen even more clearly in the stress relaxation experiments, where percentage-relaxation was gradually reduced with dehydration in collagen and removed in entirety at low hydration in the elastin fibres. The time-independent relaxation modulus (E_0) displayed a similar inverse relationship with water content, to that of the Young's modulus of the same fibres. However, given the time to relax, the E_0 values of the collagen fibres at all hydrations and those of elastin at 100 and 85% RH, were slightly lower than those obtained from fits of the stress-strain plots (strain rate of 0.25 mm/min), further demonstrating the viscoelastic nature of the fibres.

Collagen shows a double decay as reported widely in the literature [5, 59] with a fast relaxation component at around 20 seconds (except in the low-strain regime of the 46 and 21% RH fibres, where the extension was not sufficient to activate the fast element) and a longer component in excess of 600 seconds. Unlike the time-independent modulus, these times were the same – within the error – at all hydrations, suggesting that water does not govern the relaxation time, only the magnitude of the response. These two relaxation regimes have previously been attributed to collagen fibrils (fast element) and the inter-fibrillar ground substance (slow element), a gel consisting predominantly of proteoglycans (PG) and surrounding water [5]. The ground substance has been associated with fibrillar sliding, determined to be the primary mechanism of collagen fibre extension [57, 58], and is considered to play a key role in mediating the viscoelastic response of the fibres under tensile strain in a growing number of works [66, 67]. Considering this in light of my results, where only the magnitude of relaxation is altered with changes in hydration, it is suggested that water actually mediates the mobility of the ground substance, acting as a lubricant to maximise both the motion and thus the extensibility of the collagen fibre at large. Further to this, the absence of the fast component in the low-strain regime at low hydration, implies that mobility of the ground substance is *so* hampered, that the fibrils and the interfibrillar material are essentially an unbroken continuum in these conditions. The glycosaminoglycan (GAG) component of PGs, are highly hydrophilic molecules and are thought to be involved in controlling fibre hydration, maximising the presence of water [156-158]; although the opposite effect has also

been observed, with their removal increasing the water content of the fibres and consequently the percentage relaxation [66, 159], in agreement with my results. Chemical control of the hydration alone (PG content unaffected) in the medial collateral ligament of New Zealand White rabbits [160] and the human patellar tendon [161], produced similar changes to the percentage relaxation measured in *this* thesis. Given the similarity between my purely water related results and those considering the PG matrix specifically, it would seem likely that the two are correlated, perhaps even interdependent, and future investigations should be designed to consider both components simultaneously.

The elastin stress decay is markedly different from collagen, with just a single, long exponential in excess of the 600 second holding time used in the experiment at 100 and 66% RH. However, the stress decay at 85% RH deserves particular attention. Here the fibres have a large relaxation – up to 80% of the peak stress within the experimental holding time – over 50% of which is achieved rapidly within the first 15 seconds, and is best described by a triple decay with two fast components, approx. 4 and 30 seconds, and a long decay in excess of 600 seconds. Despite this large percentage change, all fibres recover their initial length at rest and maintain a relaxation modulus in line with their Young's modulus, suggesting that this is not a result of mechanical creep but rather the product of the poroelastic nature of the elastin fibre; perhaps a damage limiting mechanism that allows them to transmit higher stresses when exposed to sudden deformations, and retain the ability to recover elastically at speed with comparatively low hysteresis. This reinforces the concept of a critical hydration for the elastin fibre (~85% RH) introduced above. These properties seem ideal for the role of elastin in the body, suggesting that a natural hydration is closer to 85% RH than 100%RH, which is plausible given the presence of salts in its native environment. Physiological salts do not act directly on the protein, i.e. they do not bind to the elastin molecules themselves; however, they are of a sufficiently low molecular weight (less than 1kDa [98]) to penetrate the ~3 nm wide intrafibrillar pores, where they may reduce the activity of the hydration water, effectively dehydrating the protein and leading to an increase in internal hydrogen bonding within the elastin [101, 162]. This may therefore be a more accurate description of the physical working conditions of elastin fibres in the body and further work should focus around this hydration range to determine the exact critical point.

To my knowledge, this is the first report of relaxation times for bovine nuchal elastin fibres, though recent work reported similar multi-component exponential decay times in purified porcine aorta, where the effects of glycation were studied [163]. There was an attempt here to allocate the various relaxation components to the ultrastructure of the fibres, with particular mention of hydrogen bond rearrangement being responsible for the fast component, and hydrophobic hydration driven reactions responsible for the slow. However, these molecular level effects may be overwhelmed by macroscopic factors such as the hierarchical organisation of the fibres. These factors may be investigated by a MEMS, AFM or indeed a Brillouin light scattering approach. Weinberg *et al* discussed fluid flow rates within a relaxing elastin fibre in the presence of different osmotic fluids after the removal of applied strain, and determined that water returned to the fibre in two distinct phases: intrafibrillar pore spaces recovered water at a very fast rate, whilst the interfibrillar spaces expanded only slowly, if at all [98]. The porous nature of the fibres thus offers a phenomenological explanation for the macroscopic stress relaxation observed in the current work. Using Weinberg's attribution, the *inter*fibrillar pore relaxation represents the slow Maxwell component beyond 600 seconds, and the *intra*fibrillar pore relaxation is associated with one of the two fast components. It should be acknowledged that the elastin blocks were not tested for purity after digestion, so mechanical contributions from non-elastin remnants (possibly microfibrils [164, 165]) cannot be completely discounted; however, the other fast component is likely a combination of molecular reorganisations within the elastin structure itself, being by far the highest density of material present other than water. Molecular motions occur at high frequency, so these likely account for the most rapid component of the relaxation (<4 seconds), thus the intrafibrillar component is assigned to the second Maxwellian element (~30 seconds).

The reduction in bulk water at 85% RH may promote a change in the hydration forces between the intra and interfibrillar pore spaces, explaining the transition from a single decay at 100% RH to the triple decay at 85% RH, although further work in determining the rate of flow of water back into the relaxing pore spaces should help confirm this. It would be equally useful to determine how much bulk water resides in the pore spaces at hydrations below this critical point, though it seems that below 66% RH, hydration forces are no longer active as the fibres no longer relax macroscopically, suggesting also that the elastin ultrastructure is now in a plastic state. The allocation of relaxation times together with the suggestion of critical water contents may help to inform future poroelastic models of the elastin fibres.

Fluid flow within porous fibres such as elastin and collagen is a growing topic of interest in the biomechanics field, and the mediating role of proteoglycans and other ECM components are now being explored [166, 167], with study no longer confined to the tissues which routinely experience compressive forces, bone and cartilage being a common examples. Certainly, water is critical to the normal function of the fibrous proteins. This chapter has identified critical hydrations for both collagen and elastin and has attempted to build a macroscopic view of some of the structural changes that occur during the dehydration of the fibres. But this picture is limited by the macroscopic techniques employed, with sensitivity down only to the fibrillar scale. Below this, and in the next chapters I will deal with the micromechanics and chemical composition of the molecular scale.

4

Protein Fibre Micromechanics

4.1.   Introduction

The previous chapter explored the mechanical changes induced by dehydration in collagen and elastin fibres on a macro-scale. In this chapter, I move down the structural hierarchy, to probe the viscoelasticity of each fibrous protein at the molecular scale using Brillouin light scattering (BLS) spectroscopy. In addition to type-I collagen from rat tail tendon and elastin from bovine nuchal ligament, cartilage from equine metacarpophalangeal joint (mainly type-II collagen) is also analysed to compare between different collagen types. The role of the ground substance in the micromechanics of rat tail tendon is also considered through the analysis of purified, trypsin-digested type-I collagen. The role of water in these fibres and tissues is explored at the hydration extremes (100 and 21% RH) and the longitudinal modulus obtained through BLS in the GHz range is compared to the Young's modulus measured in chapter 3 to assess the dual-frequency response of these samples. General features of the BLS spectra are outlined, together with potential applications of this emerging technique within the biomedical field.

4.2. BLS Spectra of Dried Protein Fibres

4.2.1. Type-I Collagen Fibres

As already mentioned (§2.4), in the platelet-like configuration, two peaks are present either side of the central Rayleigh line due to phonon modes propagating parallel to the surface of the fibre (PS – the lower frequency peak) and bulk modes propagating quasi-radially to the fibre axis (B – the higher frequency peak). Figure 4.2a shows the evolution of the BLS spectrum of a dry native collagen fibre as a function of the angle of rotation, θ (figure 2.18b), where the PS mode probes all orientations of the acoustic
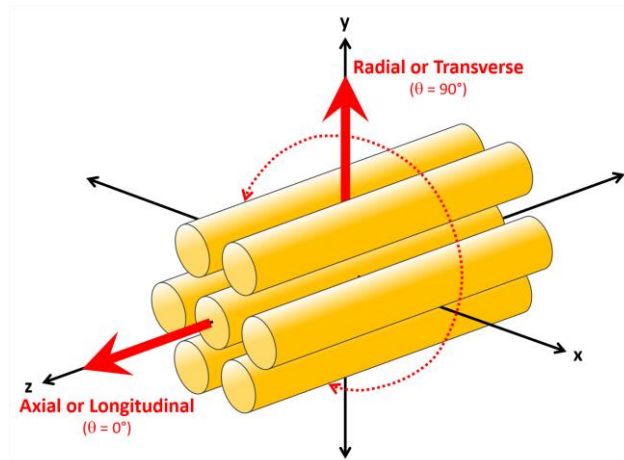

Figure 4.1: Diagram showing the axial (longitudinal) and radial (transverse) directions probed by BLS with respect to the fibrils – aligned along the z-axis. Note that the radial direction points anywhere within the xy-plane as indicated by the dashed circle.

wave relative to the fibre axis, from parallel ($\theta = 0°$; phonon wavevector q_s parallel to z – axial) to perpendicular ($\theta = 90°$; q_s orthogonal to z – radial) as shown in figure 4.1. The PS
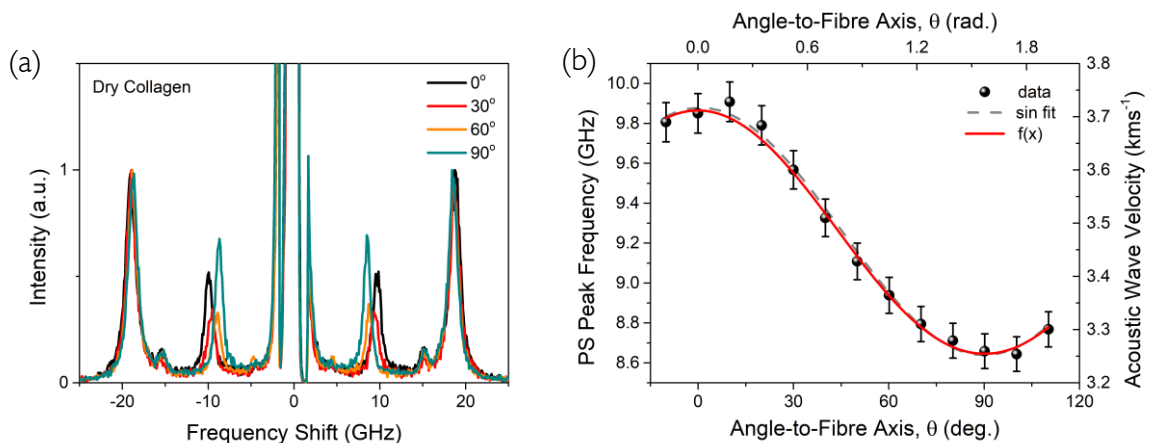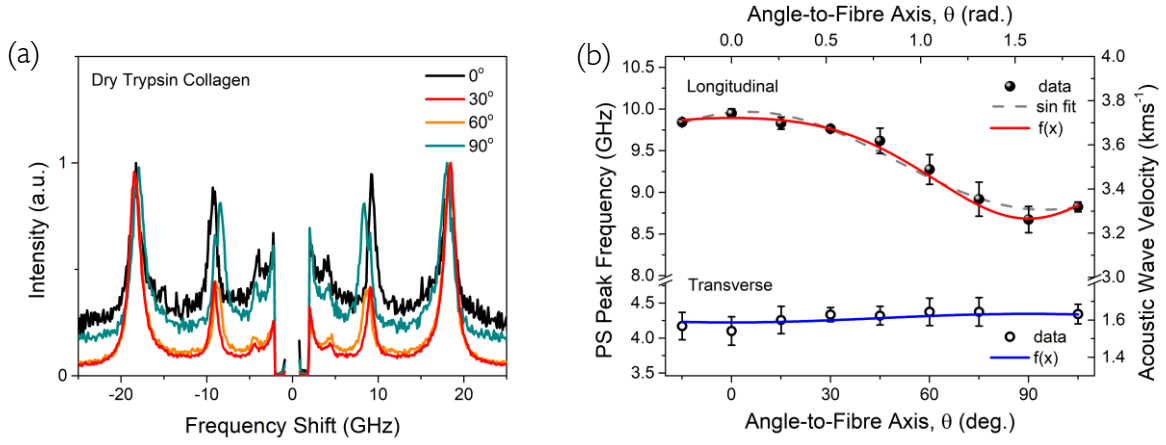

Figure 4.2: (a) BLS spectra in VU polarisation of air-dried type-I collagen from RTT at various angles, θ, to the fibre axis (in degrees), normalised to the height of the bulk peaks. (b) Plot of the PS peak frequency and resultant longitudinal acoustic wave velocity as a function of the angle-to-fibre axis θ, in degrees and radians respectively. f(x) indicates the resulting fit of equation (27) for wave propagation in a hexagonally symmetric elastic medium (reduced $\chi^2 = 1.9 \times 10^{-4}$). A sin function (fixed at 90° period) is also fitted to the data to demonstrate the periodicity ($R^2 = 0.994$). Error bars indicate the standard errors obtained from the Levenburg-Marquardt nonlinear least squares fit of the Brillouin spectra.

peak of dry collagen shows a clear redshift in frequency as the phonon wavevector probes from an axial to a radial orientation within the fibre. This is shown in figure 4.2b where mechanical anisotropy of the fibre is indicated by a good sinusoidal fit. The bulk peak meanwhile undergoes a far smaller redshift (approx. 2% compared to 13% for the PS peak) upon changing θ, as is expected for modes that probe a quasi-radial direction throughout the angular scan. In fact, α only changes from 62° to 90° for θ varying from 0 to 90°. This is highlighted in figure 4.3 where the acoustic wave velocity obtained from the PS and bulk peaks are plotted based on equation 24b against the angles θ and α (in degrees), respectively. It can be seen that the angle dependency of the acoustic wave velocity is the same within the error for both the PS and bulk longitudinal phonon modes. The elastic coefficients and corresponding viscoelastic properties of the air-dried native type-I collagen fibre were extracted by fitting the acoustic wave velocity plotted as a function of the angle-to-fibre axis, θ (in radians) to equation 27 in figure 4.2b. Table 4.1 lists the five independent elastic constants together with the loss tangent, $\tan(\delta)$, taken as the ratio of the linewidth to frequency derived from fit analysis of the bulk peaks. The major (ν_{13}) and the second (ν_{12}) Poisson's ratios are also reported, showing some degree of anisotropy. Using the relationship between the bulk and PS peaks (equation 25), the refractive index of the native air-dried collagen was found to be 1.51 ($\pm$ 0.02).
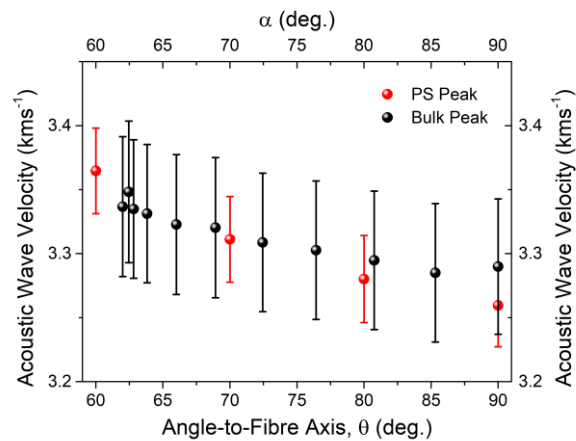
Figure 4.3: PS and bulk peak acoustic wave velocities of air-dried type-I collagen from RTT as a function of the angles θ and α (see Figure 2.18a). Error bars indicate the standard errors obtained from the Levenburg-Marquardt nonlinear least squares fit of the Brillouin spectra.

Figure 4.4a presents the angularly resolved spectra of an air-dried purified type-I collagen fibre. The spectra show a similar periodic change in the PS peak frequency (indicated by the good sinusoidal fit), whilst the VH spectra present a transverse peak (phonon) with a small blueshift from 0° to 90° at around 4.1 GHz. This is seen in figure 4.4b, which also shows the results of

Figure 4.4: (a) BLS spectra at various angles, θ, to the fibre axis (in degrees) of air-dried trypsin digested type-I collagen from RTT in VH polarisation, normalised to the height of the bulk peaks. Note the small transverse peak visible around 4.2 GHz. (b) Plot of the PS (longitudinal) and transverse peak frequencies for the air-dried tissue and resultant longitudinal acoustic wave velocity as a function of the angle-to-fibre axis θ, in degrees and radians respectively. Fitting functions are as in Figure 4.2 (red line: $R^2 = 0.992$; sin function: $R^2 = 0.983$), with the addition of the resulting fit of equation (28) for transverse wave propagation in a hexagonally symmetric elastic medium (blue line – $R^2 = 0.36$). Error bars indicate the standard errors obtained from the Levenburg-Marquardt nonlinear least squares fit of the Brillouin spectra.

the fit of the acoustic wave velocities obtained from longitudinal and transverse modes as a function of the angle θ (in radians) to equations 27 and 28. The resulting components of the elasticity tensor are presented in table 4.1 (square brackets). Coefficients are similar to those obtained in the native collagen fibres; however, a noticeable difference occurs for the coefficient c_{13} that is reflected into reversed values for the fibre's Brillouin moduli $E_{||}$ and $E_{\perp}$ (7.2 and 7.7 GPa). This can be seen in the overlaid spectra in figure 4.5 where the bulk peak frequency of the air-dried trypsin digested fibre is around 0.3 GHz lower than that of the native fibre in the radial direction (18.43 ± 0.05 GHz and 18.65 ± 0.21 GHz, respectively). The Poisson's ratios also show some differences, with a slight increase in ν_{13}, but a sizeable decrease in ν_{12} (see table 4.1). A reduction is also observed in the loss tangent. Refractive index was similar to that of the dry native fibre at 1.49 ± 0.02.

For both native and purified fibres, the anisotropy of elasticity (c_{33}/c_{11}) was equal to 1.30 (± 0.01), a small difference compared with the literature value [80] of 1.53, plausibly related to differences in sample preparation.
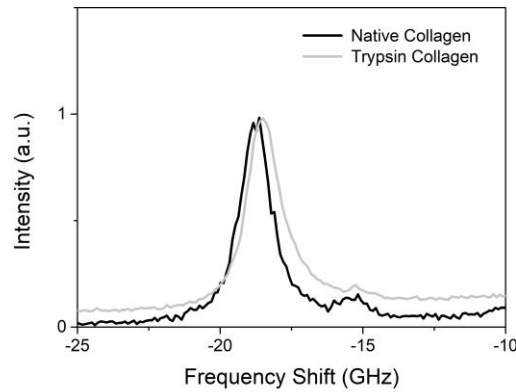
Figure 4.5: Comparison of native and trypsin digested type-I collagen fibres. Angle resolved macro-BLS spectra at $\theta = 90°$ in VU polarisation (black line – native collagen from RTT; grey line – trypsin purified collagen from RTT), normalised to the height of the bulk peaks. A difference in peak position of 0.3 GHz is observed, with the purified RTT fibre at a slightly lower frequency than the native fibre.

4.2.2.   Elastin Fibres and Bovine Nuchal Ligament

Figure 4.6a displays the BLS spectra of air-dried elastin fibres, with PS mode around 8.2 GHz and the bulk mode around 16.8 GHz; no transverse modes were detected for the elastin samples. Both peaks redshift upon rotation from $\theta = 0°$ to 90° (fig. 4.6b), although to a lesser extent than the collagen bands (PS peak shows a maximum change of 5% compared to 13% for collagen). The estimated refractive index, 1.54 ± 0.02, is similar to that previously reported (1.534 [112]) as well as to that of the collagen fibres above. Fit results from figure 4.6b are presented in table 4.1 showing lower values for the elastic tensor coefficients and mechanical moduli of elastin fibres than those of collagen. In addition, the anisotropy of elasticity is c_{33}/c_{11} = 1.11 ± 0.02, smaller than that of collagen fibres, demonstrating a lower degree of preferential orientation of the elastin fibres. The loss tangent is, however, equivalent to that of native collagen. Results show an isotropic Poisson's ratio of 0.4 for elastin.

The bovine nuchal ligament is composed of a roughly aligned assembly of the elastin fibres analysed above (see SEM figure 2.22). The lower alignment is reflected into an absence of θ-dependent peak frequencies (fig. 4.6c) and hence of mechanical anisotropy (fig. 4.6d). A second ligament sample was studied and showed very similar data, with only a 0.2% difference in the peak frequency average. The observed peaks are at 7.9 (PS mode) and 16.8 GHz (bulk mode), and the two elastic constants c_{33} and c_{11} were derived in the cases $\theta = 0°$ and 90°,

respectively, using the density of dry-purified elastin (table 4.1); their values fall between the corresponding ones of the mechanically anisotropic elastin fibres. Tan(δ) is also similar to that of the elastin fibres above. The calculated refractive index is 1.51 ± 0.02, comparable to that of both dry collagen and elastin fibres above.
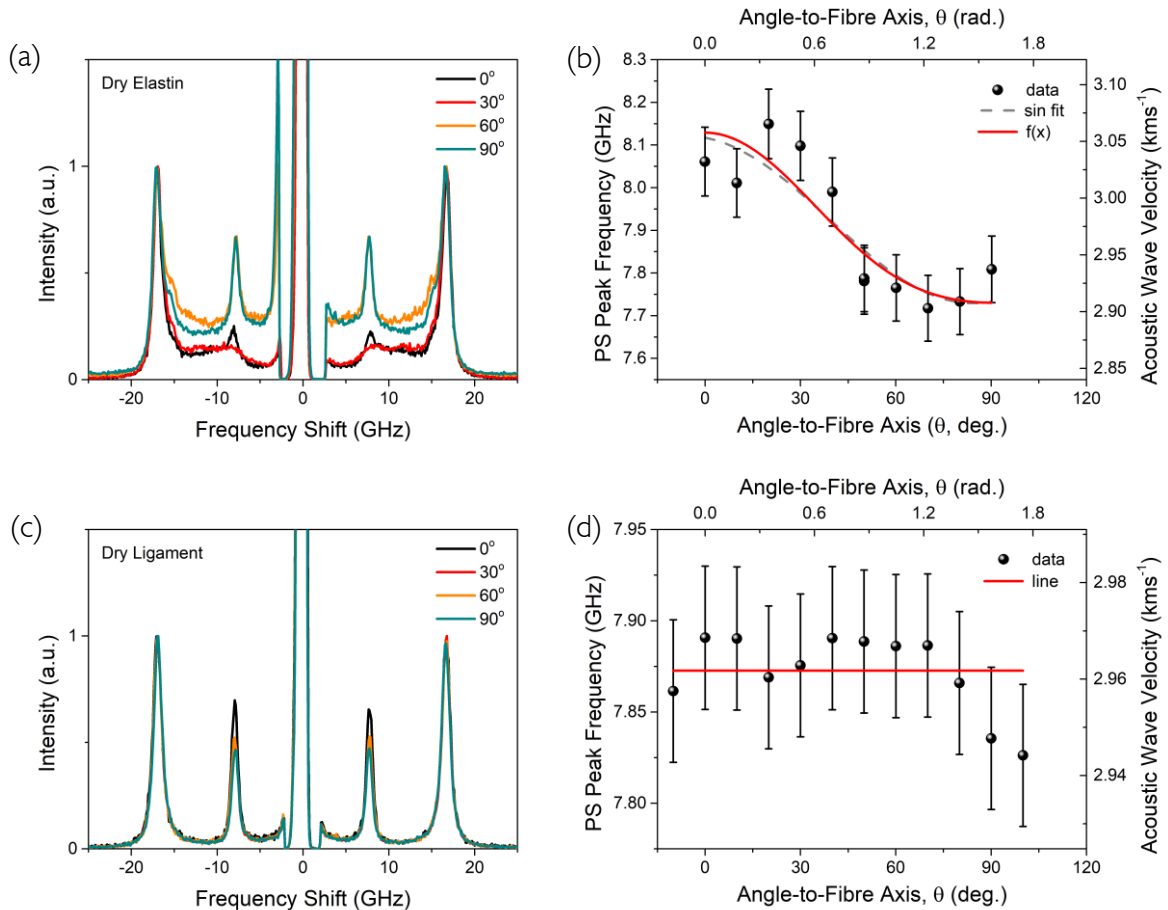

Figure 4.6: Comparison between bovine nuchal ligament and its constituent elastin fibres. BLS spectra in VU polarisation of (a) single air-dried elastin fibre and (c) bovine nuchal ligament at various angles, θ, to the fibre axis (in degrees), normalised to the height of the bulk peaks. Associated plots (b) and (d) of the PS peak frequency and resultant longitudinal acoustic wave velocity as a function of the angle-to-fibre axis θ, in degrees and radians respectively. Fitting functions in (b) are as in Figure 4.2 (f(x) reduced $\chi^2 = 0.85$; sin function $R^2 = 0.74$). Line marks the data set average. Error bars indicate the standard errors obtained from the Levenburg-Marquardt nonlinear least squares fit of the Brillouin spectra.

4.2.3.   Articular Cartilage

Air-dried cartilage displayed a similar absence of elasticity anisotropy to the bovine nuchal ligament with no θ-dependency of the peak frequencies in two sections cut parallel to the articular surface, where similar peak frequencies were observed. Figure 4.7a presents an

example of these BLS spectra, and figure 4.7b highlights the angle independence of the PS mode phonons and the resulting longitudinal acoustic wave velocity, with only a 0.2% difference between the peak positions in both sections of tissue. This correlates well with the observation of a homogeneous structure without preferential fibre alignment in the cartilage zone examined (see SEM figure 2.22d). The calculated refractive index is 1.42 ± 0.02, smaller than that of the other samples studied. As in the ligament measurement above, elastic constants c_{33} and c_{11} were derived from the spectra at $\theta = 0°$ and $90°$, using the density of wet articular cartilage [168], 1100 kg m^{-3}, and are displayed in table 4.1 together with $\tan(\delta)$ which is larger in cartilage than in collagen and elastin above.
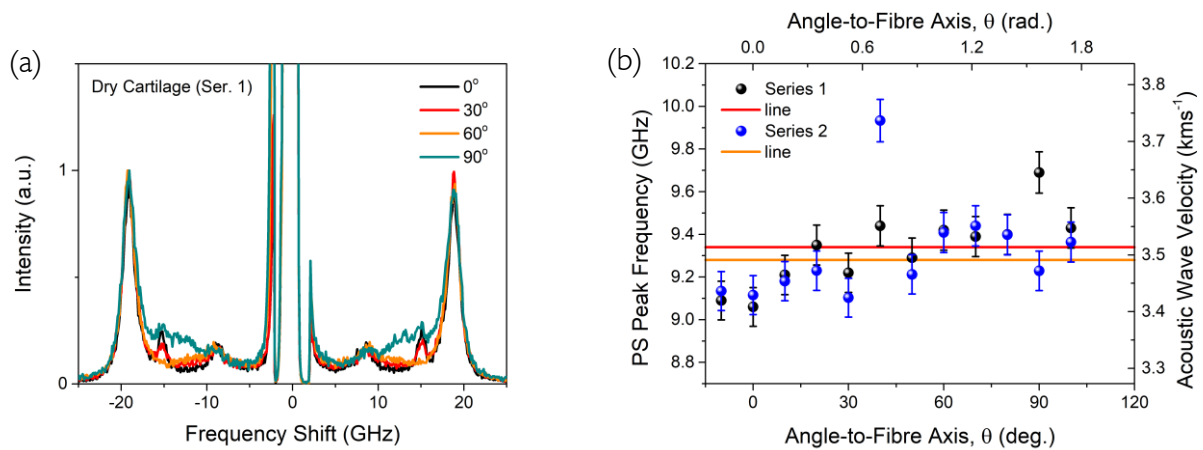
Figure 4.7: (a) Angularly resolved BLS spectra in VU polarisation from one sample of cartilage cut parallel to the articular surface, normalised to the height of the bulk peaks. (b) Plot of the PS peak frequency and resultant longitudinal acoustic wave velocity as a function of the arbitrary PS propagation angle θ, in degrees and radians respectively. Series 1 reflects data from the spectra in (a) whilst a second sample presented similar peak frequencies, well within the error at only a 0.2% difference. Lines mark the data set average for the first (red) and second (orange) tissue samples. Error bars indicate the standard errors obtained from the Levenburg-Marquardt nonlinear least squares fit of the Brillouin spectra.

4.2.4.   Micro-BLS of Dried Fibres

Figure 4.8 shows the micro-BLS spectra of elastin fibres, collagen fibres and cartilage measured using a micro-focused BLS setup (grey line). The spectra of the same specimens acquired through angle-resolved BLS measurements ($\theta = 90°$ radial; from §4.2.1-4.2.3 above) are also presented (black line). The frequencies of the bulk modes measured by the two techniques are similar within the limits of spectral resolution, though notice that the micro-BLS spectra

Table 4.1: Elastic tensor coefficients, elastic moduli, Poisson's ratios and tan(δ) of air-dried fibres and tissues. Collagen values in [square brackets] are for the trypsin digested fibres. $E_{//}$ is the axial Brillouin modulus; $E_{\perp}$, the transverse or radial Brillouin modulus; G, the shear modulus and K, the bulk modulus.

Sample	Elastic Coefficients (GPa)		Elastic Moduli (GPa)		Poisson's Ratios		tan(δ)
	c_{33}	18.6 ($\pm$0.1) [18.7 ($\pm$0.1)]	$E_{//}$	10.2 ($\pm$0.3) [7.2 ($\pm$0.2)]	ν_{13}	0.43 ($\pm$0.01) [0.52 ($\pm$0.01)]	0.063 ($\pm$0.01) [0.042 ($\pm$0.01)]
	c_{11}	14.3 ($\pm$0.1) [14.4 ($\pm$0.2)]	$E_{\perp}$	8.3 ($\pm$0.3) [7.7 ($\pm$0.2)]	ν_{12}	0.32 ($\pm$0.02) [0.06 ($\pm$0.05)]	
Collagen	c_{44}	3.2 ($\pm$0.1) [3.4 ($\pm$0.1)]	G	3.2 ($\pm$0.1) [3.4 ($\pm$0.1)]			
	c_{12}	8.0 ($\pm$0.1) [7.2 ($\pm$0.2)]	K	10.9 ($\pm$0.5) [10.8 ($\pm$0.3)]			
	c_{13}	9.7 ($\pm$0.2) [11.2 ($\pm$0.3)]					
	c_{33}	11.5 ($\pm$0.2)	$E_{//}$	6.1 ($\pm$0.4)	ν_{13}	0.40 ($\pm$0.02)	0.062 ($\pm$0.01)
	c_{11}	10.4 ($\pm$0.1)	$E_{\perp}$	5.3 ($\pm$0.6)	ν_{12}	0.40 ($\pm$0.06)	
Elastin	c_{44}	1.9 ($\pm$0.2)	G	1.9 ($\pm$0.2)			
	c_{12}	6.6 ($\pm$0.2)	K	8 ($\pm$1)			
	c_{13}	6.8 ($\pm$0.3)					
Ligament	c_{33}	10.8 ($\pm$0.1)					0.059 ($\pm$0.01)
	c_{11}	10.8 ($\pm$0.1)					
Cartilage	c_{33}	13.4 ($\pm$0.2)					0.080 ($\pm$0.01)
	c_{11}	13.4 ($\pm$0.2)					

contain no PS peak, because the measurement is performed strictly in backscattering geometry which only permits observation of bulk longitudinal modes (see §2.4). Interestingly, they also lack a small peak observed for both native and purified collagen fibres (15.3 GHz) and cartilage (15.2 GHz), and which appears as a shoulder to the bulk peak in the case of elastin (fig. 4.8a).
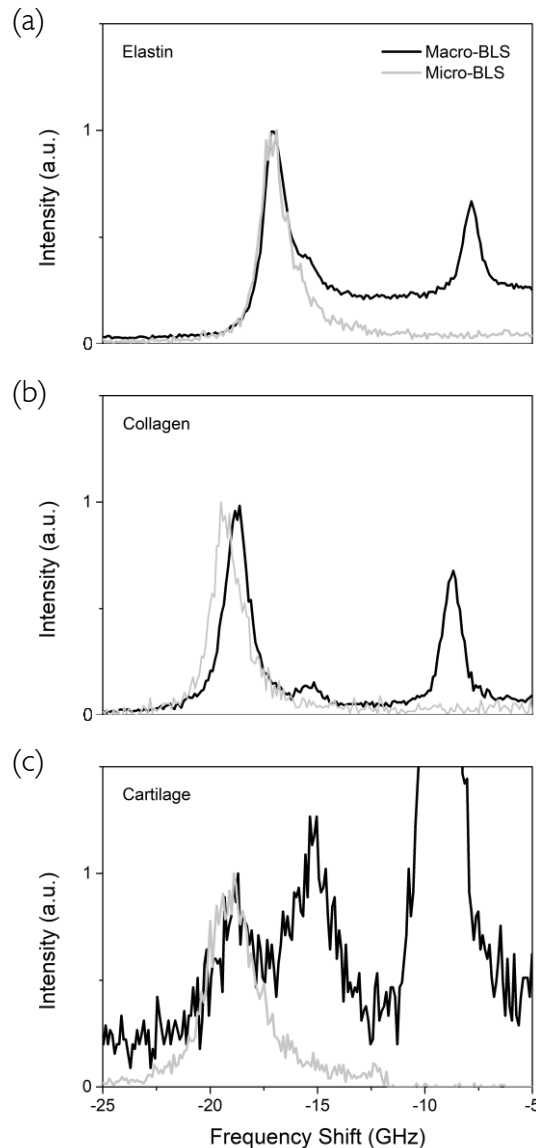

Figure 4.8: Comparison of macro-BLS and micro-BLS spectra of (a) bovine nuchal elastin fibres, (b) native RTT fibres (type-I collagen) and (c) EMJ cartilage cut parallel to the articular surface (type-II collagen fibres): angle-resolved BLS experiment with $\theta = 90°$ (black line) and micro-focussed BLS (grey line). Micro-BLS spectra were normalised to the intensity (height) of the bulk peak in the corresponding macro-BLS spectra and were less intense owing to the smaller scattering volume.

4.2.4.1.   Type-I vs. Type-II Collagen

Micromechanical differences between the collagen types were assessed by comparing the micro-BLS spectra of native air-dried type-I collagen from rat tail tendon and a sample of

articular cartilage (sectioned perpendicular to the articular surface, with fibres running parallel to the section plane) which is essentially type-II collagen. Figure 4.9 shows the two spectra, with the collagen fibre bulk peak at 19.2 GHz and that of cartilage at 19.5 GHz. A 0.3 GHz difference in peak position is resolvable by the system (spectral resolution 0.1 GHz) and may indicate a difference in micromechanics between type-I and type-II collagens.
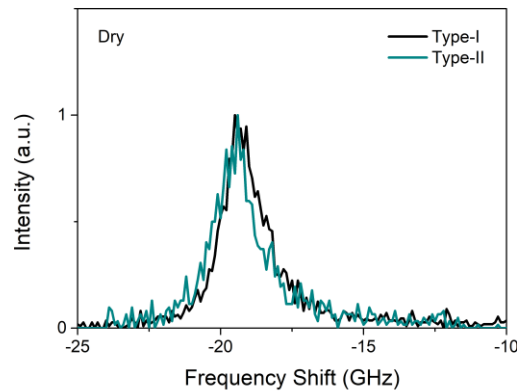
Figure 4.9: Comparison between type-I and type-II collagen. Micro-BLS spectra of articular cartilage, cut perpendicular to the articular surface (fibres running parallel to the section plane) and native RTT collagen fibre, normalised to the height of the bulk peak. A difference in peak position of 0.3 GHz is observed, with the cartilage (type-II collagen) at slightly higher frequency than the collagen fibre (type-I).

4.3.   BLS Spectra of Wet Fibres

Figure 4.10 shows the polarised BLS spectra of (a) air-dried and (b) hydrated trypsin-digested type-I collagen and elastin fibres, and EMJ cartilage cut parallel to the articular surface, measured at $\theta = 0°$. Dried collagen presents PS and bulk peaks at 9.95 ± 0.04 GHz and 18.91 ± 0.04 GHz, respectively, elastin at 8.10 ± 0.20 GHz and 16.83 ± 0.18 GHz, and cartilage at 9.37 ± 0.16 GHz and 19.06 ± 0.16 GHz. Water saturated samples present a reduction in frequency of both longitudinal phonon modes indicative of a decreased stiffness, which is accompanied by a spectral broadening of the PS and bulk peaks representative of a distribution of microscopic domains sensing slightly different mechanical properties due to heterogeneity in hydration. This is reflected in an increase of acoustic damping of the material. Wet type-I collagen and cartilage have broad peaks at 10.18 ± 0.01 GHz and 10.37 ± 0.12 GHz related to the bulk modes (a frequency reduction of $\sim$47% compared to the dry tissue), and smaller peaks at 4.81 ± 0.11 GHz and 5.01 ± 0.22 GHz related to the PS modes of the
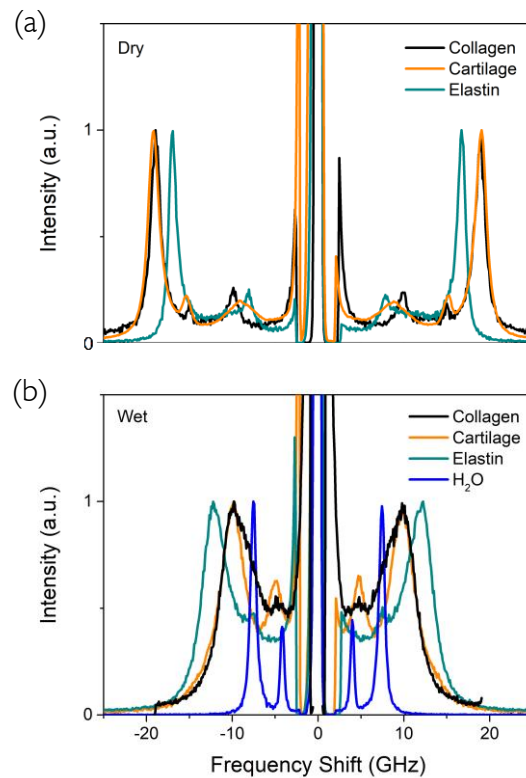
Figure 4.10: Macro-BLS spectral comparison between trypsin purified RTT collagen, bovine nuchal elastin and EMJ cartilage cut parallel to the articular surface, in (a) air-dried and (b) water saturated hydration states (VU polarisation; $\theta = 0°$). BLS spectra of water is overlaid for comparison. All spectra are normalised to the height of the bulk peaks.

wet material (frequency approximately 51 and 47% lower than that of the dry samples) mixed with the PS mode of water (blue line). Wet elastin presents a bulk peak at 12.25 ± 0.12 GHz (27% lower than the dry), however, there is no apparent PS-mode in the spectrum because of the large tail of the elastic peak at those frequencies; the peak at *ca.* 7.5 GHz is instead attributed to the bulk water. Hydration masks the mechanical anisotropy of the fibres. This is seen in figure 4.11 where the PS and bulk peaks are essentially unchanged throughout the angularly resolved experiment. Figure 4.11b shows this for the PS peak in the case of the wet purified type-I collagen fibres. No transverse modes were observed in any of the wet fibres.

The PS and bulk peaks of dry elastin are 18 and 11% lower than those of dry collagen, respectively, whereas the bulk peak of cartilage shows no resolvable difference with the purified collagen fibre in contrast to the micro-BLS results above. Elastin is the softest of the three materials whilst type-I collagen and cartilage are similar. The bulk peak of wet elastin is 17% higher than that of collagen, whilst that of cartilage is similar to the purified collagen fibre within the spectral resolution. However, any difference in peak frequency of the hydrated

tissues is likely the result of small variations in water content at the point of measurement, as the hydration state was not precisely controlled in these experiments.
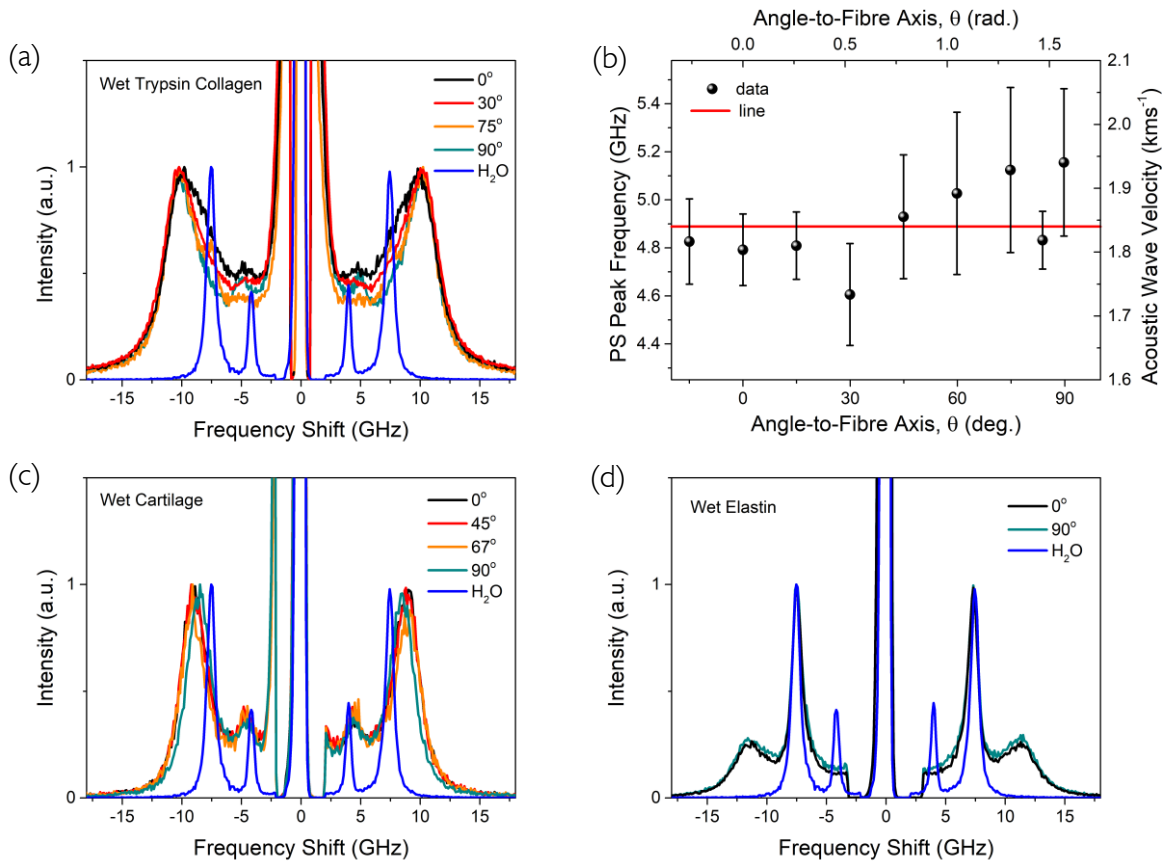

Figure 4.11: *Demonstration of water induced mechanical isotropy. VU polarised BLS spectra at various angles, θ, to the fibre axis (in degrees) of water saturated (a) trypsin digested type-I collagen from RTT, (c) EMJ cartilage sample cut parallel to the articular surface and (d) elastin fibre from bovine nuchal ligament. In each case, the BLS spectra of water is overlaid for comparison, and all spectra are normalised to the height of the bulk peaks. (b) Plot of the PS-peak frequencies of wet trypsin digested RTT fibre and resultant longitudinal acoustic wave velocity as a function of the angle-to-fibre axis, θ in degrees and radians respectively (red line marks the data set average). Error bars indicate the standard errors obtained from the Levenburg-Marquardt nonlinear least squares fit of Brillouin spectra.*

4.3.1.   Dehydration Kinetics of Cartilage

It is useful to understand the time evolution of the BLS spectra of a biological tissue with dehydration at room temperature. Figure 4.12a presents the BLS spectra of cartilage undergoing dehydration over a period of around 12 hours, detailing the first hour of the process at 10 min intervals (spectra 1-7), and subsequently every hour after that point (spectra 8-19). There is an increase in intensity of the peaks over time, indicating an increase in fibre packing as the material dehydrates. It is important to note that the bulk peaks of the dried tissue

and the peaks at *ca.* 15.2 GHz, are not apparent until 15 minutes after drying begins. The frequency of the bulk peaks then increases over the course of the experiment, until they reach a plateau at 19.1 GHz (fig. 4.12b), which indicates the stiffening of the material as it dehydrates. This is accompanied by a band narrowing (fig. 4.12c) which is indicative of a decrease in mechanical heterogeneity of the material, or of a reduction in acoustic damping related to the
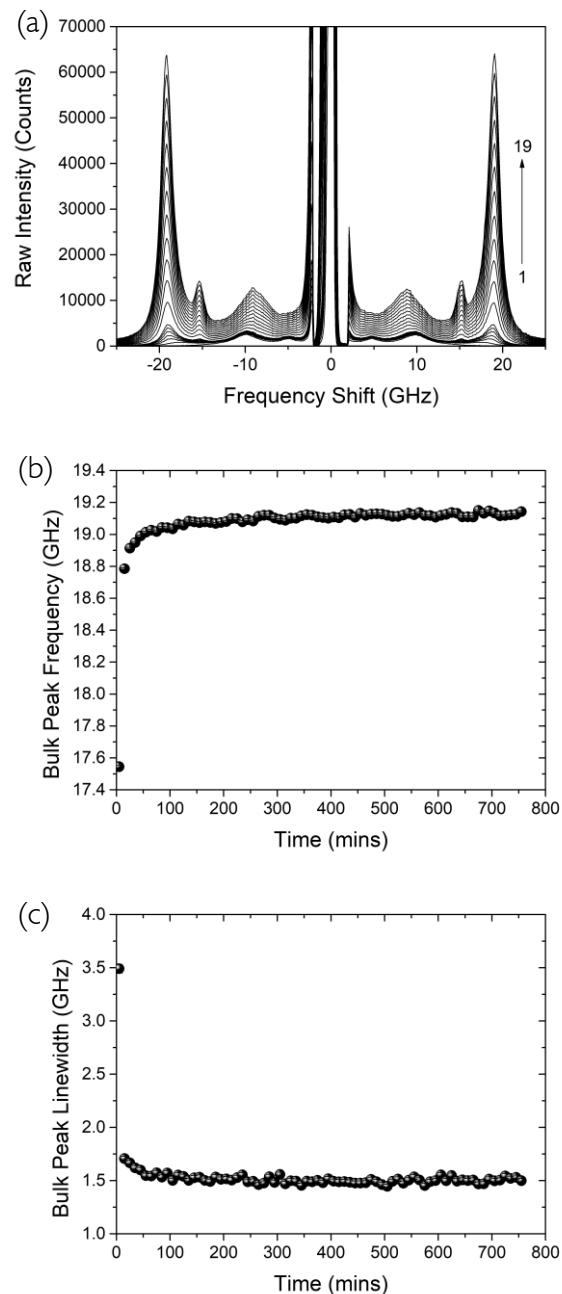
Figure 4.12: Hydration kinetics of BLS spectra. (a) BLS spectra in VU polarisation ($\theta = 0°$) of air-drying cartilage cut parallel to the articular surface measured at different times after the start of dehydration (1), until approximately 12 hrs after initiation (19). The arrow indicates the increase in intensity of the bulk peak in the range 16-25 GHz. (b) and (c) Plots of frequency and linewidth derived from DHO curve-fit analysis of the bulk peak as a function of time.

progressive slowdown of relaxation processes. Note that for a short time, the PS and bulk modes of both wet and dry cartilage coexist together, prior to the growth of the broad PS mode of the dry tissue which eventually dominates both peaks of the wet. This shows that there are distinct material phases subject to the presence of water in which the phonons propagate, and each Brillouin peak is representative of one of these, or indeed may contain a convolution of modes (in the case of the broad bands).

4.3.2.   Longitudinal Elastic Modulus

Due to the spectral changes induced by water as outlined above, the elastic moduli of the hydrated fibres cannot be extracted using the same method applied to the dry fibres, and are instead obtained from a single damped harmonic oscillator (DHO) fit of the bulk peak at $\theta = 0°$, with some approximation. Figure 4.13 presents the graphs of Brillouin shift squared $v_b{}^2$, which directly relates to the elastic modulus, for the bulk peaks of (a) collagen and (b) elastin fibres in both dry and hydrated state. The corresponding Young's moduli at five different RHs (from chapter 3) are also plotted for comparison. The quasi-radial modulus M, was obtained from the squared Brillouin frequency using the formula: $M = \rho(\lambda_i v_b / 2n)^2$, where λ_i is the wavelength of the incident light, ρ is the mass density, and n is the refractive index of the protein fibre. These values are shown in table 4.2. Note that for the dry fibres, densities are obtained from literature, and the refractive indices are as calculated above in §4.2.1 and 4.2.2). Corresponding density values for the hydrated fibres were measured using a glass pycnometer (see §2.4.5). To estimate the refractive index of the hydrated fibres, I used the relation $n = n_f - (n_f - n_w)W$ [169], where W is the percentage water content (measured to be 81 ($\pm$ 3)% and 77 ($\pm$ 2)% water content by wet-weight for collagen and elastin, respectively), and n_f and n_w are the refractive indices of the dry fibre (see table 4.2) and water (1.33), respectively.

The quasi-radial moduli of the dry fibres appear overestimated compared to the results of the PS peak analysis, perhaps because they rely on accurate values of the refractive index. The platelet-like configuration is independent of this and hence it offers the preferred approach for this analysis. Even so, a decrease in relative humidity (RH) clearly causes an increase in the longitudinal modulus of both fibres (72% for collagen and 42% for elastin), to accompany the increased mechanical anisotropy.

Table 4.2: Quasi-radial elastic moduli, M, density, ρ, and refractive index, n, for dry and wet collagen and elastin fibres.

Sample		M (GPa)	ρ (kg m⁻³)	n
Collagen	Dry	15.0 (± 0.4)	1350 [80]	1.51 (± 0.02)
	Wet	4.2 (± 0.2)	1057 (± 0.2)	1.37 (± 0.04)
Elastin	Dry	10.4 (± 0.3)	1230 [114]	1.54 (± 0.02)
	Wet	6.0 (± 0.2)	1078 (± 12)	1.38 (± 0.03)

Figure 4.13 compares the hydration dependent changes in elastic modulus of collagen and elastin observed by both BLS and the quasi-static uniaxial tensile testing from the previous chapter. A decrease in RH (upon drying) causes an increase in stiffness of both fibres determined by the macroscopic technique, although the behaviour is different between the two proteins, with elastin showing a gradual increase of stiffness with dehydration, whilst collagen displays a sharp change from 100% to 85% RH. Moreover, the increase in modulus is much more pronounced for elastin than collagen fibres (two orders of magnitude vs. three-fold), and dehydration markedly reduces the disparity in modulus between the proteins (elastin is three orders of magnitude softer than collagen in the fully hydrated state, but only five times less stiff in the 'dry' state upon desiccation in air). Using BLS, I observe an increase in stiffness at the scale of the molecules too, although here, the elastin increase is markedly smaller at only 2-times, whilst collagen is similar to its macroscopic counterpart, exhibiting a 3.5-fold rise.
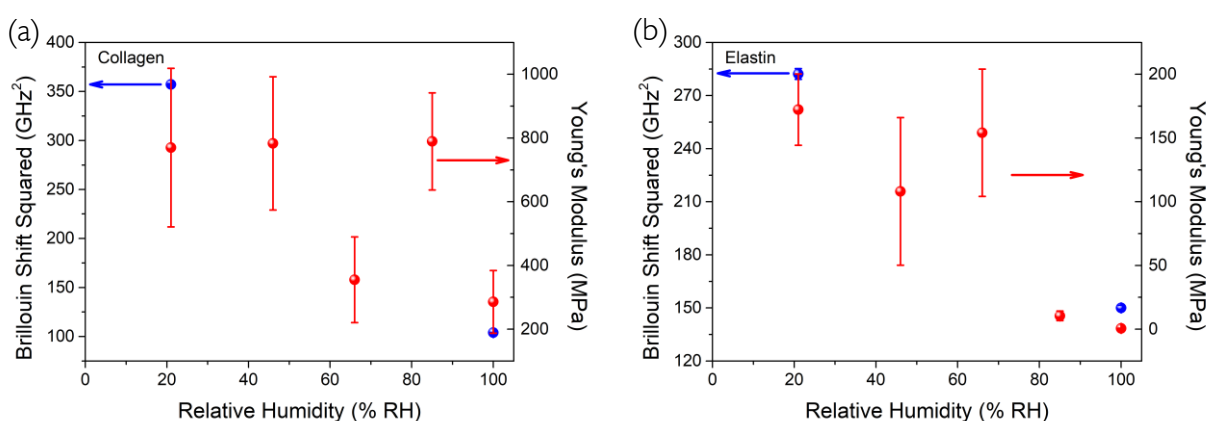
Figure 4.13: Plots of the Brillouin peak frequency shift and Young's modulus versus relative humidity for (a) type-I collagen fibres and (b) elastin fibres. Blue symbols denote the Brillouin shift squares and red symbols the Young's moduli. Error bars for the Young's moduli (± 1 std. dev.) reflect the sample variability in stress-strain response between different fibres.

4.4.   Discussion

Brillouin light scattering spectroscopy is an emerging technique for the micromechanical testing of biomaterials. It measures mechanical properties in the GHz frequency range, a domain, to-date, only very sparingly explored for natural biopolymers and it both raises and provides the means to answer fundamental questions about molecular mechanisms of elasticity in tissue. As the principal fibrous load-bearing components of the ECM, collagen and elastin are the obvious materials to begin the study of tissue micromechanics using this technique. The intact tendon from rat tail has in fact been studied before using a hexagonally symmetric elastic solid model to extract elastic moduli from BLS measurements [77, 80, 170]. My values showed satisfactory agreement with these previous studies and for the first time, the elastic constants and moduli of elastin (fibres and ligament) and cartilage were reported using BLS spectroscopy.

As this is one of the first in-depth discussions of the technique in this field, it is worth highlighting some general features in the analysis. Clearly, there is a strong dependence of the elastic moduli of viscoelastic materials such as the protein fibres on the frequency of the measurement – the higher the frequency, the bigger the moduli [171] – for example, air-dried collagen has a higher modulus than elastin, which is reflected in a 1.85 GHz increase in frequency shift of the collagen PS peak. However, this dependence becomes particularly evident when comparing between moduli obtained from corresponding elasticity measurements at lower frequencies. Dependent on the tissue hydration, I measure between a 2 to 5 order of magnitude increase in the elastic moduli obtained from BLS spectroscopy, compared to the Young's moduli obtained from quasi-static stress-strain testing outlined in the previous chapter.

The hypersonic frequencies of the BLS measurement probe the adiabatic stress-strain response of the system, which for most materials generally result in a higher modulus than the isothermal response of the quasi-static measurement. In the adiabatic case, the application of a compressive stress induces a thermal expansion, which counteracts the applied force resulting in a smaller compressive strain, whilst in the isothermal case, heat is conducted away from the compressed volume; there is intrinsically no increase in temperature and no thermal expansion to act against the compressive stress, thus the strain is larger and the modulus lower [172]. Although this can account for a difference between the resulting moduli obtained from the two techniques, it likely only contributes to a few percentage points, and the major contributor to the orders of magnitude difference in the elastic moduli is probably the substantial change in probing frequency. To explain this phenomenon in detail, the complex

pattern of dispersions should be investigated in the whole Hz-GHz frequency region and related to the molecular dynamics at the different time and space scales of this heterogeneous material.

I obtained a full description of elasticity using BLS to analyse the air-dried fibres, however, the presence of water makes obtaining the same description of hydrated fibres a challenge. Peak broadening and the overlapping of phonon modes makes accurate fitting of the BLS data difficult, and as such I am restricted at present only to extraction of the bulk peak frequency shift and an estimate for the quasi-radial modulus. In fact, the Brillouin band shape is a function of the scattering volume, the phonon wavelength and its attenuation length; three separate length scales that probe structure over a spatial range between the hundreds of nanometres to the tens of microns [143]. An individual peak therefore contains information regarding multiple levels of hierarchical structure, potentially highlighted in the dehydration kinetics of the cartilage tissue in §4.3.1 above. Deconvolving the band shape through techniques such as multivariate analysis, is a current topic of discussion in the BioBrillouin field.

Hydration has a pronounced effect on the Brillouin spectrum of the fibres: the peaks appear red-shifted and noticeably broadened upon increase of the water content. This has the effect of softening the fibres, hence reducing the velocity of the acoustic wave while broadening the distribution of local oscillators sensing slightly different humidity environments. Interestingly this peak broadening is also evident in the air-dried tissues analysed above; my measurements on intact cartilage showed a stronger attenuation of the acoustic waves, measured by $\tan(\delta)$, relative to the other materials studied here. This can be attributed to a remnant of hydration owing to tightly bound or interstitial water not removed by air drying, which causes a bigger heterogeneity in the viscoelastic behaviour of articular cartilage.

A decrease in water content causes an increase in stiffness at both the macroscopic fibre scale (Young's modulus – measured by quasi-static stress-strain tests) and at the scale of the molecules (hypersonic longitudinal modulus – measured by BLS); though there is a discrepancy in the magnitude of the changes observed by the two techniques between the hydration extremes of the respective fibres. Collagen exhibits a similar three-fold increase in both its Young's and longitudinal moduli, whilst elastin demonstrates a two-fold increase in the latter, but a pronounced two *orders* of magnitude increase in its Young's modulus. The organisation of elastin molecules to form tissue-specific fibres is much less well characterised than that of collagen and the molecular basis of the molecule's unique long-range elasticity is still

incompletely understood. I note that the angular dependence of the BLS data was weaker and their values lower than those in type-I collagen. Together with the isotropic Poisson's ratio, this probably reflects the less regular organisation (hence lesser mechanical anisotropy) of elastin microfibrils within the fibres that were examined.

An explanation for the varied magnitude changes in elastin between the two techniques can be found in the different combination of bulk (K) and shear (G) moduli measured by stress-strain and BLS experiments, illustrated in figure 4.14. Hereafter I refer to the isotropic case, anisotropy just changing the scalar notation to a more involved tensor notation.
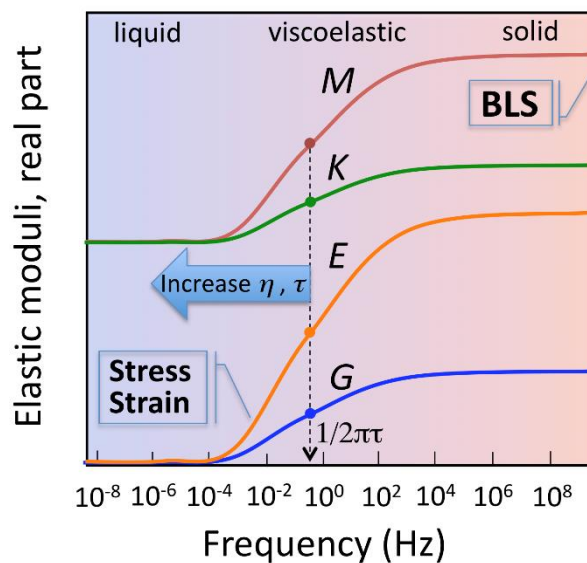
Figure 4.14: Plots of the typical behaviour of the real part of elastic moduli vs. frequency in the presence of a structural relaxation process. Symbols denote M: longitudinal modulus, K: bulk modulus, E: Young's modulus, and G: shear modulus. Brillouin scattering probes the longitudinal modulus in the GHz range, while quasi-static stress-strain measurements provide the value of the Young's modulus in the long time (sub-Hz) regime.

The Young's modulus (E) obtained from the stress-strain response is expressed by $E = 9KG/(3K + G)$, whilst the longitudinal modulus (M) probed by Brillouin scattering is given by $M = K + 4G/3$. Hence, E is more sensitive than M to those large variations of the shear modulus (G) that are typical for the transition from liquid-like to solid-like behaviour. In fact, liquids do not sustain shear stress or shear waves, which correspond to $G = 0$ and $E = 0$, while density fluctuations and longitudinal acoustic waves can propagate in liquids with velocity $c = (M/\rho)^{1/2} = (K/\rho)^{1/2}$, and the Young's modulus is thus considerably lower than the Brillouin modulus for a hydrated material. Passing from liquid-like to solid-like behaviour, the

divergence of viscosity η and of the corresponding structural relaxation time τ is associated with values of G and E that change by orders of magnitude, from zero up to a finite value, while the value of M only increases by the term $4G/3$, hence the change in the Young's modulus is considerably more than the increase in Brillouin modulus when undergoing state-changes. Such liquid-to-solid transitions correspond to the development of arrested states of matter, i.e. to the blocking of motions on a molecular scale, like in glass-transition phenomena. In the present case of wet elastin, arrested states, usually induced either by physical (temperature or pressure) or chemical (polymerization) changes, seem to be triggered by the reduction of moisture content. At room temperature, the amorphous state of elastin is known to be heavily dependent on the level of hydration, whilst collagen always bears long range order in the form of the triple helix, unless denatured above 60°C [173]. In fact, the two-orders-of-magnitude increase of the Young's modulus for reduction from 100% to 21% RH cannot be simply explained in terms of ideal mixing of elastic constants of the components. Rather, it may be generated either by the divergence of a molecular contribution to viscosity [174] – i.e. to structural relaxation time, according to the Maxwell's viscoelasticity law $\eta = G_\infty \tau$ – or by the development of an increasing number of cross-links [175] among elastin fibres, or indeed, both effects. This goes some way to explaining why I observe the remarkable increase in the Young's modulus in elastin, but not in collagen, given that the collagen triple-helix already exists in an ordered state when hydrated. It would be instructive to compare BLS spectra with the low-frequency Raman modes of both matrix protein to clarify the effects of water on the structure, and vibrational and relaxational dynamics of these materials [176-178].

It should be noted that the longitudinal Brillouin modulus should not be interpreted as a Young's modulus. However, there appears to be some correlation between the elastic moduli determined by the two techniques; irrespective of the scale of change, I do observe an increase in stiffness due to dehydration at both the molecular and macroscopic fibre level. Whilst such a relationship between moduli has long been established for crystalline materials, a definitive expression has yet to be formulated for soft matter [179], although an empirical log-log linear relationship between the moduli within the crystalline lens (porcine and bovine) [180], fibroblast cells and synthetic hydrogels [181] has been suggested. In elastin, I also observe that an increase in longitudinal modulus corresponds to a larger increase in Young's modulus of a material, though the absence of this variation in collagen suggests that this relative change may be dependent on the state of the matter in question, i.e. elastin experiences the large increase in Young's modulus due to its shift from an hydrated amorphous polymer into

a more ordered solid state upon dehydration, whereas collagen always retains its order unless denatured. Regardless, one of the prime aims of this thesis was to establish a potential functional connection between the mechanics generated at two different scales of the structural hierarchy in the ECM. Although, much more work needs to be done to allocate the precise structural contribution, these results leave open the possibility that the arrested state of the molecular composition upon dehydration actually leads to the stiffening of the fibres at higher levels, i.e. that the mechanical state of the base unit of the fibres leads to the macroscopic mechanical state of the tissue.

The angle-dependent macro-Brillouin data, acquired averaging over a large scattering volume (focus diameter approx. 40 μm; focal depth approx. 40 μm), correspond well with the bulk mode micro-BLS spectra of the elastin fibres and for the cartilage (figs. 4.8a and c), indicating that the elasticity of both materials is homogenous over these scales in the orientation probed. In contrast, the collagen spectra (fig. 4.8b) show a resolvable difference that can be related to the elastic anisotropy of the single fibril (thickness between 100-300 nm – see SEM figure 2.22), rather than the composite properties of the larger fibre. Recall that the resolution of the microfocussed approach using the 532 nm excitation light and a 0.75 NA objective, yields a laser spot approximately 250 nm in diameter and a phonon wavelength of approximately 200 nm.

A further feature highlighted by the microfocussed BLS approach can be seen in the peak *ca.* 15 GHz in the overlaid macro-BLS spectra in figure 4.8. The fact that this signal is found at similar frequency in all three samples suggests that it possibly arises from a small remnant of highly hydrated fibres within the tissue. This may be an indication of the presence of tightly bound (interstitial [182]) water which is not removed by dehydration at room conditions. The micro-BLS spectra, which were acquired after macro-BLS spectra on the same samples, show no evidence of this peak owing to the higher spatial resolution. This reflects the ability of micro-focussed BLS to select the contribution from a single fibre, whereas the macro-BLS approach collects scattered light from larger, heterogenous areas of the sample composite. In short, micro-BLS two-dimensional mapping enables the distribution of elastic properties of heterogeneous materials to be obtained.

The peak frequency observed for type-I collagen using the microfocussed approach – approximately 19 GHz – is higher than the average frequency of the fibrous type-I collagen

rich matrix of human epithelium biopsy (*ca.* 18 GHz – dry sectioned tissue) analysed by micro-Brillouin mapping [141, 183]. This indicates that other non-collagenous constituents and the structural organisation of the ECM contribute to making this tissue softer than the single collagen fibrils examined here. This is also evident in the macro-BLS approach where the differential mechanical properties observed between elastin fibres and the bovine nuchal ligament (from which they were drawn out) may reflect the role of non-elastic constituents and cross-linking of the fibre bundles in determining an absence of elasticity anisotropy for the ligament. In intact tissues, elastin is assembled on a skeleton of microfibrillar glycoproteins, and there is debate as to whether these microfibrils contribute directly to the mechanical properties of the composite elastic fibres.

There has been a long-standing debate about the extent to which biochemical and structural differences between collagen types give rise to different mechanical properties and physiological functions. Type-II collagen is found only in hyaline cartilages, where it forms arcades of fine (submicrometre) fibrils. The macro- and microfocussed BLS approaches adopted here appear to suggest that the intrinsic mechanical properties of the type-II fibril are similar to those of type-I, the only observable difference being a small 0.3 GHz frequency increase of the former in the microfocussed BLS approach (fig. 4.9). This is perhaps expected given the similarity in triple-helical structure, although a more complete picture may result from a mapping approach, wherein topological patterns of elasticity at a submicrometre level can be identified via fibril-to-fibril comparative analysis. Moreover, such an approach would supplement current efforts to understand how the differentially oriented type-II collagen fibrils within the distinct zones of articular cartilage, contribute to its stability under compressive and sometimes tensile loads [65]. Until now, this has largely been the reserve of finite element model analysis rather than direct experimental observation [184]. The advantage of BLS as an optical technique in this respect, is in the potential of combining with other imaging modalities such as two-photon fluorescence and single harmonic generation [89], to provide unprecedented detail into the structure and mechanics of this dynamic composite, at multiple scales in vitro.

A preliminary experiment allowed me to assess the controversial role of the ground substance in connective tissue for the first time using the *macro*-BLS technique, observing changes in the

micromechanics of a trypsin purified collagen fibre, with around 97% of all non-collagenous material removed [109]. The value of $\tan(\delta)$ was 33% smaller, reflecting a reduction in water content of the digested fibre. Negatively charged GAGs are responsible for binding a large component of water in tendon [185] and my results suggest that the removal of the ground substance does indeed reduce the level of bound water in the purified tissue. Elastic anisotropy (c_{33}/c_{11}) seems unchanged in the digested fibre, however, changes in the tensor values c_{12} and c_{13} reduce and homogenise the calculated longitudinal and transverse Brillouin moduli (30% and 7% lower, respectively), indicating that the purified fibres are less stiff than the native tissue. This is perhaps counterintuitive, as removal of bound water, together with the soft PG matrix, leaves only the stiffer fibrillar structure, which should result in a higher modulus. It is possible however, that the complete exchange with air of all non-collagenous material in the interfibrillar space of the dried fibres may be responsible, as air has a low viscosity and hence a lower Brillouin modulus compared to the hydrated gel matrix. Regardless, this highlights the role that the ground substance plays in mediating the fibre mechanics, particularly its role in stabilising the fibrillar structure, which is evidenced by the vastly increased anisotropy in the Poisson's ratio with the ground substance removed. Although there is much conflicting evidence of the functional role played by the material in the extrafibrillar space, the arguments generally fall under two categories; that of the ground substance mediating either fibril load transfer, or fibril sliding. For some time, it was believed that the PG matrix was responsible for bridging the discontinuous fibrils as load bearing connectors within fibres [186, 187], though more recent work demonstrated that removal of the GAG side-chains had no noticeable impact on the tensile properties of tendon [156, 188-190]. The mechanical role of PGs and GAGs thus remains to be fully determined, although their removal is known to have a deleterious impact on the relaxation and recovery mechanism of the fibres [66, 191], suggesting that the ground substance acts more as a supporting structure in which the fibrils move. A recent work by Szczesny *et al* [192] instead posits the role of interfibrillar stress mediation to a range of entangled microfibrils, yet to be classified. Interestingly, the authors noted that removal of the ground substance reduced the transverse bulk and shear properties of the fibres, which may be reflected in the markedly decreased minor Poisson's ratio ($\mathbf{v}_{12}$) in my BLS results. It is not immediately clear from this preliminary data, whether the reduction in the calculated elastic modulus indicates a load bearing role of the ground substance, given that the elastic anisotropy remains unchanged; however, the fact that BLS could identify differences between the native and purified fibres warrants a far more detailed investigation.

I suggest a microfocussed BLS mapping approach, which has the advantage of determining the specific contribution of the intra- and extrafibrillar spaces to the micromechanics of the fibres at a previously unattainable scale *in vitro*, where the functional role of the fibrils can be isolated from the ground substance and water under different strain conditions. This would be an improvement on a previous attempt using AFM, which could only assess the impact of removing GAGs in pre-strained, post-fixed and dried fibre sections, where the invasive tissue processing techniques have potentially altered the mechanics of the fibre ultrastructure [67].

Brillouin scattering spectroscopy is a unique tool by which the individual components of the elasticity tensor of a protein fibre can be characterised in unprecedented detail. Furthermore, the measurements can be made on a microscopic scale and thereby will provide novel insights into the micro-scale mechanics of biological structures, allowing for the first time, to understand the mechanical, and probably functional significance of the complexities in matrix architecture and biochemistry which has been revealed in recent years.

Potential modifications of the technique might involve the coupling with optical microscopy for microfocussed Brillouin scattering and mapping approaches [141, 143, 183] and the combination with complementary techniques such as Raman scattering [193, 194], which in a simultaneous set-up would enable the interpretation of micromechanical properties in terms of molecular composition; particularly relevant for fundamental studies of structure and function. Current applications of the technique are mainly focussed on excised biological materials (as here), or in vitro analysis of cells [195, 196], but important developments, e.g. in the spectrometer through the use of virtually imaged phase array (VIPA) etalons [197], are making possible the translation of this technique from the benchtop to the bedside, with a range of applications already demonstrated [180, 198], including *in vivo*. The VIPA approach is an alternative spectrometer – conceptually similar to a tilted Fabry-Perot etalon, but with a fixed mirror separation – with the distinct advantage of a faster acquisition time (down to milliseconds) although developments to improve contrast (the main drawback of the technique) are currently being made.

BLS promises to be a major tool in fundamental biophysical research on the extracellular matrix and thereby to produce new insights into the evolution of mechanical properties during matrix growth, and their loss in pathological degeneration. It is also important to remember that the measurements are non-invasive and might therefore be undertaken in vivo. Indeed, this has

already been achieved in the cornea [198] where clinical trials are underway, and if suitable fibre-optic devices become available [199-201], may provide a platform for the development of new, routine diagnostic tools for a wide range of connective tissue disorders.

Ultrasound Elastography and atomic force microscopy (AFM) are alternative methods of micromechanical measurement, but the BLS technique offers better spatial resolution (on a subcellular scale) than the former and, unlike AFM, imposes no mechanical forces on the specimen, and is not restricted to the analysis only of surface features. BLS can be applied to a wide range of problems and materials in biomedical science. It can help in answering questions on physiology and pathology of biological tissues, as well as provide a physical tool for the fundamental understanding and interactions at the molecular level.

5

Raman Spectral Analysis of Protein Fibre Structure

5.1.   Introduction

In the previous chapter, I explored the molecular mechanics of collagen and elastin fibres at two extremes of hydration. In this chapter, I use polarised micro-Raman measurements to understand the structural origins of the mechanical response observed in stress-strain testing of collagen and elastin fibres between 42 and 100% RH, and in a water submerged state, to elucidate the role of hydration water. Results are presented for the entire spectral range – 135 to 3800 cm^{-1} – including the analysis of the low-wavenumber region (<500 cm^{-1}). Strain-induced spectral changes are highlighted and the interaction of individual bonds with water are discussed. A schematic diagram of the chemical structure of the collagen triple helix is provided in figure 5.1 as a useful reference for the bond vibrations discussed in this chapter.
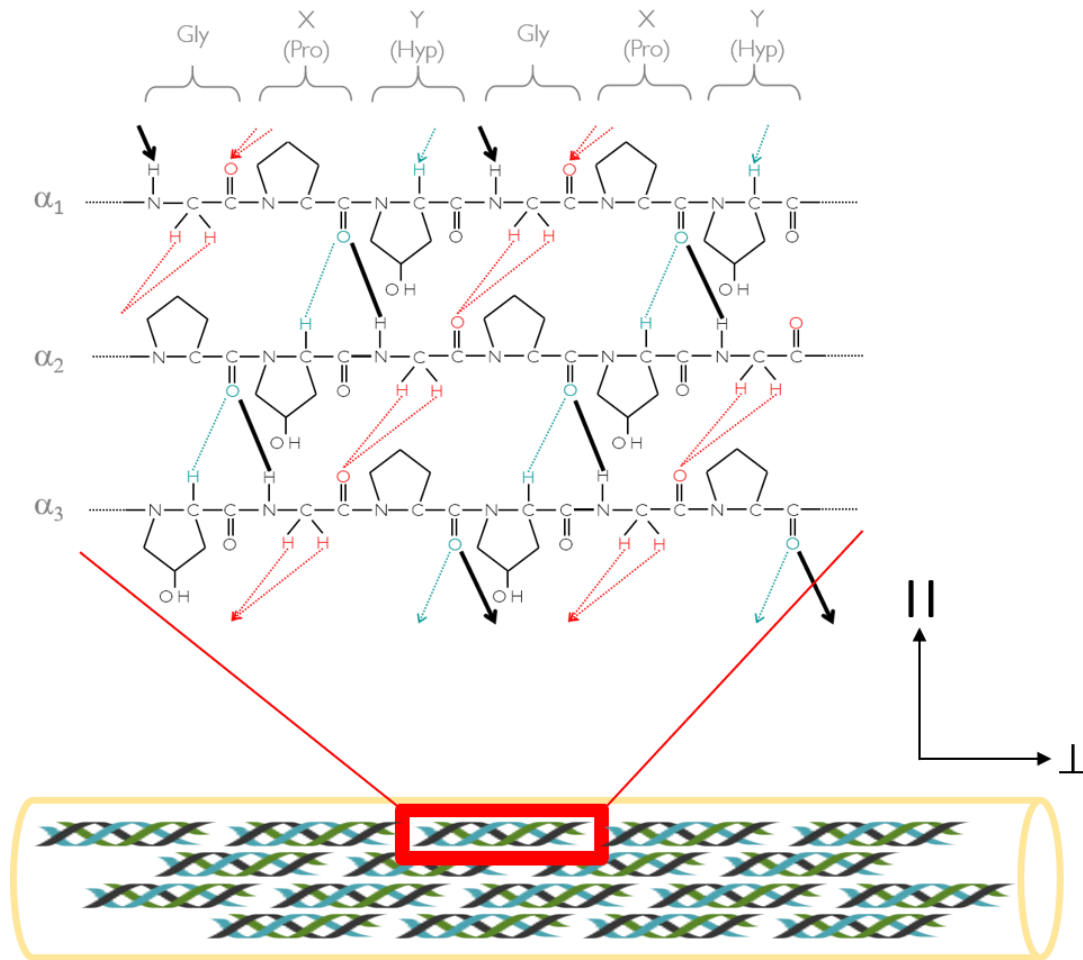
Figure 5.1: schematic diagram showing the chemical composition of a typical repeating Gly-Pro-Hyp collagen triple helix within a single collagen fibril. The tropocollagen monomer consists of three α-chains, classically hydrogen-bonded between C=O···HN (bold lines) although improper or 'weak' hydrogen bonds between C=O···HC (dashed cyan and red lines) and water bridges (not shown) are also possible. Note that the H-bonds from the third α-chain (α_3) terminate on the first α-chain (α_1). The arrows denote the orientation of the polarised ($\parallel$) and depolarised ($\perp$) scattered light with respect to the fibrillar axis, parallel to the triple helix. C – Carbon; N – Nitrogen; O – Oxygen; H – Hydrogen. Adapted from: [3]

5.2.   Polarisation-resolved Micro-Raman Spectra

5.2.1.   Type-I Collagen Fibres from Rat Tail Tendon

Figure 5.2 presents visible light micrographs of a collagen fibre crimp under increasing uniaxial tensile strain applied through a mechanical testing stage mounted on a Raman microscope. At 0% strain, collagen fibrils were aligned along this repeating sinusoidal structural motif such that at the 'apex' they were approximately parallel to the fibre axis, whilst in the 'diagonal' region

they were oriented at around 45° to the fibre axis. Strain was applied axially to the fibre at 5% increments, and the gradual opening of the crimp in the direction of applied strain was clearly observed in each successive frame, such that by 35%, all fibrils were aligned parallel to the applied strain; the crimp was removed and the fibrillar structure was completely linear. The strain needed for removing the crimp varied between fibres, but was consistently in excess of 20% at all hydrations. Throughout the application of strain, the fibrils in the apex region remained aligned approximately along the fibre axis.
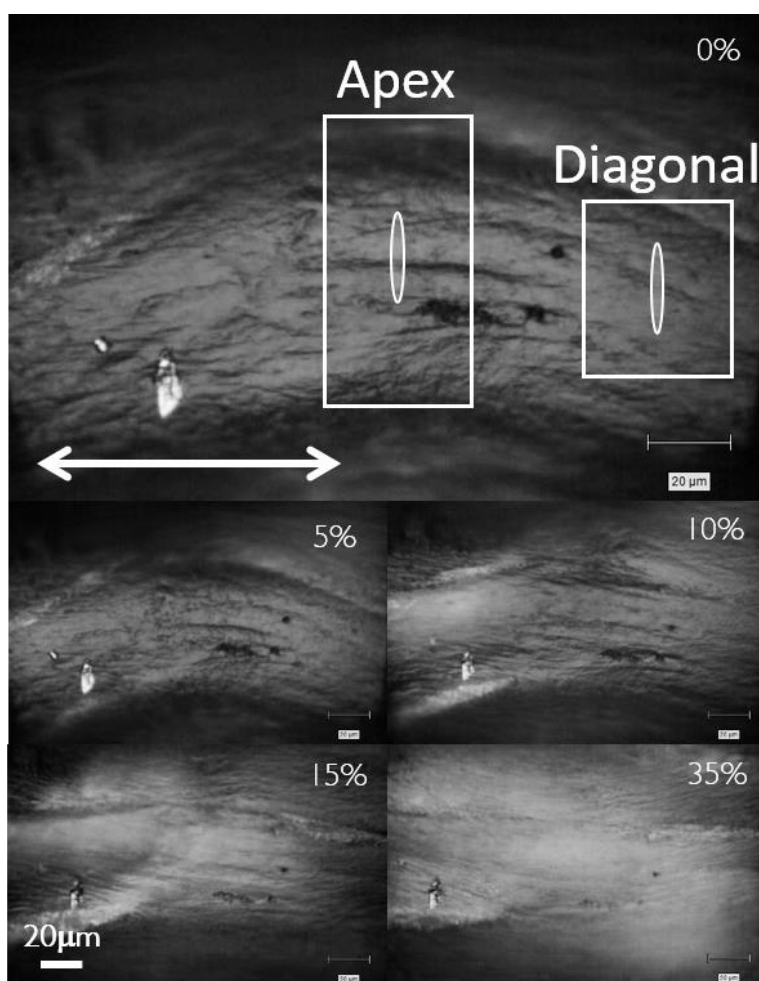

Figure 5.2: representative micrographs (x50 objective lens) of a collagen fibre crimp under increasing uniaxial tensile strain (0-35% in 5% steps). Collagen fibrils are aligned approximately parallel to the macroscopic fibre axis (denoted by the arrow) at the apex and 45° to the fibre axis in the diagonal region at 0% strain. Raman spectra were acquired in both regions at each stage of strain application. The oval at the centre of the boxes represents the laser line focus.

There is an active debate in the literature over the 2D-planar and 3D-helical arrangement of the crimp structure in tendon which recent work has posited to be dependent on the

physiological role of the tissue in question; with a helical arrangement associated with energy storing tissues and the planar-type linked to positional tendons [39]. Rat tail tendon falls under the latter category and thus I adopt the nomenclature of 'apex' and 'diagonal' when discussing the regions of the fibrillar repeating pattern. A limitation to bear in mind is that, nano-resolution is required to access the 3D conformation of the collagen molecule, whereas Raman spectroscopy is a microfocussed approach which intrinsically averages over the conformations at the nanoscale giving only a 2D view of the molecular structure.

The strain dependent changes in the Raman spectra of native type-I collagen fibres were observed under controlled hydration between 42-100% RH and in fibres submerged in distilled water. Figure 5.3-5.5 show the mean polarised Raman spectra from the apex and diagonal regions of the water submerged fibres, at incremental strains during removal of the crimp. Key peak changes are highlighted between the polarised (∥ – light scattered from vibrational modes approximately *orthogonal* to the fibre axis – radial) and depolarised (⊥ – light scattered from modes approximately *parallel* to the fibre axis – axial) spectra determined by the orientation of the laser polarisation with respect to the fibre axis. Figures highlighting these same key peaks for the intermediate hydrations may be found in the Appendix (42% RH – figs. A 1-A 3; 82% RH – figs. A 4-A 6; 100% RH – figs. A 7-A 9). The fingerprint region (650-1750 cm^{-1}) showed several clear changes under increasing strain particularly for the Amide I band between 1530-1740 cm^{-1} (peptide C=O stretching; figure 5.3a) and the peaks at 1243, 1099 and 1030 cm^{-1} (respectively: Amide III, C–N stretching and phenylalanine; figure 5.3b). Further differences were evident at 935, 920, 875, 855 and 813 cm^{-1} (C–C stretching; figure 5.4a). The low-wavenumber region (135-650 cm^{-1}) showed changes in the bands centred at ∼170, ∼260 and ∼570 cm^{-1} (figure 5.4b), whilst changes in the high-wavenumber region (2600-3800 cm^{-1}) were observed in the peak at 2970 cm^{-1} (CH$_3$ asymmetric stretch), and in the broad band between 3100-3800 cm^{-1} (mainly O–H stretching; figure 5.5). The latter band reflected the water content of each fibre and was found to be highly location-dependent in the water immersed samples.
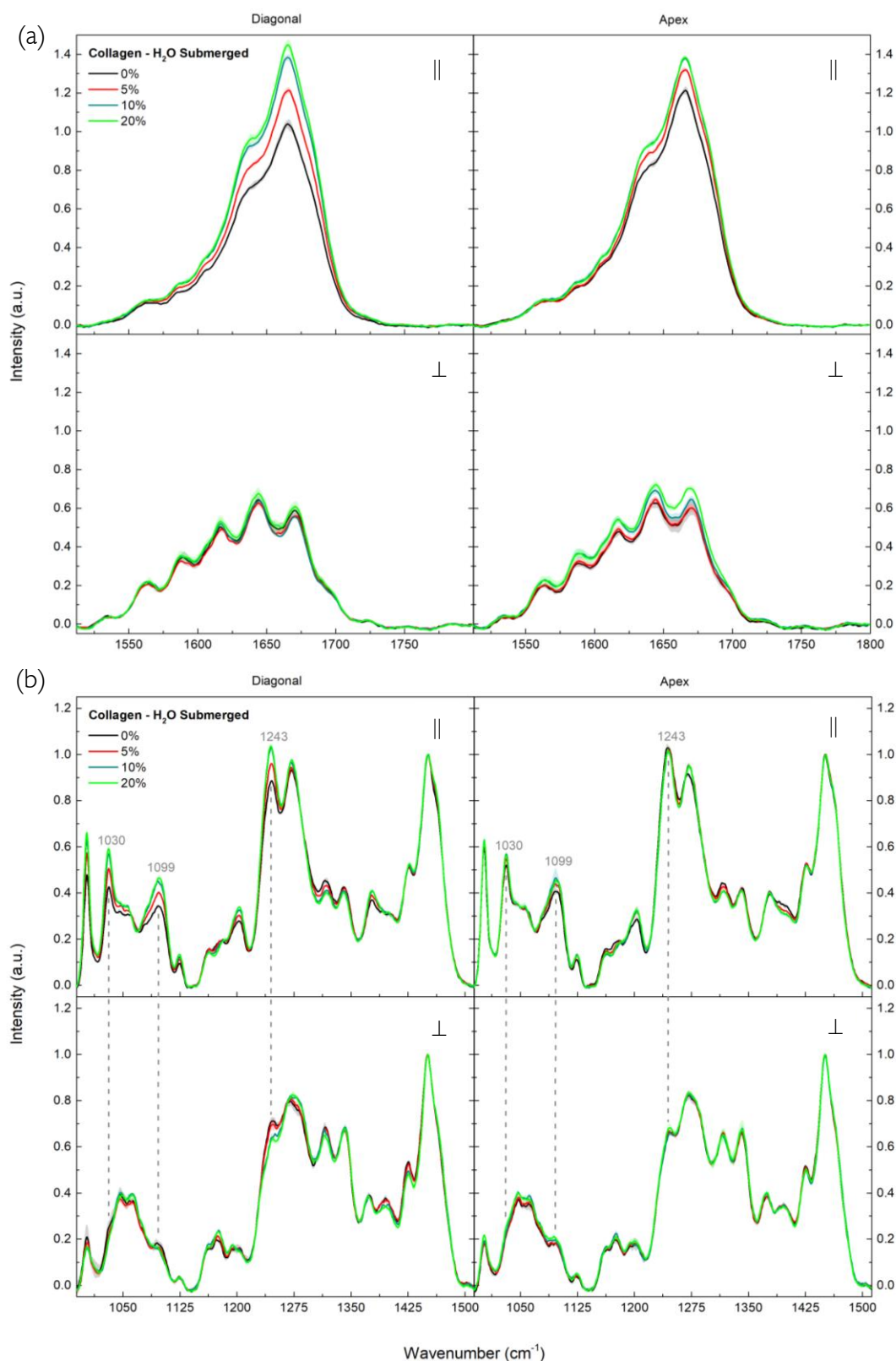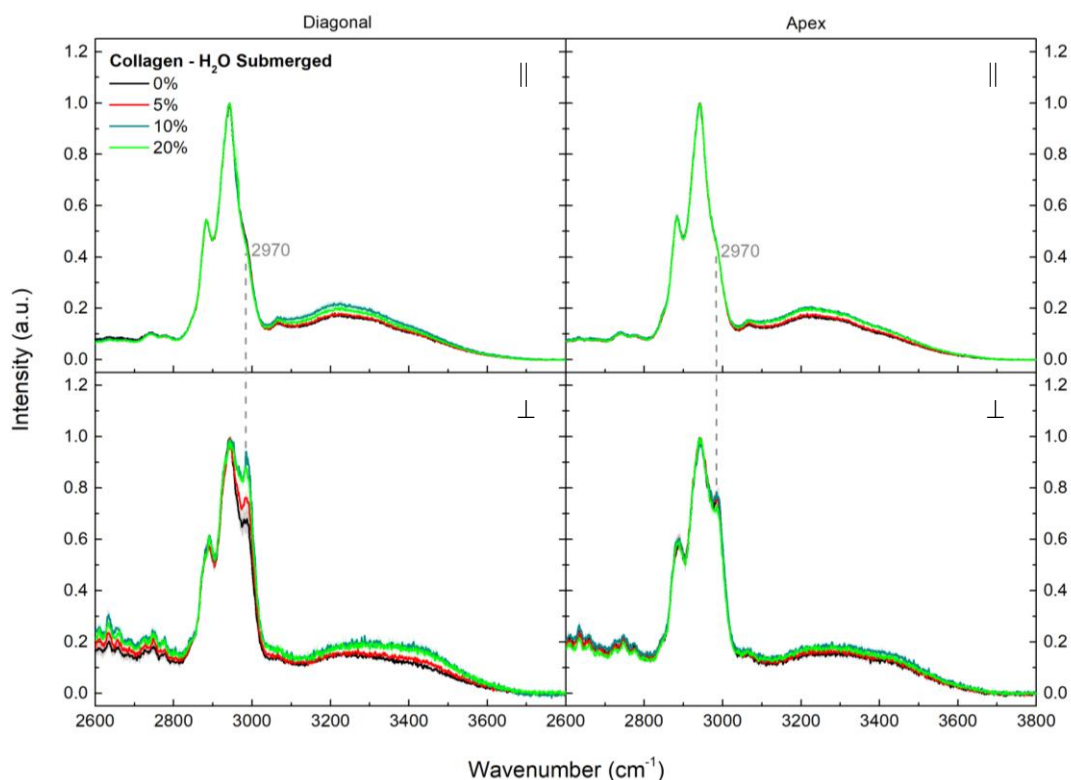
Figure 5.3: Mean polarised Raman spectra showing the (a) Amide I and (b) Amide III spectral regions, of native collagen fibres from rat tail tendon submerged in distilled water at a range of uniaxial tensile strains. Spectral changes are tracked in the diagonal (left) and apex (right) sections of the macroscopic fibre crimp as it opens under the applied strain (crimp fully opened at 20% strain). Averaged spectra (n≥3) are baselined and normalised to the intensity of the CH_2 peak (1451 cm^{-1}). Shading denotes the standard deviation. Key peaks are highlighted between the polarised (‖) and depolarised spectra (⊥).
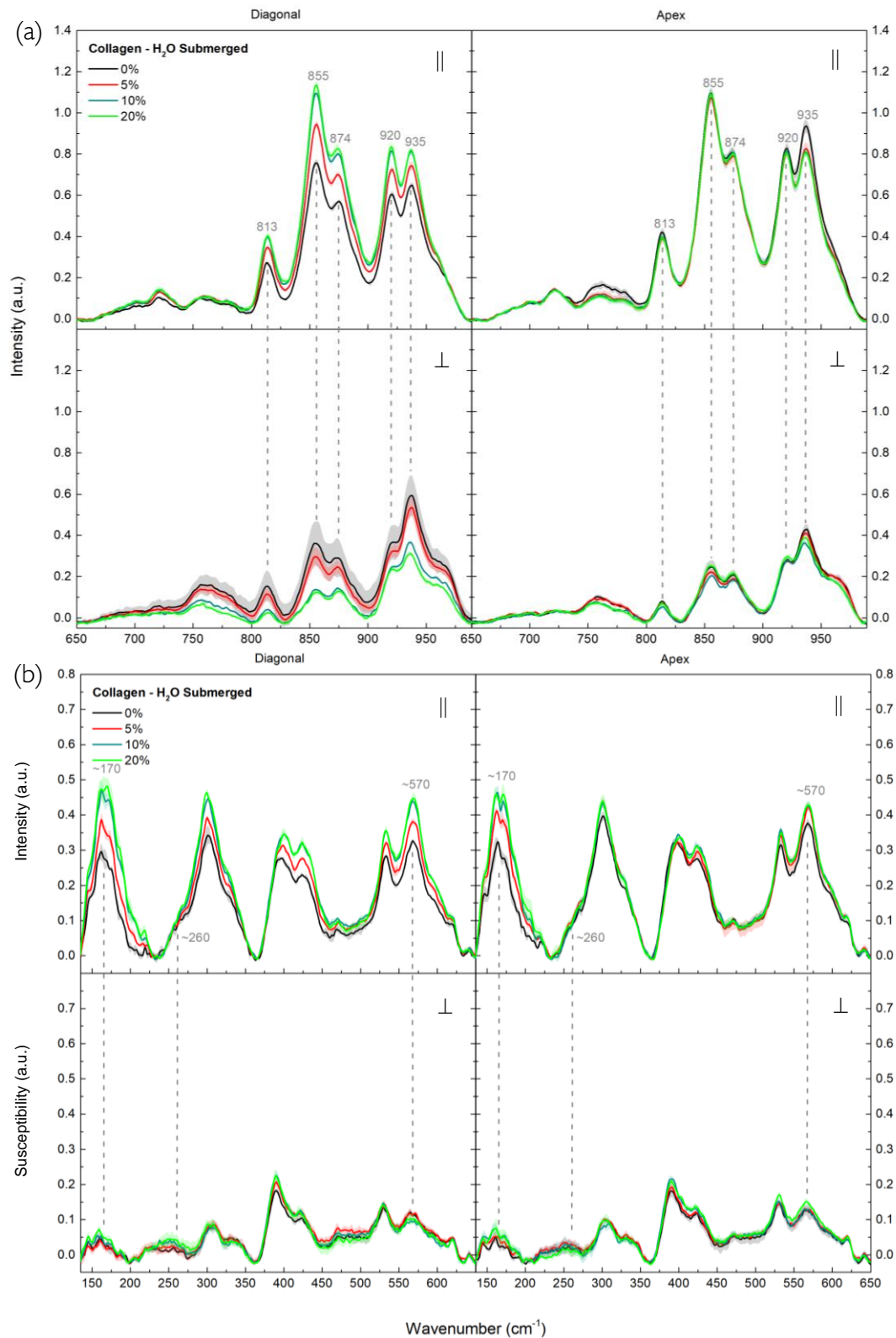
Figure 5.4: Mean polarised Raman spectra showing the (a) C-C backbone and (b) LWN spectral regions, of native collagen fibres from rat tail tendon submerged in distilled water at a range of uniaxial tensile strains. Spectral changes are tracked in the diagonal (left) and apex (right) sections of the macroscopic fibre crimp as it opens under the applied strain (crimp fully opened at 20% strain). Averaged spectra (n≥3) are baselined and normalised to the intensity of the CH_2 peak (1451 cm^{-1}). Shading denotes the standard deviation. Key peaks are highlighted between the polarised (‖) and depolarised spectra (⊥). LWN depolarised spectra are plotted as susceptibility form.

Figure 5.5: Mean polarised Raman spectra showing the HWN region, of native collagen fibres from rat tail tendon submerged in distilled water at a range of uniaxial tensile strains. Spectral changes are tracked in the diagonal (left) and apex (right) sections of the macroscopic fibre crimp as it opens under the applied strain (crimp fully opened at 20% strain). Averaged spectra ($n \geq 3$) are normalised to the intensity of the CH-band (2800-3040 cm^{-1}). Shading denotes the standard deviation. Key peaks are highlighted between the polarised ($\parallel$) and depolarised spectra ($\perp$).

5.2.1.1.   Amide I band

The amide I band at 1530-1740 cm^{-1} is attributed to the C=O stretching vibration of the peptide bond along the protein backbone [202], and is essentially polarised. Figure 5.6 is a plot of the amide I band area calculated as the integral of the polarised peak in the range 1530-1740 cm^{-1} as a function of strain at all four hydrations. An increase was observed for the diagonal region of the fibre crimp, although it was only statistically significant at and above 82% RH ($p_{82}=0.0006$; $p_{100}=0.0178$; $p_{H2O}=1.5 \times 10^{-8}$, ANOVA test). Increases were only minor in the apex region, and only significant for the 82% RH and water submerged fibres ($p_{82}=0.0074$; $p_{H2O}=1.29 \times 10^{-5}$, ANOVA test). The magnitude of the band area change was larger for the fully hydrated and water submerged fibres. At the full opening of the crimp, the spectra in the diagonal and apex region became more similar to one another. The depolarised

spectra in the amide I region (figs. 5.3a, A.1a, A.4a & A.7a) show fringes due to a coupling effect between the polariser, the analyser and the 600 l/mm diffraction grating.
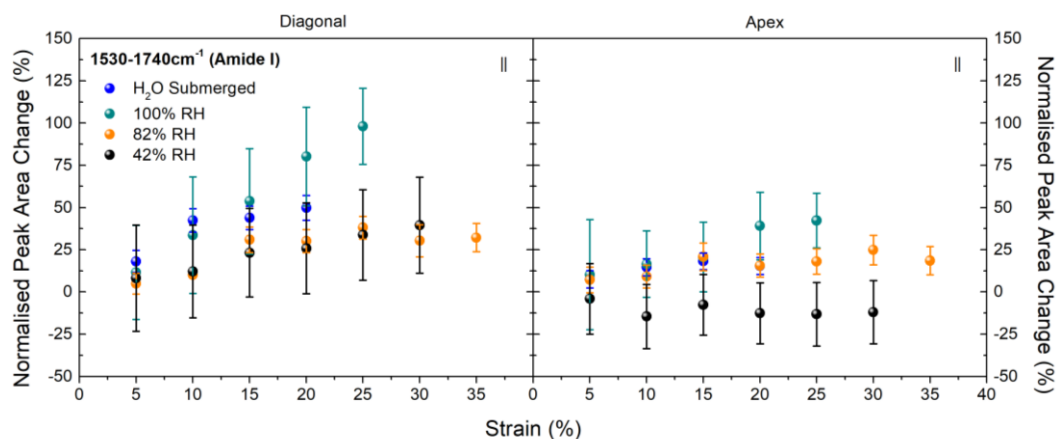
Figure 5.6: plots of the percentage change with increasing uniaxial tensile strain in the area of the Amide I band of the polarised (∥) spectra of collagen fibres from rat tail tendon at a range of hydrations. Spectral changes are tracked in the diagonal (left) and apex (right) sections of the macroscopic fibre crimp as it opens under the applied strain. Data points are presented as an average of at least two analysed spectra, normalised to the mean area of the CH_2 band (1435-1500 cm^{-1}) ± uncertainty from error propagation.

5.2.1.2.   C–N stretching bands

Figure 5.7a and 5.7b show the percentage change in the intensity of the polarised and depolarised peaks at 1243 and 1099 cm^{-1}, as a function of strain at all four hydrations. The former region is associated with the Amide III group in the protein backbone, a combination of the C–N stretching vibration, N–H bending and CH_2 wagging, whilst the latter is associated with the C–N stretching vibration of the protein backbone alone [202]. Both bands are essentially polarised (figs. 5.3b, A.1b, A.4b & A.7b). Intensity changes in the peak at 1243 cm^{-1} were observed in the diagonal region of the 100% RH and water-submerged fibres, although only the increase in the peak area of the polarised spectra of the latter was statistically significant ($p_{H2O}=3.60\times10^{-6}$, ANOVA test), whilst a decrease approximately twice as large in the corresponding depolarised spectra was apparent in at both hydrations ($p_{100}=0.0009$; $p_{H2O}=6.85\times10^{-6}$, ANOVA test). No changes were observed in this region in the dehydrated fibres; however, the polarised spectra of the apex region exhibited decreases for the 42 and 82% RH fibres ($p_{42}=0.0042$; $p_{82}=0.0037$, ANOVA test), with no significant changes at higher hydrations. The peak showed no strain dependence in the depolarised spectra of the apex region at any hydration. Intensity increases in the 1099 cm^{-1} peak were observed in the
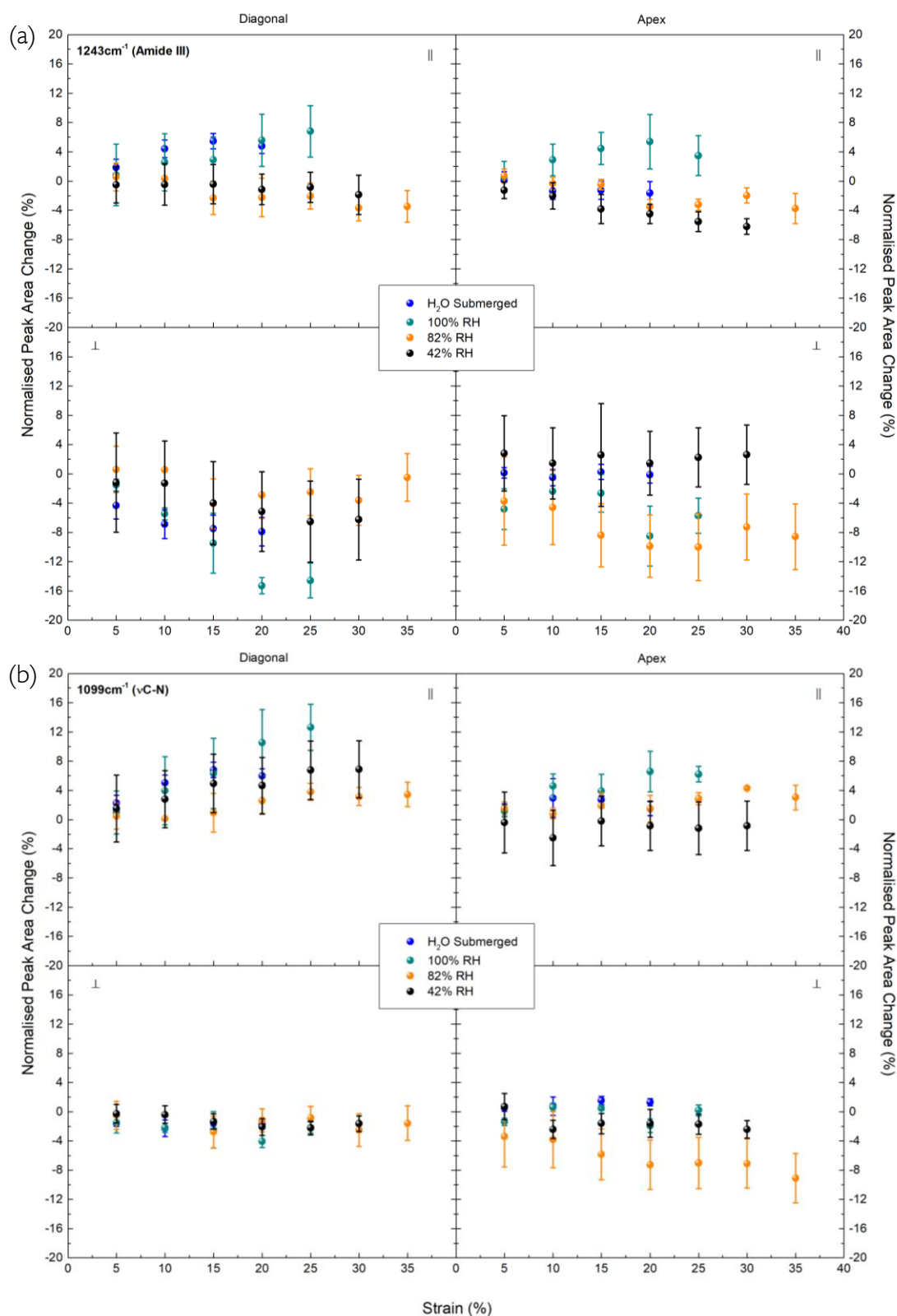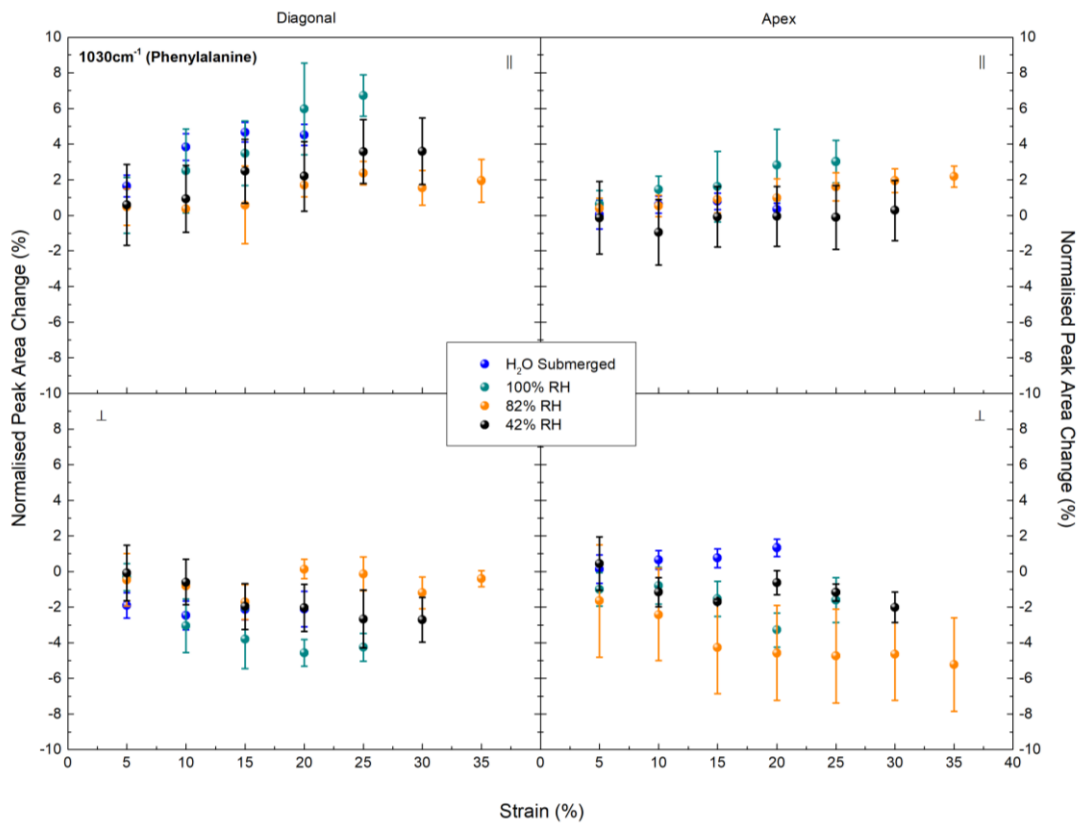
Figure 5.7: plots of the percentage change with increasing uniaxial tensile strain in the area of peaks associated with C-N bond stretching in the protein backbone; (a) 1243 cm⁻¹ and (b) 1099 cm⁻¹ of the polarised (‖) and depolarised (⊥) spectra of collagen fibres from rat tail tendon at a range of hydrations. Spectral changes are tracked in the diagonal (left) and apex (right) sections of the macroscopic fibre crimp as it opens under the applied strain. Data points are presented as an average of at least two analysed spectra, normalised to the mean area of the CH_2 band (1435-1500 cm⁻¹) ± uncertainty from error propagation.

polarised spectra from the diagonal region, though only the 100% RH and water submerged fibres were statistically significant (p_{100}=0.0481; p_{H2O}=2.29x10^{-7}, ANOVA test); no corresponding decrease occurred in the depolarised band. No clear pattern of changes was established between the intensity of the 1099 cm^{-1} peak and strain in either the polarised or depolarised spectra of the apex region. The diagonal and apex spectra of both peaks were similar at the point of full crimp opening across the hydration range.

5.2.1.3. Phenylalanine band

The band centred at 1030 cm^{-1} is attributed to the side-chain of the amino acid phenylalanine (Phe) [202], and manifested in the polarised spectra as a sharp peak, whilst in the depolarised spectrum it presented only as a small shoulder (figs. 5.3b, A.1b, A.4b & A.7b). Figure 5.8 shows the percentage change in the peak area for the polarised and depolarised spectra, as a
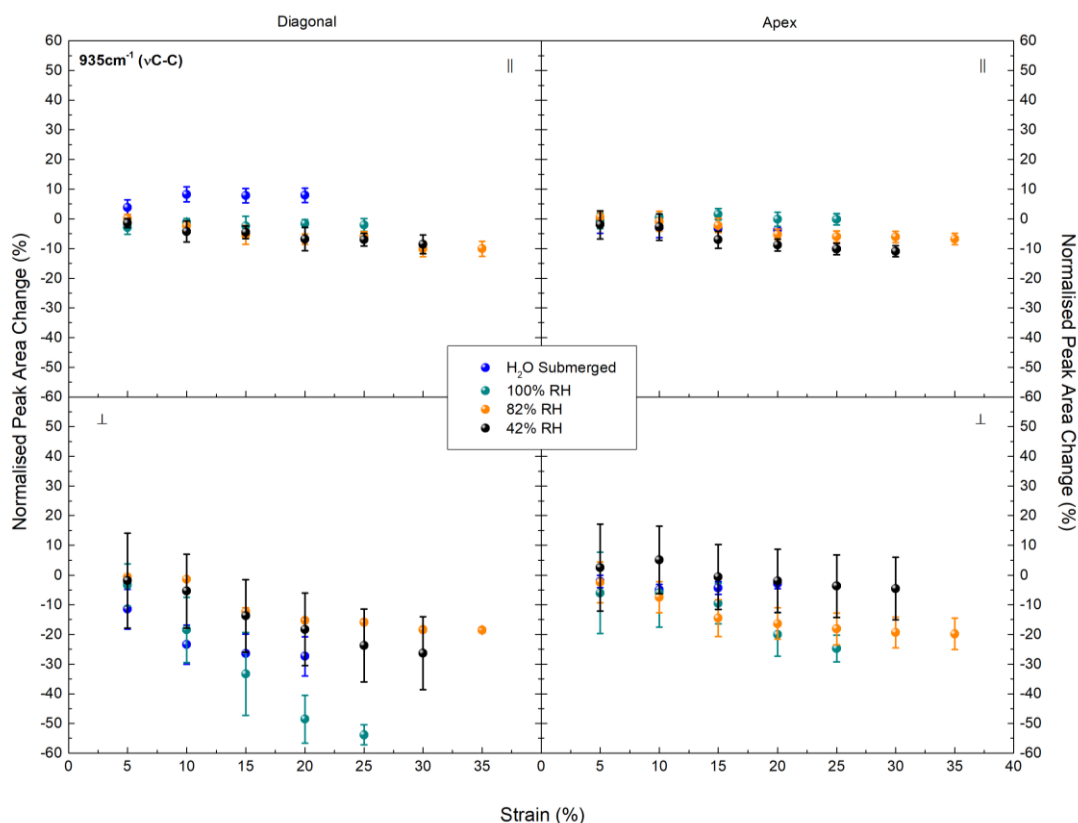

Figure 5.8: plots of the percentage change with increasing uniaxial tensile strain in the area of the peak at 1030 cm^{-1} associated with phenylalanine, in the polarised ($\parallel$) and depolarised ($\perp$) spectra of collagen fibres from rat tail tendon at a range of hydrations. Spectral changes are tracked in the diagonal (left) and apex (right) sections of the macroscopic fibre crimp as it opens under the applied strain. Data points are presented as an average of at least two analysed spectra, normalised to the mean area of the CH$_2$ band (1435-1500 cm^{-1}) $\pm$ uncertainty from error propagation.

function of strain at all four hydrations in the diagonal and apex regions of the fibre crimp. Significant changes were confined to the diagonal region, with corresponding increases and decreases in the polarised and depolarised spectra, respectively, of the 42% RH, 100% RH, and water submerged fibres (polarised: p_{42}=0.0442; p_{100}=0.0324; p_{H2O}=3.33x10^{-7}, depolarised: p_{42}=0.0084; p_{100}=0.0066; p_{H2O}=0.002, ANOVA test). The magnitude of change was lower in the dehydrated fibre. In all polarisations and crimp regions, there was considerable uncertainty attached to the area of the 1030 cm^{-1} peak at 82% RH and a relationship between strain and intensity could not be determined. When the crimp was fully opened, the diagonal and apex spectra at all hydrations were similar to one another.

5.2.1.4.   C–C stretching band

There was a consistent pattern of changes in the peaks at 813, 855, 874, 920 and 935 cm^{-1}, which are all associated with stretching of the C–C bonds in the peptide main chain and the proline ring [202]. They presented as sharp peaks in both the polarised and depolarised spectra, but had a higher intensity in the former (figs. 5.4a, A.2, A.5 & A.8). Percentage changes in peak area with hydration and strain were similar for all five peaks, and figure 5.9 shows representative results for 935 cm^{-1} as a function of strain at all four hydrations. The most consistent changes were observed in the peaks of the depolarised spectra, with marked decreases in the diagonal region; these were of a greater magnitude in the fully hydrated fibres than the dehydrated (p_{42}=0.0167; p_{82}=8.273x10^{-8}; p_{100}=0.0024; p_{H2O}=1.32x10^{-7}, ANOVA test). Decreases at the apex occurred only at 82% RH (p_{82}=0.0004, ANOVA test); with approximately the same magnitude as its diagonal counterpart. Changes in the polarised spectra from both regions were only minor in comparison to those exhibited in the depolarised spectra, but displayed a decrease in peak area of the 82% RH fibre in the diagonal region (p_{82}=0.0026, ANOVA test) and both the 42 and 82% RH fibres in the apex region (p_{42}=0.0165; p_{82}=0.0029, ANOVA test). There was no change in the polarised spectra of the 100% RH fibres and an inconsistent pattern for the water submerged fibres, with an increase in peak area in the diagonal region (p_{100}=2.89x10^{-5}, ANOVA test) and no change at the apex. In all cases, the spectra in the respective regions became similar upon full opening of the crimp.
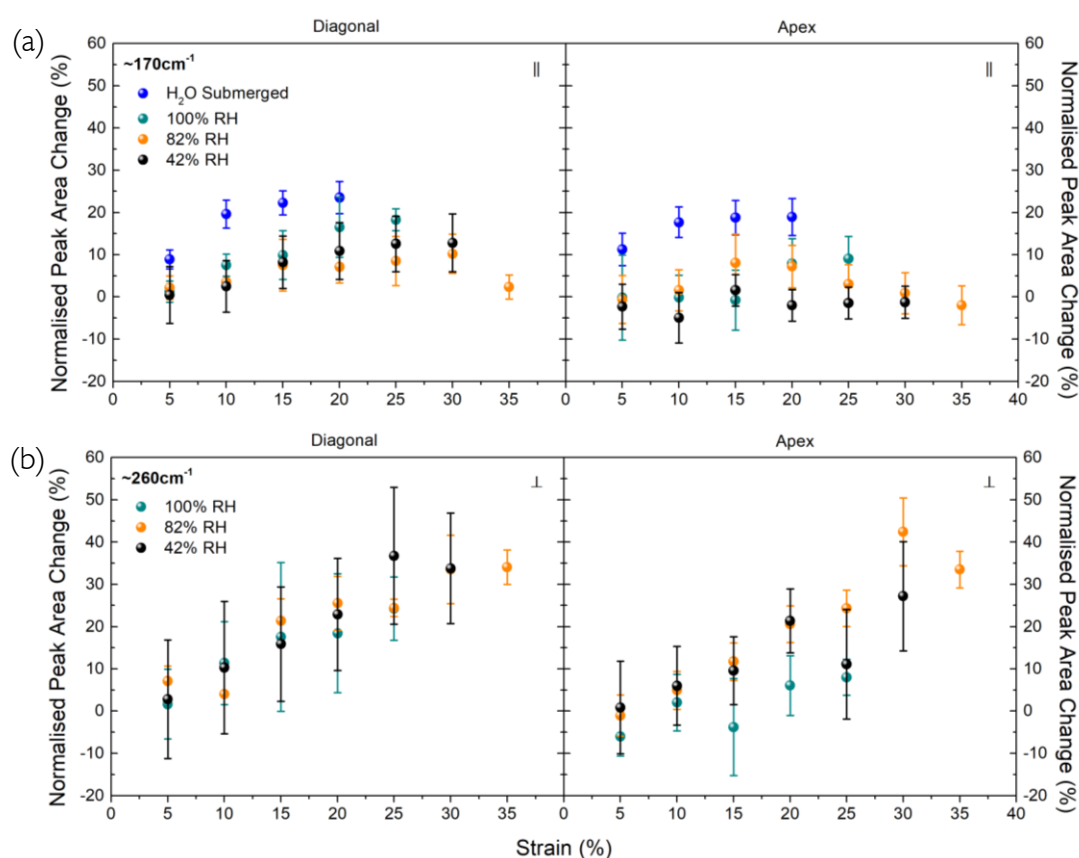
Figure 5.9: plots of the percentage change with increasing uniaxial tensile strain in the area of the peak at 935 cm^{-1}, associated with C-C bond stretching in the protein backbone of the polarised (‖) and depolarised (⊥) spectra of collagen fibres from rat tail tendon at a range of hydrations. Spectral changes are tracked in the diagonal (left) and apex (right) sections of the macroscopic fibre crimp as it opens under the applied strain. Data points are presented as an average of at least two analysed spectra, normalised to the mean area of the CH$_2$ band (1435-1500 cm^{-1}) ± uncertainty from error propagation.

5.2.1.5.   Low-Wavenumber Region

The spectral region below 650 cm^{-1} (fig. 5.4b, A.2, A.5 & A.8) is affected by the tail of the laser line – the elastic peak at zero Raman shift – and so required a baseline subtraction to assess the peaks therein (see §2.3.4). The polarisation resolved micro-Raman spectrum of type-I collagen has, to my knowledge, never been previously observed in this low-wavenumber region, and so the peak attributions will be discussed later. Figure 5.10a, 5.10b and 5.11 respectively show the percentage change in the area of the band centred at ~170 cm^{-1}, the band between 184-280 cm^{-1} (maximum at ~260 cm^{-1}) and the peak centred at ~570 cm^{-1} as a function of strain at all four hydrations – the apparent changes in the peak centred around 530 cm^{-1} were due to the changes in the neighbouring 570 cm^{-1} peak. The first of these bands (170 cm^{-1}) was visible only in the polarised spectra with the exception of the water submerged fibres, where the depolarised spectra also showed a small band, although independent of
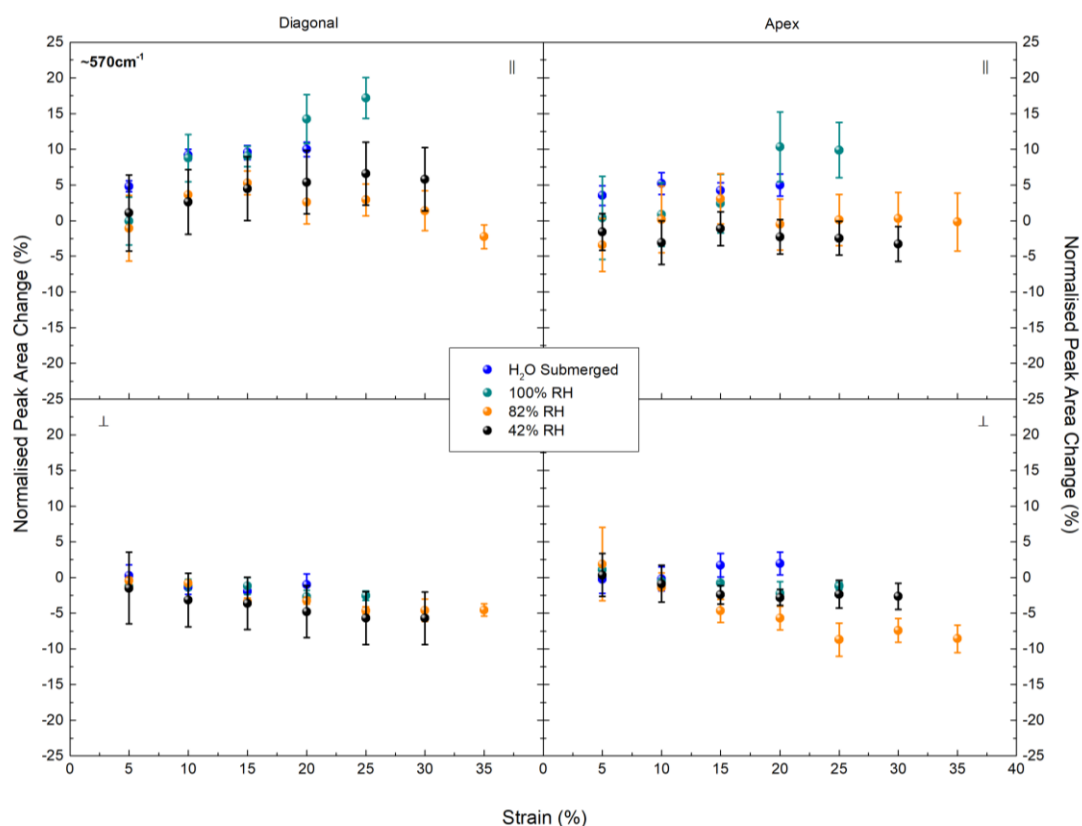
strain. The area of the polarised peak increased markedly with strain in the diagonal region at all hydrations except 82% RH (p_{42}=0.0126; p_{100}=0.0099; p_{H2O}=3.09x10^{-10}, ANOVA test), and showed no significant change at the apex of the crimp except in the water submerged fibre (p_{H2O}=6.55x10^{-9}, ANOVA test) where an increase similar to the diagonal region was observed. The broad band centred around 260 cm^{-1} was observed at all fibre hydrations except in the water submerged state and was most prominent in the depolarised spectra; it contributed to the shoulder of the larger peak at 300 cm^{-1} of the polarised spectra, but strain dependent changes were only evident in the depolarised spectra. Here, similar increases in the band areas were observed at 42 and 82% RH; the former in the diagonal region only (p_{42}=0.0113, ANOVA test), and the latter in both the diagonal and apex regions of the crimp (diagonal: p_{82}=0.001, apex: p_{82}=7.16x10^{-6} ANOVA test) (fig. 5.10b). No significant change was observed at 100% RH. The peak centred around 570 cm^{-1} was visible in both the polarised and depolarised spectra, although more strongly in the former. Significant intensity

Figure 5.10: plots of the percentage change with increasing uniaxial tensile strain in the area of the LWN Raman spectral bands centred at (a) ~170 cm^{-1} and (b) ~260 cm^{-1} for collagen fibres from rat tail tendon in the polarised (∥) and depolarised (⊥) spectra respectively, at a range of hydrations. Spectral changes are tracked in the diagonal (left) and apex (right) sections of the macroscopic fibre crimp as it opens under the applied strain. Data points are presented as an average of at least two analysed spectra, normalised to the mean area of the CH$_2$ band (1435-1500 cm^{-1}) ± uncertainty from error propagation.

increases were observed only in the peak of the polarised spectra in the diagonal region of the highly hydrated fibres (p_{100}=0.0018; p_{H2O}=1.63x10^{-11}, ANOVA test), with the exception of the water submerged fibre, where a small increase was also observed in the polarised spectra of the apex region (p_{H2O}=1.75x10^{-5}, ANOVA test) (fig. 5.11). The magnitude of the peak changes was larger in the fully hydrated fibres than in the dehydrated ones. At all hydrations, when the crimp was fully opened, the spectra in the low-wavenumber region of the diagonal and apex became the same.
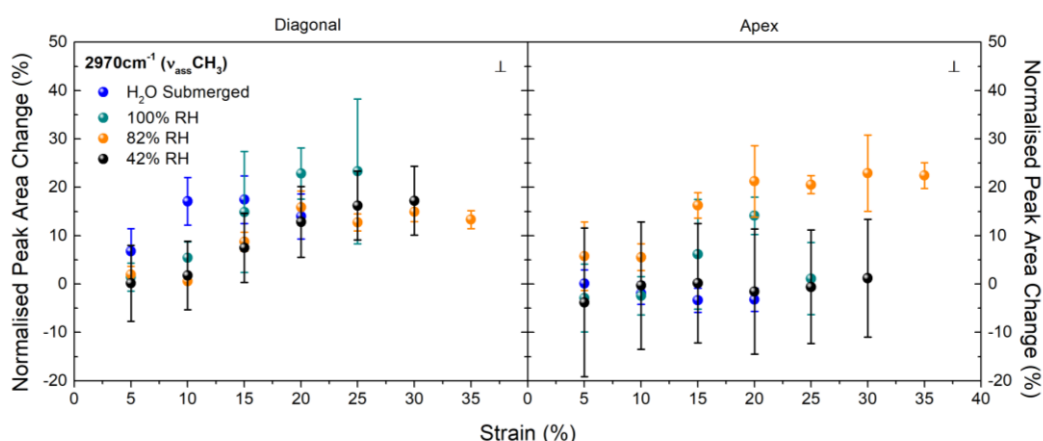

Figure 5.11: plots of the percentage change with increasing uniaxial tensile strain in the area of the band centred at ~570 cm^{-1}, attributed to amide VI in the protein backbone of the polarised (‖) and depolarised (⊥) spectra of collagen fibres from rat tail tendon at a range of hydrations. Spectral changes are tracked in the diagonal (left) and apex (right) sections of the macroscopic fibre crimp as it opens under the applied strain. Data points are presented as an average of at least two analysed spectra, normalised to the mean area of the CH$_2$ band (1435-1500 cm^{-1}) ± uncertainty from error propagation.

5.2.1.6.   High-Wavenumber Region

Figure 5.12 shows the percentage change in the area of the depolarised peak at 2970 cm^{-1}, in the diagonal and apex region of the fibre crimp as a function of strain at all four hydrations. This

peak is associated with the asymmetric stretching of the methyl group (CH_3) [202] and was visible as a strain-independent shoulder of the CH stretching band in the polarised spectra, but presented a distinctive peak in the depolarised band that significantly increased upon the application of strain (figs. 5.5, A 3, A 6 & A 9) at 42% RH, 82% RH and in the water submerged state ($p_{42}=0.0028$; $p_{82}=6.11 \times 10^{-6}$; $p_{H2O}=9.37 \times 10^{-6}$, ANOVA test). This change was similar, for each of these hydrations in the diagonal region, but there was no significant change at the apex. When fully opened, the spectra from the two regions of the crimp were similar.

Strain dependent changes in the 3100-3800 cm^{-1} band, which is mainly associated with the O–H stretching of water [75], were observed only in the water submerged fibre (fig. 5.5), where an increase of 36 ($\pm$ 4)% in the diagonal region and 21 ($\pm$ 6)% in the apex region, marked the spectral change from the unstrained to the fully opened crimp. This band showed no strain dependence at the lower hydrations (figs. A 3, A 6 & A 9).


Figure 5.12: plots of the percentage change with increasing uniaxial tensile strain in the area of the band centred around 2970 cm^{-1} (v_{ass} CH_3) of the depolarised ($\perp$) spectra of collagen fibres from rat tail tendon at a range of hydrations. Spectral changes are tracked in the diagonal (left) and apex (right) sections of the macroscopic fibre crimp as it opens under the applied strain. Data points are presented as an average of at least two analysed spectra, normalised to the mean area of the CH-band (2815-2940 cm^{-1}) $\pm$ uncertainty from error propagation.

5.2.2.   Elastin Fibres from Bovine Nuchal Ligament

The strain dependent changes in the Raman spectra of elastin from bovine nuchal ligament, were observed under the same controlled hydration conditions as the collagen fibres above. The highly hydrated fibres were capable of extending recoverably in excess of 80% their rest lengths (maximum possible strain for the uniaxial testing stage), whilst the brittle, air-dried fibres

broke repeatedly at around 12% strain. Figure 5.13 presents micrographs of a representative elastin fibre bundle in the fully hydrated state, under increasing uniaxial tensile strain during the micro-Raman experiments. Strain was applied axially in 10% increments and, at all stages, the individual fibres remained aligned approximately parallel to one another along the axis of the bundle. The stretch is clearly visible in each successive frame, and is accompanied by a radial constriction of the fibre. Raman spectra were acquired as an average of points (n≥3) in two distinct groups, with a line scan running radially to the axis of the bundle over approximately four individual elastin fibres, and a separate scan along the axis of a single fibre. At each strain, irrespective of hydration, the mean spectra from these two groups were found to be identical to one another. Moreover, no spectral changes were observed as a result of the increased
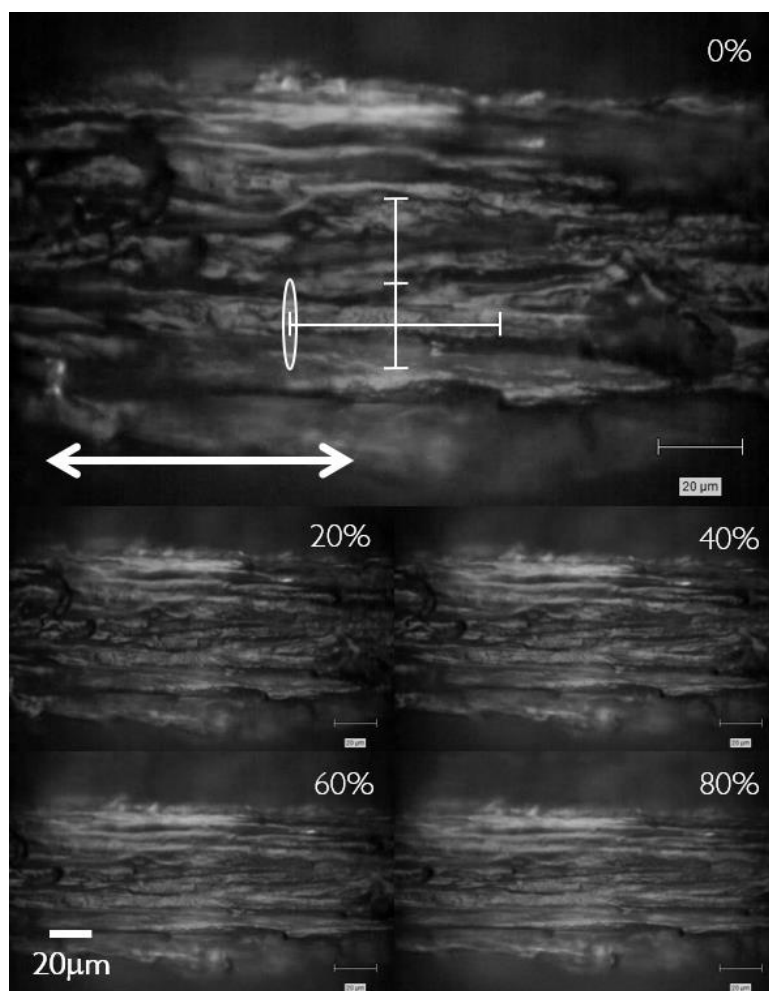
Figure 5.13: micrographs showing a 100% RH elastin fibre bundle under increasing uniaxial tensile strain (0-80% in 20% steps). Individual fibres are aligned approximately parallel to one another running horizontally left to right, along the axis of the fibre bundle (denoted by the arrow). Raman spectra were acquired over multiple spots (shown by the white crosshair) in two lines: *vertically* – scanning over approx. four individual elastin fibres (each ~5 μm diameter) and *horizontally* – acquiring spectra from a single fibre, at each stage of strain application. ROI lies along the axis at the centre of the suspended fibre bundle. The oval represents the size of the laser line.

strain, as evidenced in figure [5.14](#) and [5.15](#), which show the mean polarised and depolarised Raman spectra from the horizontal scan of the water submerged fibres at incremental strains.
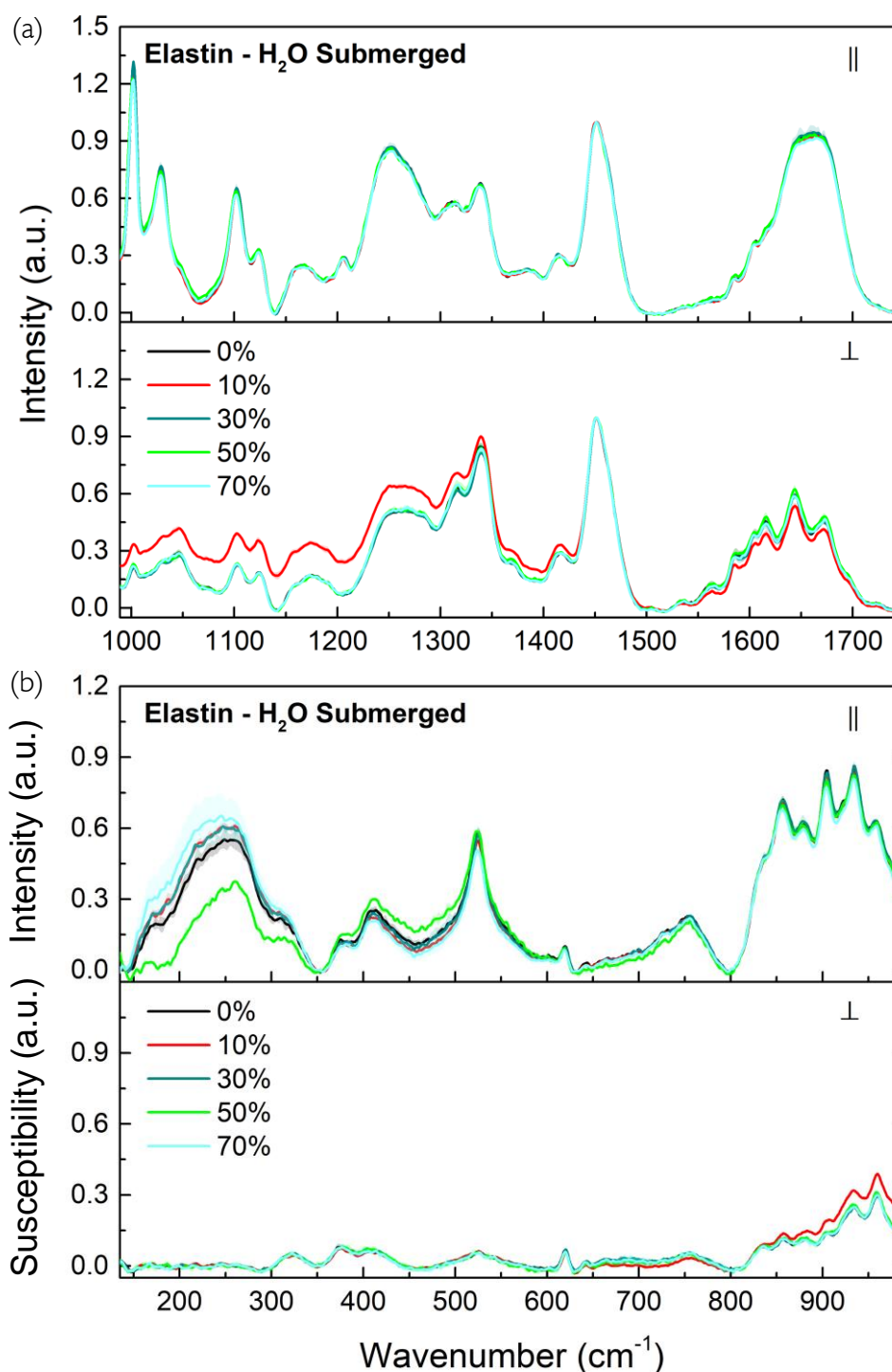
Figure 5.14: Mean polarised (∥) and susceptibility corrected depolarised (⊥) Raman spectra comparing the (a) 989-1750 cm^{-1} and (b) 135-989 cm^{-1} spectral regions of elastin fibres from bovine nuchal ligament submerged in distilled water, at a range of uniaxial tensile strains. Each spectrum is an average of at least two points, baselined and normalised to the intensity of the CH_2 peak (1451 cm^{-1}). Shading denotes the standard deviation. LWN depolarised spectra are plotted as susceptibility form.
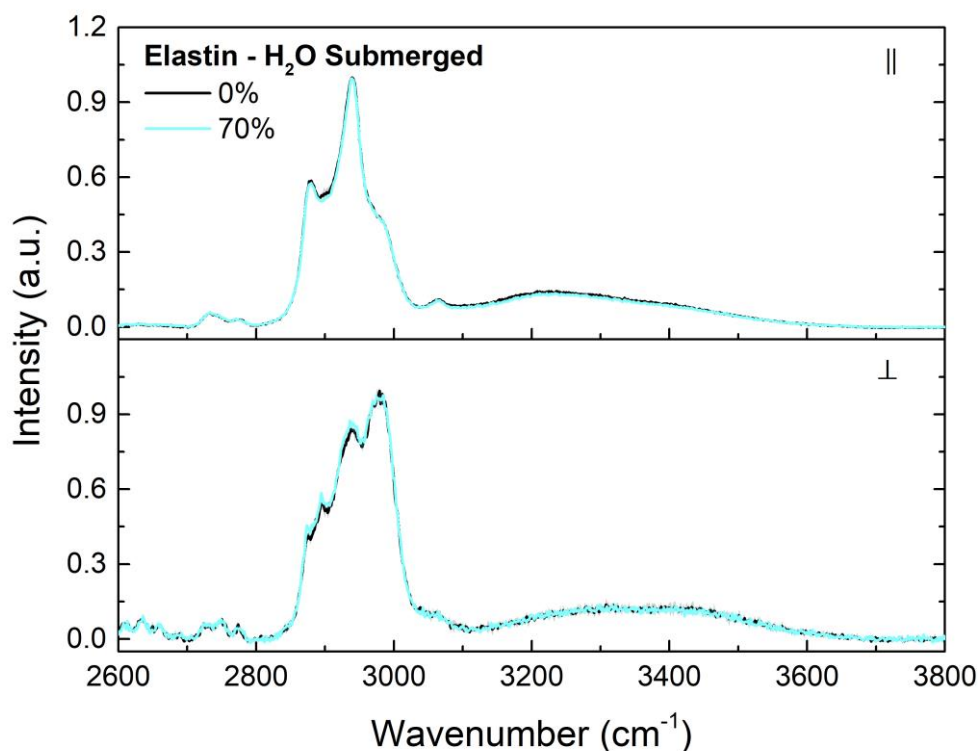
Figure 5.15: Mean polarised (∥) and susceptibility corrected depolarised (⊥) Raman spectra showing the HWN region of elastin fibres from bovine nuchal ligament submerged in distilled water at minimum and maximum uniaxial tensile strains. Each spectrum is an average of at least two points, baselined and normalised to the intensity of the CH-band (2800-3040 cm^{-1}). Shading denotes the standard deviation.

Figures showing the strain independence of the spectra for the remaining hydrations may be found in the appendix (42% RH – figs. A.10-A.11; 100% RH – figs. A.12-A.13). As with the collagen fibres above, the broad band between 3100-3800 cm^{-1}, reflecting the amount of water in at each focal point, was found to be highly location dependent in the water submerged samples. The mean spectra presented in figure 5.14 and 5.15 are averaged from the points with the most comparable water content. No such variation was present at the other hydrations.

5.3. Hydration Dependence of the Polarised Micro-Raman Spectra

Figure 5.16 shows the amide I band from the polarised spectra of both collagen and elastin fibres between 42 and 100% RH and in their water submerged state. Due to their strain

independence, elastin spectra are presented in these figures as an average over all strains at a given hydration, whilst collagen is represented by spectra from the apex region at the full crimp-removal strain. In both cases, the fibrillar and individual fibre components are aligned parallel to the macroscopic fibre axis, so that direct structural comparisons can be made. Both protein fibres exhibited hydration dependence in the amide I band. The dehydration of collagen resulted in a gradual reduction in intensity of the amide I band below the water submerged state with a significant decrease of approximately 6 ($\pm$ 2)% and 12 ($\pm$ 3)% at 82 and 42% RH, respectively (p=0.0007, ANOVA test). Conversely, elastin showed a significant increase in band area of up to 10 ($\pm$ 2)% from the water submerged state to the 'dry' state at 42% RH (p=5.76x10^{-5}, ANOVA test). Moreover, there were clear band shape changes associated with the removal of water in the amide I of elastin, whereas the band shape of collagen did not change.
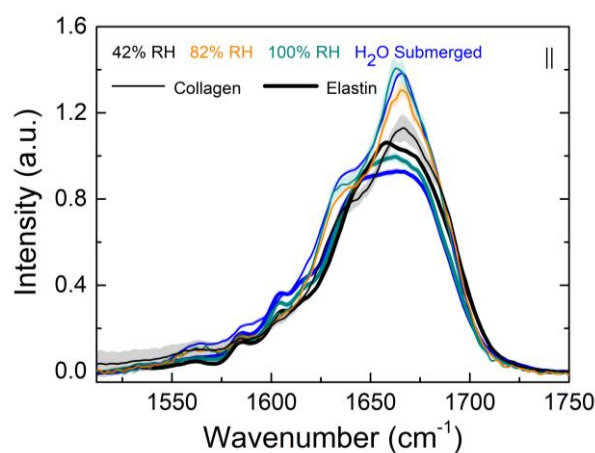
Figure 5.16: Mean polarised ($\parallel$) Raman spectra comparing the hydration dependence of the amide I band of collagen (n$\geq$2) and elastin fibres (n$\geq$15) between 42-100% RH and in the water submerged state. Spectra are baselined and normalised to the intensity of the CH$_2$ peak (1451 cm^{-1}). Shading denotes the standard deviation.

Hydration dependent changes were also observed in the low-wavenumber region of both protein fibres as shown in figure 5.17. In collagen, the band centred at approximately 170 cm^{-1} and the peak at around 570 cm^{-1} in the polarised spectra, both decreased gradually in intensity with dehydration; the former (not present in the depolarised spectra) was significant at and below 82% RH (p=8.95x10^{-8}, ANOVA test) reaching a low of 64 ($\pm$ 3)% the water submerged band area in the 'dry' state at 42% RH, and the latter, also significant at and below 82% RH (p=0.0001, ANOVA test) by 32 ($\pm$ 3)% to the 'dry' state. No clear pattern of change was established in the depolarised peak at 570 cm^{-1}. A broad band centred at around

260 cm^{-1} was observed in the depolarised spectra of both collagen and elastin at hydrations between 42 and 100% RH. The band was not present in the water submerged spectra of either fibre. Dehydration from 100% RH was associated with a significant (p=0.035, ANOVA test) increase in band area of 82 ($\pm$ 30)% in the 42% RH collagen fibres, whilst elastin showed around a 34 ($\pm$ 17)% increase to the same 'dry' state. This was the only hydration-dependent peak in the low-wavenumber region of the elastin spectra; however, this band was also present in the polarised spectra (unlike in collagen) and was the dominant feature of this spectral region. Although the intensity was variable point-to-point in the highly hydrated fibres, a significant (p=4.44x10^{-10}, ANOVA test) gradual increase in band area by approximately 25 and 50% was observed with dehydration to the 100 and 42% RH states, respectively.
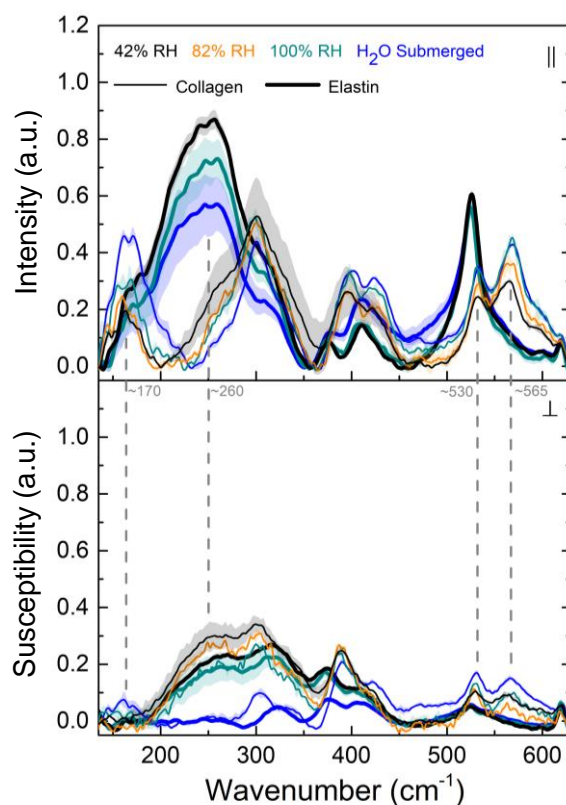
Figure 5.17: Mean polarised (||) and susceptibility corrected depolarised (⊥) Raman spectra comparing the hydration dependence of the LWN region (135-630 cm^{-1}) of collagen (n≥2) and elastin fibres (n≥15) between 42-100% RH and in the water submerged state. Spectra are baselined and normalised to the intensity of the CH$_2$ peak (1451 cm^{-1}). Shading denotes the standard deviation. Key peaks are highlighted between the polarised (||) and depolarised spectra (⊥). Depolarised spectra are plotted as susceptibility form.

In the high-wavenumber region, the broad band associated with water (3100-3800 cm^{-1}) exhibited similar changes during dehydration of both protein fibres. Figure 5.18 shows that a

marked reduction in the band area of between 70-80%, occurred in the polarised and depolarised spectra between the water submerged fibres and those suspended at 100% RH. Further dehydration led to smaller gradual reductions such that at 42% RH the band was between 85-90% its initial intensity.
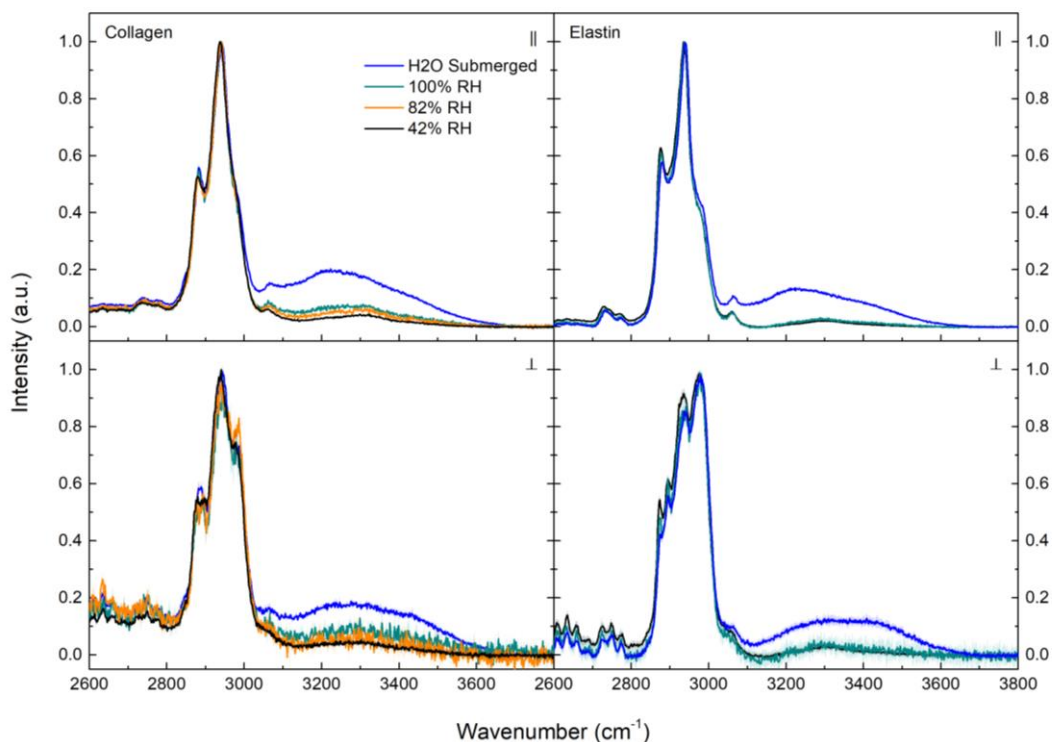

Figure 5.18: Mean polarised (∥) and susceptibility corrected depolarised (⊥) Raman spectra comparing the hydration dependence of the HWN region (2600-3800 cm^{-1}) of *left:* collagen (n≥2) and *right:* elastin fibres (n≥15) between 42-100% RH and in the water submerged state. Spectra are normalised to the intensity of the CH-band (2800-3040 cm^{-1}). Shading denotes the standard deviation.

5.4.　Discussion

The micro-Raman spectra presented above are consistent with the literature on type-I collagen from rat tail tendon [75, 203] and elastin from bovine nuchal ligament [106], and all the major peaks are reliably reproduced here. However, this is to my knowledge the first report of the low-wavenumber region for these protein fibres, so peak attributions are discussed in light of changes with hydration and strain.

For type-I collagen, polarisation sensitivity of the Raman spectra has previously been reported in the amide I (C=O), amide III (mixture of C–N stretching, N–H bonding and CH_2 wagging) and C–C stretching bands (800-1000 cm^{-1}) [204, 205]. I also observe a strain dependence in these peaks, although my results suggest that the changes observed in the amide III band are associated mainly with the peak at 1243 cm^{-1} rather than at 1271 cm^{-1} as was previously suggested. In addition, I also observe previously unremarked changes with strain in the peak at 1099 cm^{-1}, attributed to the C–N stretching, and in the phenylalanine peak at 1030 cm^{-1}. The polarisation sensitivity of the 2970 cm^{-1} peak associated with the methyl C–H stretching, was also observed here for the first time.

The notation used in this work of 'polarised' and 'depolarised' spectra, describes the plane of the electric field of the scattered light with respect to that of the incident laser; thus the *polarised* spectrum refers to scattered light in a plane parallel to the laser polarisation, and *depolarised* spectrum to scattered light in a plane orthogonal to the laser polarisation. The axis of the fibre suspended in the humidity chamber is orthogonal to the plane of polarisation of the laser. Therefore, an increase in the intensity of bands in the polarised spectra and or a decrease in the depolarised, would reflect a reorientation of the relevant mode's coordinate radially to the fibre, and vice versa, a decrease in the polarised and increase in the depolarised spectra, correspond to a reorientation towards the fibre axis. At all hydrations upon application of strain, the white light images of the collagen fibre crimps show that the primary straightening of the fibrils occurs within the diagonal region, whilst the apex remains essentially unchanged. This is reflected in the amide I band of the polarised spectra, where an increase in band intensity with increasing strain is observed predominantly in the diagonal region, consistent with the C=O bond becoming increasingly radially aligned (orthogonal to the fibre axis) in this area. Any variations in the spectra from the apex region are small, as they reflect the essentially unchanged orientation of the fibrils relative to the axis during the tensile testing. The straightening of the fibrils is further indicated by the similarity between spectra from the diagonal and apex regions upon the full removal of the crimp, indicating a complete alignment of the fibrils along the fibre axis. This is consistent with a previous work that utilised the amide I band to map fibrillar orientation within a collagen crimp [68, 206]; made possible due to the preferential orientation of the carbonyl bond, which is uniquely aligned orthogonal to the backbone of the repeating Gly-X-Y unit of the collagen triple helix, and thus is perpendicular to the fibril axis.

The magnitude of the changes in the amide I band appears to be smaller in the lower RH fibres (42 and 82% RH). This is plausibly attributed to differences in the frequency of the sinusoidal crimp and consequently the crimp angle – the initial angle-to-fibre axis of the collagen fibrils within the diagonal region – which was not controlled between fibres and hydrations in these experiments, but now raises an important concern about how water affects the periodicity of the crimp in collagen. Given the smaller magnitude of the change in band area, the data suggests that the dehydrated fibre has a lower crimp frequency i.e. that the diagonal fibrillar component is initially aligned closer to the fibre axis than in the hydrated fibres. Collagen fibres are known to shrink when dehydrated, producing remarkable passive contractile forces in the process [69]. If held at a fixed length (as during the RH equilibration in this experiment), the build-up of uniaxial tensile forces could reduce the angle-to-fibre axis. Data on crimp frequency, angle and crimp-removal-strain, together with an assessment of the scale of macroscopic fibre shrinkage – all as a function of hydration – are lacking in the literature, and should be explored as an extension to my work here. However, given that the crimp opens fully at all hydrations, my results suggest that water does not play a functional role in the opening of the crimp, though it may be instrumental in determining the crimp angle and frequency and thus may be a functional part of fibre relaxation (see below).

Due to its unique alignment orthogonal to the triple helical axis, the carbonyl bond is useful for determining fibrillar alignment within the microscopic crimp. The other polarisation sensitive peaks in the fingerprint region are more complex, as they either constitute a combination of vibrational modes, or have multiple incidences in different planes within the triple helical structure, making it difficult to isolate the specific contribution of any one particular bond. The C–N bond lies along the main chain of the peptide backbone, present in both glycine (Gly) and proline (Pro) residues of the Gly-X-Y repeating unit, though due to the pitch of the triple helix, this stretching vibration is oriented at various angles along the axis of the monomer. Comparing the intensity of the polarised and depolarised peaks at 1099 cm^{-1}, the data suggest the C–N bond is more closely aligned perpendicular to the fibril axis, and indeed as the crimp opens, the polarised peak increases in intensity exclusively in the diagonal region at all hydrations. With no clear change at the apex, this bond appears to maintain a constant orientation with respect to the fibril, suggesting similarly to the carbonyl bond, that its conformation within the triple helix is unaltered by macroscopic strain.

The amide III band of the highly hydrated fibres (100% RH and water submerged) behaved similarly to the amide I band, with intensity changes confined to the diagonal region of the crimp, consistent with the vibrational mode being radially aligned within the fibril, in agreement with Janko et al [204]. However, the amide III response was markedly different in the dehydrated fibres (42 and 82% RH). Here no change was evident within the diagonal region, but the band in the polarised spectra decreased in intensity at the apex of the crimp, consistent with a reorientation of the vibrational mode towards the fibrillar axis. This is interesting given that the fibrils in the apex remain essentially parallel to the axis of the fibre, and therefore implies that the triple helix is undergoing some structural reconfiguration with increasing macroscopic strain. This may explain the absence of a peak intensity change in the diagonal region at these hydrations, i.e. if the reorientation of the bond within the collagen monomer occurs throughout the length of a fibril it could plausibly cancel out its relative rotation with respect to the fibril in the straightening section. Thus the data suggest that dehydration results in a strain induced reorientation of the amide III mode within the triple helix, which otherwise maintains a fixed angle with respect to the fibril in the presence of higher levels of water.

The reduction in depolarised band intensity of the C–C bond vibration (800-1000 cm^{-1}) in the diagonal region, is the most prominent spectral change caused by the application of macroscopic strain at all hydrations. However, smaller reductions were also observed in the polarised spectra of the dehydrated fibres in this region. These changes are opposite to one another, as the reduction in the depolarised intensity reflects a strong reorientation of the bond vibration *away* from the fibre axis, whilst the polarised decrease suggests a smaller reorientation *towards* the axis. Moreover, decreases similar to those observed in the diagonal region were seen at the apex of the dehydrated fibres. This likely reflects the multiple conformations of the C–C bond along the peptide main chain in the Gly residues and in the pyrrolidine rings of the Pro and hydroxyproline (Hyp) residues, indicating how challenging it is to attribute these changes to specific structural motifs. Given the magnitude of the change in the depolarised spectra of the diagonal region, it seems likely that the primary orientation of the C–C stretching vibrations is in a plane orthogonal to the fibrillar axis, and that the predominant spectral change results simply from the straightening of the fibrils in the crimp. However, as with the amide III band, the changes in the apex region of the dehydrated fibres possibly reflect subtle, strain induced structural changes within the triple helix, associated with the reduction in water content.

The triple helix is stabilised by maximising the number of hydrogen bonds (H-bonds) between the three α-chains. Direct interchain H-bonding is achieved principally through the strong H-bond between the carboxyl oxygen of the residue in the X-position in one chain (usually Pro), and the hydrogen of the Gly amide bond of the neighbouring peptide chain. A further two 'improper' direct H-bonds are formed between: 1) the two hydrogens of a Gly residue in one chain and the carboxyl oxygen of a Gly residue in the neighbouring chain; and 2) the hydrogen in the Y-position of one chain and the carboxyl oxygen of the residue at the X-position (Pro) of the neighbouring chain. A mediating system of helical 'water bridges' also provides a system of H-bonding options, though the precise constitution of these bridges is highly chain dependent [207, 208] and can consist of multiple water molecules [3, 10, 209, 210].

The low-wavenumber spectrum of collagen contains a band centred at around 170 cm^{-1}, which has previously been associated with the stretching mode of intermolecular H-bonding of water (O···H) [211]. The band is highly directional, being present only in the polarised spectra of the fibres in both the diagonal and apex regions of the microscopic crimp, experiencing an increase in the former as the crimp opens (no change at apex), suggesting it is aligned exclusively orthogonal to the fibrillar axis. This is consistent with the H-bonds that constitute the water bridges found both within the collagen triple helix (inter-chain bonds – introduced above) and in those separating individual tropocollagen monomers (inter-protein bonds). The band intensity decreases markedly with dehydration, suggesting that the number of water bridges reduces as the ambient humidity drops. Two-thirds of this reduction occurs between the water submerged and 100% RH states, and overall the peak reduces by around 65% to the 'dry' state at 42% RH. However, the band is not totally extinguished, suggesting that even at low-RH, water bridges are still present, whilst bulk water has been almost entirely removed – indicated by a 90% reduction in the broad OH band in the high-wavenumber region, of which the largest drop also occurs when the fibre is removed from aqueous medium. An absence of hydration dependence in the hydrophobic side-chains (phenylalanine and the methyl group – see below), suggests that bound water inside the triple helix remains unchanged by desiccation to 42% RH; therefore, it seems likely that the changes observed here in the 170 cm^{-1} band are associated primarily with water bridges of the inter-protein phase.

There are conflicting discussions in the literature regarding how individual collagen monomers associate laterally with one another. One work concludes that interaction is predominantly through direct bonding of side-chain molecules in the overlap region of the D-period, with a

smaller percentage of water bridges linking opposing triple helices [212]; but most works conclude that interaction is mediated by the water bridges alone [10, 182, 213]. My data suggests that the number of water-mediated H-bonds between the tropocollagen monomers decreases when the RH decreases. This condenses the space between adjacent triple helices [214] (increased packing – as demonstrated by the increased peak intensity in the BLS spectra of the dried fibres §4.3), and is likely the primary cause of the reduced fibril diameter reported in the literature [69, 71]. In fact, the reduced separation between triple helices, makes the shorter range, direct backbone-backbone H-bonds between charged groups in neighbouring peptide trimers, more likely [215]. Such bonds are plausibly stronger or more numerous than the water-mediated interactions [216-218] and would correspond well with the increased stiffness that I observe in the BLS data in chapter 4, and indeed the biphasic increase in hypersonic velocity observed in the dehydrating fibre by Cusack and Lees [170]. This also well explains the reduction in monomer sliding predicted by Gautieri et al [73], showing the potential for the transfer of strain to the triple helix in the dehydrated state.

The broad band centred at around 260 cm^{-1} in the depolarised spectrum, lies in a spectral region associated with backbone torsions and the deformation of helical structures [219-222]; it is not present in the water submerged spectra, but grows gradually with dehydration. I postulate that the presence of bulk water increases the mobility of the H-bonded water bridges in the hydration water surrounding the triple helix, and in-turn, promotes a higher conformational freedom in the protein itself. Indeed, it has been suggested that the local conformation of the triple helix is more flexible in the presence of water [223]. The data suggest that torsional motions of the collagen backbone are thus unconstrained whilst the fibre is submerged in solute, and the vibration has no global directionality and hence no band at 260 cm^{-1}. Dehydration promotes an increase in torsional rigidity – as previously indicated in the literature [170, 217] – and the band increases as the plane of vibration becomes increasingly defined in the radial direction, throughout the fibrils. This likely explains the increase in the 170 cm^{-1} band at the apex, uniquely exhibited by the water submerged fibres during straightening of the crimp. Given that the fibrils remain aligned essentially parallel to the fibre axis in this region, the increase suggests that some reorganisation is occurring within the water bridging network to accommodate the increased order within the fibre. This is perhaps evidence of an entropy driven elastic mechanism, which enables the recovery of the crimp only in the presence of bulk water, otherwise permanently removed after straining in dehydrated fibres

(as I observe in chapter 3). It is also worth considering that the contraction observed in the triple helix [69], may be a result of the reduced range of allowed motion within the backbone.

The low-wavenumber peak at around 570 cm^{-1} is attributed to the amide VI group, which is a combination of NH and C=O out-of-plane bending [219]. Its prevalence in the polarised spectrum, together with the increases observed in the peak for the diagonal region during crimp opening (no changes at apex), are consistent with their alignment orthogonal to the axis of the triple helix, radial to the collagen fibril at all hydrations. The presence of a small intensity increase in the polarised spectra of the apex is consistent with the argument developed above, that the protein is more mobile in the hydrated state, and experiences an entropic reorientation with increased order within the fibre. Crucially, the relative intensity of the peak reduces with dehydration, suggesting that there is a reduction in the number of out-of-plane bending motions as the water content of the fibres decreases. This is plausibly interpreted as an increase in direct hydrogen bonding between the amine and carbonyl bonds, if not between the α-chains within the tropocollagen, more likely in the lateral space between monomers as suggested above.

Generally in the hydrated state, stress is considered to be dissipated by the opening of the microscopic crimp and by the sliding of individual fibrils – only 10% of macroscopic strain is transferred to the triple helix in native fibres [224]. Whilst fibrillar sliding has been determined to be a crucial component in fibre extensibility and recovery [55], the effects of dehydration have been speculated upon [72], but not been directly explored, and moreover its existence during the opening of the microscopic crimp, is yet to be established. In chapter 3, the reduction in percentage-relaxation of dehydrated fibres, demonstrated that removal of water decreased sliding between fibrils. If sliding indeed occurs during the opening of the hydrated crimp, it is plausible that the absence of this stress relief mechanism in the water depleted fibres, may lead to a transfer of macroscopic strain to the collagen monomer. Thus structural changes in the triple helix of dehydrated fibres – indicated by the spectral changes in the amide III and C–C bands of the apex region – are facilitated by a reduction in intra- and interfibrillar packing and an increase in direct H-bonding, whilst hydrated fibres remain unperturbed, in keeping with the literature [68]. This agrees well with the model proposed by Gautieri et al [73], but not with another experimental work [69], where no changes were detected in the pitch of the triple helix. In this latter case, fibres were passively stretched by fixing their length *during* dehydration, whilst in this current work they were actively strained *after* dehydration and this could explain the difference. Further work should be conducted to determine if fibrillar

sliding occurs during uncrimping in different hydration conditions, and whilst returning fibres to their rest length. An x-ray scattering study of the triple helix pitch (similar to that recently applied to human corneal collagen [52]), in fibres actively strained in different hydration conditions, should be performed to determine unambiguously, if it experiences macroscopically applied strain in the dehydrated state.

The fibrillar gap region contains the C- and N-terminal telopeptides of the collagen triple-helix which are rich in phenylalanine (Phe). The exact conformation of this amino acid within collagen is unknown, but their organisation is posited to confer structural stability to the fibrils in the flexible gap region [225, 226], and to enable the formation of long triple helical chains [9]. The telopeptides contain a high degree of order [227], so it stands to reason that Phe is also highly aligned. This is reflected in the strength of the 1030 cm^{-1} peak in the polarised spectra. The spectral changes suggest an increasingly radial orientation of the amino acid within the diagonal region as the crimp opens, with no definitive changes at the apex. This is consistent with Phe as a hydrophobic aromatic side-chain, which would be expected to align orthogonally to the main chain of the peptide backbone. Given its hydrophobic nature, it is interesting that there are no clear variations in the peak with hydration. This perhaps suggests that the side-chain projects radially into the triple helical structure, internalised in the core of the monomer and that there is still sufficient water present here in the 'dry' state at 42% RH, that the conformation remains unchanged.

The literature is not clear on the orientation of the methyl group (CH$_3$) in type I collagen. However, my data suggests that it does possess some distinct order, unlike the more prevalent methylene (CH$_2$) group which shows no polarisation dependence. The intensity of the CH$_3$ peak of the depolarised spectra increases exclusively in the diagonal region, suggesting that the asymmetric stretch of the CH$_3$ group vibrates in a fixed plane aligned along the fibrillar axis. The absence of changes at the apex suggest that, if strain is transferred to the triple helix (in the dehydrated fibres) as suggested above, then the orientation of this group remains unaffected. This correlates well with its proposed role of controlling the strength [228] of the primary interchain H-bond and shielding it from solvent interaction [229]. The absence of a hydration dependence suggests that the methyl group protects the bond even at low ambient RH, indicating that the internal (inter-chain) water content of the collagen monomer may not be altered at this level (much as the Phe amino acid suggests above). Alternately, several works

suggest that the methyl group is associated closely with the pyrrolidine rings, and that its conformation is preorganised and subsequently stabilised by stereoelectronic interactions alone [9, 230, 231].

At all hydrations, the crimp removal-strain was consistently above 20% which is markedly higher than the 4% strain widely established in the literature [40]. This is unlikely to be accounted for by the non-uniform opening of individual crimp periods, which are removed at a slower rate towards the centre of a fibre under strain [232] (where the Raman spectra were acquired). Zero-strain was determined by removing fibre slack after equilibration to a given RH. This determination could be improved by including a force transducer in the mechanical testing stage to more accurately determine the rest length of the fibres. Moreover, fibres were not preconditioned prior to acquiring the Raman spectra – as I wanted to observe the crimp opening at all hydrations and it does not reappear after preconditioning in the dehydrated conditions – so macroscopic defects such as kinking were not removed when the rest length was set. These could all contribute to an overestimate of the macroscopic fibre strain. The use of clamps in place of epoxy adhesive may also reduce the error in the strain estimation and enable observation of changes in Raman spectra beyond the opening of the microscopic crimp; having been limited here to comparatively low strains, equivalent to the toe and heel regions of the macroscopic stress-strain curve. Incidentally, this likely accounts for the lack of a plateau in the observed spectral changes near the maximum strain, as the fibres were only stretched until the crimp visibly disappeared. Larger macroscopic strains may help to further emphasise the transfer of stresses to the triple helix in the dehydrated state.

Unlike collagen, the elastin fibres showed no spectral changes as a result of straining at either hydration extreme, with identical spectra across multiple fibres even at strains of 80%. The absence of strain-induced spectral changes has been observed before in an earlier polarisation resolved microspectroscopic Raman study by Green et al [106], which found no secondary structural changes resulting from macroscopically straining the fibre bundles. They did however, detect a hydration dependence within the amide I band, reflecting an increase in the percentage of β-structures present in the dehydrated fibres, together with a concomitant decrease in the α-helical content. The similarity with the amide I band shapes at the hydration extremes in this present work, suggests that such a trade-off between secondary structures is indeed an effect of dehydration. Furthermore, β-structures are stiffer than α-helices and other

secondary structures [143, 233, 234], so this corresponds well with the increased stiffness I observe at the molecular level of the dehydrated fibres.

The broad band attributed to backbone torsions and helix deformations in collagen (centred around 260 cm^{-1}), also appears in elastin, although it differs notably by being present in the depolarised spectrum, *and* as a very strong band in the polarised. Both increase in intensity with dehydration; however, the polarised band is present at all hydrations, whilst the depolarised band – similar to collagen – appears only after removing the fibre from solute. This difference implies that the two orthogonal modes may represent scattering from two distinct structural components within the elastin fibre. However, elastin structure is highly dynamic [17] and given uncertainty over the precise secondary structure of the elastin monomer, it is difficult to attribute them to specific structural moieties; though it is evident that the proposed increases in torsional rigidity (in support of the work by Lillie et al [101]) are commensurate with an increasing stiffness in the dehydrated fibres.

It is worth noting that the increase in torsional rigidity between the water-submerged and 100% RH states, does not necessarily preclude the elastic behaviour of the protein, as I have shown in chapter 3 that the elastin fibre is still very much extensible and can recover elastically at 100% RH. Rather it may reflect a loss of disorder upon deswelling of the fibre out of water [101], supporting the reduction in the percentage of unordered structures in dehydrated elastin found in the Raman study by Green et al [106].

The absence of spectral changes in the extended fibres suggest that macroscopic strain, to the extent studied here, does not affect the orientation of the elastin ultrastructure, and the lack of any obvious peak shifts indicates that the monomer itself is not perturbed by strain at any hydration. The implication is thus that stress is dissipated at a higher level of the fibre structure, or is simply a reflection of the highly dynamic nature of the elastin ultrastructure. It is interesting to note the absence of strain or hydration related changes in the water H-bonding band at 170 cm^{-1} (shoulder to the larger 260 cm^{-1} band in the polarised spectra). This suggests that, should direct inter-chain H-bonding play a part in the extension of the fibres, the elastin structure is not further stabilised by additional water-bonding during stretching. Water does not compensate for the rupture in inter-chain bonds in its extended state and elastin is thus confirmed as a purely self-associating protein, i.e. it is insoluble and its conformation is chiefly driven by hydrophobic effects, as widely stated in the literature [11, 102, 103, 235]. It is curious therefore, that I do not observe alterations during fibre extension in the OH stretching

band. This band has been used in collagen to indicate entropic changes in the conformation of the surrounding water structure caused by the presence of the protein [75], and is liable to change under the application of strain, reflecting a change in the order of the protein structure. The absence of such a change for elastin is evidence against the entropic mechanism of elasticity, or else simply a reflection of macroscopic strain not reaching the monomer.

I was limited in my analysis of the polarisation specific changes between samples, by a laser only approximately aligned perpendicular to the fibre axis. The polarisation setup in the Raman system used for this study does not allow for easy optimisation on an experiment-to-experiment basis, and it is possible that small variations occur between experiments. This is particularly pertinent given the angular variation in the collagen fibre crimp. Discrepancies in the sample-to-sample orientation were minimised by careful arrangement of the fibre during anchoring, but ideally, a rotating polariser would be placed in the incident beam path to enable the alignment of the linearly polarised laser with the axis of the fibre. This would minimise ambiguity in the magnitude of percentage change observed between the peak intensities at different hydrations, and thus give a more reliable estimation of the orientation of the vibrational mode. I have identified the primary areas of the polarisation resolved protein spectra that are affected by strain, and isolated changes that appear to have a dependence on the fibre hydration. The immediate continuation of the work conducted in this experiment, involves a more rigorous analysis of these specific polarised bond angles in collagen, using the approach outlined in references [106, 120]; employing two orthogonal laser polarisations in the measurement of the sample. Although I found no polarisation dependent changes in elastin, a secondary test using the method outlined in these references may be warranted, as Green et al [106] found small strain induced bond orientation changes in the peptide backbone of the helical domains and in the aromatic side-chains (Phe and Tyr) from the cross-linking regions. I should determine if these are indeed present and if hydration affects the magnitude of the change. Future work might also include investigation of interactions with microfibrillar glycoproteins.

6

Concluding Remarks & Future Work

In this thesis the mechanical properties of collagen and elastin, the main fibrous proteins of the extracellular matrix were investigated, using a novel combination of macroscopic stretching techniques and microspectroscopic analyses to develop a multiscale understanding of the fibre mechanochemistry. I set out to investigate the possible mechanisms by which the structure regulates the functional biomechanics of fibres. At various stages throughout this thesis, I have suggested areas where further research would be of interest, and have identified ways in which my current results may be extended. These suggestions are consolidated in the sections below.

6.1.   Collagen

I obtained polarisation resolved Raman spectra from collagen throughout the opening of the microscopic crimp. In highly hydrated conditions, when submerged in aqueous solution and when suspended at 100% RH, I found no indication of stress being transmitted to the tropocollagen monomer; the action of the macroscopically applied strain was simply to straighten the fibrils within the crimp, in agreement with previous works in the literature. However, below these hydrations, I observed spectral changes in the stationary fibrils of the apex region which indicated a subtle reorienting of the amide III and C–C modes of the protein

peptide chains, suggesting that the triple helix was being perturbed during the crimp opening. Novel observations in the low-wavenumber region provided a possible explanation for this. For the first time in collagen, I observed a highly directional band centred at around 170 cm^{-1} associated with the stretching mode of intermolecular hydrogen bonding of water, aligned purely radially to the fibrillar axis. This was attributed specifically to the water bridges that reside in the lateral space between neighbouring tropocollagen monomers. Another band centred at around 260 cm^{-1} was attributed to backbone torsions of the collagen peptide, and a third peak at approximately 570 cm^{-1}, was associated with the amide VI mode, a combination of out-of-plane bending of NH and C=O bonds, which are nominally aligned orthogonal to the peptide backbone. The hydrophobic side-chain amino acid phenylalanine and the CH$_3$ group, were found to maintain a fixed orientation in the core of the triple helix, suggesting that desiccation to 42% RH was not sufficient to remove the strongly bound interstitial water that stabilises the α-chains of the trimer. However, completely removing bulk water by lowering the ambient humidity, led to a reduction in the number of water bridges between monomers. I propose that this increases the packing density of collagen, enabling the formation of stronger, direct (backbone-backbone) hydrogen bonds in the shrunken lateral spacing between adjacent monomers. I believe these stabilise the collagen structure, compensating for the reduced number of (long-range) water-mediated bonds between adjacent charged residues, reducing the conformational freedom of the protein. Direct hydrogen bonding occurs principally between the amine and carbonyl bonds of neighbouring triple helices, hence the observed reduction in bending mode activity for the NH and C=O bonds, which were confined increasingly to a radial orientation as dehydration progressed. This in-turn increases the torsional rigidity of the protein backbone, restricting its motion to the fibrillar axis alone. This probably produces the forces that, when unrestrained, contract the length of the tropocollagen monomer and alter the pitch of the triple helix, and is possibly responsible for setting the microscopic crimp frequency. Although, as I suggested in chapter 5, data on crimp frequency, angle and crimp-removal-strain, together with an assessment of the scale of macroscopic fibre shrinkage – all as a function of hydration – is lacking in the literature, and should be explored as an extension to my work here.

The micromechanical impact of these structural changes was reflected in my Brillouin data which showed a stiffening of the collagen monomer upon dehydration. I further propose that the removal of the relatively mobile water bridges strips the microfibrils – the chains of single tropocollagen monomers – of their ability to slide with respect to one another when exposed

to external strain. This stress relief mechanism is analogous to fibrillar sliding within the ground substance at the next scale of the structural hierarchy; a mechanism which I also observed to be severely degraded by lowering the ambient RH in my macroscopic stress relaxation experiments; so much so, that I think the fibrils and the non-collagenous matrix essentially become a single continuum when dehydrated. It is therefore plausible that macroscopic strain was transferred to the triple helix in the dehydrated states, hence I observed the slight perturbation of the triple helix through subtle orientation changes to the amide III and C–C modes, whereas in highly hydrated conditions strain is dissipated by the sliding of successive hierarchical elements.

Given that Raman spectra were only acquired during the opening of the microscopic crimp, my results suggested that fibrillar and monomer sliding likely occurred during the crimp straightening process, not only once the fibrils were fully linear. Hierarchical sliding as a function of hydration has, to my knowledge, never been investigated, and should be a topic of interest for further work, as it has implications in the elastic response of collagen. In fact, observation of reorienting water bridges in the otherwise stationary apex region of the water submerged fibres, hinted at a possible entropy driven elastic mechanism that might drive crimp recovery upon fibre relaxation in the presence of bulk water. Dehydration did not prevent the opening of the crimp, nor does it appear to preclude the sliding of fibrils – although it likely makes this a more energetically demanding process, contributing to the stiffness increase – but it certainly influences relaxation processes and the ability to recover from applied strain, as demonstrated by the permanent fibre elongation in my macroscopic stress-strain tests. A further assessment of the Raman spectrum of fibres undergoing cyclic extension around the critical hydration, may shed further light on this.

I initially drew the analogy between the role of hydration and the part played by the components of the non-collagenous matrix in chapter 3, as it seemed that the hydration related changes observed in the stress relaxation results, i.e. the reduction in fibrillar sliding, were equivalent to the results obtained in the literature when reducing the glycosaminoglycan (GAG) and proteoglycan (PG) content of the fibres. This suggested a potential interdependency. Indeed, my Brillouin data confirmed that removal of the non-collagenous matrix resulted in a noticeable reduction in acoustic damping, confirming that GAGs and PGs are responsible for binding a large component of fibre water. Furthermore, my micro-Brillouin data showed that the ground substance was mechanically distinct from the fibrils, indicating that non-collagenous constituents of the ECM contribute to making the tissue softer than the

single collagen fibrils themselves. Crucially though, I noted a marked increase in anisotropy of the Poisson's ratio, which I believe demonstrates that the primary role of water and the non-collagenous matrix, is to stabilise the fibrillar structure during stretching. A future Brillouin mapping approach to fibres under strain would provide a better picture of the active role played by GAGs, PGs and water in this respect.

For the first time, I identified a critical hydration range between 100 and 85% RH, where the transition from a viscoelastic to a plastic material state occurs in collagen. Through analysis of the entire polarisation resolved Raman spectral range, I have identified the primary structural elements that are affected by strain, and isolated changes that appear to have a dependence on the fibre hydration. Taken together, this work shows that water is a primary mediator of the mechanics between the various scales of the structural hierarchy in collagen. A combination of increasing molecular rigidity coupled with the decline in micro-fibrillar and fibril sliding, leads to the overall increase that I observe in the Young's modulus of the dehydrating macroscopic fibre, bridging the spatial gap between the smallest structural scale of the protein and the functional mechanics of the extracellular matrix.

6.2.   Elastin

As in collagen, I observed that dehydration increased the stiffness of elastin fibres, and simultaneously stripped them of their ability to stretch recoverably from applied strain, changing their physical nature from viscoelastic to plastic materials at a critical hydration. This was identified as below 85% RH for elastin, again to my knowledge, the first time that a native working range has been identified for this protein. In fact, observation of a remarkable macroscopic stress relaxation behaviour at this point, led me to propose that the natural hydration of elastin in the body is probably closer to 85% RH than 100% RH, plausible due to the presence of salts in the native environment. Under rapid extension at this hydration, the fibre bore comparatively high stress (an order of magnitude greater than at 100% RH), whilst maintaining the ability to relax elastically at speed – a possible indication of a damage limitation mechanism for fibres exposed to sudden deformation, and potentially ideal behaviour for the role of elastin in the body.

I determined that stress decay in elastin was principally governed by its porous nature, with two of the three relaxation components attributed to the expulsion of water from the intra- and interfibrillar pore spaces, in support of previous work regarding the poroelastic nature of the fibre. The third and fastest component was generally attributed to a convolution of molecular relaxations; although I highlighted that it was impossible to attribute these more specifically, simply through the use of a macroscopic technique, being several orders of magnitude removed from the spatial range of the tropoelastin monomer. A MEMS or an AFM approach coupled with a spectroscopic technique to analyse single elastin fibres, may make it possible to determine the molecular contribution to the stress relaxation. The sudden inability of elastin to relax below 66% RH, was attributed to a loss of free aqueous solution from the pore spaces, removing the hydration forces that I believe drive the re-expansion of the pores, simultaneously promoting the ultrastructure of the fibres into a plasticised state.

In this respect, one of the few changes that I observed in the Raman spectra of the fibre was associated with a band in the low-wavenumber region at approximately 260 cm^{-1}. As in collagen, this was associated with protein backbone torsions and helical deformations, a similarly novel observation for Raman studies of the elastin fibre. This band markedly increased with dehydration in both the polarised and depolarised spectra, indicating an increase in rigidity of the elastin monomer and a restriction of molecular freedom, in agreement with the observation made in the macroscopic measurements, and commensurate with greater order and increasing stiffness at the molecular scale of the elastin fibre. I noted however, that due to uncertainty over the precise secondary structure of tropoelastin, it was difficult to attribute the changes in the Raman spectrum to any specific structural moiety; although a tentative connection might be drawn between the observed increase in the percentage of stiff β-structures, and decreases in the softer α-helical content. The increased presence of stiffer, molecular scale structures upon dehydration was reflected in my Brillouin results, the first ever measurement of hypersonic wave velocities within the elastin protein.

Both the macroscopic and microscopic elastic moduli were thus observed to increase in elastin as a result of dehydration, although unlike in collagen, their respective magnitude changes were quite different. Between the fully hydrated state at 100% RH and the 'dry' condition at 21% RH, I observed a two-fold increase in the Brillouin modulus, but a two-*order* of magnitude increase in the Young's modulus. In comparison, collagen saw a three-fold increase in each modulus between the hydration extremes. I believe that this is a result of elastin undergoing a state-change from liquid-like to solid-like behaviour. This markedly reduces the relaxation time

associated with the molecules, which translates directly to increases in the shear modulus of the protein, to which the quasi-static elastic modulus is more sensitive than the longitudinal modulus, hence the far more considerable change. I did not observe this in collagen because long range order persists in the form of the triple helix at all hydrations and temperatures used in this work. However, elastin has an amorphous structure in its hydrated state to which order is introduced upon drying, resulting in an arrested state of matter, highlighted by the increased torsional rigidity I conclude from the changes in the low-wavenumber Raman spectra.

No changes were detected in the Raman spectra as a result of stretching whole fibres, in agreement with previous works. This implied that macroscopic strain was not being transferred to the elastin ultrastructure, even though the fibre was visibly extending – in the case of the dehydrated fibres, irreversibly so. The absence of changes in the broad band associated with OH stretching of bulk water, provided evidence against the entropic mechanism of elasticity; however, the notion of this being a primary source of elastic recovery in elastin is so widespread in the literature, that this was likely a better indication of macroscopic strain not reaching the tropoelastin monomer. I suggested therefore, that this was either further evidence of elastin's dynamic ultrastructure, or that stress was dissipated at a higher level of the fibre structure, perhaps through sliding of adjacent microfibrillar chains of tropoelastin monomers; although such a mechanism has, to date, not been experimentally observed, due in large part to the challenges of optically imaging below the diffraction limit (diameters are approximately 100 nm) in a native hydration environment. I would strongly encourage future investigations in this area, possibly through super-resolution microscopy.

An absence of changes in the band at 170 cm^{-1}, indicated that water mediated H-bonding does not play a part in fibre extension, and indeed, an absence of intensity changes in the same band at different hydrations, suggested that the H-bonding structure of the fibre remains unperturbed in the experimental conditions employed here. This further confirms that elastin is a hydrophobically driven, purely self-associating protein and likely explains why the micro-BLS data revealed a mechanically contiguous fibre when probed in the radial orientation.

It is more challenging than in collagen to conclude how the molecular scale structure of elastin determines the micromechanics of the fibres, as I observed very few changes under strain; an indication of either elastin's dynamic molecular structure, or of higher levels of the fibre hierarchy actively facilitating the stretching of the fibres. However, as with collagen, I note again

that it is water that provides the common connection between the elastic moduli of the fibres at each scale of the structural hierarchy and which principally provides the drive for both the variation in hydration forces and the changes of state in the molecular assembly that influence these mechanics of the protein fibre.

References

1. Renishaw, *inVia Reflex Image*, http://resources.renishaw.com/gen/details/invia-reflex-enclosure--5500 (Accessed: April 2018).

2. B. J. Berne and R. Pecora, *Dynamic Light Scattering: With Applications to Chemistry, Biology and Physics*, Dover Publications (2000).

3. V. K. Pálfi and A. Perczel, *Journal of Computational Chemistry*, **31**: 764-777 (2010).

4. G. Rodriguez Luis, *et al.*, *Cytometry Part A*, **69A**: 779-791 (2006).

5. Zhilei L. Shen, *et al.*, *Biophysical journal*, **100**: 3008-3015 (2011).

6. H. Lodish, *et al.*, *Collagen: The Fibrous Proteins of the Matrix.*, in Molecular Cell Biology, W. H. Freeman, 4th Edition edition (2000).

7. N. Verzijl, *et al.*, *Journal of Biological Chemistry*, **275**: 39027-39031 (2000).

8. B. H. Toyama and M. W. Hetzer, *Nature reviews. Molecular cell biology*, **14**: 55-61 (2013).

9. M. D. Shoulders and R. T. Raines, *Annual review of biochemistry*, **78**: 929-958 (2009).

10. J. Bella, *Biochemical Journal*, **473**: 1001 (2016).

11. L. D. Muiznieks and F. W. Keeley, *Biochimica et biophysica acta*, **1832**: 866-875 (2013).

12. K. E. Kadler, *et al.*, *Biochemical Journal*, **316**: 1-11 (1996).

13. J. P. R. O. Orgel, *et al.*, *Proceedings of the National Academy of Sciences*, **103**: 9001-9005 (2006).

14. B. Vrhovski and A. S. Weiss, *European Journal of Biochemistry*, **258**: 1-18 (1998).

15. L. Robert, *et al.*, *Biogerontology*, **9**: 119-133 (2008).

16. C. Baldock, *et al.*, *Proceedings of the National Academy of Sciences*, **108**: 4322-4327 (2011).

17. L. D. Muiznieks, *et al.*, *Biochemistry and cell biology = Biochimie et biologie cellulaire*, **88**: 239-250 (2010).

18. S. Rauscher and R. Pomès, *Structural Disorder and Protein Elasticity*, in Fuzziness: Structural Disorder in Protein Complexes, eds. M. Fuxreiter and P. Tompa, Springer US (2012), pp. 159-183.

19. L. D. Muiznieks and F. W. Keeley, *ACS Biomaterials Science & Engineering*, **3**: 661-679 (2017).

20. C. M. Kielty, *et al.*, *Journal of Cell Science*, **115**: 2817 (2002).

21. S. M. Mithieux and A. S. Weiss, *Elastin*, in Advances in Protein Chemistry, Academic Press (2005), pp. 437-461.

22. E. M. Green, *et al.*, *Interface Focus*, **4** (2014).

23. R. P. Mecham, *Matrix Biology* (2018).

24. O. Paris, *et al.*, *Cell Mol Biol (Noisy-le-grand)*, **46**: 993-1004 (2000).

25. V. Ottani, *et al.*, *Micron*, **33**: 587-596 (2002).

26. H. S. Gupta and P. Zioupos, *Medical Engineering & Physics*, **30**: 1209-1226 (2008).

27. P. Fratzl and R. Weinkamer, *Progress in Materials Science*, **52**: 1263-1334 (2007).

28. J. P. R. O. Orgel, *et al.*, *Connective Tissue Research*, **52**: 2-17 (2011).

29. C. T. Thorpe and H. R. C. Screen, *Tendon Structure and Composition*, in Metabolic Influences on Risk for Tendon Disorders, eds. P. W. Ackermann and D. A. Hart, Springer International Publishing (2016), pp. 3-10.

30. F. Fang and S. P. Lake, *Journal of Orthopaedic Research*, **35**: 1353-1365 (2016).

31. I. Goldberga, *et al.*, *Accounts of Chemical Research*, **51**: 1621-1629 (2018).

32. W. R. Gray, *et al.*, *Nature*, **246**: 461 (1973).

33. D. W. Urry, *et al.*, *Ciba Foundation symposium*, **192**: 4-22; discussion 22-30 (1995).

34. L. Debelle and A. M. Tamburro, *The International Journal of Biochemistry & Cell Biology*, **31**: 261-272 (1999).

35. L. Debelle and A. J. P. Alix, *Biochimie*, **81**: 981-994 (1999).

36. D. W. Urry and T. M. Parker, *Journal of muscle research and cell motility*, **23**: 543-559 (2002).

37. D. W. Urry, *et al.*, *Philosophical Transactions of the Royal Society B: Biological Sciences*, **357**: 169-184 (2002).

38. S. G. Wise, *et al.*, *Acta Biomater*, **10**: 1532-1541 (2014).

39. K. Legerlotz, *et al.*, *Acta Biomaterialia*, **10**: 4447-4455 (2014).

40. B. J. Rigby, *et al.*, *The Journal of General Physiology*, **43**: 265-283 (1959).

41. J. Diamant, *et al.*, *Proceedings of the Royal Society of London. Series B, Containing papers of a Biological character. Royal Society*, **180**: 293-315 (1972).

42. P. Fratzl, *et al.*, *Journal of Structural Biology*, **122**: 119-122 (1998).

43. K. Misof, *et al.*, *Biophysical journal*, **72**: 1376-1381 (1997).

44. R. Puxkandl, *et al.*, *Philosophical Transactions of the Royal Society B: Biological Sciences*, **357**: 191-197 (2002).

45. S. Rigozzi, *et al.*, *Journal of Structural Biology*, **176**: 9-15 (2011).

46. Z. L. Shen, *et al.*, *Biophysical journal*, **95**: 3956-3963 (2008).

47. Z. L. Shen, *et al.*, *Biophysical journal*, **99**: 1986-1995 (2010).

48. Y. Liu, *et al.*, *Interface Focus*, **6**: 20150080 (2016).

49. H. S. Gupta, *et al.*, *Nano Letters*, **5**: 2108-2111 (2005).

50. H. S. Gupta, *et al.*, *Proceedings of the National Academy of Sciences*, **103**: 17741 (2006).

51. C. Vergari, *et al.*, *Biomechanics and modeling in mechanobiology*, **16**: 1475-1484 (2017).

52. J. S. Bell, *et al.*, *Acta Biomaterialia*, **65**: 216-225 (2018).

53. R. B. Svensson, *et al.*, *Acta biomaterialia*, **50**: 293-301 (2017).

54. L. Yang, *et al.*, *Biophysical journal*, **94**: 2204-2211 (2008).

55. S. E. Szczesny and D. M. Elliott, *Acta biomaterialia*, **10**: 2582-2590 (2014).
56. H. R. Screen, *et al.*, *Proceedings of the Institution of Mechanical Engineers. Part H, Journal of engineering in medicine*, **218**: 109-119 (2004).
57. V. W. T. Cheng and H. R. C. Screen, *Journal of Materials Science*, **42**: 8957-8965 (2007).
58. H. R. Screen, *J Mech Behav Biomed Mater*, **1**: 51-58 (2008).
59. H. S. Gupta, *et al.*, *Journal of Structural Biology*, **169**: 183-191 (2010).
60. R. B. Svensson, *et al.*, *Journal of the Mechanical Behavior of Biomedical Materials*, **3**: 112-115 (2010).
61. L. Yang, *et al.*, *Journal of the Mechanical Behavior of Biomedical Materials*, **6**: 148-158 (2012).
62. L. Bozec and M. Horton, *Biophysical journal*, **88**: 4223-4231 (2005).
63. N. Sasaki and S. Odajima, *Journal of Biomechanics*, **29**: 1131-1136 (1996).
64. N. Sasaki and S. Odajima, *Journal of Biomechanics*, **29**: 655-658 (1996).
65. S. R. Inamdar, *et al.*, *ACS Nano*, **11**: 9728-9737 (2017).
66. K. Legerlotz, *et al.*, *Acta Biomaterialia*, **9**: 6860-6866 (2013).
67. S. Rigozzi, *et al.*, *Journal of Biomechanics*, **46**: 813-818 (2013).
68. A. Masic, *et al.*, *Biomacromolecules*, **12**: 3989-3996 (2011).
69. A. Masic, *et al.*, *Nat Commun*, **6**: 5942 (2015).
70. L. Bertinetti, *et al.*, *J Mech Behav Biomed Mater*, **52**: 14-21 (2015).
71. O. G. Andriotis, *et al.*, *Journal of The Royal Society Interface*, **12** (2015).
72. H. C. Wells, *et al.*, *ACS Biomaterials Science & Engineering*, **3**: 2524-2532 (2017).
73. A. Gautieri, *et al.*, *Journal of Biomechanics*, **45**: 2079-2083 (2012).
74. A. Gautieri, *et al.*, *International Journal of Non-Linear Mechanics*, **56**: 25-33 (2013).
75. S. Leikin, *et al.*, *Proceedings of the National Academy of Sciences*, **94**: 11312-11317 (1997).
76. L. Brillouin, *Ann. Phys.*, **9**: 88-122 (1922).
77. R. Harley, *et al.*, *Nature*, **267**: 285-287 (1977).
78. J. Randall, *et al.*, *Philosophical Transactions of the Royal Society of London A: Mathematical, Physical and Engineering Sciences*, **293**: 341-348 (1979).
79. J. M. Vaughan and J. T. Randall, *Nature*, **284**: 489-491 (1980).
80. S. Cusack and A. Miller, *Journal of Molecular Biology*, **135**: 39-51 (1979).
81. M. Spina, *et al.*, *Biopolymers*, **49**: 255-265 (1999).
82. K. H. Parker and C. P. Winlove, *Engineering in Medicine*, **17**: 175-180 (1988).
83. P. Farand, *et al.*, *Microvascular Research*, **73**: 95-99 (2007).
84. R. R. Mercer and J. D. Crapo, *Journal of Applied Physiology*, **69**: 756-765 (1990).
85. Y. Luo, *et al.*, *Scientific Reports*, **8**: 8334 (2018).
86. J. Yu and J. P. G. Urban, *Journal of Anatomy*, **216**: 533-541 (2010).
87. B. He, *et al.*, *J Orthop Res*, **31**: 1345-1353 (2013).
88. E. M. Green, *et al.*, *The structure and micromechanics of elastic tissue* (2014).
89. J. C. Mansfield, *et al.*, *Osteoarthritis and Cartilage*, **23**: 1806-1816 (2015).
90. Y. Mikawa, *et al.*, *Archives of orthopaedic and traumatic surgery. Archiv fur orthopadische und Unfall-Chirurgie*, **105**: 343-349 (1986).
91. Y. Jing, *et al.*, *Journal of Anatomy*, **201**: 465-475 (2002).
92. J. Yu, *et al.*, *J Anat*, **210**: 460-471 (2007).
93. M. Kobielarz, *et al.*, *Journal of the Mechanical Behavior of Biomedical Materials*, **62**: 45-56 (2016).
94. B. B. Aaron and J. M. Gosline, *Nature*, **287**: 865-867 (1980).
95. M. A. Kewley, *et al.*, *Journal of Anatomy*, **123**: 129-134 (1977).
96. S. Partridge, *Biochim. Biophys. Acta*, **140**: 132-141 (1967).

97.   C. P. Winlove and K. H. Parker, *Biopolymers*, **29**: 729-735 (1990).

98.   P. D. Weinberg, *et al.*, *Biopolymers*, **35**: 161-169 (1995).

99.   J. M. Gosline and C. J. French, *Biopolymers*, **18**: 2091-2103 (1979).

100. M. A. Lillie and J. M. Gosline, *Biopolymers*, **39**: 641-652 (1996).

101. M. A. Lillie, *et al.*, *Biopolymers*, **39**: 627-639 (1996).

102. E. Green, *Mechanisms of Elasticity in Elastin*, University of Exeter (2012).

103. B. Li, *et al.*, *Journal of the American Chemical Society*, **123**: 11991-11998 (2001).

104. G. C. Yeo, *et al.*, *Science Advances*, **2** (2016).

105. L. Ali, *et al.*, *Radiation Physics and Chemistry*, **71**: 951-952 (2004).

106. E. Green, *et al.*, *Biopolymers*, **89**: 931-940 (2008).

107. D. A. D. Parry and A. S. Craig, *Biopolymers*, **17**: 843-855 (1978).

108. C. C. Danielsen and T. T. Andreassen, *Journal of Biomechanics*, **21**: 207-212 (1988).

109. S. S. Sivan, *et al.*, *The Biochemical journal*, **399**: 29-35 (2006).

110. E. G. Cleary, *et al.*, *The Journal of Cell Biology*, **33**: 469 (1967).

111. K. D. Budras, *et al.*, *Bovine Anatomy: An Illustrated Text*, Second edition, Schlüetersche (2011).

112. A. I. Lansing, *et al.*, *The Anatomical Record*, **114**: 555-575 (1952).

113. F. S. Steven, *et al.*, *Connective Tissue Research*, **2**: 85-90 (1974).

114. M. Scandola and G. Pezzin, *Density of Elastin-Water System*, in Water in Polymers, AMERICAN CHEMICAL SOCIETY (1980), pp. 225-234.

115. R. E. Shadwick, *Journal of applied physiology (Bethesda, Md. : 1985)*, **68**: 1033-1040 (1990).

116. Y. Wang, *et al.*, *Journal of the Mechanical Behavior of Biomedical Materials*, **49**: 244-254 (2015).

117. N. B. Colthup, *et al.*, *Introduction to Infrared and Raman Spectroscopy*, Second edition, Academic Press (1975).

118. N. Stone, *Raman Spectroscopy of Biological Tissue for Application in Optical Diagnosis of Malignancy*, Cranfield University (2001).

119. D. A. Long, *The Raman Effect: A Unified Treatment of the Theory of Raman Scattering by Molecules*, John Wiley a& Sons (2002).

120. M. E. Rousseau, *et al.*, *Biomacromolecules*, **5**: 2247-2257 (2004).

121. E. Smith and G. Dent, *Modern Raman Spectroscopy - A Practical Approach*, John Wiley & Sons (2005).

122. M. Diem, *Modern Vibrational Spectroscopy and Micro-Spectroscopy: Theory, Instrumentation and Biomedical Applications*, John Wiley & Sons (2015).

123. C. V. Raman and K. S. Krishnan, *Nature*, **121**: 501 (1928).

124. F. Bonnier, *et al.*, *Vibrational Spectroscopy*, **61**: 124-132 (2012).

125. M. Y. Berezin and S. Achilefu, *Chemical Reviews*, **110**: 2641-2684 (2010).

126. R. Steiner, *Laser-Tissue Interactions*, in Laser and IPL Technology in Dermatology and Aesthetic Medicine, eds. C. Raulin and S. Karsai, Springer (2011), pp. 23-36.

127. J. B. Slater, *et al.*, *Raman Spectrometry and Its Adaptation to the Industrial Environment*, in Handbook of Raman Spectroscopy: From the Research Laboratory to the Process Line, eds. I. R. Lewis and H. G. M. Edwards, Marcel Dekker (2001), pp. 41-145.

128. E. Spinner, *Journal of the Chemical Society B: Physical Organic*: 879-885 (1967).

129. Z.-X. Qin, *et al.*, *The Journal of Chemical Physics*, **136**: 024503 (2012).

130. T. Shinoda, *The Raman Spectra of Solid and Liquid Tetramethylsilane* (1977).

131. F. Palombo, *et al.*, *Physical Chemistry Chemical Physics*, **13**: 16197-16207 (2011).

132. E. Gross, *Nature*, **126**: 201 (1930).

133. D. Fioretto, *et al.*, *Physical Review B*, **47**: 15286-15289 (1993).

134.   B. Ruta, *et al.*, *Journal of Non-Crystalline Solids*, **357**: 563-566 (2011).

135.   C. J. Montrose, *et al.*, *The Journal of the Acoustical Society of America*, **43**: 117-130 (1968).

136.   F. Palombo, *et al.*, *Journal of the Royal Society, Interface / the Royal Society*, **11**: 20140739 (2014).

137.   J. R. Sandercock, *Proc. 2nd Int. Conf. Light Scattering in Solids*, Paris (1971), ed. M. Balkanski, Flammarion, pp. 9-12.

138.   R. Mock, *et al.*, *Journal of Physics E: Scientific Instruments*, **20**: 656 (1987).

139.   L. Comez, *et al.*, *Progress in Liquid and Glass Physics by Brillouin Scattering Spectroscopy*, in Solid State Physics, eds. R. E. Camley and R. L. Stamps, Academic Press (2012), pp. 1-77.

140.   D. Fioretto and F. Scarponi, *Materials Science and Engineering: A*, **521-522**: 243-246 (2009).

141.   F. Palombo, *et al.*, *Analyst*, **139**: 729-733 (2014).

142.   M. Madami, *et al.*, *Application of Microfocused Brillouin Light Scattering to the Study of Spin Waves in Low-Dimensional Magnetic Systems*, in Solid State Physics, eds. R. E. Camley and R. L. Stamps, Academic Press (2012), pp. 79-150.

143.   S. Mattana, *et al.*, *Journal of Innovative Optical Health Sciences*, **10**: 1742001 (2017).

144.   K. J. Koski, *et al.*, *Nature Materials*, **12**: 262-267 (2013).

145.   R. S. Edginton, *et al.*, *JoVE*: e54648 (2016).

146.   M. P. E. Wenger, *et al.*, *Biophysical journal*, **93**: 1255-1263 (2007).

147.   J. Gosline, *et al.*, *Philosophical transactions of the Royal Society of London. Series B, Biological sciences*, **357**: 121-132 (2002).

148.   H. R. C. Screen, *et al.*, *Acta Biomaterialia*, **2**: 505-513 (2006).

149.   E. Gentleman, *et al.*, *Biomaterials*, **24**: 3805-3813 (2003).

150.   Y. Goulam Houssen, *et al.*, *Journal of Biomechanics*, **44**: 2047-2052 (2011).

151.   K. Legerlotz, *et al.*, *Journal of Biomechanics*, **43**: 2274-2280 (2010).

152.   E. M. Green and C. P. Winlove, *Biopolymers*, **103**: 187-202 (2015).

153.   B. B. Aaron and J. M. Gosline, *Biopolymers*, **20**: 1247-1260 (1981).

154.   Y. P. Kato, *et al.*, *Biomaterials*, **10**: 38-42 (1989).

155.   A. Sionkowska and T. Wess, *Int J Biol Macromol*, **34**: 9-12 (2004).

156.   T. J. Lujan, *et al.*, *Journal of applied physiology (Bethesda, Md. : 1985)*, **106**: 423-431 (2009).

157.   J. H. Yoon and J. Halper, *Journal of musculoskeletal & neuronal interactions*, **5**: 22-34 (2005).

158.   J. M. Mattson, *et al.*, *Biomechanics and modeling in mechanobiology*, **16**: 213-225 (2017).

159.   H. R. C. Screen, *et al.*, *Annals of biomedical engineering*, **33**: 1090-1099 (2005).

160.   D. Chimich, *et al.*, *J Biomech*, **25**: 831-837 (1992).

161.   T. L. Haut and R. C. Haut, *J Biomech*, **30**: 79-81 (1997).

162.   M. A. Lillie and J. M. Gosline, *Biorheology*, **30**: 229-242 (1993).

163.   Y. Wang, *et al.*, *Journal of the Mechanical Behavior of Biomedical Materials*, **77**: 634-641 (2018).

164.   W. F. Daamen, *et al.*, *Biomaterials*, **22**: 1997-2005 (2001).

165.   W. F. Daamen, *et al.*, *Tissue Engineering*, **11**: 1168-1176 (2005).

166.   T. Thorpe Chavaunne, *et al.*, *International Journal of Experimental Pathology*, **94**: 248-259 (2013).

167.   B. K. Connizzo and A. J. Grodzinsky, *Journal of Biomechanics*, **54**: 11-18 (2017).

168.   M. R. Homicz, *et al.*, *Archives of Facial Plastic Surgery*, **5**: 53-58 (2003).

169.   S. L. Jacques, *Physics in Medicine and Biology*, **58**: R37 (2013).

170. S. Cusack and S. Lees, *Biopolymers*, **23**: 337-351 (1984).
171. L. Holliday, *The Stiffness of Polymers in Relation to Their Structure*, in Structure and Properties of Oriented Polymers, ed. I. M. Ward, Springer Netherlands (1975), pp. 242-263.
172. R. G. Leisure, *Elastic Constants*, in Ultrasonic Spectroscopy: Applications in Condensed Matter Physics and Materials Science, ed. R. G. Leisure, Cambridge University Press (2017), pp. 120-165.
173. V. Samouillan, *et al.*, *Journal of Functional Biomaterials*, **2**: 230 (2011).
174. S. Corezzi, *et al.*, *The Journal of Chemical Physics*, **117**: 2435-2448 (2002).
175. S. Corezzi, *et al.*, *Nature*, **420**: 653 (2002).
176. S. Corezzi, *et al.*, *The Journal of Physical Chemistry B*, **117**: 14477-14485 (2013).
177. S. Caponi, *et al.*, *Physical Review B*, **76**: 092201 (2007).
178. T. Still, *et al.*, *The Journal of Physical Chemistry Letters*, **1**: 2440-2444 (2010).
179. J. Zhang, *et al.*, *Lab on a Chip*, **17**: 663-670 (2017).
180. G. Scarcelli, *et al.*, *Biophysical journal*, **101**: 1539-1545 (2011).
181. G. Scarcelli, *et al.*, *Nature methods*, **12**: 1132-1134 (2015).
182. J. Bella, *et al.*, *Structure*, **3**: 893-906 (1995).
183. F. Palombo, *et al.*, *Journal of Biophotonics*, **9**: 694-700 (2016).
184. Q. Meng, *et al.*, *Journal of the Mechanical Behavior of Biomedical Materials*, **65**: 439-453 (2017).
185. C. N. M. Ryan, *et al.*, *Bioconjugate Chemistry*, **26**: 1237-1251 (2015).
186. A. M. Cribb and J. E. Scott, *Journal of Anatomy*, **187**: 423-428 (1995).
187. A. Redaelli, *et al.*, *Journal of Biomechanics*, **36**: 1555-1569 (2003).
188. S. Rigozzi, *et al.*, *Journal of Biomechanics*, **42**: 1547-1552 (2009).
189. G. Fessel and J. G. Snedeker, *Matrix Biology*, **28**: 503-510 (2009).
190. R. B. Svensson, *et al.*, *Connective Tissue Research*, **52**: 415-421 (2011).
191. P. S. Robinson, *et al.*, *Journal of biomechanical engineering*, **127**: 181-185 (2005).
192. S. E. Szczesny, *et al.*, *J Orthop Res*, **35**: 2127-2134 (2017).
193. F. Scarponi, *et al.*, *Physical Review X*, **7**: 031015 (2017).
194. S. Mattana, *et al.*, *Biophysical Chemistry*, **229**: 123-129 (2017).
195. K. Elsayad, *et al.*, *Science Signaling*, **9**: rs5 (2016).
196. G. Antonacci and S. Braakman, *Scientific Reports*, **6**: 37217 (2016).
197. G. Scarcelli and S. H. Yun, *Optics Express*, **19**: 10913-10922 (2011).
198. G. Scarcelli and S. H. Yun, *Optics Express*, **20**: 9197-9202 (2012).
199. J. C. Day, *et al.*, *Phys Med Biol*, **54**: 7077-7087 (2009).
200. J. C. C. Day and N. Stone, *Appl Spectrosc*, **67**: 349-354 (2013).
201. O. Stevens, *et al.*, *Chemical Society Reviews*, **45**: 1919-1934 (2016).
202. A. C. S. Talari, *et al.*, *Applied Spectroscopy Reviews*, **50**: 46-111 (2015).
203. S. Jaisson, *et al.*, *Chemistry & biology*, **13**: 149-159 (2006).
204. M. Janko, *et al.*, *Opt. Lett.*, **35**: 2765-2767 (2010).
205. A. Bonifacio and V. Sergo, *Vibrational Spectroscopy*, **53**: 314-317 (2010).
206. L. Galvis, *et al.*, *PLOS ONE*, **8**: e63518 (2013).
207. A. De Simone, *et al.*, *Biochemical and biophysical research communications*, **372**: 121-125 (2008).
208. M. Ravikumar Krishnakumar and W. Hwang, *Proteins: Structure, Function, and Bioinformatics*, **72**: 1320-1332 (2008).
209. J. Bella and H. M. Berman, *Journal of molecular biology*, **264**: 734-742 (1996).
210. B. Brodsky, *Proceedings of the Indian Academy of Sciences - Chemical Sciences*, **111**: 13-18 (1999).

211. G. E. Walrafen and M. R. Fisher, *Low-frequency raman scattering from water and aqueous solutions: A direct measure of hydrogen bonding*, in Methods in Enzymology, Academic Press (1986), pp. 91-105.

212. I. Streeter and N. H. de Leeuw, *Soft Matter*, **7**: 3373-3382 (2011).

213. G. D. Fullerton and A. Rahal, *Journal of Magnetic Resonance Imaging*, **25**: 345-361 (2007).

214. L. V. Krasnosselskaia, *et al.*, *Magnetic Resonance in Medicine*, **54**: 280-288 (2005).

215. E. A. Kramer, *Thermal Fusion for Sutureless Closure: Devices, Composition, Methods*, University of Colorado (2016).

216. H. Susi, *et al.*, *Biopolymers*, **10**: 1597-1604 (1971).

217. M. H. Pineri, *et al.*, *Biopolymers*, **17**: 2799-2815 (1978).

218. G. D. Fullerton, *et al.*, *Cell Biology International*, **30**: 66-73 (2006).

219. M. C. Tobin, *Raman spectroscopy*, in Methods in Enzymology, Academic Press (1972), pp. 473-497.

220. J. D. Eaves, *et al.*, *Chemical Physics Letters*, **376**: 20-25 (2003).

221. G. Giraud, *et al.*, *Biophysical journal*, **85**: 1903-1913 (2003).

222. F. Palombo and S. R. Meech, *The Journal of Physical Chemistry B*, **116**: 13481-13489 (2012).

223. X. Teng and W. Hwang, *Biomacromolecules*, **15**: 3019-3029 (2014).

224. F. H. Silver and W. J. Landis, *Viscoelasticity, Energy Storage and Transmission and Dissipation by Extracellular Matrices in Vertebrates*, in Collagen: Structure and Mechanics, ed. P. Fratzl, Springer (2008), pp. 133-154.

225. K. Kar, *et al.*, *Biochemistry*, **48**: 7959-7968 (2009).

226. A. V. Persikov, *et al.*, *Biochemistry*, **39**: 14960-14967 (2000).

227. J. P. R. O. Orgel, *et al.*, *Structure*, **9**: 1061-1069 (2001).

228. R. J. Radmer and T. E. Klein, *Biophysical journal*, **90**: 578-588 (2006).

229. K. Mizuno, *et al.*, *Journal of Biological Chemistry*, **278**: 32373-32379 (2003).

230. R. T. Raines, *Protein Science : A Publication of the Protein Society*, **15**: 1219-1225 (2006).

231. F. W. Kotch, *et al.*, *Journal of the American Chemical Society*, **130**: 2952-2953 (2008).

232. K. A. Hansen, *et al.*, *Journal of biomechanical engineering*, **124**: 72-77 (2001).

233. J. M. Berg, *et al.*, *Secondary Structure: Polypeptide Chains Can Fold Into Regular Structures Such as the Alpha Helix, the Beta Sheet, and Turns and Loops*, in Biochemistry, W H Freeman, 5th edition (2002).

234. S. Perticaroli, *et al.*, *Biophysical journal*, **106**: 2667-2674 (2014).

235. S. Perticaroli, *et al.*, *The Journal of Physical Chemistry Letters*, **6**: 4018-4025 (2015).
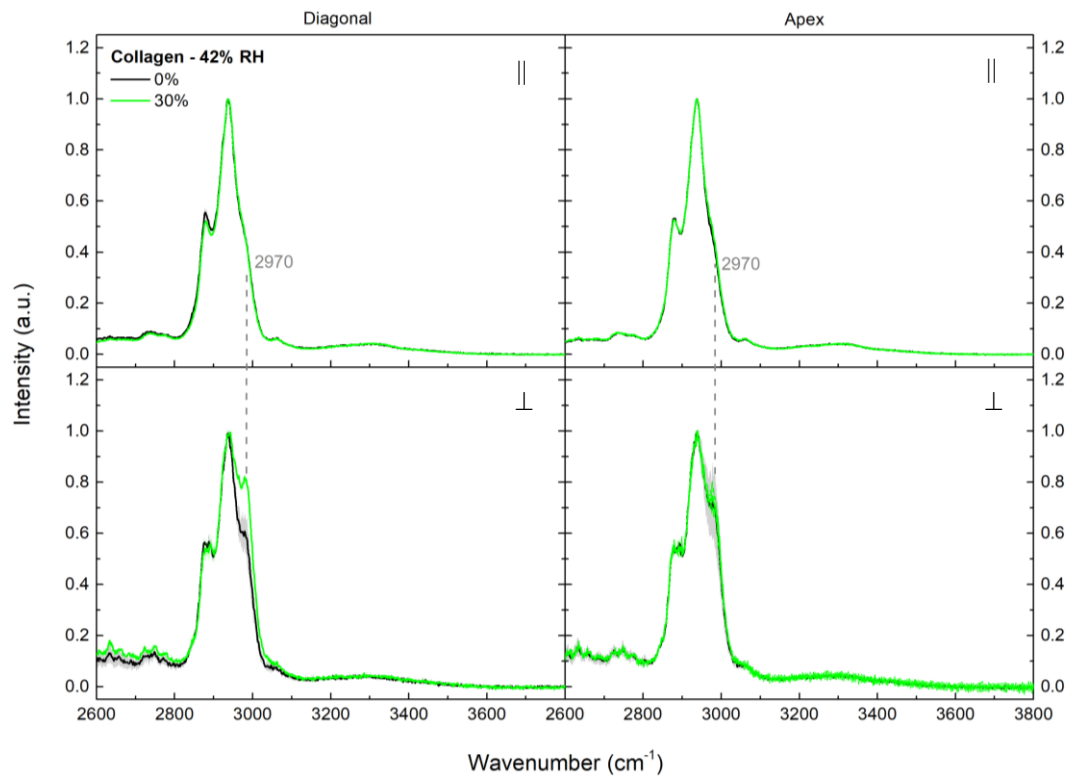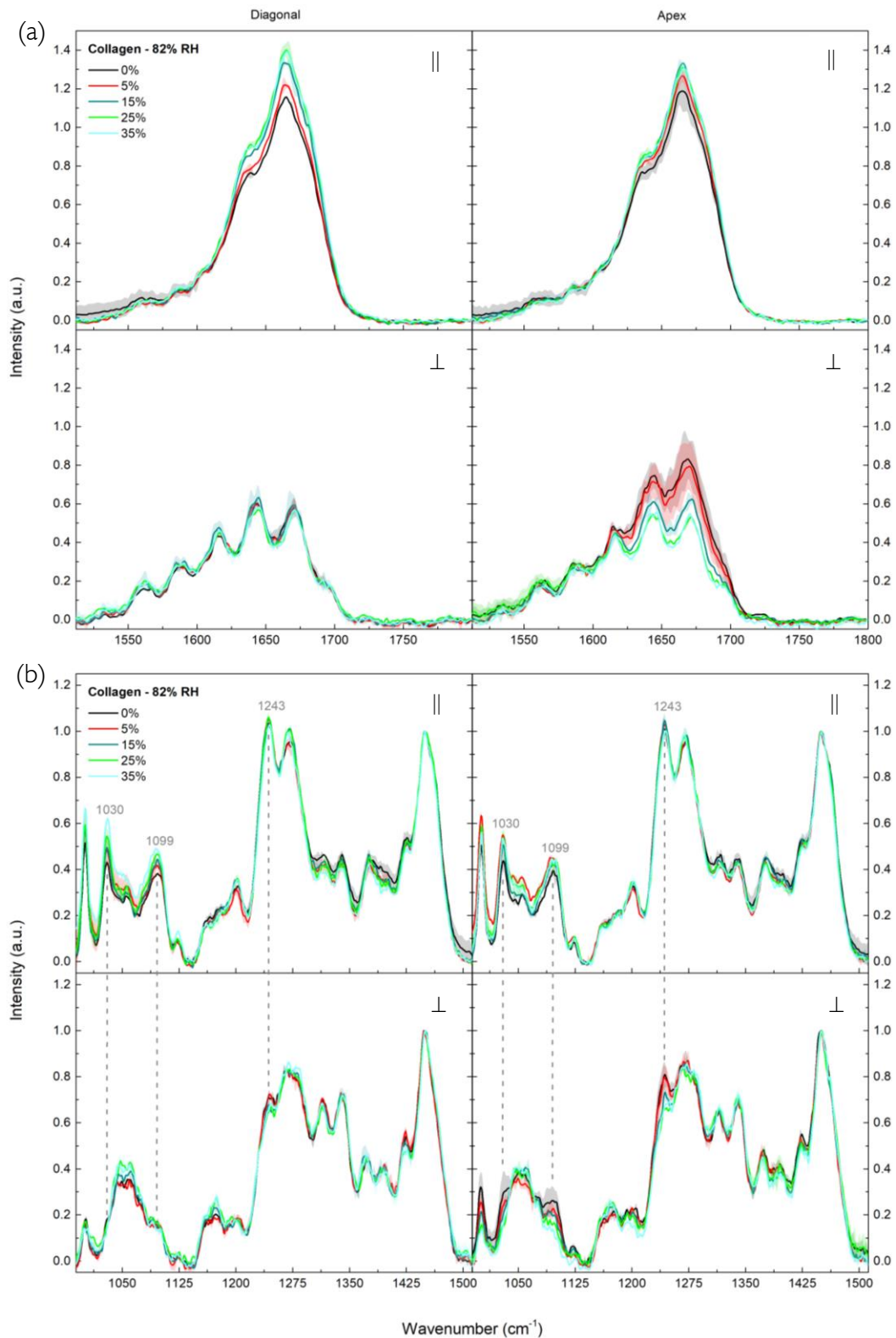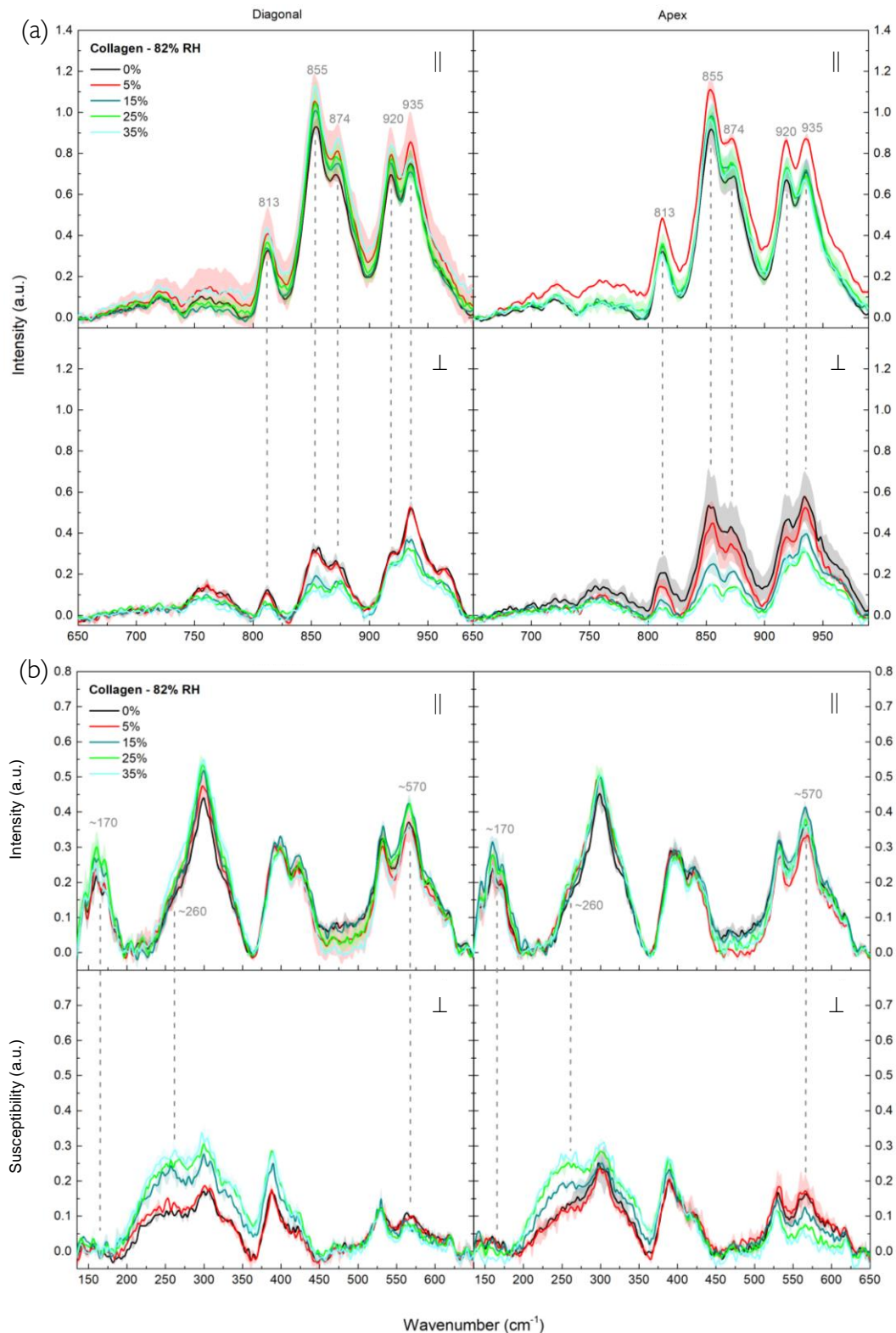
Appendix
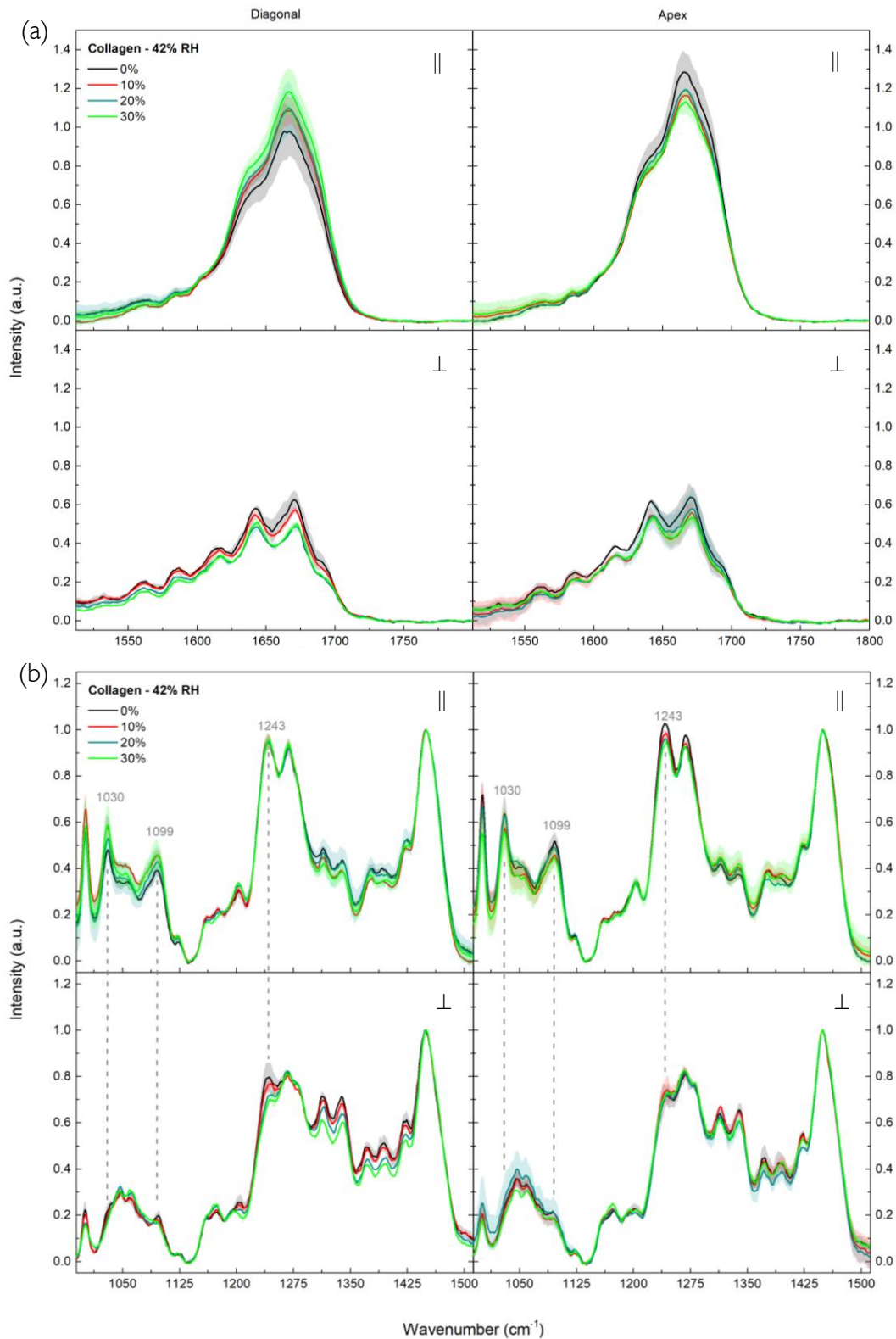
Figure A 1: Mean polarised Raman spectra showing the (a) Amide I and (b) Amide III spectral regions, of 42% RH native collagen fibres from rat tail tendon at a range of uniaxial tensile strains. Spectral changes are tracked in the diagonal (left) and apex (right) sections of the macroscopic fibre crimp as it opens under the applied strain (crimp fully opened at 30% strain). Each spectrum is an average of two points, baselined and normalised to the intensity of the CH_2 peak (1451 cm^{-1}). Shading denotes the standard deviation. Key peaks are highlighted between the polarised ($\parallel$) and depolarised spectra ($\perp$).
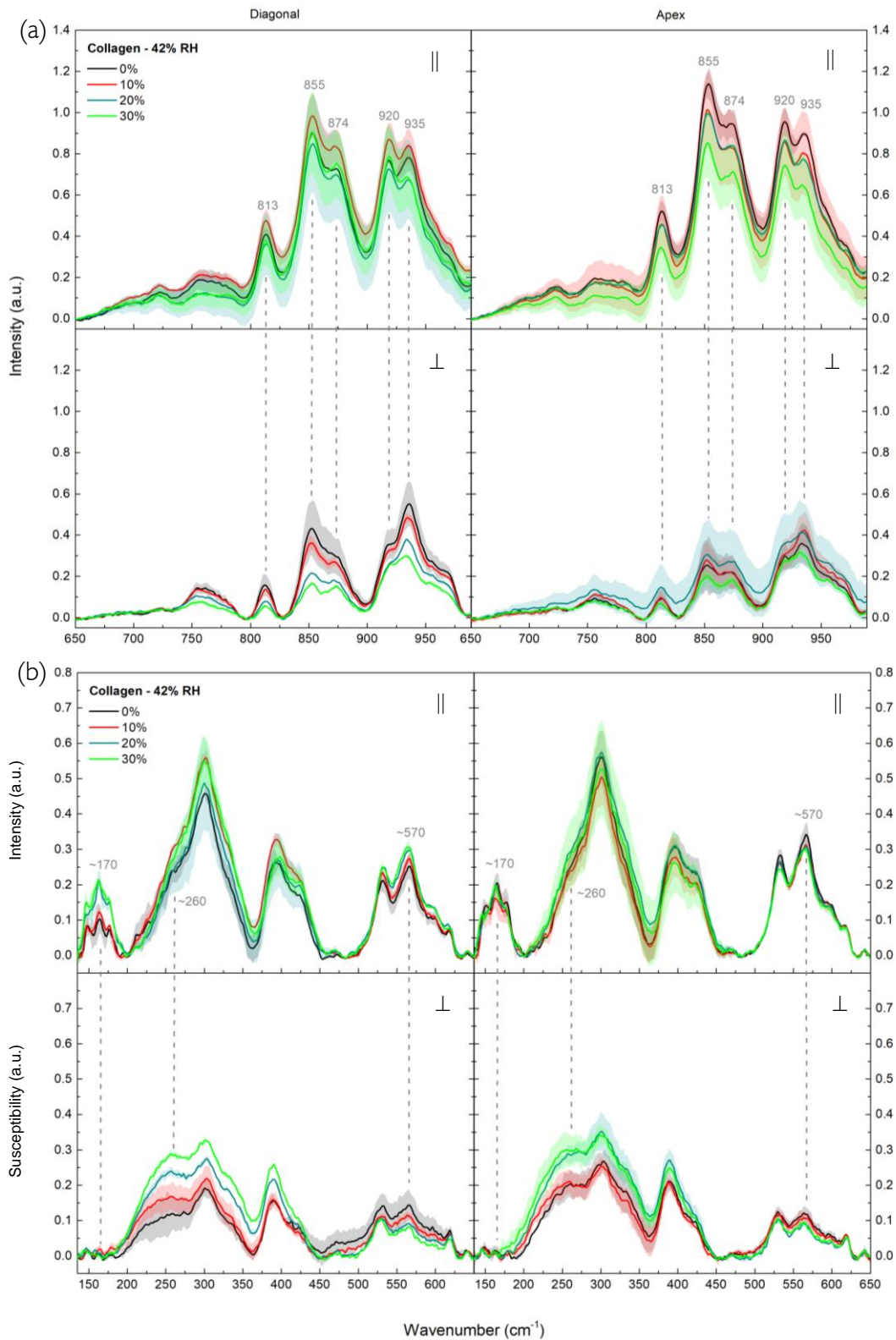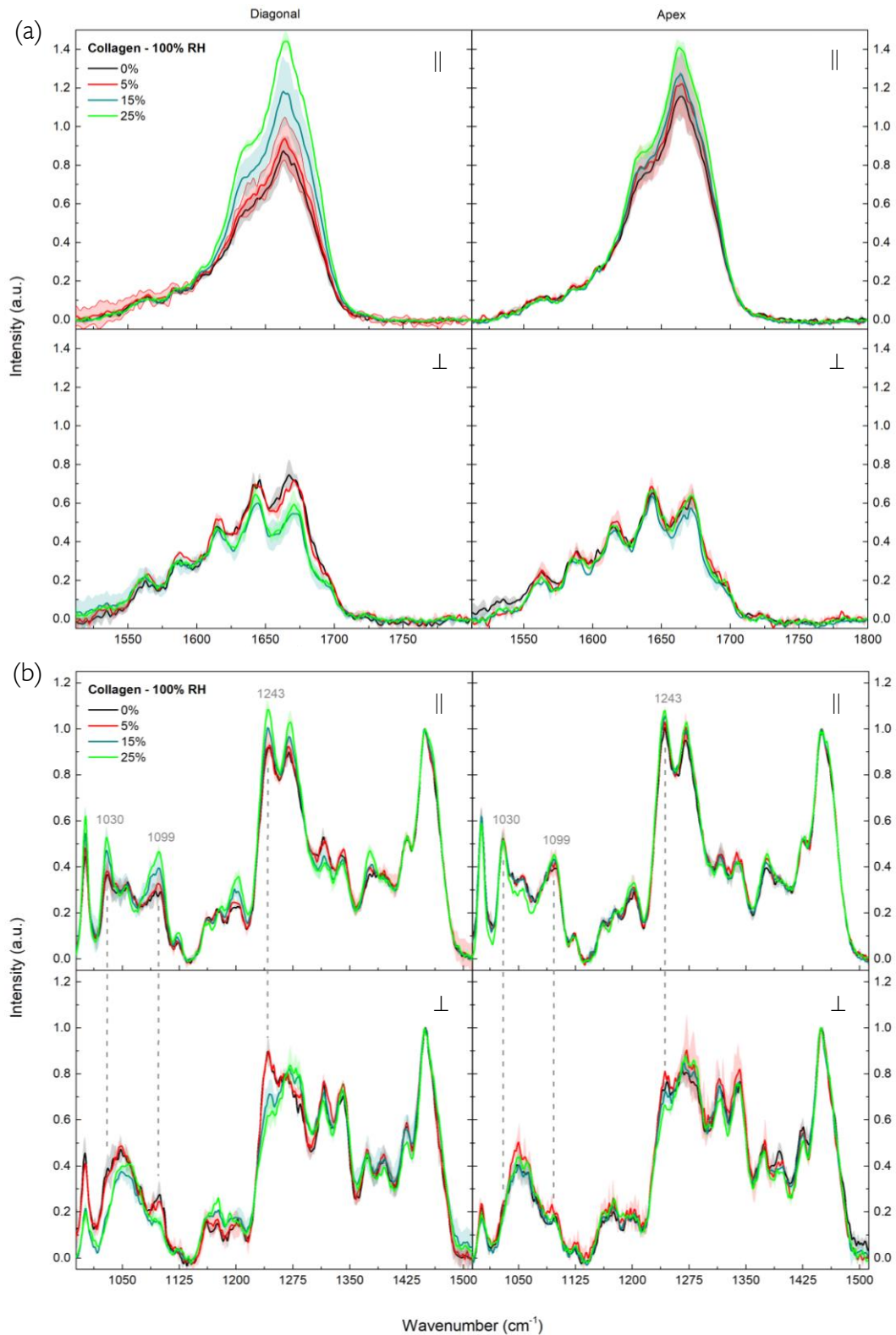
Figure A 2: Mean polarised Raman spectra showing the (a) C-C backbone and (b) LWN spectral regions, of 42% RH native collagen fibres from rat tail tendon at a range of uniaxial tensile strains. Spectral changes are tracked in the diagonal (left) and apex (right) sections of the macroscopic fibre crimp as it opens under the applied strain (crimp fully opened at 30% strain. Each spectrum is an average of two points, baselined and normalised to the intensity of the CH_2 peak (1451 cm^{-1}). Shading denotes the standard deviation. Key peaks are highlighted between the polarised ($\parallel$) and depolarised spectra ($\perp$). LWN depolarised spectra are plotted as susceptibility form.

Figure A 3: Mean polarised Raman spectra showing the HWN region of 42% RH native collagen fibres from rat tail tendon at minimum and maximum uniaxial tensile strains. Spectral changes are tracked in the diagonal (left) and apex (right) sections of the macroscopic fibre crimp as it opens under the applied strain (crimp fully opened at 30% strain). Each spectrum is an average of two points and is normalised to the intensity of the CH-band (2800-3040 cm^{-1}). Shading denotes the standard deviation. Key peaks are highlighted between the polarised (||) and depolarised spectra ($\perp$).

Figure A 4: Mean polarised Raman spectra showing the (a) Amide I and (b) Amide III spectral regions, of 82% RH native collagen fibres from rat tail tendon at a range of uniaxial tensile strains. Spectral changes are tracked in the diagonal (left) and apex (right) sections of the macroscopic fibre crimp as it opens under the applied strain (crimp fully opened at 35% strain). Each spectrum is an average of two points, baselined and normalised to the intensity of the CH_2 peak (1451 cm^{-1}). Shading denotes the standard deviation. Key peaks are highlighted between the polarised ($\parallel$) and depolarised spectra ($\perp$).

Figure A 5: Mean polarised Raman spectra showing the (a) C-C backbone and (b) LWN spectral regions, of 82% RH native collagen fibres from rat tail tendon at a range of uniaxial tensile strains. Spectral changes are tracked in the diagonal (left) and apex (right) sections of the macroscopic fibre crimp as it opens under the applied strain (crimp fully opened at 35% strain). Each spectrum is an average of two points, baselined and normalised to the intensity of the CH_2 peak (1451 cm^{-1}). Shading denotes the standard deviation. Key peaks are highl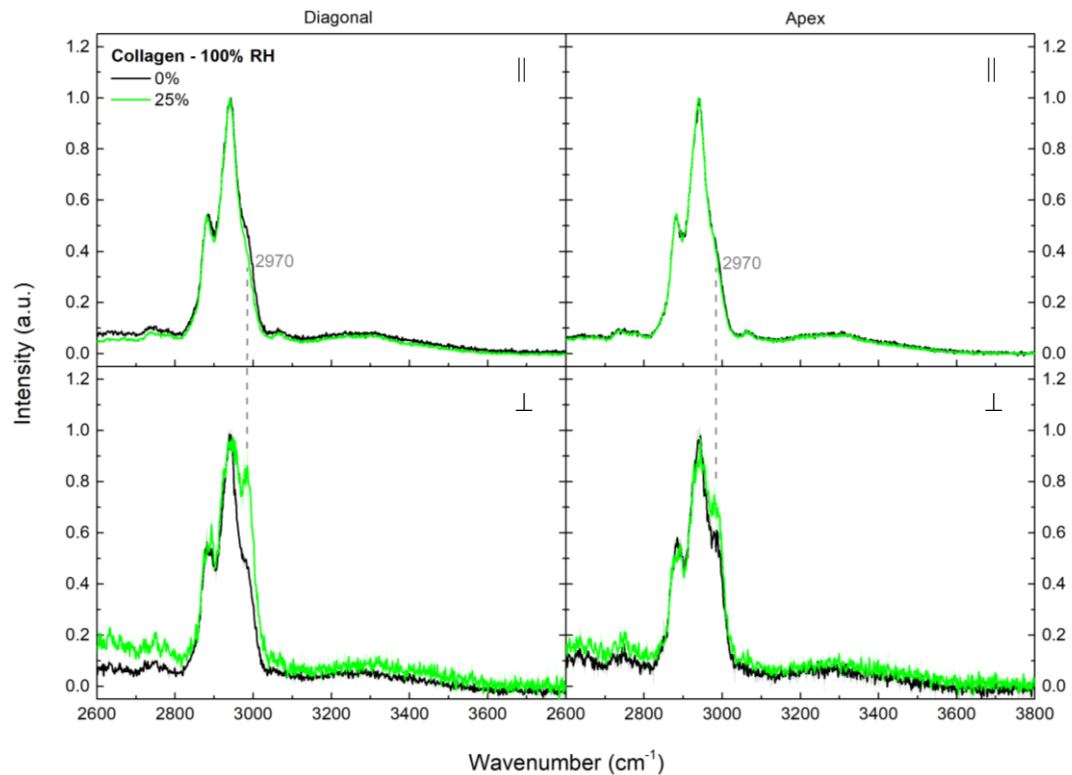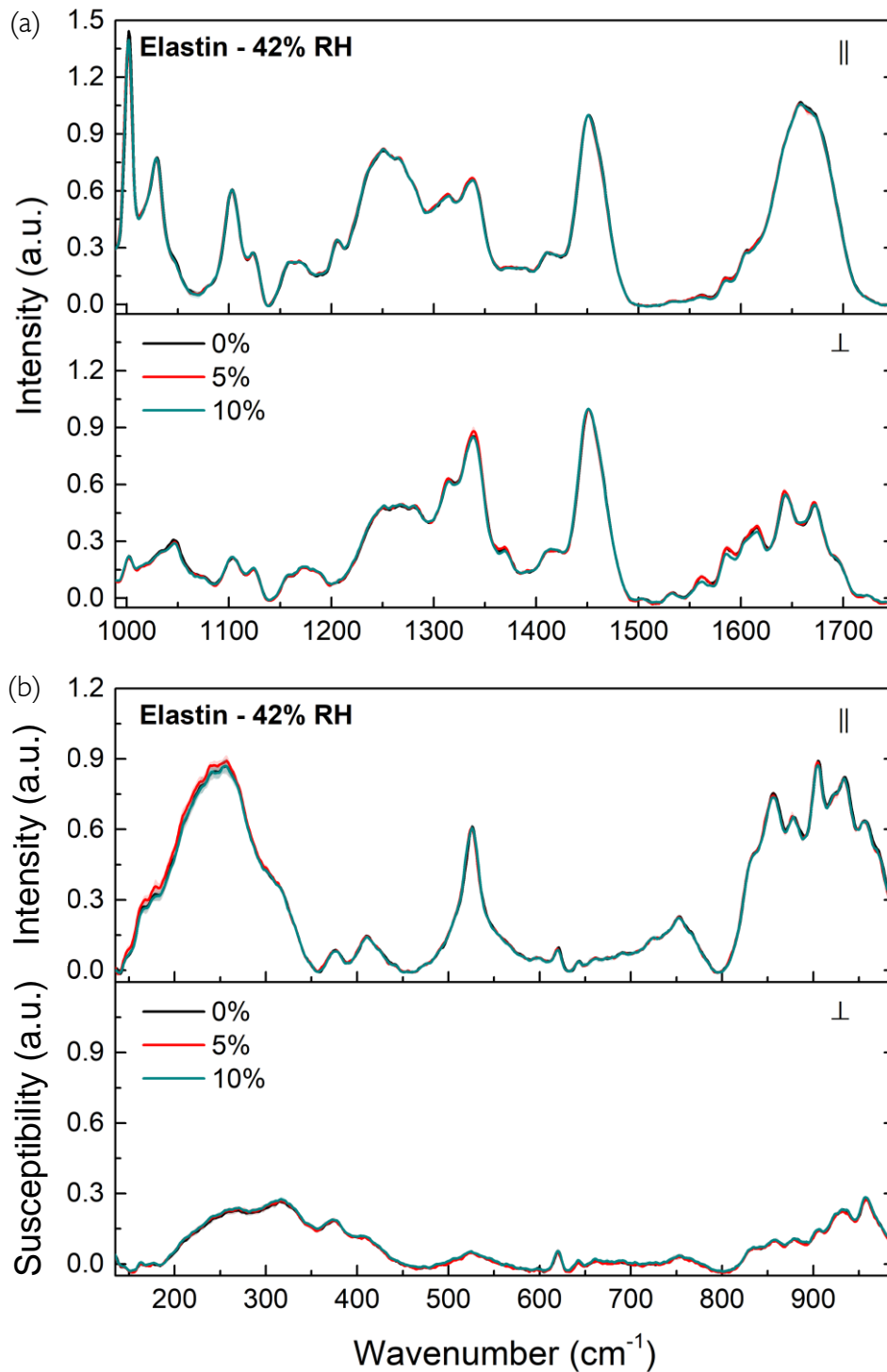ighted between the polarised (‖) and depolarised spectra ($\perp$). LWN depolarised spectra are plotted as susceptibility form.
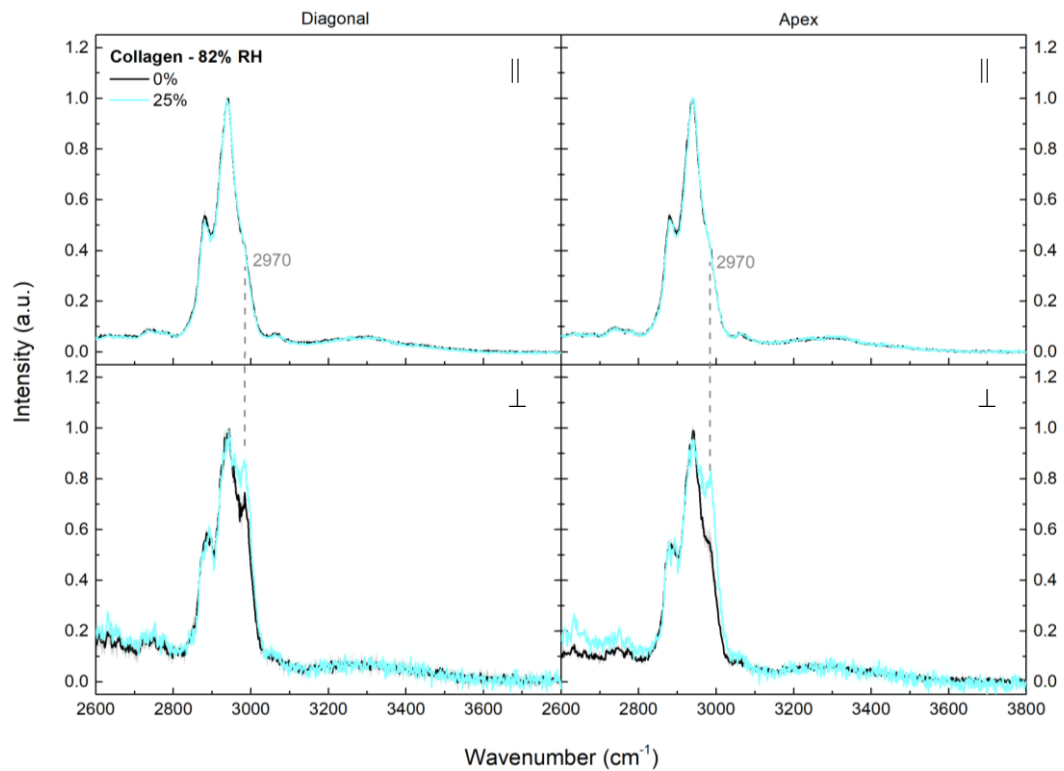
Figure A 6: Mean polarised Raman spectra showing the HWN region of 82% RH native collagen fibres from rat tail tendon at minimum and maximum uniaxial tensile strains. Spectral changes are tracked in the diagonal (left) and apex (right) sections of the macroscopic fibre crimp as it opens under the applied strain (crimp fully opened at 35% strain). Each spectrum is an average of two points and is normalised to the intensity of the CH-band (2800-3040 cm^{-1}). Shading denotes the standard deviation. Key peaks are highlighted between the polarised (‖) and depolarised spectra ($\perp$).
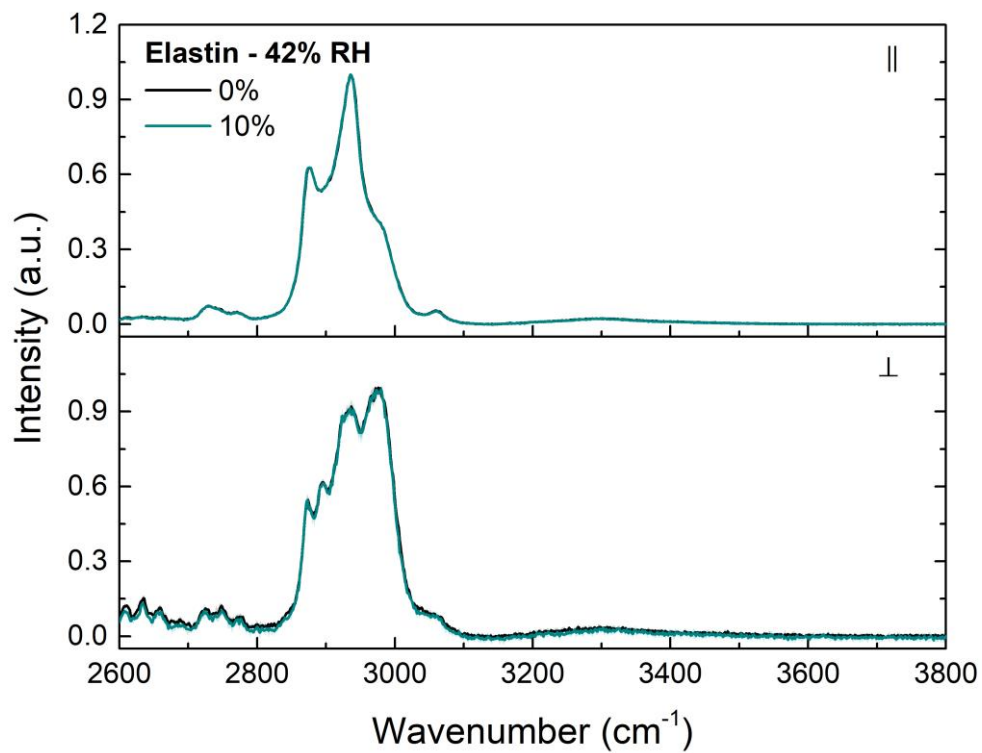
Figure A 7: Mean polarised Raman spectra showing the (a) Amide I and (b) Amide III spectral regions, of 100% RH native collagen fibres from rat tail tendon at a range of uniaxial tensile strains. Spectral changes are tracked in the diagonal (left) and apex (right) sections of the macroscopic fibre crimp as it opens under the applied strain (crimp fully opened at 25% strain). Each spectrum is an average of two points, baselined and normalised to the intensity of the CH_2 peak (1451 cm^{-1}). Shading denotes the standard deviation. Key peaks are highlighted between the polarised ($\parallel$) and depolarised spectra ($\perp$).
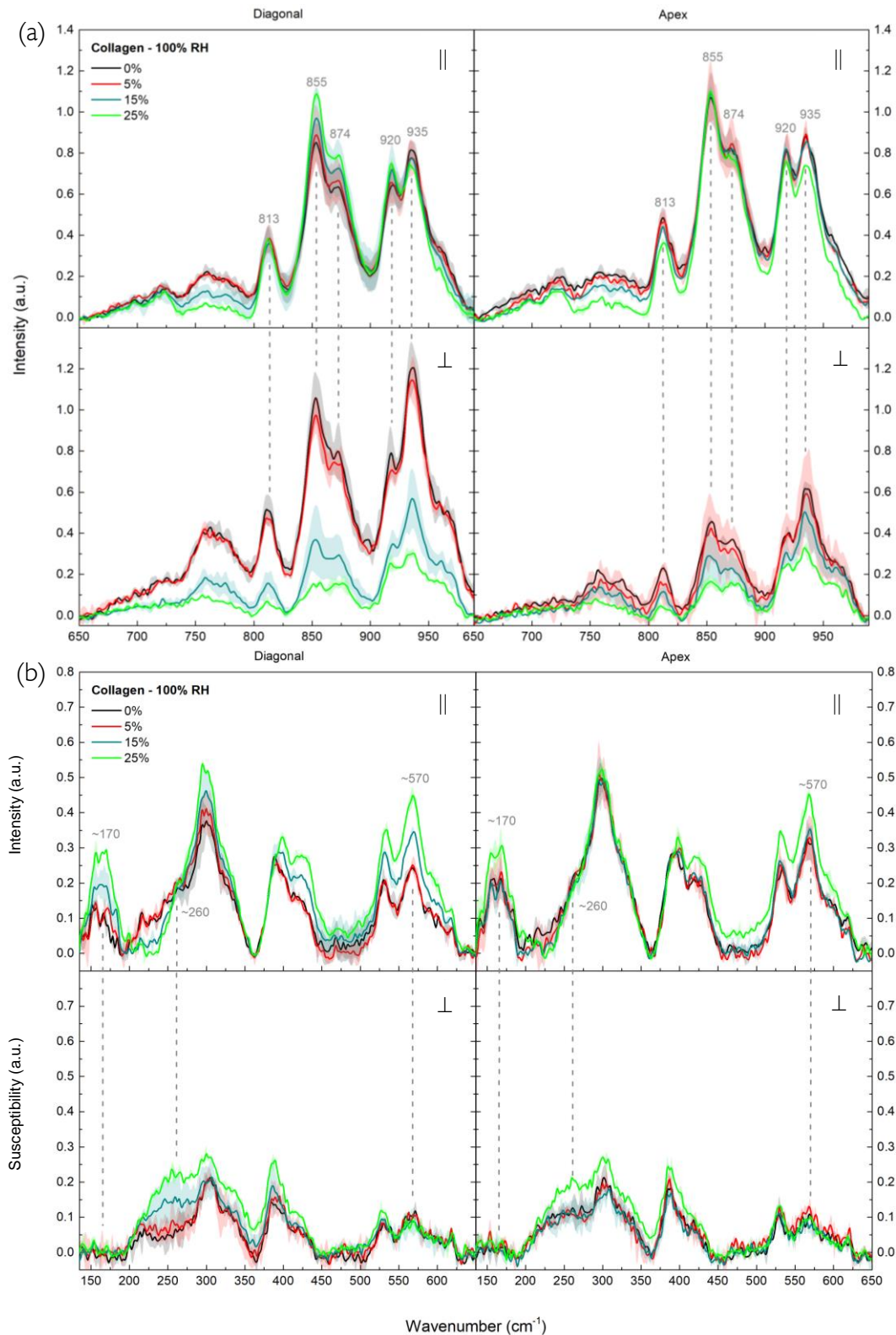
Figure A 8: Mean polarised Raman spectra showing the (a) C-C backbone and (b) LWN region, of 100% RH native collagen fibres from rat tail tendon at a range of uniaxial tensile strains. Spectral changes are tracked in the diagonal (left) and apex (right) sections of the macroscopic fibre crimp as it opens under the applied strain (crimp fully opened at 25% strain). Each spectrum is an average of two points, baselined and normalised to the intensity of the CH_2 peak (1451 cm^{-1}). Shading denotes the standard deviation. Key peaks are highlighted between the polarised (∥) and depolarised spectra (⊥). LWN depolarised spectra are plotted as susceptibility form.
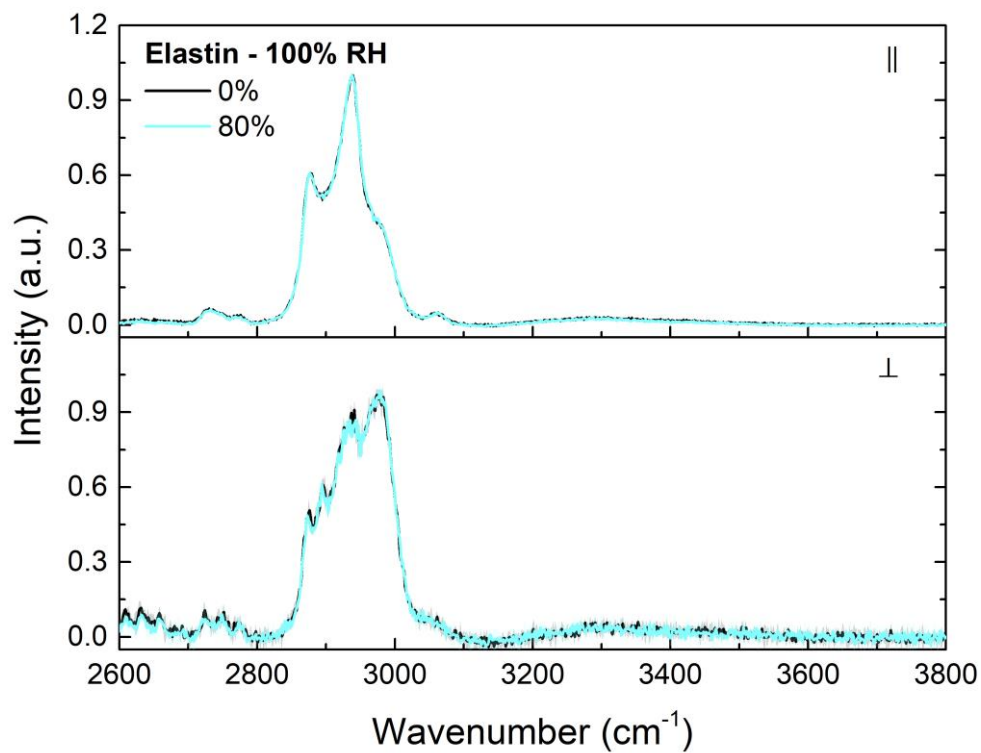
Figure A 9: Mean polarised Raman spectra showing the HWN region of 100% RH native collagen fibres from rat tail tendon at minimum and maximum uniaxial tensile strains. Spectral changes are tracked in the diagonal (left) and apex (right) sections of the macroscopic fibre crimp as it opens under the applied strain (crimp fully opened at 25% strain). Each spectrum is an average of two points and is normalised to the intensity of the CH-band (2800-3040 cm^{-1}). Shading denotes the standard deviation. Key peaks are highlighted between the polarised (‖) and depolarised spectra ($\perp$).

Figure A 10: Mean polarised (∥) and susceptibility corrected depolarised (⊥) Raman spectra comparing the (a) 989-1750 cm⁻¹ and (b) 135-989 cm⁻¹ spectral regions of 42% RH elastin fibres from bovine nuchal ligament at a range of uniaxial tensile strains. Each spectrum is an average of five points, baselined and normalised to the intensity of the CH_2 peak (1451 cm⁻¹). Shading denotes the standard deviation. LWN depolarised spectra are plotted as susceptibility form.

Figure A 11: Mean polarised (∥) and susceptibility corrected depolarised (⊥) Raman spectra showing the HWN region of 42% RH elastin fibres from bovine nuchal ligament at minimum and maximum uniaxial tensile strains. Each spectrum is an average of four points, baselined and normalised to the intensity of the CH-band (2800-3040 cm^{-1}). Shading denotes the standard deviation.
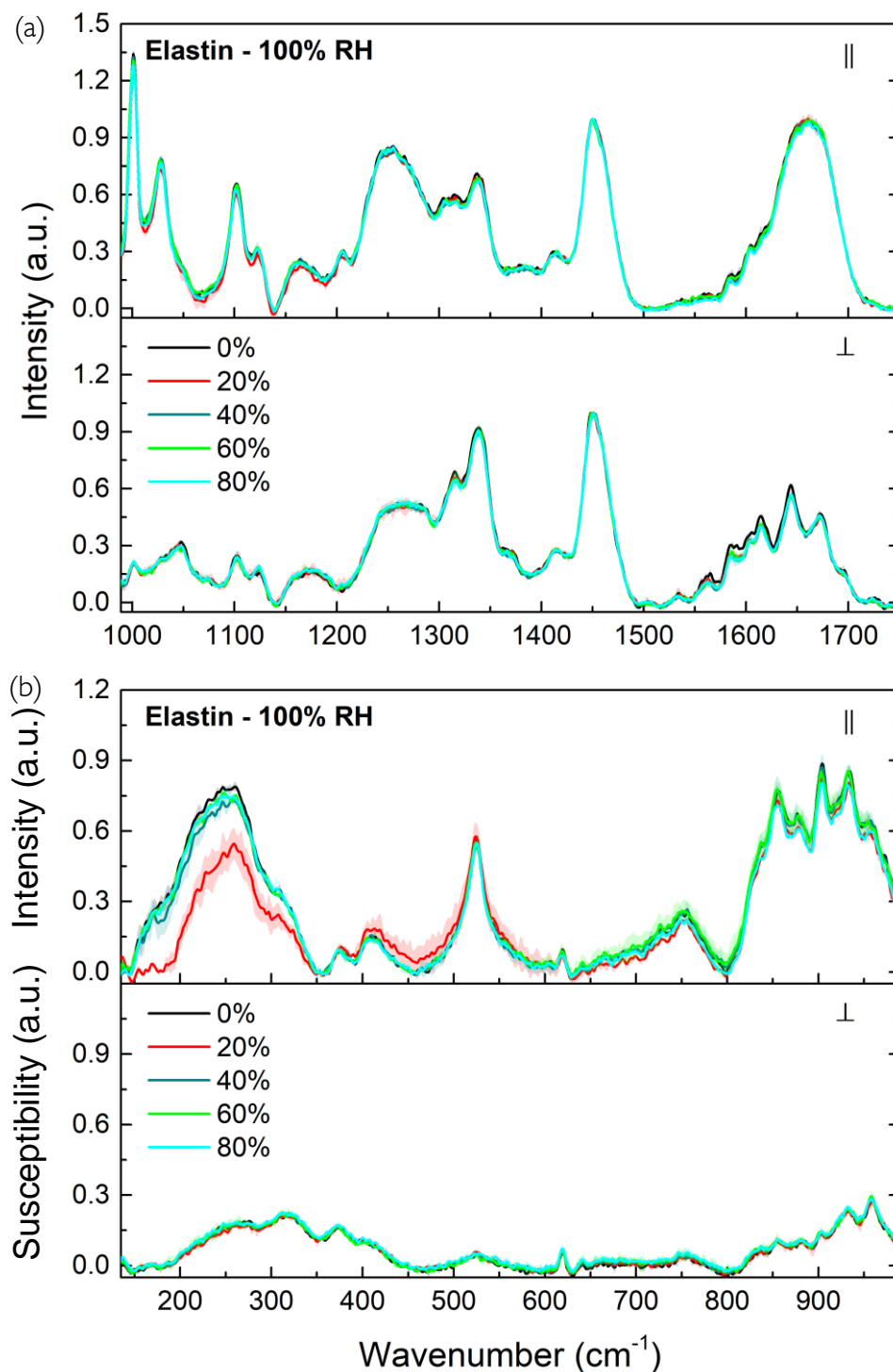
Figure A 12: Mean polarised (∥) and susceptibility corrected depolarised (⊥) Raman spectra comparing the (a) 989-1750 cm^{-1} and (b) 135-989 cm^{-1} spectral regions of 100% RH elastin fibres from bovine nuchal ligament at a range of uniaxial tensile strains. Each spectrum is an average of at least two points, baselined and normalised to the intensity of the CH$_2$ peak (1451 cm^{-1}). Shading denotes the standard deviation. LWN depolarised spectra are plotted as susceptibility form.

Figure A 13: Mean polarised (∥) and susceptibility corrected depolarised (⊥) Raman spectra showing the HWN region of 100% RH elastin fibres from bovine nuchal ligament at minimum and maximum uniaxial tensile strains. Each spectrum is an average of two points, baselined and normalised to the intensity of the CH-band (2800-3040 cm^{-1}). Shading denotes the standard deviation.
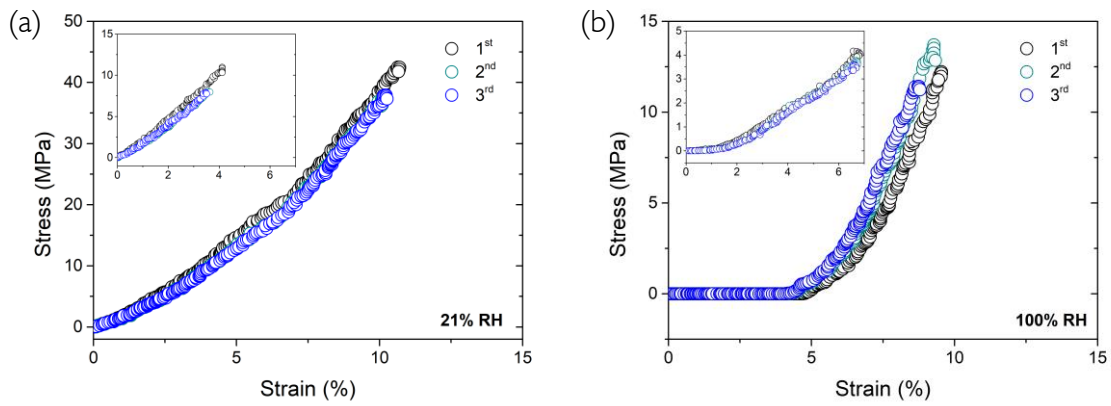
Figure A 14: stress-strain plots to qualify the similarity between the second and third extension cycles (to 10% strain) of a representative type-I collagen fibre at the hydration extremes (a) 21% RH and (b) 100% RH. The first three cycles are displayed. Inset shows the same fibres in the low-strain regime (to 5% strain).
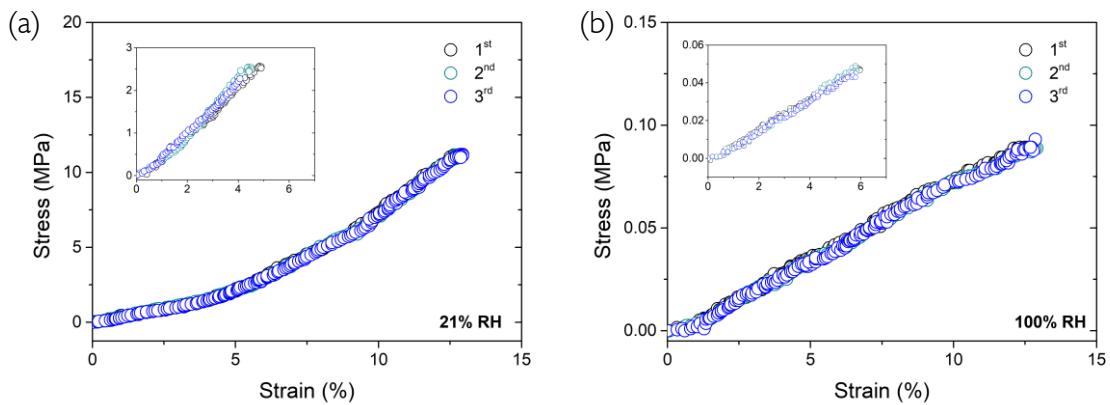
Figure A 15: stress-strain plots to qualify the similarity between the second and third extension cycles (to 10% strain) of a representative elastin fibre at the hydration extremes (a) 21% RH and (b) 100% RH. The first three cycles are displayed. Inset shows the same fibres in the low-strain regime (to 5% strain).
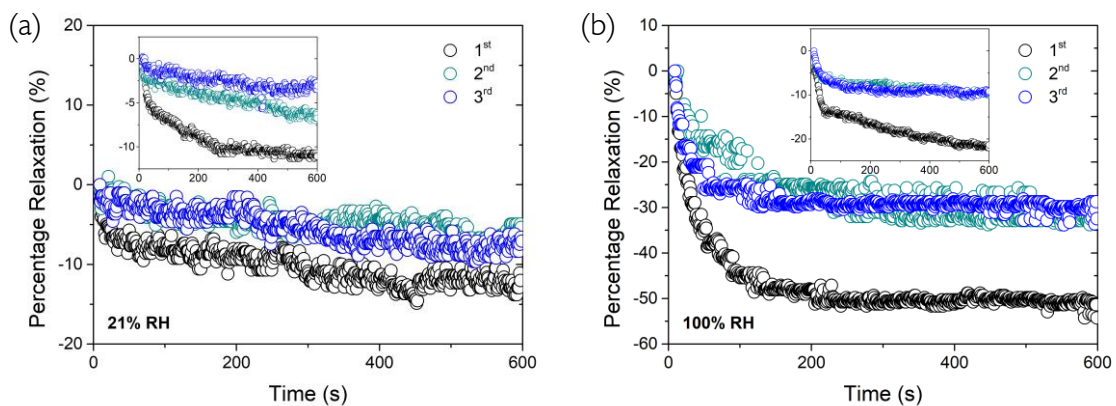
Figure A 16: percentage relaxation plots to qualify the similarity between the second and third rapid extension cycles (to 5% strain) of a representative type-I collagen fibre at the hydration extremes (a) 21% RH and (b) 100% RH. The first three cycles are displayed. Inset shows the same fibres in the high-strain regime (to 10% strain).

"Your Majesty, I beg you. They're all waiting down there. What shall we say to them? What can we say to them?" came Chernov's desperate plea.

"Nothing." She replied emphatically, turning towards the sea of sound flowing down the grandiose hallway. "Paul, your arm. I will speak to them."

"Oh thank you, your Majesty!" relief palpable in his voice, Chernov scurried ahead to announce the arrival of the Dowager Empress. The Prince of Haraldberg rose and took her hand in escort, "Forgive me Marie, but what will you say?".

"Say?", she replied lightly, the music swelling in the ballroom broiling with guests, "Oh, I shall say, 'The play is over. Go home.'

-    Anastasia (1956)